Desgin and Characterization of an Optoelectronic Laser Synchronization System for Spectrum and Network Analysis

Dissertation

Alexander Theis

RPTU Rheinland-Pfälzische Technische Universität Kaiserslautern Landau

Design and Characterization of an Optoelectronic Laser Synchronization System for Spectrum and Network Analysis

Dissertation

Alexander Theis

Vom Fachbereich Physik der Rheinland-Pfälzischen Technischen Universität Kaiserslautern - Landau zur Verleihung des akademischen Grades „Doktor der Naturwissenschaften“ genehmigte Dissertation

durchgeführt am

Fraunhofer-Institut für Techno- und Wirtschaftsmathematik in Kaiserslautern

unter Anleitung von

Prof. Dr. Georg von Freymann
Fachbereich Physik der Rheinland-Pfälzischen Technischen Universität Kaiserslautern - Landau

Zweitgutachter: Prof. Dr. Mathias Weiler

Datum der wissenschaftlichen Aussprache:
22. Oktober 2025

DE-386

Inhaltsverzeichnis

Abstract

As global reliance on high-speed data communication and advanced sensing technologies intensifies, the need for precise, high-performance measurement tools has become a strategic necessity for developing the next-generation devices and systems. Especially, test platforms for the characterization of signals and components in the upper microwave to terahertz frequency range are gaining critical relevance, as these spectral regions are expected to unlock new capabilities in bandwidth, resolution, and reliability for upcoming scientific and industrial applications. Nowadays, electronic spectrum and network analyzers are well-established instruments to perform these measurement tasks. Such platforms operate by sweeping the frequency across the desired measurement bandwidth to analyze signal parameters like amplitude, phase, impedance, and noise characteristics. In the radio, microwave, and millimeter-wave domains — ranging up to several tens of gigahertz — testing is typically carried out using commercially available, standalone systems that integrate signal generation, processing, and analysis in a single unit.

However, due to inherent limitations in scaling to higher frequencies, extending the frequency coverage into the terahertz band usually requires the addition of electronic extension modules. These modules upconvert lower-frequency signals into the terahertz range using nonlinear mixing processes and dedicated multiplier chains, while the received signals are similarly downconverted for analysis within the native bandwidth of the base instrument. Since each module is constrained in both bandwidth and output power, multiple units are often needed to cover a broad spectral range — significantly increasing the complexity and cost of such test solutions. Moreover, even in today's most advanced systems, the maximum achievable frequency remains limited to around 1.5 THz.

In this work, a novel approach to high-resolution spectrum and network analysis in the terahertz domain is presented, combining electronic and photonic technologies to enable high-frequency operation and precise signal characterization. The developed measurement systems are based on an optoelectronic — also called hybrid — concept for the frequency synchronization of laser beat signals with electronic narrow-band emitters. By phase-locking the laser difference frequency to the highly stable output of the electronic multiplier chains, the fundamental linewidth limitation of the individual lasers — typically in the megahertz range — can be effectively suppressed, resulting in a beat signal whose spectral purity is defined by the electronic reference. Sending these phase-locked signals to a biased photoconductive antenna (PCA), the narrow linewidth directly translates into the generation of highly coherent continuous-wave terahertz radiation. Similarly, at the receiver side, illuminating a second PCA with the phase-locked optical tones enables coherent detection of terahertz radiation, where the induced photocur-

rent carries both amplitude and phase information of the incoming terahertz wave. This optically driven heterodyne approach shifts generation and detection into the photonic domain, offering a reliable and accurate measurement platform for terahertz analysis with exceptional spectral resolution and phase stability, surpassing traditional photonic analyzer systems in terms of precision and versatility.

Unfortunately, the bandwidth and upper frequency limit of the system remain bound to the specifications of the electronic reference source. To overcome this constraint and extend the frequency range while preserving high spectral purity and phase coherence, additional lasers can be integrated in a cascaded configuration. Incorporating a third laser allows for the generation and detection of terahertz signals at frequencies up to twice the range defined by the electronic multiplier chain. Furthermore, by introducing a second reference source and accordingly tuning the laser frequencies relative to one another, seamless spectral coverage can be achieved, effectively closing gaps in the measurement bandwidth. Leveraging this hybrid concept, it is demonstrated in this thesis that nearly arbitrary terahertz signals can be generated and detected with hertz precision, extending up to 1 THz.

Building on this synchronization approach, a high-resolution photonic spectrum analyzer (PSA) and a photonic vector network analyzer (PVNA) were developed. While the PSA is designed as a standalone system capable of analyzing signals up to 1 THz, the PVNA is realized as an extension module for electronic network analyzers, serving as the backend. Owing to the PVNA configuration, one laser pair must be allocated to generate the stable intermediate frequency expected by the electronic backend, which, given the availability of only three lasers, restricts the measurement range to 70 GHz to 520 GHz. To evaluate the performance of the developed photonic systems, spurious harmonics from different multiplier chains are analyzed with the PSA, while the PVNA extender is used to characterize various bandpass filters and waveguides. The resulting measurements demonstrate strong agreement with comparison data from simulations and commercial extension modules, confirming the accuracy and reliability of the concepts.

Lastly, four-wave mixing (FWM) is explored as an alternative to laser cascading for extending the measurement range, where the beat signal from a laser pair is fed into an optical amplifier that generates conjugate frequencies through the nonlinear FWM process. By mixing the two conjugate frequencies, bandwidth tripling is achieved, significantly increasing the spectral coverage of the photonic systems. However, since the conjugate frequencies are significantly weaker than the original pump signals, effective filtering of the pump is required to use the signal for terahertz generation and detection. To address this, an experimental filtering setup is presented, utilizing two transmission gratings to spatially isolate and filter the respective frequency components. As a result, phase-locked beat signals with frequencies of more than 1 THz can be achieved using just a single laser pair, demonstrating potential for reaching even higher measurement bandwidths in future photonic concepts.

Kurzzusammenfassung

Mit dem wachsenden globalen Bedarf an schnellen Datenübertragungen und fortschrittlicher Sensortechnik steigt auch die Bedeutung präziser, leistungsfähiger Messinstrumente für die Entwicklung künftiger Hochfrequenz-Komponenten und -Systeme. Besonders Testplattformen zur Charakterisierung von Signalen im Mikrowellen- bis Terahertzbereich gewinnen zunehmend an Relevanz, da diese Spektralbereiche neue Möglichkeiten in Bandbreite, Auflösung und Zuverlässigkeit für wissenschaftliche und industrielle Anwendungen eröffnen. Elektronische Spektrum- und Netzwerkanalysatoren gelten dabei als etablierte Standardinstrumente. Sie analysieren Signalparameter wie Amplitude, Phase, Impedanz und Rauschen, indem sie die Frequenz innerhalb ihrer Messbandbreite durchstimmen. Im Radio-, Mikrowellen- und Millimeterwellenbereich bis zu mehreren zehn Gigahertz kommen hierfür meist kompakte Standalone-Lösungen zum Einsatz, die Signalverarbeitung und Analyse in einem Gerät vereinen.

Trotz steigender Leistungsfähigkeit stoßen elektronische Systeme bei sehr hohen Frequenzen schnell an physikalische Grenzen. Um dennoch den Terahertzbereich adressieren zu können, sind in der Regel zusätzliche Erweiterungsmodule notwendig. Diese wandeln niederfrequente Signale über nichtlineare Mischprozesse und Multiplikatorketten in höhere Frequenzen um, während eingehende Signale zurück in den Arbeitsbereich des Grundgeräts konvertiert werden. Da jedes Modul nur eine begrenzte Bandbreite und Ausgangsleistung bietet, sind oft mehrere Module notwendig, was Komplexität und Kosten der Messsysteme erheblich erhöht. Selbst modernste Systeme erreichen so derzeit maximal Frequenzen von 1,5 THz.

In dieser Arbeit wird ein neuer Ansatz für hochauflösende Spektrum- und Netzwerkanalysen im Terahertzbereich vorgestellt, der elektronische und photonische Technologien kombiniert, um Hochfrequenzsignale präzise zu charakterisieren. Die entwickelten Messsysteme beruhen auf einem optoelektronischen Verfahren, das Laserbeatfrequenzen mit elektronischen Schmalbandquellen synchronisiert und daher auch als hybrides Konzept bezeichnet wird. Die Phasensynchronisation der Laserdifferenzfrequenz mit der hochstabilen elektronischen Vervielfacherkette ermöglicht es, die Linienbreite des Beatsignals von einigen Megahertz auf die deutlich geringe Breite der Referenz zu reduzieren. Wird dieses Signal auf eine vorgespannte photoleitende Antenne gerichtet, erzeugt diese hochkohärente, kontinuierliche Terahertzstrahlung. Ebenso ermöglicht das Beleuchten einer zweiten photoleitenden Antenne mit dem phasensynchronisierten optischen Beat die kohärente Detektion der Terahertzstrahlung, wobei der induzierte Photostrom sowohl Amplituden- als auch Phaseninformationen der einfallenden Terahertzwelle enthält. Dieser Heterodyn-Ansatz verlagert sowohl die Erzeugung als auch die Detektion

in den optischen Bereich und bietet eine hochpräzise Messplattform für die Analyse von Terahertzsignalen, die durch überlegene spektrale Auflösung und Phasenstabilität herkömmliche photonische Systeme in puncto Genauigkeit und Vielseitigkeit übertrifft.

Trotz der hohen spektralen Auflösung und Phasenkohärenz bleibt die nutzbare Bandbreite des Systems durch die Spezifikationen der elektronischen Referenzquelle begrenzt. Um den Frequenzbereich dennoch erweitern zu können, lässt sich das Konzept durch zusätzliche Laser in kaskadierter Anordnung ergänzen. Die Integration eines dritten Lasers ermöglicht die Erzeugung und Detektion von Terahertzsignalen bei Frequenzen von bis zu zweimal der oberen Grenzfrequenz der elektronischen Multiplikatorkette. Wird zusätzlich eine zweite Referenzquelle eingesetzt und die Frequenzen der beteiligten Laser präzise aufeinander abgestimmt, lässt sich eine nahtlose spektrale Abdeckung erzielen, die bestehende Frequenzlücken in der Messbandbreite effektiv schließt. Mithilfe dieses Hybrid-Konzepts können nahezu beliebige Terahertzsignale mit Hertz-Präzision erzeugt und detektiert werden, wobei der Frequenzbereich auf bis zu 1 THz erweiteret wird.

Auf Grundlage dieses Synchronisations-Konzepts wurden im Rahmen dieser Arbeit ein hochauflösender photonischer Spektrumanalysator (PSA) sowie ein photonischer Vektor-Netzwerkanalysator (PVNA) entwickelt. Während der PSA als eigenständiges System zur Analyse von Signalen bis zu 1 THz konzipiert ist, wurde der PVNA als Erweiterungsmodul für elektronische Netzwerkanalysatoren realisiert. In der PVNA-Konfiguration ist ein Laserpaar für die Erzeugung der stabilen Zwischenfrequenz erforderlich, weshalb bei nur drei zur Verfügung stehenden Lasern die Messbandbreite auf 70 GHz bis 520 GHz beschränkt ist. Zur Demonstration der Leistungsfähigkeit der entwickelten photonischen Systeme wird der PSA zur Analyse parasitärer Harmonischer verschiedener Multiplikatorketten eingesetzt, während der PVNA zur präzisen Charakterisierung von Bandpassfiltern und Wellenleitern dient. Die Messergebnisse stimmen hervorragend mit Vergleichsdaten aus Simulationen und kommerziellen Erweiterungsmodulen überein und belegen damit die hohe Genauigkeit und Zuverlässigkeit der entwickelten Konzepte.

Abschließend wird Vier-Wellen-Mischen (VWM) als Alternative zur Laserkaskadierung zur Erweiterung der Messbandbreite untersucht. Dabei wird das Beatsignal eines Laserpaars in einen optischen Verstärker eingespeist, der durch den nichtlinearen VWM-Prozess konjugierte Frequenzen erzeugt. Durch das Mischen dieser konjugierten Frequenzen lässt sich eine effektive Bandbreitenverdreifachung erzielen, wodurch die spektrale Abdeckung der photonischen Systeme deutlich vergrößert wird. Da die konjugierten Frequenzen jedoch signifikant schwächer sind als die ursprünglichen Pumpsignale, ist eine effektive Filterung der Pumpfrequenzen erforderlich. Zu diesem Zweck wird ein experimentelles Filtersystem vorgestellt, das zwei Transmissiongitter verwendet, um die jeweiligen Frequenzkomponenten räumlich zu isolieren und anschließend zu filtern. Auf diese Weise können phasensynchronisierte Beatsignale mit Frequenzen von mehr als 1 THz mit nur einem einzigen Laserpaar erzeugt werden, was das Potenzial eröffnet, in zukünftigen photonischen Konzepten noch größere Messbandbreiten zu realisieren.

1 Introduction

Since the 1980s, mobile communication systems have evolved from analog voice transmission (1G) to today's high-speed, low-latency networks (5G), with each generation introducing significant advances in bandwidth, connectivity, and functionality (see Fig. 1.1). This evolution has not only transformed how we interact and exchange information but also laid the groundwork for rapid advancements across a broad spectrum of novel research areas — including next-generation wireless technologies [1–3], innovative sensing solutions [4–6], high-performance computing [7, 8], and artificial intelligence (AI) [9–11].

However, applications such as autonomous vehicles, smart factories, immersive extended reality, and AI-driven networks are already pushing current infrastructures to their technical and physical limits. As demands for higher data rates, ultra-low latency, greater precision, and seamless integration into intelligent systems continue to rise, this progression must accelerate to keep pace with the growing requirements of future key

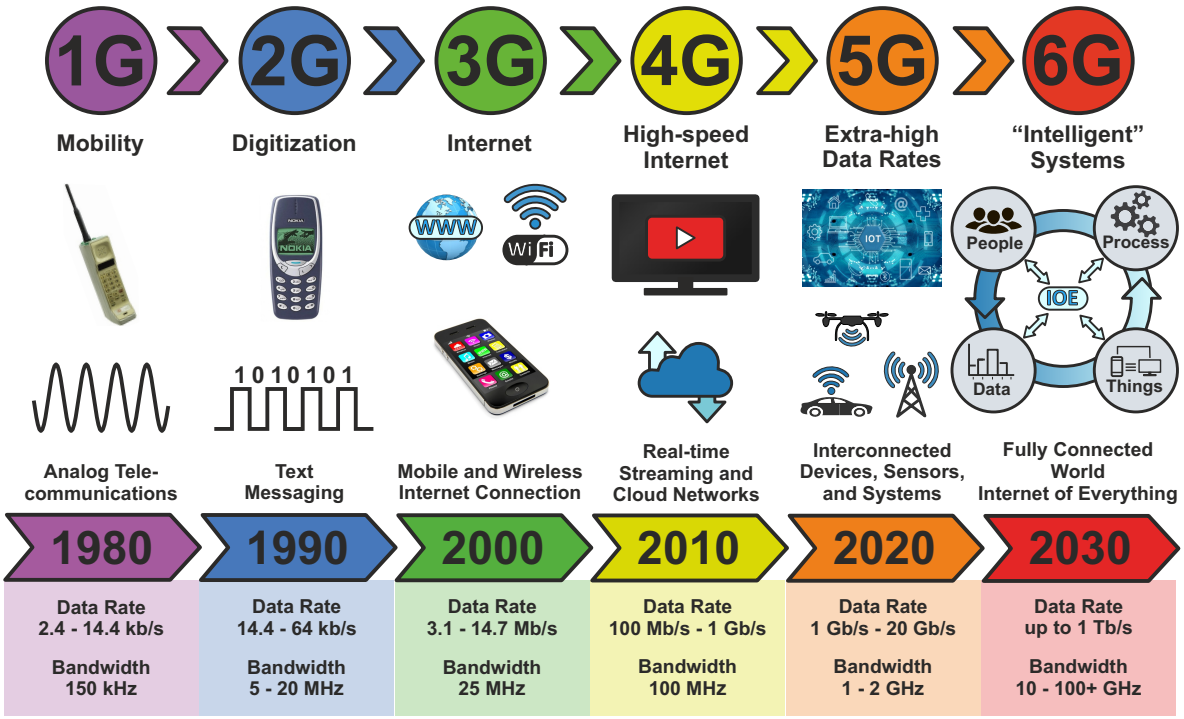

Figure 1.1: Timeline illustrating the evolution of mobile network generations from 1G to the anticipated 6G, highlighting key advancements in technology, bandwidth, and data rates.

technologies. In response, emerging visions such as 6G aim to meet these challenges by delivering terabit-per-second wireless communication, tightly integrated sensing, and enhanced network reliability — all by the end of this decade [12]. These ambitious goals, thus, raise fundamental questions: **Can today's systems and devices scale to this level of performance? And if not, what modifications in operating frequency, signal processing, and hardware design would be necessary to support these extremely high data rates?**

In this context, the terahertz domain is envisioned as a key technology enabler, due to the unique characteristics of terahertz waves and the largely unoccupied, unregulated spectrum available in this frequency range. Current wireless systems, including those based on 5G standards, primarily operate within the sub-6 GHz band and the lower millimeter-wave (mm-wave) spectrum between 30 GHz and 100 GHz. To overcome the inherently limited bandwidth in these regions and boost data rates, advanced communication techniques such as orthogonal frequency division multiplexing (OFDM) and large-scale multiple input multiple output (MIMO) are employed to enhance efficiency. While OFDM divides the available bandwidth into multiple subcarriers to minimize interference and maximize data transmission, MIMO systems use multiple antennas at both the transmitter and receiver to increase throughput by creating parallel data streams. For instance, in long-term evolution advanced (LTE-A) networks, peak transmission speeds of around 1 Gbps can be achieved using a four-by-four MIMO configuration over an aggregated bandwidth of 100 MHz [13]. Still, these transfer rates remain three orders of magnitude lower than the anticipated 1 Tbps target. To bridge this gap, the transition to the terahertz band becomes the only viable solution, offering a significantly larger bandwidth capable of supporting the required ultra-high data rates. Recent major initiatives have been launched to realize the 6G vision, including the U.S.-led Next G Alliance [14], Europe's Hexa-X-II flagship project [15], and Germany's 6G-ANNA program (6G Access, Network of Networks and Automation) [16], funded by the German Federal Ministry of Research, Technology, and Space (BMFTR). These efforts increasingly focus on the terahertz spectral region, highlighting the need for novel technologies and architectures to harness its potential.

However, before delving into the opportunities and challenges this frequency domain presents for next-generation 6G systems and, particularly in the scope of this thesis, the associated measurement and development tools, it is crucial to first explore the terahertz spectrum itself — a previously overlooked part of the electromagnetic spectrum.

1.1 The Terahertz Spectral Range

Spanning frequencies from 0.1 THz to 10 THz, the terahertz band is located between the microwave and infrared regions of the electromagnetic spectrum, corresponding to wavelengths from 3 mm down to 30 µm (see Fig. 1.2). Accordingly, this spectral range connects the domains of electronics and photonics, characterized by unique physical

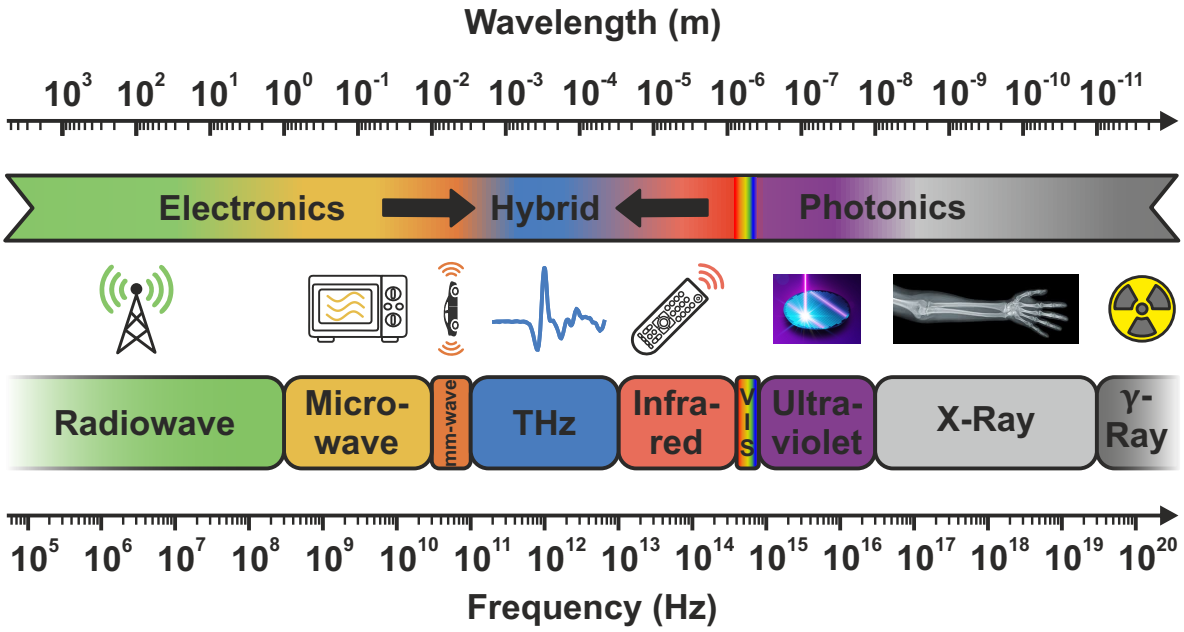

Figure 1.2: Illustration of the terahertz domain within the electromagnetic spectrum, spanning frequencies from 0.1 THz to 10 THz and corresponding wavelengths from 3 mm to 30 µm. This region marks the transition between electronic and photonic technologies.

properties such as non-ionizing photon energies, sub-millimeter spatial resolution, and strong penetration capabilities through a wide range of non-metallic materials. These features make terahertz radiation particularly attractive not only for upcoming wireless communication technologies but also for applications in materials science and characterization [17–19], non-destructive testing (NDT) [20–22], (bio-)medical imaging [23, 24], security screening [25–27], and ultrafast spectroscopy [28, 29].

Although scientific interest in terahertz radiation dates back to as early as 1893 [30], the field remained difficult to access for much of the 20th century due to the lack of suitable sources and detectors. This persistent technological limitation led to the introduction of the term “terahertz gap” [31], revealing the stark contrast between the rapid advancements in microwave and optical technologies and the relative stagnation in the terahertz domain. However, in recent decades, significant breakthroughs in both electronics and photonics have paved the way for the development of efficient terahertz sources and detectors, gradually closing this gap. As the terahertz region lies at the border between microwave and optical domains, two primary strategies for generation and detection have emerged: upconversion of microwave frequencies, where an electrical signal is converted into the terahertz band through frequency multiplication, and heterodyne downconversion, where a terahertz signal is generated by beating two lightwaves on a photomixer. Moreover, pulsed radiation — fundamental to terahertz time-domain spectroscopy (TDS), one of the most powerful techniques for investigating material properties in the terahertz range — can be produced through optical rectification in nonlinear crystals or by using photoconductive switches driven by femtosecond lasers.

Despite the advancements in terahertz technology, the field still faces several challenges. One limitation is its penetration capability, which is restricted when interacting with dense materials or metals, as terahertz waves are strongly absorbed or reflected by them. Additionally, terahertz radiation suffers from significant atmospheric attenuation, particularly due to water vapor, which reduces its effectiveness for long-range free-space communication. Nevertheless, specific transmission windows exist within the terahertz spectrum — such as the bands from 121 GHz to 154 GHz and from 252 GHz to 296 GHz — where atmospheric attenuation remains below 10 dB over distances exceeding several kilometers, making them suitable for medium- to long-range wireless communication links [12]. Beyond these inherent physical constraints, a number of technical hurdles still need to be overcome. In particular, generating terahertz radiation with sufficient power and spectral purity is a demanding task, especially at higher frequencies. Conventional electronic sources often lack the bandwidth needed for broadband applications, while photonic approaches typically experience limitations in frequency stability. Furthermore, the high cost of terahertz technologies, combined with the complexity of advanced system architectures, presents a significant barrier to their widespread adoption.

Nevertheless, the unique position of terahertz radiation in the electromagnetic spectrum allows for hybrid approaches that integrate both electronic and photonic techniques. This synergy enhances the performance and flexibility of terahertz systems while also reducing costs. Building on this hybrid concept, the measurement platforms developed in this thesis combine the frequency stability of electronic sources with the broad bandwidth of photonic schemes to enable high-resolution spectrum and network analysis in the terahertz domain, an essential tool for the design, testing, and optimization of next-generation high-frequency (HF) components and devices.

1.2 Terahertz Network Analysis

Generally, spectrum (SAs) and (vector) network analyzers (VNAs) are fundamental instruments that measure and visualize the frequency characteristics of electronic or optical signals. While SAs analyze the amplitude across different frequencies, VNAs are primarily used to evaluate the transmission and reflection properties of networks or devices over a broad frequency range. For this purpose, the frequency is swept through the measurement bandwidth, capturing key metrics like power level, phase shift, and impedance matching to characterize the behavior of the component or material under test. To ensure the accuracy and resolution of such measurements — especially when analyzing narrow-band features or subtle variations in sample response — high frequency stability is essential.

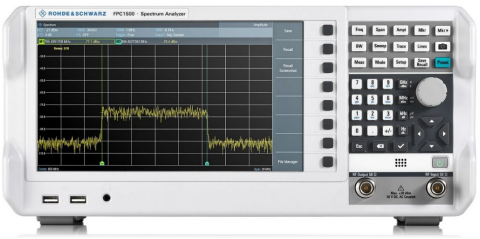

Figure 1.3: Example of a commercial electronic microwave spectrum analyzer [32].

In traditional radio and microwave applications, this requirement is less critical, as the core architectures of spectrum and network analyzers rely on purely electronic signal generation and detection, where sufficient stability is more easily achieved. In contrast, when using heterodyne photonic approaches, frequency stability becomes a major challenge. As the intrinsic linewidth of the laser sources is typically limited to the kilohertz or even megahertz range, significant phase noise and frequency drift can occur, substantially degrading the accuracy and resolution of the measurement system.

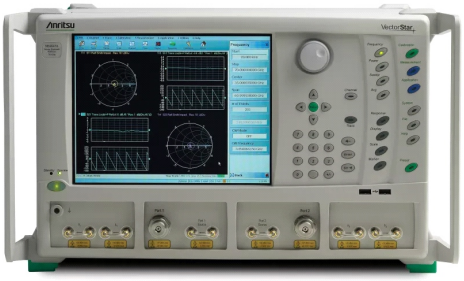

Figure 1.4: Commercial electronic vector network analyzer system [33].

Therefore, SAs and VNAs operating in the radio-frequency (RF) to upper microwave domain (up to around 20 GHz) primarily rely on direct electronic signal generation using voltage-controlled oscillators (VCOs) or other tunable sources.

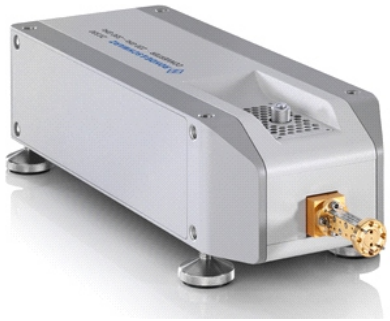

Figure 1.5: Frequency extension module for electronic microwave vector network analyzers [34].

However, at frequencies reaching into the upper millimeter-wave and the terahertz band, this approach becomes impractical due to fundamental limitations of electronic devices. Conventional oscillators experience a sharp decline in gain and output power at higher frequencies because of increased parasitic capacitances and reduced carrier mobility, preventing stable and efficient signal generation. Consequently, to cover the intended frequency range, diodes with highly nonlinear I-V characteristics are employed to multiply the electrical baseband signals from the microwave oscillator. In commercial systems, this is typically accomplished with frequency extension modules, which can be integrated into existing microwave SAs and VNAs to expand their measurement capabilities to the terahertz domain.

1.3 State-of-the-art Solutions

Relying on external extension modules, modern state-of-the-art analyzers are capable of generating and measuring signals at frequencies of up to 1.5 THz [35]. Achieving such high frequencies generally requires several multiplier stages for signal generation, along with harmonic mixers to downconvert the received terahertz tone to the baseband. While this approach enables precise and calibrated measurements within defined frequency bands, it comes with inherent trade-offs. The output power available from frequency multipliers decreases significantly with increasing frequency, often resulting in signal levels below 1 µW in the upper terahertz range. This substantially limits the overall system dynamic and degrades measurement sensitivity at higher frequencies. Moreover,

Table 1.1: Overview of commercial frequency extension modules. Data taken from [36].

Waveguide Band	Frequency Coverage (GHz)	Dynamic Range (BW = 10 Hz, dB)	Test Port Power (dBm, typical)
WR10	75–110	120	18
WR8.0	90–140	120	16
WR6.5	110–170	120	13
WR5.1	140–220	120	6
WR4.3	170–260	115	4
WR3.4	220–330	115	1
WR2.2	330–500	110	−3
WR1.5	500–750	110	−12
WR1.0	750–1100	95	−23
WR0.65	1100–1500	60	−45

limitations due to frequency cutoffs and multimode behavior toward the upper end of the frequency band restrict each module's bandwidth to about 50% of its center frequency. As a result, at least eight distinct modules are needed to cover the range from 0.075 THz to 1.5 THz (see Table 1.1). This increases system complexity and cost, while also complicating calibration and alignment, especially at higher frequencies where smaller waveguide dimensions demand tighter tolerances.

In response, photonic approaches for spectrum and network analysis have attracted increasing attention over the past decades. By employing optical heterodyning or pulsed techniques for generating and detecting terahertz signals, these systems offer significant advantages such as broad frequency tunability, reduced system complexity, and compatibility with fiber-coupled or free-space configurations. Photonic architectures are therefore emerging as a promising alternative to traditional electronic solutions for future terahertz metrology, particularly in broadband and high-resolution applications.

Although still limited in number, photonic techniques for terahertz spectrum analysis are already commercially available. For example, Toptica Photonics offers two systems for terahertz spectrum analysis, both utilizing optical signal detection with photoconductive antennas (PCAs). While TeraScan [37] facilitates frequency-domain measurements with megahertz resolution across a tunable range up to 2.7 THz, TeraFlash [38] provides time-domain spectroscopy with broadband coverage up to 6 THz and a resolution of 0.4 GHz. However, these systems are specialized spectrometers optimized for the characterization of specific terahertz signals under controlled excitation conditions, rather than multipurpose spectrum analyzers in the classical sense.

Looking toward photonic vector network analyzers (PVNA), no commercially available solutions exist at present. Nevertheless, numerous research efforts have demonstrated the potential of photonic VNAs, following the introduction of the PVNA concept for terahertz measurements by Criado *et al.* in 2012 [39]. For example, two pulsed PVNA systems have been demonstrated with frequency ranges of 0.07 THz to 2.5 THz [40] and 0.2 THz to 2 THz [41], along with a continuous-wave (CW) concept covering 0.1 THz to 1 THz [42]. In the pulsed systems, a femtosecond laser is used to drive different PCAs for network analysis. Owing to the pulsed nature of the generated terahertz signal, these approaches can span extremely broad frequency ranges within relatively short acquisition times. However, the architecture typically involves bulky setups with mechanical delay stages and various free-space optics, limiting the spectral resolution to a few gigahertz. Moreover, characterizing nonlinear devices such as mixers or diodes presents additional challenges for time-domain techniques. The simultaneous presence of multiple frequencies can lead to complex interference patterns and signal distortions, making it difficult to isolate and analyze specific nonlinear effects. Thus, CW methods are generally preferred for VNA applications as they allow precise control over individual frequencies. The CW system outlined in [42] utilizes two temperature-stabilized semiconductor laser diodes to drive emitting and receiving photomixers. In this configuration, the achievable measurement accuracy is limited by the frequency stability of the lasers, typically within the megahertz range. Still, the frequency resolution attainable with this approach lags far behind that of modern electronic VNAs, which can resolve frequencies with sub-hertz precision, exceeding the CW system's precision by more than six orders of magnitude.

To overcome these limitations, a promising strategy is to phase-lock both lasers to a common reference, thereby stabilizing the laser beat note. In 2024, Rohde & Schwarz introduced a proof-of-concept demonstrating an ultra-stable, tunable terahertz system based on frequency comb technology [43]. This system relies on two CW lasers, each phase-locked to a different line of a highly stable optical frequency comb (OFC) that provides a common frequency reference. The OFC consists of a series of equally spaced spectral lines defined by $f_n = f_0 + nf_{\mathrm{rep}}$, where n is an integer, f_{rep} is the repetition rate, and f_0 is the frequency offset. By locking each CW laser to a selected comb line — generally by stabilizing the beat note between the laser and its nearest comb tooth — their absolute frequencies become traceable to the same RF reference. Although the concept is primarily designed for 6G wireless communication, it can also be extended to component characterization in VNA-like setups, enabling coherent detection of terahertz signals with high amplitude and phase resolution.

Additionally, complementary photonic spectrum analyzer (PSA) concepts have been proposed based on mode-locked laser (MLL) sampling [44, 45], dual-comb detection [46], or frequency-swept photonic local oscillators [47], each offering frequency stability down to the hertz level.

1.4 Scope and Structure of the Thesis

Although photonic concepts for spectrum and network analysis have been explored for nearly two decades and some systems are commercially available, they have not yet achieved widespread practical use. A key reason is the complexity and size of these architectures, which perform well in laboratory settings but are not suited for industrial settings. Systems based on OFCs or MLLs require numerous optical components, precise timing, and stable environmental conditions, making robust, compact integration challenging. As a result, terahertz spectrum and network analysis remains almost entirely based on electronically frequency-extended systems, which dominate due to their maturity and integration capabilities.

In light of these aspects, this thesis aims to design and develop a space-efficient, frequency-stabilized system platform for high-resolution spectrum and network analysis deep in the terahertz range. The approach merges the frequency stability of electronic sources with the broad bandwidth of photonic techniques in a hybrid strategy. Beat signals from narrow-band CW distributed feedback (DFB) laser diodes are synchronized via optical phase-locked loops (OPLLs) to one or more electronic frequency multiplier chains (FMCs) and then cascaded. This enables the generation of nearly arbitrary difference frequencies deep in the terahertz regime. Driving photomixers with these stabilized beat signals allows integration into PSA and PVNA platforms for precise signal and device characterization. Beyond the proof-of-concept, the system's potential for future commercial adaptation is also addressed, particularly regarding scalability and feasibility.

Following the introduction to terahertz radiation and its application in spectrum and network analysis, **Chapter 2** presents theoretical foundations relevant to this work. It covers terahertz generation and detection techniques, the principles of DFB lasers and OPLLs, and a detailed overview of SA and VNA architectures. **Chapter 3** focuses on laser frequency synchronization, evaluating methods — such as photomixers, electro-optic detection, and Schottky diodes — for phase-locking laser pairs. The cascading scheme is introduced as a way to extend frequency coverage and eliminate spectral gaps. In **Chapter 4**, the integration of laser synchronization into a high-resolution PSA system is described, including its operation, calibration, and use in analyzing spurious harmonics of FMCs. **Chapter 5** extends this concept to a PVNA system, enabling phase-resolved measurements and the characterization of passive devices. The PVNA is designed as an add-on for an electronic VNA, offering substantially broader bandwidth than existing commercial extenders. Its capabilities are demonstrated through measurements of bandpass filters and waveguides, benchmarked against simulations and commercial systems. **Chapter 6** explores an alternative method to further extend the frequency range, using four-wave mixing (FWM) in an optical amplifier. Filtering setups and initial results are presented, along with integration challenges. Finally, **Chapter 7** concludes the findings and discusses the prospects of the developed platforms for integration into future high-performance, commercially viable terahertz measurement systems.

2 Fundamentals

This chapter gives the theoretical background to the key topics essential for understanding the physical methods and techniques employed in this thesis. It begins with a general overview of concepts for the generation and detection of terahertz waves, with particular emphasis on photoconductive antennas as photomixers for continuous-wave radiation. Additionally, electro-optic sampling is introduced as an alternative terahertz detection approach. Beyond optical concepts, purely electronic terahertz devices, relying primarily on nonlinear diode characteristics, are discussed. Following this, the focus shifts on laser sources, particularly distributed feedback lasers, as they play a crucial role in providing stable and narrow-linewidth optical beat signals for photomixing systems. Their integration with a reference source in phase-locked loops allows a precise frequency synchronization, a concept that is further elaborated upon. The chapter concludes by addressing spectrum and vector network analyzers, as they are powerful measurement tools, offering comprehensive insights into the performance of components and devices in the terahertz regime. Moreover, their general principles of operation serve as the foundation for the measurement part of the system platform developed within the scope of this thesis.

However, it is important to note that a complete and exhaustive explanation of each concept can not be included here. For a more in-depth discussion, relevant references to specialized literature will be provided throughout the chapter for further reading.

2.1 Terahertz Generation and Detection

The ability to effectively generate and detect terahertz radiation is crucial for realizing numerous applications within the terahertz frequency range. Historically, the development of practical terahertz technologies lagged behind those in neighboring microwave and optical domains due to technical challenges in both generation and detection. Recent advancements in optics and electronics, however, have led to the emergence of a wide variety of terahertz sources and sensors. In this section, a general overview of the most common methods and techniques for terahertz generation and detection is presented. The focus is placed on the approaches utilized in this work, with particular attention to their operating principles as well as their advantages and limitations within the terahertz domain.

Generation Approaches

Nowadays, terahertz radiation can be generated using several techniques and concepts, which can be broadly categorized into four main groups[1]: nonlinear optical methods, photoconductive sources, electronic oscillators, and intersubband transitions (Fig. 2.1).

Nonlinear optical methods exploit the interaction of intense light with nonlinear media to generate terahertz radiation. Two key techniques within this category are optical rectification and difference frequency generation.

Optical rectification is a process where a femtosecond laser pulse interacts with a nonlinear crystal, generating terahertz radiation due to the material's nonlinear polarization response. In this case an intense light pulse, typically in the near-infrared range, is incident on a nonlinear crystal (such as ZnTe or $LiNbO_3$), causing an oscillating dipole moment within the crystal, which produces terahertz radiation. The emitted terahertz waves have a wide frequency spectrum, with the bandwidth primarily determined by the inverse of the laser pulse duration. For instance, an optical pulse lasting 100 fs results in radiation that includes frequency components exceeding 10 THz; however, the effective bandwidth is often limited by the properties of the nonlinear crystal, such as phonon resonances and material absorption. The shape of the generated terahertz pulses closely resembles the envelope of the original optical pulse [48]. **Difference frequency generation** (DFG) is a $\chi^{(2)}$ nonlinear process for generating terahertz radiation, in which two optical fields at distinct frequencies (ω_1 and ω_2) interact within a nonlinear medium. This interaction gives rise to a new wave at the frequency difference ($\omega_{\mathrm{THz}} = \omega_1 - \omega_2$). Efficient DFG relies on phase matching, which ensures momentum conservation among the interacting waves and enables optimal energy transfer to the generated terahertz wave. To improve efficiency, various phase-matching strategies — such as temperature tuning and quasi-phase matching — can be employed [49]. Still, the crystal type and orientation determine phase-matching and bandwidth, while optical power affects nonlinear interaction strength, with efficiency improving at higher intensities until absorption or damage occurs.

Another way of generating terahertz radiation involves photogenerated current oscillations in semiconductors. Here, a biased photoconductive antenna serves as the terahertz source. As with nonlinear media, PCAs can emit both pulsed and continuous-wave radiation. **Photoconductive switching** is a technique based on the ultrafast optical excitation of semiconductor materials. Femtosecond laser pulses with photon energy exceeding the semiconductor's bandgap generate electron-hole pairs in the region between the electrodes. The static bias field accelerates these carriers, while their density decreases primarily due to carrier trapping at defect sites, occurring over the timescale of their lifetimes. The resulting transient current, produced by the acceleration and

[1] Electron acceleration in free-electron lasers (FELs) and backward wave oscillators (BWOs) is another effective technique for terahertz generation but requires large-scale laboratory equipment or specialized facilities. Due to their scale and limited suitability for industrial applications, these methods are not covered in this thesis.

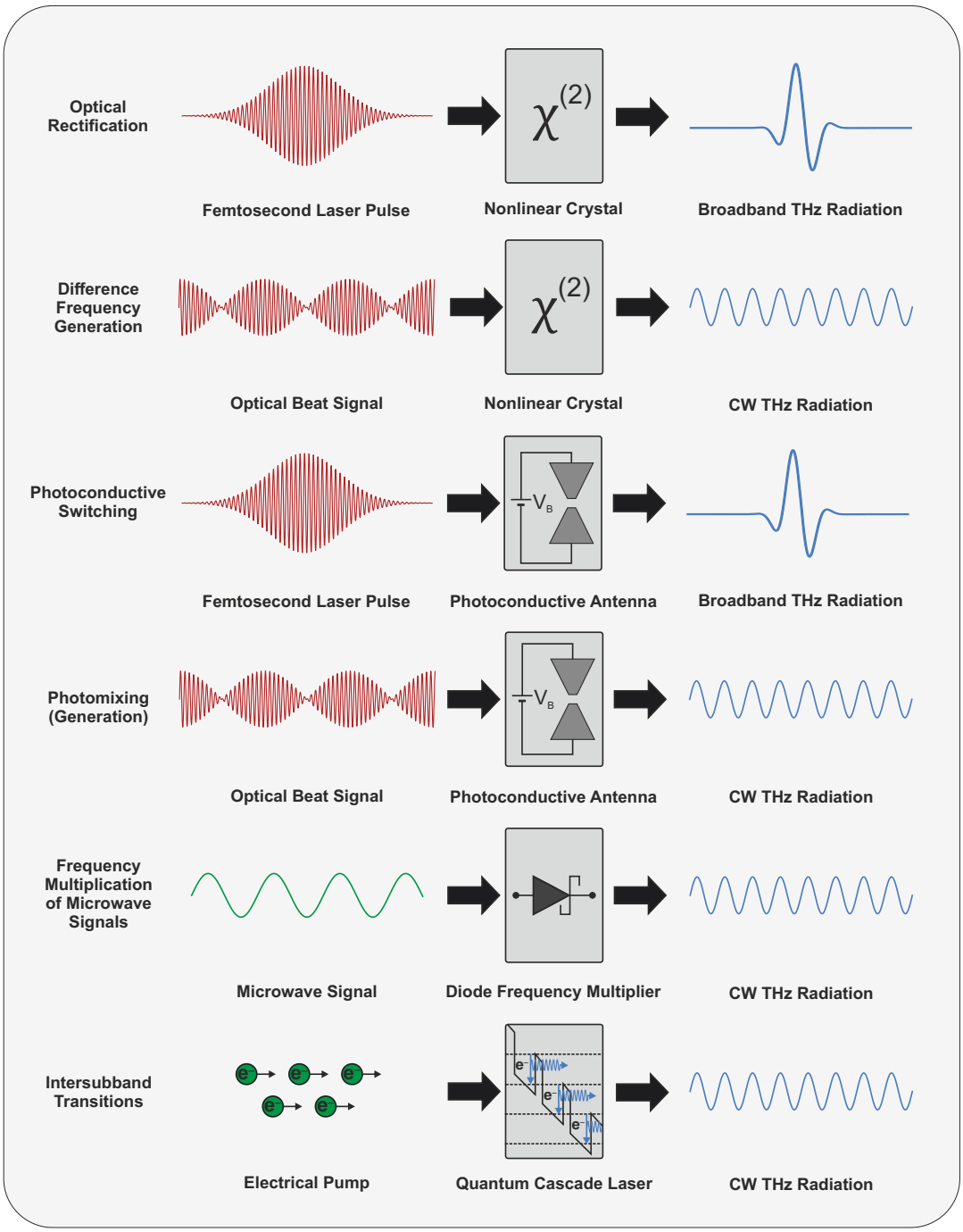

Figure 2.1: Overview of various terahertz generation techniques, including nonlinear optical methods, photogenerated approaches, electrical systems, and semiconductor lasers.

decay of these carriers, serves as the source of subpicosecond electromagnetic pulses. A photoconductive technique for CW terahertz radiation is referred to as **photomixing**. In the process, two CW laser beams with with frequencies ω_1 and ω_2 (typically in the near-infrared range) are directed onto the photoconductive material. When these two

laser beams overlap in the semiconductor, they interfere and create a beat signal with frequency $\omega_{\mathrm{THz}} = \omega_1 - \omega_2$. Similar to the case with femtosecond lasers, the semiconductor absorbs the laser light, resulting in the generation of electron-hole pairs. When a bias voltage is applied, these charge carriers are accelerated within the semiconductor. As the intensity of the laser interference pattern oscillates at the beat frequency ω_{THz}, the resulting photocurrent also oscillates at that same frequency, producing a continuous-wave terahertz signal.

The third approach for generating CW terahertz radiation involves electronic oscillators. This principle relies on solid-state terahertz sources that utilize microwave technology to convert incoming radio-frequency signals into their harmonic frequencies. This transformation is achieved through the use of diodes with highly nonlinear current-voltage (I-V) characteristics, allowing for efficient harmonic generation. Incoming microwave signals created by electronic synthesizers — typically functioning within the GHz range — are fed into a sequence of **frequency multipliers**. These multipliers are generally constructed from nonlinear diodes, such as Schottky diodes or varactor diodes, which facilitate the upconversion of the microwave signals to the terahertz range. As the output power decreases with increasing frequency and the number of multiplication stages, conversion efficiency becomes a critical factor at each multiplier stage. Depending on the design, efficiencies can reach up to 30% at 0.3 THz [50], but this typically drops to just a few percent for frequencies exceeding 1 THz [51]. Consequently, the output power of these devices significantly declines from several hundreds of mW in the lower terahertz range to only a few µW at higher frequencies.

The last technique briefly discussed in this chapter are quantum cascade lasers (QCL). QCLs for terahertz generation were first established by Köhler *et al.* in 2002 [52]. The mechanism is based on **intersubband transitions** in semiconductor heterostructures. Alternating layers of different semiconductor materials, mostly indium gallium arsenide (InGaAs) and aluminum gallium arsenide (AlGaAs) create a series of quantum wells and barriers that confine electrons in a way that allows for discrete energy levels. A QCL consists of multiple stages of quantum wells, where each stage can emit a photon. When a bias voltage is applied, electrons are injected into the laser structure. The injection process typically occurs from a higher energy state in the conduction band of the barrier layer into the lowest energy state of the quantum well. When an electron transitions from a higher energy subband to a lower energy subband within the quantum well, it releases energy in form of a photon. This photon corresponds to the difference in energy between the two subbands. This process continues as the electron moves through the structure, making successive intersubband transitions until it reaches the end of the lattice. The term “cascading” refers to the repetitive nature of these multiple transitions. Through this mechanism, the light is amplified, as each photon stimulates the emission of additional photons from other electrons. The QCL is designed with an optical cavity formed by the reflective surfaces of the structure, which enhances light output through constructive interference, enabling the coherent emission of CW terahertz radiation. QCLs with emission frequencies ranging from 1.2 THz to 4.9 THz have been developed [53], offering continuous-wave power levels in the tens of milliwatts, particularly in the

higher terahertz range [54]. However, none of these lasers covers a very broad frequency spectrum, with each single mode typically spanning only around 10 GHz. Additionally, it is very challenging to operate QCLs below 1 THz [55]. A further limitation of quantum cascade lasers is their reliance on cryogenic cooling, often below 100 K, to achieve efficient lasing and stable performance. This requirement increases system complexity and limits their practicality for widespread or portable use. As a result, current research is actively exploring high-temperature and even room-temperature QCLs to overcome these constraints and broaden their applicability [56].

Detection Approaches

On the detection side, terahertz sensing methods are typically classified into two main categories: coherent techniques and incoherent techniques. The key distinction between them is that coherent detection captures both the amplitude and phase of the electromagnetic field, while incoherent detection measures only the intensity of the radiation. Additionally, terahertz sensing can be further categorized based on the nature of the terahertz signal, distinguishing between pulsed and continuous-wave detection methods. Pulsed systems provide short bursts of terahertz radiation, enabling time-resolved measurements, while CW systems generate steady-state signals for frequency-specific analysis.

Fig. 2.2 illustrates the commonly used **coherent** terahertz detection techniques including nonlinear optical sampling, photoconductive sensing, and frequency downconversion. To analyze terahertz pulses time-domain electro-optical (EO) sampling in a nonlinear crystal or photoconductive antennas can be employed. **Time-domain EO sampling** relies on a second-order nonlinear effect known as the Pockels effect[2], which is closely related to optical rectification. It occurs in specific non-centrosymmetric crystals, where the absence of inversion symmetry allows the refractive index to change linearly in response to an applied electric field. When a terahertz field is present, it induces a transient birefringence in the crystal, which is directly proportional to the instantaneous terahertz field amplitude. A weak femtosecond probe pulse, co-propagating through the crystal, experiences this birefringence as a change in its polarization state. This change is subsequently converted into a measurable intensity difference between two orthogonal polarization components using a polarization-sensitive detection scheme (e.g., balanced photodiodes). By scanning the relative time delay between the terahertz and probe pulses, the probe samples the terahertz field at successive time points. The resulting time-dependent intensity change is proportional to the instantaneous terahertz electric field, allowing the full temporal waveform of the terahertz pulse to be reconstructed. Sensing with a photoconductive antenna, referred to as **photoconductive sampling**, also enables detecting broadband terahertz pulses in the time domain. Like its counterpart used for the generation of terahertz radiation, the detection mode relies on the same physical principle of ultrafast carrier generation in semiconductors via photoex-

[2]Named after Friedrich Pockels, who first described this phenomenon in 1893.

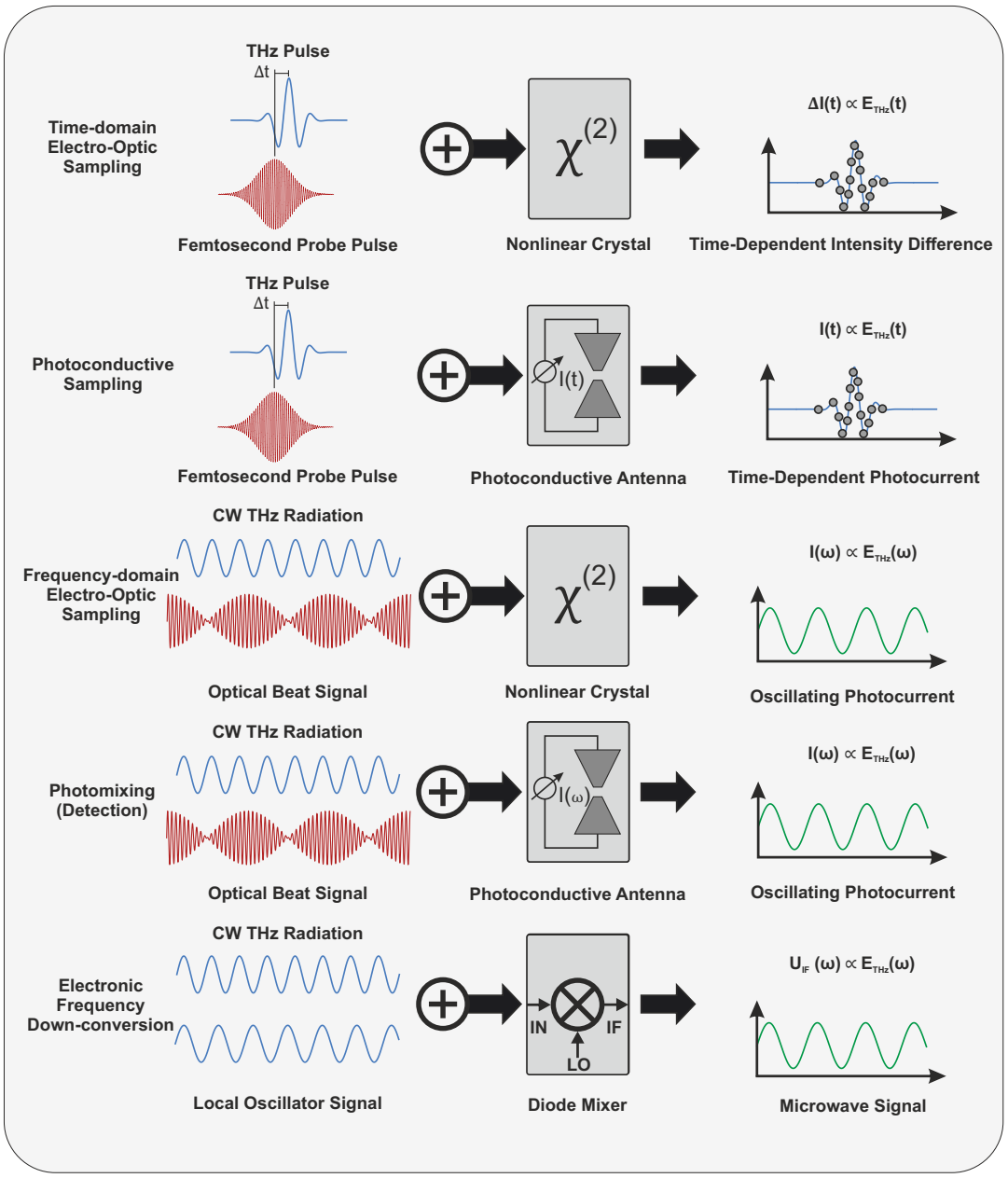

Figure 2.2: Illustration of different coherent terahertz detection techniques, including nonlinear optical methods, photoconductive mechanisms, and frequency mixing.

citation. However, instead of applying a bias voltage as in the generation process, the transient photocurrent induced by the terahertz field across the photoconductive gap is measured. This current is directly proportional to the amplitude of the terahertz electric field. By varying the time delay between the terahertz pulse and the optical probe, the time-domain waveform of the terahertz pulse can be reconstructed. In both approaches, applying a Fast Fourier Transform (FFT) to the acquired time-domain data transforms the information into a frequency spectrum. Adding an EO crystal or photoconductive

antenna for the terahertz pulse generation, both the change in amplitude and phase of terahertz pulses induced by a sample can be measured. By capturing these variations, the measurement enables a detailed analysis of the terahertz pulse interaction with the sample, revealing essential properties. This method, known as time-domain spectroscopy [57], is a well-established technique to analyze ultrashort terahertz pulses for material characterization. It provides sufficient information to simultaneously extract the absorption and dispersion properties of the sample.

Both methods described above can also be utilized for the detection of CW terahertz radiation. In **frequency-domain electro-optic sampling**, a laser beat generated by two CW lasers is combined coherently with a CW terahertz wave inside an EO crystal. The optical beat acts as a stable reference frequency rather than a time delay for the sampling process. The coherent interaction of these waves induces a modulation of the laser beam's polarization state via the electro-optic effect. This polarization modulation translates into intensity variations that are analyzed using a polarization-sensitive optical setup. For example, a balanced photodetector detects these intensity fluctuations, providing information about both the amplitude and phase of the terahertz signal. Thus, the measured photocurrent is proportional to the amplitude of the terahertz electric field. **Photomixing** measures CW terahertz radiation by exploiting the principles of heterodyne detection[3]. In this process, the superposition of the laser beat and the terahertz wave generates an oscillating photocurrent in the photoconductive antenna. This oscillation corresponds to the frequency difference between the laser beat and the terahertz signal. Consequently, the amplitude of the measured current is directly related to the strength of the electric field of the terahertz wave at that specific frequency.

Another technique based on a heterodyne detection scheme is the **electronic frequency downconversion** of CW terahertz radiation with a reference signal. In this approach, the terahertz signal and the reference signal are both directed to a nonlinear device that functions as a mixer. The reference signal, typically generated by a local oscillator (LO), has a stable and well-defined frequency close to that of the incoming terahertz radiation. When both signals enter the mixer, the nonlinear properties of the device cause them to interact, producing two new frequencies: one that is the sum of the frequencies of the terahertz and LO signals, and another that is the difference between them. This lower-frequency component, referred to as the intermediate frequency (IF), is simpler to process using conventional electronic equipment. The IF signal carries essential information from the original terahertz wave, such as its amplitude, phase, and modulation characteristics. For the downconversion, Schottky diodes are often used as mixers due to their ability to operate effectively at high frequencies [58]. Schottky diodes differ from standard diodes by utilizing a metal-semiconductor junction instead of a p-n junction. This design creates a lower energy barrier, allowing the diode to respond rapidly to high-frequency signals. As a result, Schottky diodes can operate at frequencies reaching well into the gigahertz and terahertz ranges.

[3]Homodyne detection is also possible. In this case, the photocurrent shows sinusoidal dependence on the phase difference between the optical beat and the terahertz radiation. The photoconductive antenna is therefore a homodyne mixer where both field amplitude and phase are detectable.

Commonly used **incoherent** terahertz detectors include thermal sensors such as bolometers, Golay cells, and pyroelectric devices. All thermal detectors share a common feature: a radiation absorber connected via a thermal link to a heat sink (Fig. 2.3). The radiation energy is measured using a thermometer that detects the temperature increase in the absorber. Each type of thermal detector employs a distinct physical method for measuring this temperature rise.

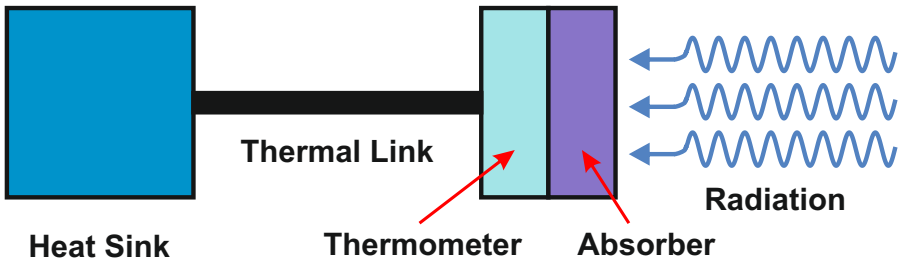

Figure 2.3: Operation principle of thermal terahertz detectors: The incoming radiation is absorbed, causing a temperature increase measured by the thermometer. The excess heat is dissipated to the heat sink via a thermal link.

Bolometers utilize an electrical resistance thermometer made from heavily doped semiconductors like silicon or germanium. In the presence of an electric field, the dominant conduction mechanism is the hopping of carriers within the semiconductor. This phenomenon results in a temperature-dependent resistance, as the probability of carriers successfully hopping between localized states increases with temperature. When radiation is absorbed by the bolometer, it raises the temperature of the sensing element, causing a significant change in resistance due to increased carrier hopping. This resistance change is measured by passing a small, constant current through the sensing element and detecting the resulting voltage, which directly indicates the intensity of the radiation. To optimize sensitivity and minimize noise, bolometers must operate at cryogenic temperatures. Unlike bolometers, pyroelectric detectors, and Golay cells do not require cooling and can operate at room temperature, but they are less sensitive to continuous signals and are better suited for detecting pulsed or modulated radiation. This is because these devices rely on detecting dynamic changes in temperature or pressure, which are more prominent with varying, rather than continuous, signals. **Pyroelectric detectors** contain pyroelectric crystals, where changes in temperature lead to spontaneous electric polarization. In these crystals an axis with a permanent electrical dipole moment exists. This dipole moment suggests that a surface perpendicular to this axis should exhibit an electrical charge. However, this effect is normally neutralized by stray charges in the material. When exposed to radiation, the temperature changes, slightly modifying the position of atoms within the crystal structure. This alteration induces a small change in polarization, resulting in a voltage across the pyroelectric material. As the intensity of the radiation increases, the corresponding temperature changes lead to a proportional increase in the generated voltage, allowing for precise measurement of the incoming signal. In **Golay cells**, heat is transferred to a small volume of gas within a sealed chamber behind a terahertz transparent window. Inside the cell there is a thin absorbing metallic film with an impedance approximately matching that of free space.

When radiation is incident on the Golay cell, the energy is absorbed by the metal film, causing it to heat up. This temperature change results in an increase in pressure within the cell due to the thermal expansion of the gas. A flexible mirror, located at the end of the cell, responds to the pressure change. This movement is subsequently converted into an electrical signal using an optical system. Since movements of less than 10 nm are detectable with the optical system, Golay detectors exhibit a very high sensitivity.

Thermal detectors typically show a relatively slow response because the radiation absorber must reach thermal equilibrium before temperature sensitive measurements can be made. A positive feature of thermal detectors is their ability to cover a wide spectral range. Ideally, absorption would be independent of frequency, but achieving this can be challenging, particularly at lower frequencies. The input window of the detector also affects responsivity, as dispersion and coupling become increasingly difficult at lower frequencies due to the larger aperture size required. Another significant issue is measurement of absolute power in the terahertz regime. In addition to thermal detectors, incoherent detection can also be performed using semiconductor-based devices such as Schottky diodes and TeraFETs [59], which offer faster response times and can be integrated into compact systems. A more detailed theoretical overview of various incoherent detection methods can be found in [60].

In this initial overview of different terahertz generation and detection methods, only a brief introduction is provided. The following subsections of this chapter will delve into a detailed explanation of the specific techniques that were employed in this work, with a particular focus on continuous-wave systems, as this type of terahertz radiation was exclusively used in this thesis.

2.1.1 Photoconductive Antennas

Nowadays, photoconductive antennas, also known as photoconductive switch antennas or photomixers, are among the most popular laser-based terahertz sources [61–63]. PCAs are devices that utilize the photoconductive effect to generate or detect electromagnetic radiation in the radio or terahertz frequency ranges. The photoconductive effect is the change in electrical conductivity of certain materials when exposed to light. It is also often referred to as the internal photoelectric effect, essentially based on the photoelectric effect discovered by Heinrich Hertz in 1887 [64] and theoretically described by Albert Einstein in 1905 in his famous work "*Über einen die Erzeugung und Verwandlung des Lichtes betreffenden heuristischen Gesichtspunkt*" [65] (Nobel Prize 1921).

The first successful photoconductive generation and detection of terahertz radiation was demonstrated by Auston *et al.* in 1984, using photoconductive Hertzian dipoles [66]. In their setup, inspired by the symmetry of Hertz's original dipole experiments, two identical photoconductors were placed on opposite sides of an alumina slab. Using ultrafast optical pulses from a mode-locked laser, one photoconductor was biased to emit terahertz radiation, while the other detected it by measuring the average current, with precise timing enabled by a controlled optical delay. Nearly a decade later, the first

continuous-wave terahertz generation using photoconductive antennas was reported by Brown's group at MIT [67, 68]. Instead of short pulses, they used an optical beat to drive the photoconductive antenna, a technique termed "photomixing" or "optical heterodyning", originally proposed almost forty years earlier for generating coherent microwave radiation [69].

While both approaches rely on the photoconductive effect, they differ significantly in operation and performance. Pulsed systems, such as Auston's original design, use ultrafast laser excitation to generate short terahertz transients and are ideally suited for time-domain spectroscopy due to their broad bandwidth and femtosecond timing resolution. In contrast, photomixing employs two continuous-wave lasers to produce a narrowband, continuous terahertz output at their difference frequency. This method allows for precise frequency tunability and high spectral resolution but typically suffers from lower output power and conversion efficiency.

Similar to nonlinear terahertz generation in electro-optic crystals, photomixers down-convert optical photons to terahertz frequencies. However, the underlying mechanisms differ. EO crystals rely on a second-order nonlinear polarization, where each pair of photons contributes to generating a single terahertz photon. In photomixers, by contrast, each photon pair creates an electron–hole pair, which can contribute to multiple terahertz cycles before recombination. This carrier-based emission process can lead to higher efficiency, particularly in the lower terahertz range. Another key advantage of photomixing is its wide tunability, which is readily controlled via the laser frequency offset — something that is not easily achieved in EO-based systems.

A typical photoconductive antenna used here, shown in Fig. 2.4, consists of the photoconductor, electrodes, and antenna.

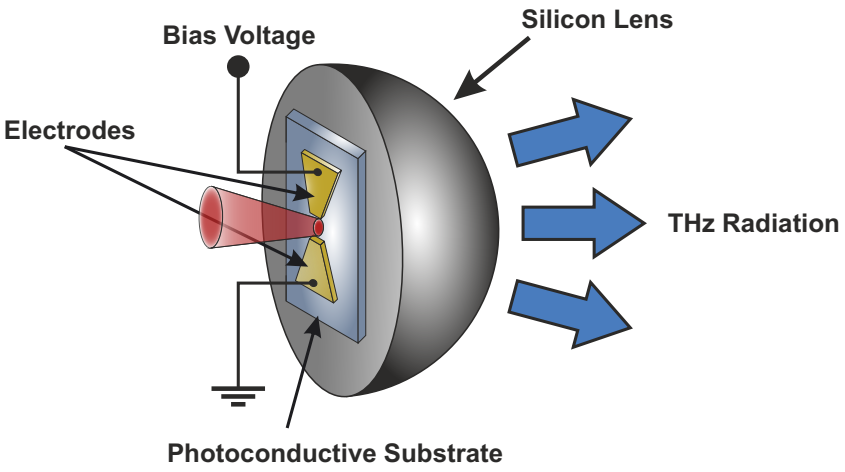

Figure 2.4: Operation principle of a photoconductive antenna: The incoming laser excites charge carriers in the photoconductive material. An applied bias voltage accelerates the carriers, which are collected by the electrodes and drive the antenna. This configuration allows for terahertz radiation emission (emitter) or detection (receiver), with the antenna designed to efficiently couple the electromagnetic radiation with free space.

The photoconductor generates electron-hole pairs in response to optical excitation, leading to modulated conductivity. It is made from a III-V compound such as gallium arsenide (GaAs), indium antimonide (InSb), or other semiconductors. The electrodes form a metallic layer on the photoconductor, connecting it to the antenna and external circuit. This layer acts as a resonant structure that enhances optical modulation efficiency and supplies the bias voltage for operation. Electrodes and the photoconductive gap together form the photomixer, which modulates the circuit's response based on the optical field. The antenna is designed to maximize coupling of radiation with free space, enabling efficient terahertz signal generation and detection. For emitters, this configuration enables biasing of the photoconductive gap (as shown in Fig. 2.4), while for receivers, it allows for measurement of current flow. The performance of a photoconductive antenna can be analyzed by examining its components individually. An equivalent circuit model, shown later in Fig. 2.7, illustrates how these parts interact, clarifying the operating principle.

In the following, we focus on the generation and detection of continuous waves in the terahertz frequency range using optical heterodyne techniques in **photomixers**. These devices combine characteristics of electronic and optical systems to produce and detect widely tunable coherent terahertz radiation at room temperature. Suitable photomixers include photoconductive antennas, uni-travelling-carrier photodiodes (UTC-PDs) [70], travelling-wave UTC-PDs (TW-UTC-PDs) [71], and n-i-p-n-i-p superlattice photomixers [72]. As briefly mentioned earlier, all these techniques involve interference of two slightly detuned, spatially overlapping infrared laser beams to generate terahertz radiation from the beat note (see Fig. 2.5).

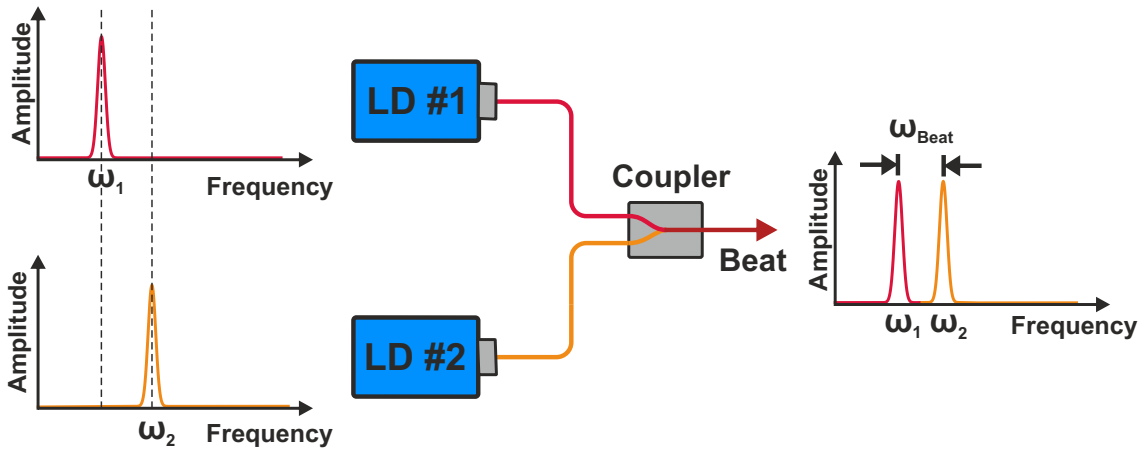

Figure 2.5: Schematic representation of the beat signal ω_{Beat} generation by combining two slightly different optical frequencies ω_1 and ω_2 from two CW laser diodes (LD).

However, this thesis will delve deeper in standard photoconductive mixers, often constructed from semiconductor materials with sub-picosecond carrier trapping times, such as low-temperature grown GaAs (LT-GaAs). For further details on the other techniques, please refer to [73].

Photomixing Principle

In a photomixing process the photoconductive semiconductor is excited by two laser signals with angular frequencies $\omega_1 = 2\pi f_1$ and $\omega_2 = 2\pi f_2$. For the generation of electron–hole pairs through absorption, the lasers must operate at sufficiently high frequencies $\omega_{1,2} > \frac{E_G}{\hbar}$, where E_G represents the semiconductor's band gap energy and $\hbar$ is the reduced Planck constant. The lasers with electric field strengths E_1 and E_2 are heterodyned, resulting in the total field strength in the beat signal of

$$E_{\text{Beat}}(t) = E_1 e^{-i\omega_1 t} + E_2 e^{-i\omega_2 t+\phi} = E_1 \cos(\omega_1 t) + E_2 \cos(\omega_2 t + \phi), \tag{2.1}$$

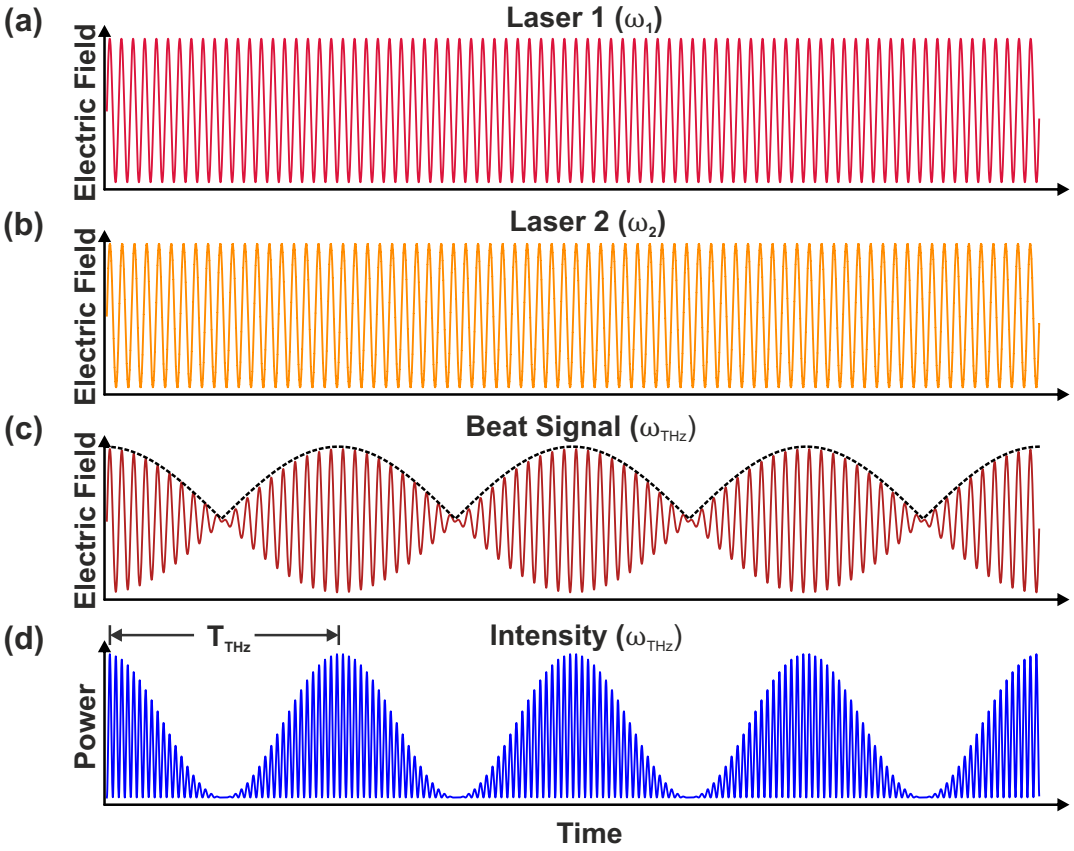

Figure 2.6: Time-domain representation of the photomixing process: Two lasers with ω_1 (a) and ω_2 (b) are heterodyned to generate a beat signal (c) at the difference frequency $\omega_{\text{THz}} = |\omega_1 - \omega_2|$. This beat frequency corresponds to the envelope of the beat signal, depicted by the black dashed line. The resulting power modulation (d) oscillates with a period of $T_{\text{THz}} = \frac{2\pi}{\omega_{\text{THz}}}$.

where ϕ is the relative phase between the two signals. The optical intensity at the photomixer, defined as the square of the total electric field, is given by

$$I_{\text{Optical}}(t) = |E_{\text{Beat}}(t)|^2 = (E_1 \cos(\omega_1 t) + E_2 \cos(\omega_2 t + \phi))^2 \tag{2.2}$$

$$= E_1^2 \cos^2(\omega_1 t) + E_2^2 \cos^2(\omega_2 t + \phi) + 2E_1 E_2 \cos(\omega_1 t) \cos(\omega_2 t + \phi). \tag{2.3}$$

Next, we apply the trigonometric identity $\cos^2(x) = \frac{1+\cos(2x)}{2}$ to the first two terms:

$$I_{\text{Optical}}(t) = E_1^2 \left(\frac{1 + \cos(2\omega_1 t)}{2} \right) + E_2^2 \left(\frac{1 + \cos(2\omega_2 t + 2\phi)}{2} \right) + 2E_1 E_2 \cos(\omega_1 t) \cos(\omega_2 t + \phi). \tag{2.4}$$

Using the trigonometric identity $\cos(x)\cos(x) = \frac{1}{2}(\cos(x+y) + \cos(x-y))$, we find the final expression for the optical intensity:

$$I_{\text{Optical}}(t) = \frac{1}{2}E_1^2 + \frac{1}{2}E_2^2 + \frac{1}{2}E_1^2 \cos(2\omega_1 t) + \frac{1}{2}E_2^2 \cos(2\omega_2 t + 2\phi) + E_1 E_2 \left(\cos((\omega_1 + \omega_2)t + \phi) + \cos((\omega_1 - \omega_2)t - \phi) \right). \tag{2.5}$$

Equation (2.5) indicates that the optical intensity comprises of constant and oscillating components. If a material or device can respond to this instantaneous intensity, various nonlinear optical processes can occur. The first two terms of the optical intensity correspond to the average intensities from each electric field, which may result in optical rectification. The remaining terms represent the modulation effects, which include second harmonic generation (the third and fourth terms) as well as sum and difference frequency generation (the fifth and sixth terms). This applies to nonlinear optical crystals with second-order optical susceptibility. However, due to the phase matching requirements, typically only one of these processes is efficient in actual nonlinear crystals.

For photoconductive antennas or photomixers the fast oscillating terms from the third to fifth contributions can be disregarded due to the slow response of the photoconductivity. Consequently, it is sufficient to focus on the averaged optical intensity, which represents a DC component, along with the optical beat intensity corresponding to the difference frequency, $\omega_{\text{THz}} = |\omega_1 - \omega_2|$ (see Fig. 2.6). Thus, the optical power incident on the photomixer can be expressed as

$$P(t) = \int cn\epsilon_0 I_{\text{Optical}}(t)\, \mathrm{d}S = P_1 + P_2 + 2\sqrt{mP_1P_2}\cos(\omega_{\text{THz}} t - \phi), \tag{2.6}$$

where c is the speed of light, n is the refractive index of the material, and ϵ_0 is the permittivity of free space. $P_{1,2} = \frac{1}{2}cn\epsilon_0 E_{1,2}^2 \int \mathrm{d}S$ represents the average power associated with E_1 and E_2, respectively. The last term in equation (2.6) describes the beat frequency component, which modulates the optical power. Here, m denotes the spatial-mixing efficiency between the two beams, ranging from 0 (no overlap) to 1 (complete overlap) [68].

To determine the terahertz generation efficiency in a photoconductive antenna, it is essential to understand the behavior of the photoconductance $G(t)$, which can be modeled by considering the dynamics of photo-excited carriers within the material. If we neglect the contribution of holes to the photocurrent and assume that the carrier scattering time is much shorter than the period of the optical beat, the photoconductance of a photoconductive antenna can be expressed as being proportional to the number of photo-excited free electrons $N(t)$. The relationship for the direct current conductance is given by:

$$G(t) = eN(t)\mu, \tag{2.7}$$

where e is the charge of an electron and μ is the electron mobility. The number of photo-excited electrons $N(t)$ is governed by the rate equation:

$$\frac{\mathrm{d}N}{\mathrm{d}t} + \frac{N}{\tau_{\mathrm{trap}}} = \eta P(t), \tag{2.8}$$

where η represents the excitation efficiency, τ_{trap} denotes the carrier trapping time, which determines how long the carriers remain mobile and thus contribute to the photocurrent. This equation captures how the number of free carriers evolves in response to optical excitation, modulating the photoconductance accordingly. Substituting equation (2.6) in (2.8) gives us the following expression for the number of photo-excited carriers $N(t)$:

$$\frac{\mathrm{d}N}{\mathrm{d}t} + \frac{N}{\tau_{\mathrm{trap}}} = \eta \left(P_1 + P_2 + 2\sqrt{mP_1P_2}\cos(\omega_{\mathrm{THz}}t + \phi) \right). \tag{2.9}$$

To solve this linear first-order differential equation, we multiply both sides by the integrating factor $e^{t/\tau_{\mathrm{trap}}}$. After integrating both sides with respect to t and applying initial conditions, we obtain an expression for $N(t)$:

$$N(t) \approx \tau_{\mathrm{trap}}\eta(P_1 + P_2) + 2\tau_{\mathrm{trap}}\eta\sqrt{mP_1P_2}\cos(\omega_{\mathrm{THz}}t + \phi). \tag{2.10}$$

The approximation (2.10) is only valid under the assumption that the system has reached a steady-state condition, where the transient dynamics of the photo-excited carriers have sufficiently decayed. Finally, substituting $N(t)$ back into the expression for conductance yields:

$$G(t) = G_0 \left(1 + \frac{2\sqrt{mP_1P_2}\sin(\omega_{\mathrm{THz}}t + \alpha)}{P_0\sqrt{1 + (\omega_{\mathrm{THz}}\tau_{\mathrm{trap}})^2}} \right), \tag{2.11}$$

where $G_0 = e\tau_{\mathrm{trap}}\eta(P_1 + P_2)\mu$ is the time-averaged photoconductance for the total incident power $P_0 = P_1 + P_2$. The phase shift $\alpha = \tan^{-1}(1/\omega_{\mathrm{THz}}\tau_{\mathrm{trap}})$ represents the delay in the response of the photoconductive material to the oscillating signal, which arises due to the finite carrier trapping time τ_{trap}. Meanwhile, the term $\sqrt{1 + (\omega_{\mathrm{THz}}\tau_{\mathrm{trap}})^2}$ effectively accounts for this frequency-dependent attenuation, reducing the amplitude of the oscillating term when $\omega_{\mathrm{THz}}\tau_{\mathrm{trap}}$ becomes significant. This is the case when the optical beat frequency approaches or exceeds the inverse of the carrier trapping time. At this point, the response of the photoconductor is no longer perfectly in-phase with the

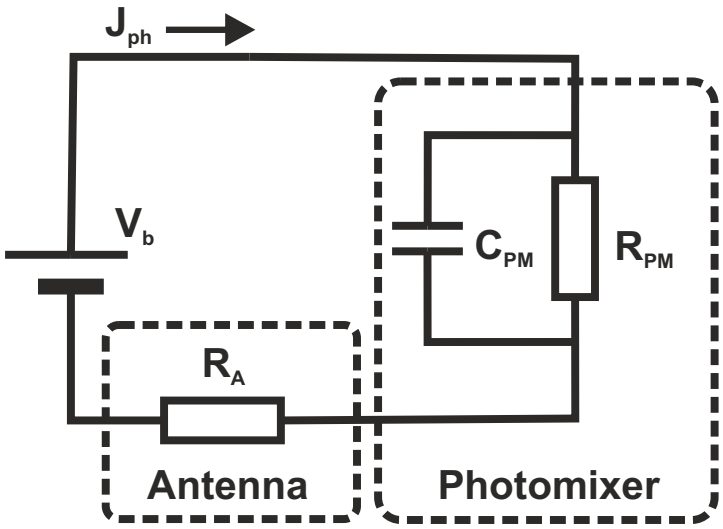

Figure 2.7: Equivalent circuit diagram of a biased photoconductive antenna: The model represents the photomixer as a capacitance C and a time-dependent conductance $G(t)$, which accounts for the varying resistance of the photomixer R_{PM} under optical excitation. The applied bias voltage V_{b} drives the induced photocurrent $J_{\mathrm{ph}}(t)$. The antenna is characterized by its radiation resistance R_{A}.

driving signal, resulting in a decrease in the amplitude of the modulated conductance [74].

To evaluate the induced photocurrent $J_{\mathrm{ph}}(t)$ in the antenna, the equivalent circuit shown in Fig. 2.7 can be employed.

$$J_{\mathrm{ph}}(t) = C\frac{\mathrm{d}V(t)}{dt} + G(t)V(t) = \frac{V_{\mathrm{b}} - V(t)}{R_{\mathrm{A}}}, \tag{2.12}$$

where C represents the capacitance of the photoconductive gap, $V(t)$ denotes the voltage across the gap, V_{b} is the bias voltage, and R_{A} refers to the radiation resistance of the antenna. Although this equation can not be solved analytically, an approximate solution can be derived by assuming that $V(t)$ takes on a harmonic form. This approach also involves neglecting the phase shift in photoconductance α, as the phase of the carrier density is arbitrary. The approximate solution for the terahertz output power can be expressed as follows [67, 68]:

$$P_{\mathrm{THz}}(\omega_{\mathrm{THz}}) = \frac{1}{2}\frac{(V_{\mathrm{b}}G_0\beta)^2 R_{\mathrm{A}}\left[(1+G_0R_{\mathrm{A}})^2 + (\omega_{\mathrm{THz}}R_{\mathrm{A}}C)^2\right]}{(1+G_0R_{\mathrm{A}})^2\left[(1+G_0R_{\mathrm{A}})^2 + (\omega_{\mathrm{THz}}R_{\mathrm{A}}C)^2 - \frac{1}{2}(G_0R_{\mathrm{A}}\beta)^2\right]^2}, \tag{2.13}$$

where

$$\beta = \frac{2\sqrt{mP_1P_2}}{P_0\sqrt{1+(\omega_{\mathrm{THz}}\tau_{\mathrm{trap}})^2}}.$$

This expression is maximized for $m = 1$ and $P_1 = P_2 = \frac{P_0}{2}$. In the small signal limit,

where $G_0 R_\mathrm{A} \ll 1$, the equation reduces to

$$P_\mathrm{THz}(\omega_\mathrm{THz}) = \frac{J_0^2 R_\mathrm{A}}{2[1 + (\omega_\mathrm{THz}\tau_\mathrm{trap})^2][1 + (\omega_\mathrm{THz} R_\mathrm{A} C)^2]}, \tag{2.14}$$

where $J_0 = G_0 V_\mathrm{b}$ is defined as the DC photocurrent. With this equation, we can understand the basic characteristics of photomixing efficiency with photoconductive antennas. Equation (2.14) indicates that the terahertz output power is directly proportional to three factors: the square of the DC conductance ${G_0}^2$, the square of the bias voltage ${V_\mathrm{b}}^2$, and the radiation resistance R_A of the antenna. In moderate excitation regimes, the conductance is primarily influenced by the carrier mobility μ and the carrier trapping time τ_trap. Thus, G_0 increases with total optical power P_0, enhancing terahertz generation efficiency. For self-complementary antennas such as spiral or log-periodic designs, where the radiation resistance R_A is frequency-independent [75], the carrier trapping time and the RC time constant are the limiting factors for the spectral bandwidth. At high frequencies, where $\omega_\mathrm{THz}\tau_\mathrm{trap} \gg 1$ and $\omega_\mathrm{THz} R_\mathrm{A} C \gg 1$ (2.14) reduces to

$$P_\mathrm{THz}(\omega_\mathrm{THz}) = \frac{1}{2}\frac{G_0^2 V_\mathrm{b}^2 R_\mathrm{A}}{\omega_\mathrm{THz}^4 (\tau_\mathrm{trap} R_\mathrm{A} C)^2}. \tag{2.15}$$

This indicates that in the high-frequency limit, the terahertz power drops at a rate of -12 dB per octave, indicating a considerable decline in efficiency as the frequency increases. In the low-frequency limit, the available terahertz power can be estimated by a measurement of the DC photocurrent J_0. Therefore, (2.14) simplifies to

$$P_\mathrm{THz}(\omega_\mathrm{THz}) = \frac{1}{2} J_0^2 R_\mathrm{A}. \tag{2.16}$$

As equations (2.15) and (2.16) illustrate, several factors determine the performance and output of terahertz generation in photomixers. The next sections will take a closer look at these limitations, along with other key aspects that influence the overall efficiency of photomixing devices.

Optical Pumping Efficiency

High optical pumping efficiency is essential for effectively converting optical signals into terahertz radiation. Two key factors that significantly influence this efficiency are reflection and absorption. Reflection R refers to the portion of the incident optical pump light that bounces off the surface of the photoconductor. To minimize reflection, antireflective coatings can be applied to the semiconductor. Even with a minimal reflection, not all the photons that are incident get absorbed. A practical device has a finite absorption length d (typically in the µm range) and an absorption coefficient α around $10^4\,\mathrm{cm}^{-1}$. For example, common materials such as GaAs ($\alpha = 8000\,\mathrm{cm}^{-1}$ at 800 nm [76]) and InGaAs ($\alpha = 10000\,\mathrm{cm}^{-1}$ at 1550 nm [77]) exhibit absorbances of 0.67 and

0.55, respectively, for a 1 µm absorption length. The decrease in both the DC and AC photocurrents can be summarized in a reduced excitation efficiency

$$\eta_{\mathrm{OPE}} = (1 - R)(1 - e^{-\alpha d})\eta. \tag{2.17}$$

Since the terahertz power is proportional to the square of the photocurrent, the effect on the radiated signal is also quadratic. Consequently, even small losses in absorption and reflection can have a significant impact on the resulting terahertz power generated. Therefore, photomixer devices typically exhibit optical-to-terahertz conversion efficiencies from 10^{-6} to 10^{-5}, leading to output powers only in the microwatt range [78].

Charge Carrier Characteristics

In addition to high absorption efficiency of the pump power, properties related to carrier transport — including carrier lifetime, mobility, and breakdown field — are crucial for efficient terahertz generation. Achieving ultrafast current modulation demands a carrier lifetime shorter than one picosecond without sacrificing high carrier mobility for photoconductive gain. A high bias voltage is also required to maximize the photocurrent. Thus, the key characteristics for photoconductive materials include: (i) a very short carrier lifetime, (ii) high carrier mobility, and (iii) a large breakdown field. However, because carrier trapping involves scattering processes, semiconductors with shorter carrier lifetimes generally exhibit lower mobility, and vice versa. In materials like low-temperature-grown GaAs, the more relevant parameter is the **carrier trapping time**, which determines how long carriers remain mobile and contribute to the photocurrent — rather than the total recombination lifetime. Therefore, achieving all of these requirements simultaneously, particularly the first two, is quite challenging. A material that fulfills these criteria is LT-GaAs, typically fabricated as 1.5 µm to 2 µm thin films, grown by epitaxial growth on a semi-insulating GaAs substrate at low temperatures (200 - 300 °C), significantly lower than the standard growth temperature of GaAs, approximately 600 °C. After the growth process, the films undergo annealing at around 600 °C for 5 to 10 minutes. LT-GaAs is notable for its extremely short carrier trapping time, which can be finely tuned through careful control of the growth temperature, allowing it to be reduced to below 200 fs [79]. Despite its high defect density, which enables ultrafast trapping, while the carrier mobility remains within an acceptable range ($\sim 150\,\mathrm{cm}^2/\mathrm{Vs}$) [80]. Together with its high electric breakdown field (> 300 kV/cm) and high resistivity ($> 10^6$ Ωcm) [81], LT-GaAs stands out as one of the most widely used semiconductor materials for photomixer substrates.

RC Roll-off

At higher frequencies, a significant effect that reduces the AC photocurrent — and thus the emitted terahertz power — is known as RC roll-off. Like any electronic device, a photomixer has a certain capacitance C, which can be modeled as a simple plate capacitor in parallel with the radiation resistance R_{A}. At higher frequencies, this capacitance

effectively shorts the antenna, reducing the power delivered to it. Consequently, the overall efficiency of the terahertz emission decreases as the operating frequency increases, following the relation

$$\eta_{RC} = \frac{1}{1 + (\omega_{\mathrm{THz}} R_{\mathrm{A}} C)^2}. \tag{2.18}$$

To operate effectively in the high-frequency range, the photomixer must therefore maintain low values of C.

Antenna Designs

Another important parameter is the design of the antenna structure. Equation (2.15) indicates that the terahertz output power is proportional to the radiation resistance of the antenna. The most common antennas used for CW operation are self-complementary configurations, such as log-spiral, bow-tie, and log-periodic antennas (Fig. 2.8). They are composed of planar conductors that are directly patterned onto the semiconductor substrate. **Log-spiral antennas** are characterized by their circularly polarized radiation, where the type of polarization is determined by the direction of the spiral winding. The logarithmic design of the spiral enables broadband operation, with the bandwidth primarily set by the antenna's dimensions. A low-frequency cutoff occurs when the total length of the spiral arm is approximately equal to the wavelength of the emitted radiation. Conversely, the smallest inner radius at the center of the spiral dictates the high-frequency cutoff, which normally corresponds to the size of the photomixer. **Bow-tie antennas** are characterized by their distinctive V-shaped structure, which provides linear polarization across a broad range of frequencies. The design, typically with opening angles of around 90 degrees, ensures a relatively stable radiation resistance over the entire operating bandwidth. However, the radiation pattern of bow-tie antennas strongly depends on frequency due to their geometry. As the frequency changes, the antenna's effective electrical length varies relative to the wavelength, influencing its radiation characteristics. At higher frequencies, bow-tie antennas produce a more fo-

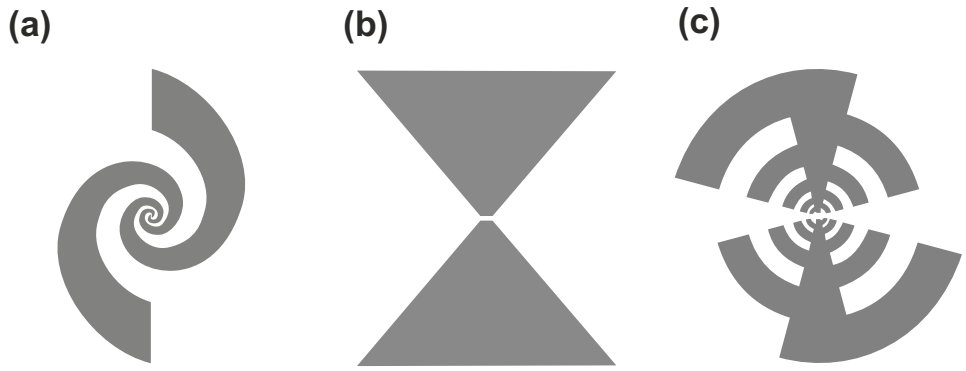

Figure 2.8: Most common antennas used for CW photomixers. (a) Log-spiral (b) Bow-tie (c) Log-periodic.

cused, directional beam, whereas at lower frequencies, they exhibit a broader and less concentrated radiation pattern. **Log-periodic antennas** consist of an array of resonant dipoles with tooth-like shapes attached perpendicularly to the bow-tie arms. The operational bandwidth of this antenna type is determined by the sizes of the smallest and largest resonant teeth. At each resonant frequency, the radiated field is linearly polarized parallel to the corresponding tooth. Unlike log-spiral antennas, the frequency dependency of the radiation impedance in log-periodic antennas is not as smooth, which affects the frequency response of output power in photomixers coupled with these antennas. While the radiation resistance varies more significantly than in bow-tie or spiral antennas, log-periodic antennas exhibit a high directivity. They exhibit linear polarization, with the polarization direction oriented perpendicular to that of bow-tie antennas, while the teeth introduce subtle variations in polarization across different frequencies.

The radiation resistance of the planar broadband antennas on semiconductors is generally below 100 Ω, which limits the output power and frequency range of the photomixer. For instance, the radiation resistance of a log-spiral antenna on a semi-infinite GaAs substrate is $R_\mathrm{A} = 72\,\Omega$. With the carrier lifetime of LT-GaAs and the RC time constant of a typical log-spiral photomixer in the range of a few hundred femtoseconds, this results in a output power of approximately 1 μW and a starting frequency roll-off at 1 THz [82].

As can be seen from equation (2.16), higher antenna impedance can significantly improve the output power and the efficiency of the photomixing process. Resonant antennas, such as dipole and slot antennas, are particularly effective in achieving these higher impedances at their resonant frequencies. It is important to note that these improvements are achieved not only by means of increased impedance but also through optimal matching conditions that occur near resonance in a narrow frequency band. This matching condition allows the capacitance of the photodetector to be compensated by the inductive behavior of the antenna. Therefore, the increase in terahertz output power at resonance is attributed to both the high impedance and the absence of limitations imposed by the RC time constant. However, as no resonant antenna structures were utilized in this work, a specific description will be omitted at this point. For a more detailed evaluation of the various antenna types and their theoretical background, please refer to [83].

Thermal Effects and Bias Field Dependence

According to equation (2.15) or (2.16), the terahertz output power increases quadratically with the pump laser power, as G_0 is directly proportional to the pump power. However, the maximum input power to the photoconductive gap is limited by the risk of thermal failure. Given that photomixing necessitates continuous optical excitation, the maximum terahertz output power is constrained by the thermal conductivity of the photoconductive material. For LT-GaAs with a low thermal conductivity of $\sim 15\,\mathrm{W/mK}$, the damage threshold of a small-area photoconductive gap is $\sim 10^5\,\mathrm{W/cm^2}$ [84], which

corresponds to an optical excitation of $\sim 100\,\mathrm{mW}$ for a $100\,\mu\mathrm{m}^2$ photoconductive gap. Methods such as employing a buffer layer with high thermal conductivity or increasing the optical excitation area to illuminate it with an extended beam can significantly enhance the radiation power. More details on the thermal behavior of CW photomixers and potential improvements can be found in [85]. An additional aspect to consider in this context is the applied bias voltage. As indictated by the equations (2.15) and (2.16), the terahertz power increases quadratically with the bias field. However, due to ohmic heating effects a high bias voltage will also contribute to the thermal limit of the photomixer. Therefore, a trade-off must be made between maximizing terahertz output power and managing the thermal stability of the device.

Frequency Limitations

In addition to power, the attainable spectral quality of the terahertz radiation is a fundamental feature of a photomixing system. For CW photomixers, the terahertz resolution and bandwidth are limited by the linewidth and tuning range of the laser sources, respectively. The corresponding wavelength tuning for a frequency change can be calculated by

$$\Delta\lambda = \frac{\lambda^2 \Delta f}{c}. \tag{2.19}$$

This expression is a first-order approximation derived from a truncated Taylor expansion of the relation $\lambda = c/f$, which is valid here because typical wavelength shifts (e.g., a few nanometers) are much smaller than the central wavelength (e.g., $850\,\mathrm{nm} \gg 5\,\mathrm{nm}$). For example, a beat signal detuning of 1 THz requires a wavelength shift of $\sim 2.4\,\mathrm{nm}$ at 850 nm. Commonly used laser sources include DFB lasers and external cavity diode lasers (ECDLs), with tuning ranges of a few nanometers to several tens of nanometers, respectively. In terms of linewidth, there are many commercially available and cost-effective lasers that feature linewidths in the megahertz and sub-megahertz range. However, the best solution for generating a CW frequency-tunable beat signal in the terahertz range is the use of two independent single wavelength-tunable laser diodes. To minimize noise and drift in the terahertz signal, several synchronization techniques have been developed to lock the optical wavelengths of the two independent sources. These methods include phase-locked loops (PLLs) [86], optical frequency combs [87], and optical injection locking (OIL) [88, 89]. A comprehensive discussion on DFB laser sources and frequency synchronization is given in Sections 2.2 and 2.3, respectively.

2.1.2 Photomixers as Detectors

Photomixers can also be used for the detection for terahertz radiation. This technique is called photomixing detection (PMD) or simply photomixing[4]. In PMD, photoconduc-

[4]To avoid confusion, the term photomixing detection (PMD) is used to distinguish the detection of terahertz radiation via photomixers from the generation of terahertz waves through photomixing.

tive antennas act as receivers by converting incident terahertz waves into measurable photocurrent. As stated before, the performance of a PCA is influenced by a trade-off between carrier mobility and lifetime in the semiconductor material. While high mobility enhances efficient terahertz emission, longer carrier lifetimes can limit the dynamic range of the detector due to increased frequency roll-off and higher Nyquist noise [90]. Therefore, very short carrier lifetimes are preferable for enhancing high-frequency sensitivity and reducing noise in PMD.

In the absence of an applied bias, electron-hole pairs generated by optical illumination simply recombine without producing measurable current. However, in continuous-wave systems, the photoconductor is typically equipped with interdigitated (finger-like) electrodes that are integrated with an antenna. This structure captures the incoming terahertz radiation and induces an oscillating electric field across the photoconductive region. Finger structures are preferred in CW operation because they increase the active area and improve carrier collection efficiency under weak optical excitation. The resulting field acts as a dynamic bias, proportional to the amplitude of the received wave. For an incoming CW signal, this bias is given by $U_{\mathrm{THz}}(t) \propto E_{\mathrm{THz}} \cos(\omega_{\mathrm{THz}} t + \phi)$. As the photoconductor receives both the terahertz and laser beat signals (Fig. 2.9 (a)), the photocurrent generated within the device can be expressed as a product of the modulated carrier generation and the oscillating electric field due to the terahertz bias (Fig. 2.9 (b)). The resulting current $J(t)$ is modulated at the intermediate frequency

$$J(t) \propto n(t)v(t) \propto \cos(\omega_{\mathrm{THz}} t + \phi_{\mathrm{THz}}) \cos(\omega_{\mathrm{Beat}} t + \phi_{\mathrm{Beat}}), \tag{2.20}$$

where $n(t)$ is the carrier concentration modulated by the laser beat, and $v(t)$ is the carrier velocity influenced by the oscillating electric field.

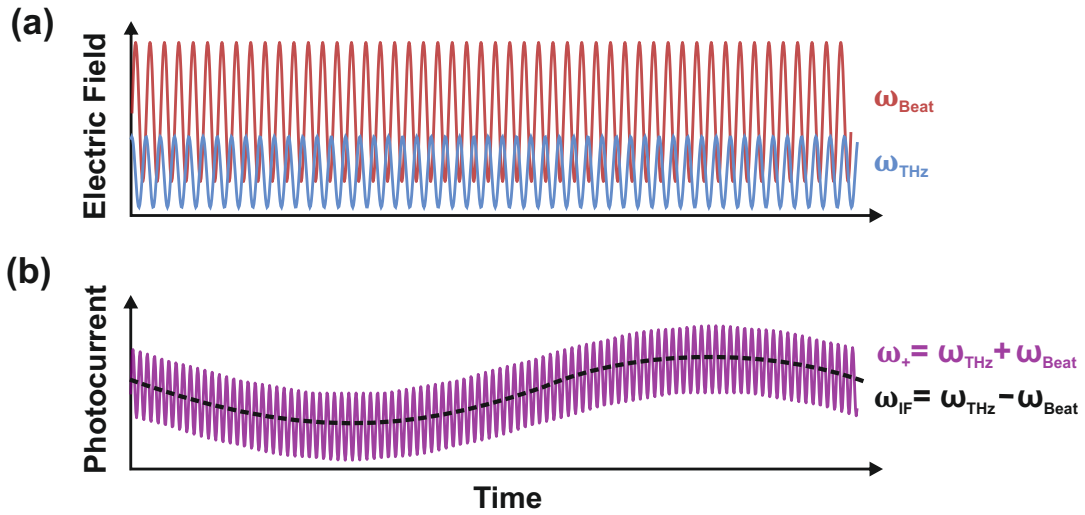

Figure 2.9: Time-domain representation of the photomixing detection (PMD) process. (a) Incoming laser beat (ω_{Beat}) and terahertz (ω_{THz}) radiation. (b) Resulting photocurrent oscillating with $\omega_+ = \omega_{\mathrm{THz}} + \omega_{\mathrm{Beat}}$ and $\omega_{\mathrm{IF}} = |\omega_{\mathrm{THz}} - \omega_{\mathrm{Beat}}|$.

Applying the same trigonometric identity as before yields

$$J(t) \propto \frac{1}{2}\left(\cos\left((\omega_{\mathrm{THz}}+\omega_{\mathrm{Beat}})t+(\phi_{\mathrm{THz}}+\phi_{\mathrm{Beat}})\right)\right. \\ \left.+\cos\left((\omega_{\mathrm{THz}}-\omega_{\mathrm{Beat}})t+(\phi_{\mathrm{THz}}-\phi_{\mathrm{Beat}})\right)\right). \quad (2.21)$$

Here, only the difference frequency $\omega_{\mathrm{IF}} = |\omega_{\mathrm{THz}} - \omega_{\mathrm{Beat}}|$ (black dashed) is of particular interest, as it falls within the radio frequency range. This IF signal can be more easily processed and analyzed using conventional electronic components and techniques. The output of the heterodyne detection setup carries information about both the amplitude and phase of the incoming terahertz wave. An essential advantage of heterodyne detection is the ability to convert frequency and phase information from the signal frequency ω_{THz} to a lower intermediate frequency ω_{IF}, making it suitable for electronic time response. By analyzing the resulting intermediate frequency signal, one can extract valuable information regarding the characteristics of the terahertz radiation, such as material properties or spectral features.

2.1.3 Electro-optic Sampling

Since its independent demonstration by three groups in 1995 [91–93], free-space electro-optic sampling (EOS) has emerged as a powerful technique for detecting freely propagating terahertz signals. EOS relies on the Pockels effect where an electric field — in this case the terahertz radiation — induces birefringence in an electro-optical crystal. This linear effect produces birefringence proportional to the field strength, enabling direct field measurement. EOS thus preserves coherence and allows full waveform reconstruction, including amplitude and phase, for both pulsed and continuous-wave signals [94]. As this thesis focuses solely on detecting CW radiation with EOS, the following discussion is limited to this case.

Detection Principle

Fig. 2.10 illustrates a typical setup of free-space EO sampling to measure field-induced birefringence. It consists of an electro-optic crystal, a $\lambda/4$-plate, a polarization beam splitter (PBS), and a balanced photodiode detector. In the lower part of Fig. 2.10, the evolution of the laser polarization is shown sequentially for the different steps of polarization manipulation with or without a terahertz field. In the absence of the terahertz beam, the linearly polarized laser beam with intensity I_{Beat} maintain its polarization while passing through the electro-optic crystal. The angle of the $\lambda/4$-plate is adjusted to convert the linear polarization into circular polarization. Subsequently, a PBS splits the two orthogonal polarization components into separate beams directed towards the balanced photodiode detector. A balanced detector functions as a differential amplifier, with its output signal being proportional to the difference between the outputs of the two photodiodes.

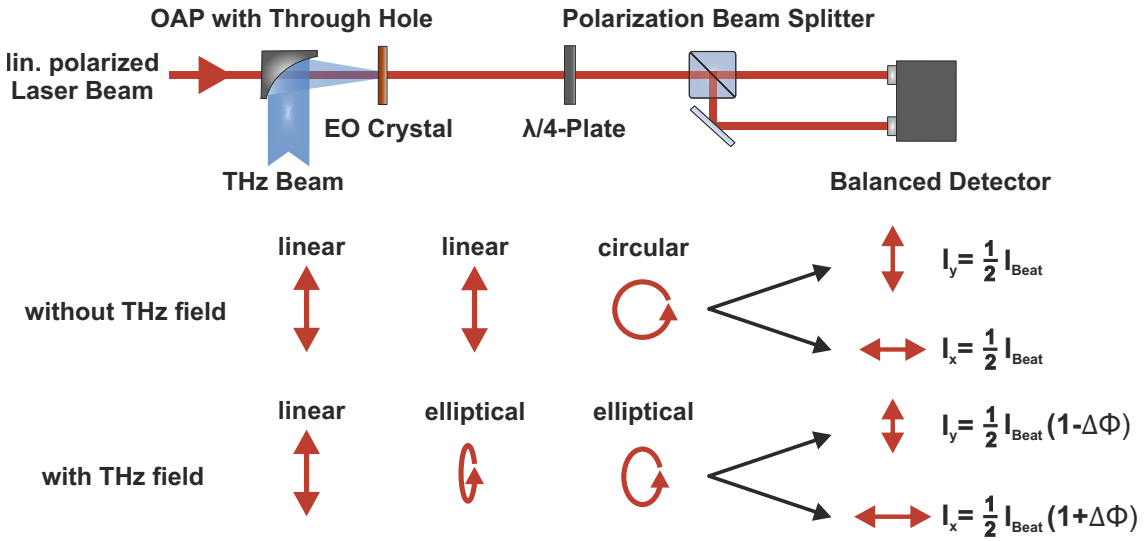

Figure 2.10: Schematic diagram of a typical setup for free-space EO sampling: The setup consists of an electro-optic crystal, a $\lambda/4$-plate, a polarization beam splitter (PBS), and a balanced photodiode detector. The terahertz field induces birefringence in the electro-optic crystal, which modulates the polarization of the probe laser. The signal detected by the balanced photodiode detector is proportional to the intensity difference between the two polarization components of the laser, which are split by the PBS and analyzed in the presence or absence of the terahertz field. The laser beam polarizations with and without a terahertz field are depicted before and after the polarization optics.

If no terahertz field is present, the two polarization components of the probe have equal intensity, resulting in a zero signal $\Delta I_{\mathrm{EO}} = |I_y - I_x| = 0$. In the presence of a terahertz field, the beam is guided by an off-axis parabolic (OAP) mirror to copropagate with the linearly polarized laser beam through the EO crystal. Focusing the beam allows for a higher intensity in the overlapping region. While both beams propagate through the crystal, the field-induced birefringence results in a slightly elliptical polarization of the optical beam. After passing through the $\lambda/4$-plate, the polarization evolves into an almost circular, yet still elliptical, polarization. Consequently, the two beams emerging from the PBS are no longer equal in intensity, creating a nonzero signal at the detector.

The signal measured by the balanced detector is proportional to the difference in intensity between the two beams reaching the photodiodes. For small values of differential phase retardation $\Delta\Phi$, which is typical in terahertz field detection, the effective electro-optic signal can be expressed as

$$\Delta I_{\mathrm{EO}} = \frac{1}{2} I_{\mathrm{Beat}} (1 + \sin \Delta\Phi) - \frac{1}{2} I_{\mathrm{Beat}} (1 - \sin \Delta\Phi) = I_{\mathrm{Beat}} \sin \Delta\Phi \approx I_{\mathrm{Beat}} \Delta\Phi. \quad (2.22)$$

The influence of the applied terahertz field on the phase or polarization retardation of the optical beam depends on the direction of propagation and polarization of the lasers, as well as on the strength and orientation of the field. A complete mathematical framework describing EO detection in isotropic nonlinear crystals, is provided in [95]. As

demonstrated in [96], the field-induced birefringence — and, consequently, the measured intensity modulation — reaches its maximum when both the terahertz electric field and the optical polarization are aligned orthogonal to the [001] axis in an ⟨110⟩-oriented crystal. The differential phase retardation experienced by the laser beam due to the terahertz field over a propagation distance L, is given by

$$\Delta\Phi = (n_y - n_x)\frac{\omega_{\mathrm{Beat}} L}{c} = \frac{\omega_{\mathrm{Beat}} L}{c} n^3 r_{41} E_{\mathrm{THz}}, \tag{2.23}$$

where c is the speed of light, n is the refractive index at the optical beat frequency ω_{Beat}, and r_{41} is the EO coefficient. Inserting equation (2.23) into equation (2.22) yields

$$\Delta I_{\mathrm{EO}} = \frac{I_{\mathrm{Beat}} \omega_{\mathrm{Beat}} L}{c} n^3 r_{41} E_{\mathrm{THz}}. \tag{2.24}$$

From equation (2.24), we find that the measured effective electro-optic signal $\Delta I_{\mathrm{EO}}(t)$ is proportional to the product of the optical laser beat intensity and the terahertz field $\Delta I_{\mathrm{EO}}(t) \propto I_{\mathrm{Beat}}(t) E_{\mathrm{THz}}(t)$. The laser beat intensity can be derived from equation (2.5), resulting in

$$I_{\mathrm{Beat}}(t) = \frac{1}{2}E_1^2 + \frac{1}{2}E_2^2 + E_1 E_2 \cos(\omega_{\mathrm{Beat}} t). \tag{2.25}$$

By substituting $I_0 = \frac{1}{2}E_1^2 + \frac{1}{2}E_2^2$ and assuming a CW terahertz signal with amplitude E_0 and frequency ω_{THz}, we obtain

$$\Delta I_{\mathrm{EO}}(t) \propto (I_0 + E_1 E_2 \cos(\omega_{\mathrm{Beat}} t)) E_0 \cos(\omega_{\mathrm{THz}} t). \tag{2.26}$$

Applying the trigonometric identity for products and rearranging the terms leads to

$$\begin{aligned} \Delta I_{\mathrm{EO}}(t) \propto\ & I_0 E_0 \cos(\omega_{\mathrm{THz}} t) \\ & + \frac{1}{2} E_1 E_2 E_0 \left[\cos\left((\omega_{\mathrm{Beat}} + \omega_{\mathrm{THz}})t\right) + \cos\left((\omega_{\mathrm{Beat}} - \omega_{\mathrm{THz}})t\right)\right]. \end{aligned} \tag{2.27}$$

The first term represents a constant amplitude oscillation at the terahertz frequency, while the second term contains two components oscillating at the sum and difference frequencies of the beat and terahertz signals. By choosing a suitable laser beat frequency, the component of the signal oscillating at the difference frequency $\omega_{\mathrm{EO}} = |\omega_{\mathrm{Beat}} - \omega_{\mathrm{THz}}|$ can be shifted within the bandwidth of conventional photodiodes. Therefore, the effective electro-optic signal at the balanced detector measures an intensity modulation oscillating at ω_{EO}, which is linearly proportional to the terahertz field amplitude.

Crystal Properties

As equation (2.23) indicates, desired properties of an electro-optic crystal used for terahertz detection are large electro-optic coefficient and high transparency at optical and terahertz frequencies. Another important consideration is the need to match the optical group velocity of the laser beat with the phase velocity of the terahertz beam. This

alignment is necessary to maintain a constant incremental phase retardation in the laser signal as it propagates through the crystal, which is crucial for preserving coherence between the two interacting waves. A thicker crystal extends the interaction time between the optical beat and the terahertz signal, increasing the phase difference between polarization components and therefore the detectable signal. However, this also reduces the detector bandwidth due to the group-velocity mismatch. Therefore, a trade-off must be made between achieving sufficient interaction length and maintaining the desired phase matching conditions. One material that fulfills many of the desired characteristics is zinc telluride (ZnTe). It offers a high electro-optic coefficient ($r_{41} = 4$ pm/V), superior phase matching at the wavelength of 800 nm, and high optical transparency for both laser and terahertz beams [97], making it a popular choice for electro-optic sampling. Still, it suffers from absorption losses, especially for frequencies above 3 THz. In contrast, gallium phosphide (GaP) presents advantages for ultra-broadband detection due to its lower absorption losses, although it may not provide the same level of electro-optic coefficient ($r_{41} = 1$ pm/V) and transparency in the relevant wavelength range [98]. For applications at 1.5 µm, GaAs crystals are preferred due to the long coherence length at this optical wavelength [99]. Alternatively, organic crystals like DAST, OH1, and DSTMS have been developed, offering significantly higher electro-optic coefficients [100]. Accordingly, the selection of the appropriate electro-optic crystal depends strongly on the specific frequency range and required sensitivity.

In this thesis, only 1 mm thick ZnTe crystals were employed, as the electro-optic sampling setup utilized electronic terahertz emitters with emission frequencies below 1 THz in combination with laser systems operating at 850 nm.

2.1.4 Electronic Terahertz Devices

Rather than focusing solely on photonic methods, electronic devices based on microwave technology provide an alternative approach for generating and detecting terahertz radiation. Electronic terahertz generation typically involves techniques that build on existing microwave and millimeter-wave technologies, utilizing high-frequency oscillators, frequency multipliers, and advanced semiconductor components. One of the most widely used methods are frequency multiplier chains (Fig. 2.11). Conceptually, the frequency

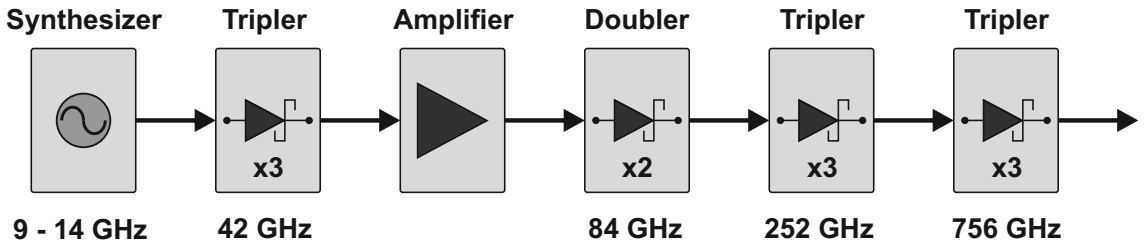

Figure 2.11: Schematic block diagram of a typical electronic terahertz source based on harmonic generation. This type of source relies on an amplified cascaded multiplier chain (doublers and triplers), which is driven by a high-power microwave synthesizer.

multiplication of microwaves is analogous to the harmonic generation of optical waves in a nonlinear crystal. Here, the signal of a high-power microwave synthesizer is sent to a cascaded frequency multiplier chain, where nonlinear devices, such as Schottky diodes or transistors, upconvert the frequency into the terahertz range. These nonlinear components generate harmonics of the fundamental frequency, with filtering and amplification stages isolating the desired harmonic. Since the efficiency and performance tend to decline at higher harmonics, multiplication factors are generally limited to doublers or triplers. This limitation arises from the intrinsic properties of Schottky structures, such as their junction capacitance and resistance, which can adversely affect the diode's ability to effectively generate higher-order harmonics as the frequency increases [101]. At the end of the chain, the output power can be controlled smoothly by changing the gain of the last amplifier or by integrating a variable attenuator. To realize a high-frequency operation, Schottky barrier diodes are commonly employed due to the high conductivity of the metal contact, enabling very high switching rates (>10 GHz).

Schottky Barrier Diodes

A Schottky barrier diode (SBD)[5] is a two-terminal semiconductor device that uses a metal-semiconductor junction, referred to as a Schottky barrier. The barrier forms due to the difference in work functions between the metal and semiconductor. When they are brought into contact, electrons flow between them until an equilibrium is reached, creating a depletion region on the semiconductor side. The conduction is primarily controlled by thermionic emission, where electrons in the semiconductor gain enough thermal energy to "jump" over the barrier into the metal. To operate at high frequencies a low series resistance and a low junction capacitance are required. Therefore, semiconductors with a high carrier mobility and a high saturation velocity, such as n-type silicon and n-type gallium arsenide are used in commercially available Schottky diodes.

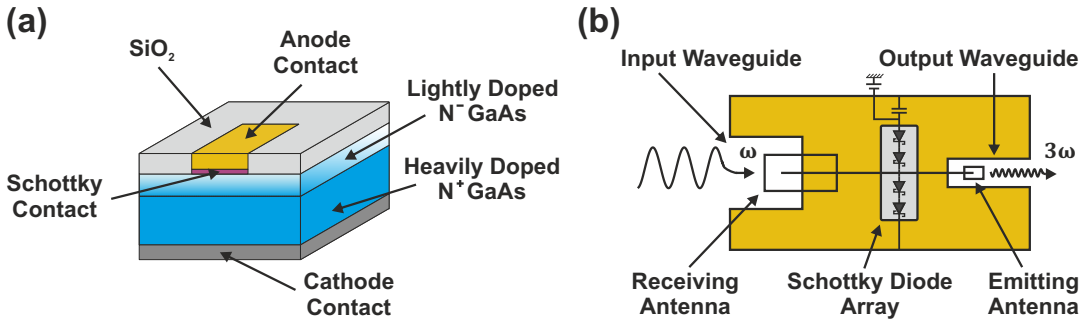

Figure 2.12: (a) Cross-section view of a Schottky barrier diode. (b) Schematic diagram of a balanced frequency tripler using an array of four Schottky diodes for efficient harmonic generation, based on the device architecture described in [102].

[5] named after the German physicist Walter Schottky, who developed the model of the metal-semiconductor contact in 1938.

Fig. 2.12 (a) shows a cross-section view of a GaAs Schottky barrier diode. The bottom layer of the structure consists of an ohmic contact metal (often a combination of metals, like AuGe/Ni or Ti/Pt/Au), providing a low-resistance path for the charge carriers. On top of the cathode layer a heavily doped N^+ GaAs layer is grown, acting as a buffer layer that facilitates electron injection into the Schottky junction. Above this, a thin lightly doped N^- GaAs epitaxial region follows, forming the active part of the diode. This epitaxial layer is critical for establishing the Schottky barrier, as it helps define the electrical characteristics of the diode, such as the width of the depletion region and the efficiency of carrier injection. At the top of the diode, a Schottky barrier metal contact, typically composed of materials like gold or platinum, is deposited, acting as the anode. The region between the metal anode and the epitaxial layer creates the Schottky contact, allowing for the rectification of current. Additionally, a SiO_2 passivation layer is often applied to the surface of the SBD to shield it from environmental factors while also providing electrical isolation from neighboring components. In Fig. 2.12 (b) the working principle of a balanced frequency tripler in a split-block waveguide design is illustrated. The schematic is derived from the device architecture presented in [102] and represents a monolithically fabricated circuit on a GaAs-based substrate that integrates four planar Schottky diodes in an array configuration. Growing the entire structure on a single substrate reduces parasitic losses and enables more output power at higher operational frequencies. The diode array is inserted between the input and output waveguides of the multiplier. Inside the input waveguide, a receiving antenna couples the fundamental frequency ω to a suspended microstrip line, which directs it to the diode circuit. Using an array configuration for harmonic generation allows the input power to be distributed across multiple diodes, enhancing efficiency while reducing the load on each individual diode. This setup enables the circuit to handle higher input power levels without risking thermal damage or performance degradation in any single diode. The third harmonic (3ω) generated by the diodes is coupled to the output waveguide via a second antenna.

Electronic Frequency Multiplier Chains

The two key parameters for SBDs used as frequency multipliers are conversion efficiency — the ratio of generated power at the harmonic frequency to the input power — and output power. In the case of an emitter the SBD is operated under inverse bias conditions, limiting the current flow. To maximize conversion efficiency and output power, the epitaxial layer is thicker with a relatively low doping density (10^{16} cm^{-3} to 10^{17} cm^{-3}). Additionally, the relatively large area of the Schottky junction enhances the breakdown voltage of the diode, allowing the SBD to handle higher pump power levels. However, the power-handling capacity of multiplier modules remains a significant limiting factor, primarily due to the restricted dissipation of thermal energy generated during operation at relatively high power levels. Generally, frequency doublers have a simpler design than frequency triplers and achieve higher conversion efficiency due to generating fewer unwanted harmonics. Recent advances in design and fabrication techniques have enabled terahertz frequency doublers and triplers to reach conversion efficiencies of up to

30% and 20%, respectively [103]. Employing multiple stages of doublers and triplers in a cascade configuration allows for the generation of high-frequency terahertz signals. Yet, this approach results in a decrease in the output power obtainable at each stage of multiplication. For instance, a SBD-based state-of-the-art system using three cascaded triplers can reach frequencies of up to 2.75 THz but only with an output power of 14 µW [104]. For sources working in the lower terahertz range significantly higher output powers of 250 mW at 260 GHz have been reported [105].

Another critical specification is the achievable bandwidth with a multiplier chain. Cutting-edge designs typically exhibit bandwidths of 15% to 20% around the center frequency [106]. Larger bandwidths can be achieved by sacrificing conversion efficiency, as this requires modifying the impedance matching and resonance conditions that are typically optimized for a narrow frequency range. This constraint is more pronounced at higher frequencies, where thermal losses and increased parasitic effects make it more challenging to maintain efficiency across a wide frequency range [107]. Therefore, frequency multipliers face an inherent trade-off between bandwidth and conversion efficiency. While high-efficiency multipliers are designed to maximize output power, broadband multipliers prioritize covering entire WR[6] frequency bands. As a result, each type of multiplier serves distinct application needs: high-efficiency models are preferred for applications demanding maximum power, while broadband multipliers are ideal for systems requiring wide frequency coverage.

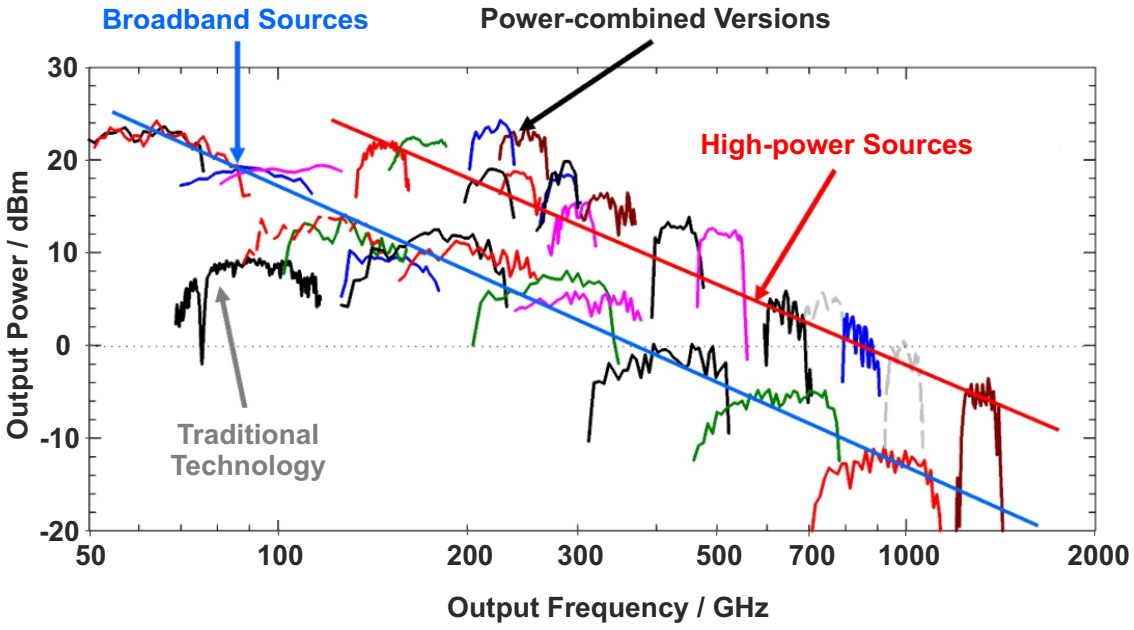

Figure 2.13: Comparison of state-of-the-art high-power vs. broadband terahertz sources based on frequency multipliers (adapted from [108]).

[6]Waveguide Rectangular (WR) is a classification standard to define specific frequency bands in waveguide systems, commonly employed in microwave and millimeter-wave communication.

A comparison of various state-of-the-art high-power versus broadband terahertz sources based on frequency multiplication for a frequency range between 50 GHz and 2 THz is presented in Fig. 2.13. High-power and broadband sources are represented by the red and blue lines, respectively. Both lines follow nearly parallel paths on the logarithmic scale, highlighting the significant power decrease for higher frequencies. As the plot shows, full-band sources provide about 10 dB less output power in comparison to high-power options while performing within the full WR frequency bandwidth of about 40% to 45%. The highest output powers can be achieved by power-combined multipliers. In this approach, a series of individual multiplier stages are synchronized to combine their output in-phase, resulting in constructive interference of the distinct signals [109]. The sources presented are based on a novel design that incorporates an integrated diamond substrate or heat spreader, which enhances thermal management and ensures efficient heat dissipation. Traditional technology refers to planar Schottky diode arrays fabricated on a thin GaAs substrate.

Schottky Diode Mixers

In addition to their role as frequency multipliers in sources, SBDs can also be employed as frequency mixers for the detection of terahertz radiation. The detection principle relies on the formation of a depleted region at the semiconductor-metal junction. This depletion zone enhances the device's sensitivity to the electron-hole pairs generated when radiation interacts with the junction [110]. When used as terahertz receivers, SBDs work by mixing an incoming low-power terahertz signal, commonly named RF, with a high-power local oscillator (LO) signal, generating an intermediate frequency (IF) that can be detected and analyzed (Fig. 2.14).

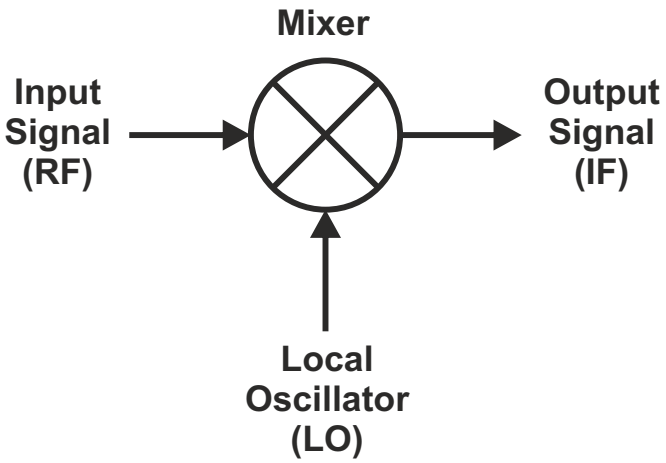

Figure 2.14: Schematic diagram of a mixer: The input frequency (RF) signal is mixed with the local oscillator (LO) signal, resulting in an intermediate frequency (IF) signal at the output.

Similar to photoconductive and electro-optic detection, this nonlinear mixing process allows for the downconversion of high-frequency signals to lower frequencies that are easier to measure with standard electronic equipment. The configuration most commonly employed is a heterodyne receiver. Heterodyne receivers function either as fundamental mixers or harmonic mixers, where the output signal can be expanded into a power series

$$J(t) = k_0 + k_1 V(t) + k_2 V^2(t) + ... \tag{2.28}$$

The voltage change is induced by the electrical field of the RF and LO signal

$$V(t) = V_{\mathrm{RF}} \cos(\omega_{\mathrm{RF}} t) + V_{\mathrm{LO}} \cos(\omega_{\mathrm{LO}} t). \tag{2.29}$$

Substituting (2.29) in (2.28) and using some trigonometric manipulation yields

$$\begin{aligned} J(t) = k_0 &+ k_1 V_{\mathrm{RF}} \cos(\omega_{\mathrm{RF}} t) + k_1 V_{\mathrm{LO}} \cos(\omega_{\mathrm{LO}} t) \\ &+ \frac{k_2 V_{\mathrm{RF}}^2}{2} \left(1 + \cos(2\omega_{\mathrm{RF}} t)\right) + \frac{k_2 V_{\mathrm{LO}}^2}{2} \left(1 + \cos(2\omega_{\mathrm{LO}} t)\right) \\ &+ k_2 V_{\mathrm{RF}} V_{\mathrm{LO}} \left(\cos((\omega_{\mathrm{RF}} - \omega_{\mathrm{LO}})t) + \cos((\omega_{\mathrm{RF}} + \omega_{\mathrm{LO}})t)\right) + ... \end{aligned} \tag{2.30}$$

If a fundamental mixer is desired, the key term responsible for frequency mixing is the $k_2 V_{\mathrm{RF}} V_{\mathrm{LO}}$ component. This term generates both the sum and difference frequencies, $\omega_{\mathrm{RF}} - \omega_{\mathrm{LO}}$ and $\omega_{\mathrm{RF}} + \omega_{\mathrm{LO}}$, which are essential for heterodyne detection. The difference frequency is typically selected as it falls within the IF range $\omega_{\mathrm{IF}} = |\omega_{\mathrm{RF}} - \omega_{\mathrm{LO}}|$, making it suitable for further processing in the receiver. The remaining terms in equation (2.30) contribute to unwanted mixing products, generating signals at frequencies $m\omega_{\mathrm{RF}} \pm n\omega_{\mathrm{LO}}$. These undesired components, called intermodulation products, are of order $m + n$, and their power typically decreases with increasing order. By appropriate filtering or reducing the input power to limit nonlinear effects, the influence of these intermodulation products can be minimized.

In contrast, harmonic mixers use higher-order harmonics of the LO (such as the second, third, or higher harmonics) for mixing. The key terms responsible for this mixing process are the higher-order components, such as $k_3 V_{\mathrm{RF}}^2 V_{\mathrm{LO}}^2$ or $k_4 V_{\mathrm{RF}} V_{\mathrm{LO}}^3$, which produce harmonics of the LO frequency. The choice of which harmonic to use depends on the design of the mixer and the frequency range of interest. Harmonic mixers offer several advantages, particularly when working with LO sources that are difficult to tune across a wide frequency range. By using the higher harmonics of the LO, the mixer can downconvert signals to a more convenient intermediate frequency without needing a LO that spans the same frequency range as the RF signal. However, using higher-order harmonics can also introduce additional challenges, such as increased noise and intermodulation products at even higher frequencies. Additionally, the power of the mixing products typically decreases for higher harmonics, which can reduce the efficiency of the mixing process. Thus, careful selection of the harmonic order and appropriate filtering is necessary to minimize these undesired effects.

To work efficiently as mixer, SBDs typically have a slightly higher doping density ($> 10^{17}$ cm^{-3}) and a thinner epitaxial layer than those used for harmonic generation. Higher

doping decreases the series resistance, while a thinner epitaxial layer helps reduce parasitic effects that could otherwise limit high-frequency performance as they slow the diode's response. In terms of the anode size, a smaller contact area is preferred for mixers, as it allows for better impedance matching with the waveguides or antennas used in the system, ensuring efficient signal coupling [111]. Current SBD mixers exhibit a high responsivity of around 1 kV/W and a fast response time of approximately 20 ps at room temperature. These characteristics make them especially well-suited for direct detection of terahertz radiation, operating efficiently across a broad frequency range from 0.1 THz to 10 THz [112].

In the present thesis, only frequency multiplier chains and harmonic mixers are employed as electronic terahertz devices, limiting the scope to these specific methods. For a more comprehensive theoretical discussion on SBDs as multipliers and mixers, as well as other electronic generation and detection techniques, please refer to [60, 113].

2.2 Distributed Feedback Lasers

In addition to photoconductive antennas and electronic terahertz components, laser sources are the key elements for the realization of a high-resolution broadband CW terahertz measurement system. As stated before, grating-stabilized semiconductor lasers, such as external cavity diode lasers or distributed feedback lasers, are widely employed due to their ability to provide narrow-linewidth, excellent wavelength stability, and tunability. Unlike Fabry-Pérot (FP) lasers, where a broad range of different wavelengths are present simultaneously, these sources operate in single frequency mode, which is essential for generating a stable and coherent beat signal. Additionally, their small packaging and high availability make them ideal for integration into compact, cost-effective measurement setups.

Generally, external cavity diode lasers (ECDLs) offer superior frequency stability, narrower linewidths, and broader tuning ranges compared to DFB lasers. For instance, ECDLs can achieve linewidths below 10 kHz [114], with relative frequency stabilities on the order of 10^{-10} [115], along with a tuning range of more than 100 nm [114]. However, their wavelength selection relies on the physical rotation of an external Bragg grating, introducing mechanical complexities, such as alignment challenges and sensitivity to vibrations, as well as slower tuning speeds. Moreover, the mode-hop-free tuning range for ECDLs is typically limited to frequency spans between 10 GHz and 100 GHz [116, 117], reducing the continuous operation bandwidth of the lasers. Therefore, temperature-stabilized DFB laser diodes are commonly applied in CW photomixing systems in the terahertz range.

A cross-section view of a DFB laser structure is shown in Fig. 2.15. On top of the n-electrode lies the lower cladding layer, typically a n-doped GaAs or InP substrate, which provides structural support as well as optical confinement by having a lower refractive index than the waveguide layers above it. The active layer, also referred to as the

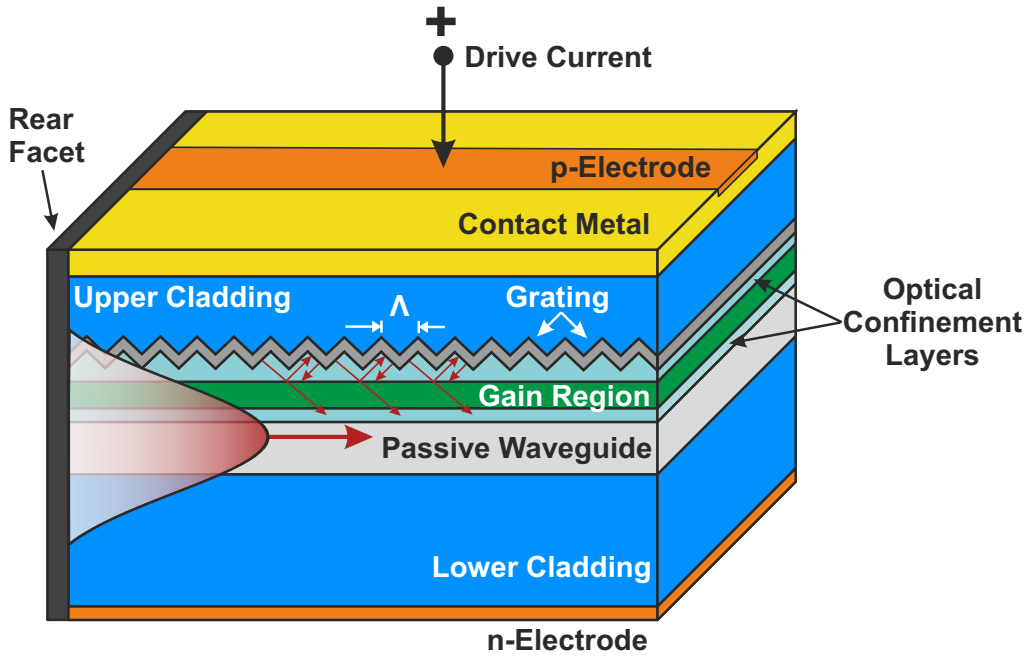

Figure 2.15: Cross-sectional view of a distributed feedback (DFB) laser diode: The structure includes an n-doped lower and p-doped upper cladding layers for optical confinement, an active region with multiple quantum wells for carrier injection, and a diffraction grating to select the wavelength. The laser cavity is formed between the grating and cleaved facets, with anti-reflective coatings to suppress Fabry-Pérot modes. The p-cladding and electrode enable current injection for lasing.

gain region, consists of multiple quantum wells (MQWs) sandwiched between separate confinement heterostructure layers, which improve carrier confinement and injection efficiency. To implement the wavelength-selective mechanism, a diffraction grating is either etched into or buried within the waveguide structure directly above the active region. One of the most common methods for generating the grating structure is through a holographic exposure technique[7] [118]. In this process, a two-arm interferometer setup is used, where two coherent light waves intersect at a predetermined angle, creating an interference pattern that forms a periodic grating. Afterward, the grating is etched onto the substrate using conventional wet chemical etching or dry ion beam etching methods. The cavity of the laser is formed between the grating layer and the cleaved facets at both ends of the laser. In order to suppress any possible FP mode in these grating structures, it is quite usual to have anti-reflective coatings on the laser facets. The upper cladding, a p-doped layer, complements the lower cladding for the vertical confinement of the optical mode. Together with the p-electrode and the contact metal, it also enables the current injection into the device for efficient lasing operation. In some designs, also a passive waveguide layer is combined with the active region to minimize the overlap between the optical mode and lossy p-doped layer, significantly reducing internal optical losses [119].

[7] Other techniques, such as electron beam lithography (EBL), can also be employed to create these patterns.

To ensure a proper single mode operation, the periodicity of the grating is precisely designed to match the Bragg condition for the desired lasing wavelength

$$\lambda_B = 2mn_{\text{eff}}\Lambda, \tag{2.31}$$

where m represents the order of diffraction, n_{eff} is the average refractive index in the waveguide, and Λ denotes the grating period. For example, an AlGaAs laser emitting at 850 nm with a first-order grating ($m = 1$) typically has an effective refractive index of $n_{\text{eff}} \approx 3.4$, resulting in a grating period of $\Lambda \approx 125$ nm. As equation (2.31) indicates, the output wavelength can be tuned by adjusting either the refractive index or the grating period. While temperature changes have only a minimal effect on the grating's dimensions, the primary tuning mechanism relies on variations in the refractive index. For this purpose, temperature or current can be modified to shift the wavelength. In both cases, variations in the carrier density of the semiconductor material cause changes in the refractive index. For temperature tuning, typical wavelength shifts are around 60 pm/K, whereas current tuning offers finer control of roughly 2.4 pm/mA. Thanks to the large free spectral range (FSR), mode-hop-free tuning is generally possible over a range of 2 nm to 4 nm [120].

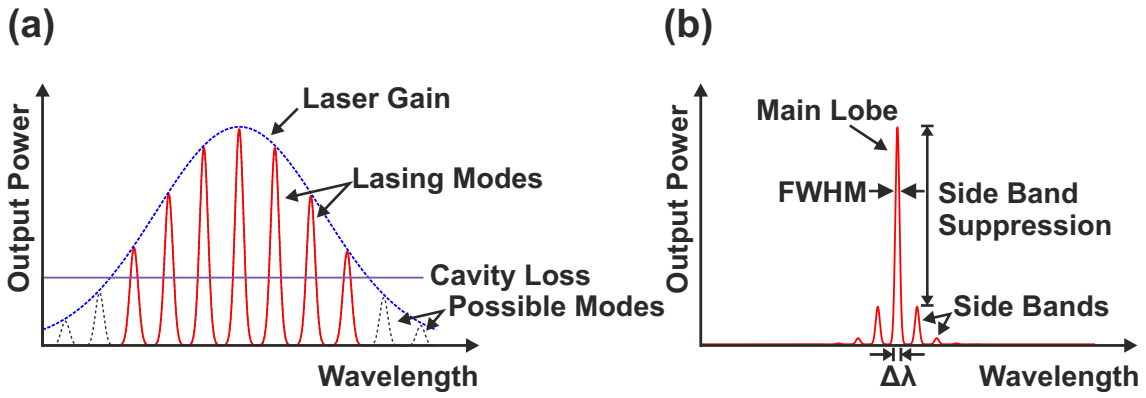

Figure 2.16: Typical gain, loss, and spectral profiles of (a) a Fabry-Pérot laser and (b) a distributed feedback laser. The Fabry-Pérot laser exhibits multiple longitudinal modes, while the DFB laser features a single, narrow mode due to the wavelength-selective grating.

Fig. 2.16 compares the typical gain, loss, and spectral characteristics of FP and DFB lasers. The spectrum of a FP laser (a) shows a series of equally spaced peaks, corresponding to the longitudinal modes of the cavity (black dashed), with the intensity shaped by the gain profile of the laser (blue dashed). Only the modes that exceed the lasing threshold, indicated by the cavity loss line (purple), experience a net gain and are therefore able to lase. In contrast, for a DFB laser (b), the periodic grating provides a strong feedback only for the longitudinal mode which is found closest to the Bragg wavelength (main lobe), while suppressing other sidemodes as a wavelength-dependent loss is introduced. Nevertheless, some sidebands can still occur due to imperfections in the grating structure or residual reflections at the facets. However, the sideband suppression is significantly higher than in FP lasers, as feedback for non-resonant wavelengths is inherently reduced by the grating design.

Even though a DFB laser operates in single mode, the output spectrum is never a perfectly narrow line. Instead, it always exhibits a finite spectral width $\Delta\lambda$, commonly defined as the full width at half maximum (FWHM). Generally, the broadening of a laser is mainly caused by quantum noise[8], particularly from spontaneous emission. The random nature of spontaneous emission induces phase fluctuations, which set a fundamental limit on the linewidth described by the Schawlow-Townes formula [121]. Unfortunately, this theoretical limit that is useful for gas and solid state lasers as well as microwave oscillators usually gives over an order of magnitude too low an estimate of the linewidth of DFB lasers. Additionally, the structural effects caused by the grating have to be considered as also changing the effective linewidth of the laser. The grating provides distributed feedback, and variations in carrier density influence both the strength and phase of this feedback. Therefore, the grating-induced coupling between carrier density and optical feedback amplifies the phase noise, further broadening the laser linewidth. Furthermore, spatial hole burning, arising from standing wave patterns in the cavity, introduces additional noise and mode competition, destabilizing the single-mode operation. Together, these intrinsic effects result in practical linewidths for DFB lasers reaching several hundred kHz [122]. Moreover, extrinsic factors such as temperature drifts and current noise further increase the laser frequency fluctuations, causing shifts of up to several tens of MHz over a time scale of milliseconds to seconds. For a more detailed explanation of the linewidth as well as additional information on other semiconductor laser sources used for terahertz systems, please refer to [123, 124].

2.3 Optical Phase-Locked Loops

As discussed in the previous section, the laser linewidth of DFB lasers is limited to the megahertz range, which directly affects the resolution of the terahertz signal. Unfortunately, combining two independent lasers intensifies this issue, as their uncorrelated noise broadens the linewidth of the beat frequency, further reducing the system's resolution. Also, the optical beams must be precisely controlled to ensure the same relative intensity and polarization, maximizing the amplitude of the beat signal. To mitigate these drawbacks, the DFB laser sources can be integrated into an active frequency stabilization scheme, establishing a common wavelength reference that minimizes frequency drift and improves coherence. As stated before, widely used synchronization techniques include phase-locked loops, optical frequency combs, and injection locking. Since the laser synchronization concept in this thesis relies on (optical) phase-locked loops, the following discussion will only focus on this approach.

Fig. 2.17 represents the block diagram of a PLL with an incorporated proportional-integral-derivative (PID) controller, serving as loop filter. Generally, a PLL is an electronic control system designed to synchronize the phase and frequency of an output signal $y(t)$ with a reference signal $r(t)$ in a closed feedback loop. It consists of the phase

[8] Also referred to as "white" noise due to its flat spectral density across frequencies.

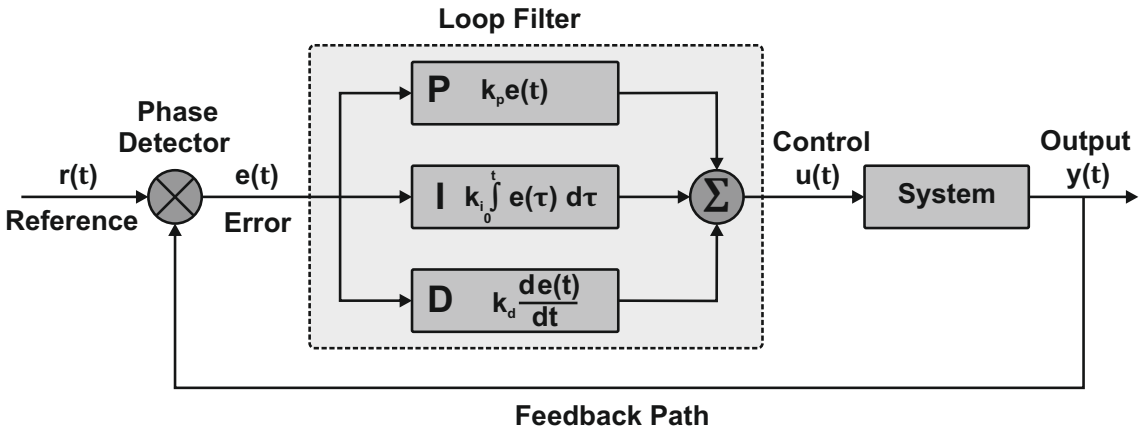

Figure 2.17: Block diagram of a phase-locked loop (PLL) including a proportional-integral-derivative (PID) controller as loop filter. In the feedback system, the phase detector compares the reference and output signals, generating an error signal that is processed by the PID controller to adjust phase and frequency of the output signal, achieving synchronization with the reference.

detector, the loop filter, and the feedback path. The phase detector compares the phase of the reference and output signals, generating an error signal that is proportional to the phase difference:

$$e(t) = r(t) - y(t). \tag{2.32}$$

This signal is then passed through the PID controller, which determines how the loop responds to disturbances in the output signal. In the shown concept, the PID controller replaces or supplements the traditional low-pass filter in the PLL, allowing more precise control of the loop dynamics. In the controller, the proportional element reacts to the immediate deviation, providing a quick response proportional to the current value of e(t). However, proportional control alone results in a steady-state error between the reference and the output value, as the controller needs a nonzero error to generate the proportional output response [125]. The integral part accumulates phase errors over time to effectively eliminate residual long-term offsets, ensuring a zero steady-state error. Meanwhile, the derivative component is included to anticipate future errors based on the current rate of change, helping to stabilize the system against high-frequency interferences and prevent overshoot. Together, these three elements form the control signal $u(t)$, which is applied to the control input of the system. Lastly, the system's output is split, with a part of the signal send through the feedback path to one inputs of the phase detector, thereby closing the loop.

The overall control function of the PLL can be defined as:

$$u(t) = K_\mathrm{p} e(t) + K_\mathrm{i} \int_0^t e(\tau)\, \mathrm{d}\tau + K_\mathrm{d} \frac{\mathrm{d}e(t)}{\mathrm{d}t}. \tag{2.33}$$

Here, K_p, K_i, and K_d are non-negative tuning constants, which must be determined individually for each control application, as they depend on the response characteristics

of the physical system external to the controller. In practical PLLs, equation (2.33) is often replaced by the so-called standard form

$$u(t) = K_\mathrm{p}\left(e(t) + \frac{1}{T_\mathrm{i}}\int_0^t e(\tau)\,\mathrm{d}\tau + T_\mathrm{d}\frac{\mathrm{d}e(t)}{\mathrm{d}t}\right), \tag{2.34}$$

where $T_\mathrm{i} = \frac{K_\mathrm{P}}{K_\mathrm{i}}$ and $T_\mathrm{d} = \frac{K_\mathrm{d}}{K_\mathrm{p}}$ represent the integration time and the derivative time, respectively. Physically, T_i denotes the timescale over which the system corrects accumulated errors, while T_d indicates how far ahead the controller attempts to predict future error trends.

If the PID controller's tuning parameters are chosen incorrectly, the system can become unstable, leading to oscillations, excessive overshoot, or slow response times. For instance, high values of K_p result in faster response times but can also make the system more sensitive to disturbances. Conversely, a very low K_p gain can cause the system to respond too slowly to changes, preventing it from reaching the desired reference point within an acceptable time. In the same way, incorrect T_i and T_d values may lead to overshooting or excessive damping, respectively.

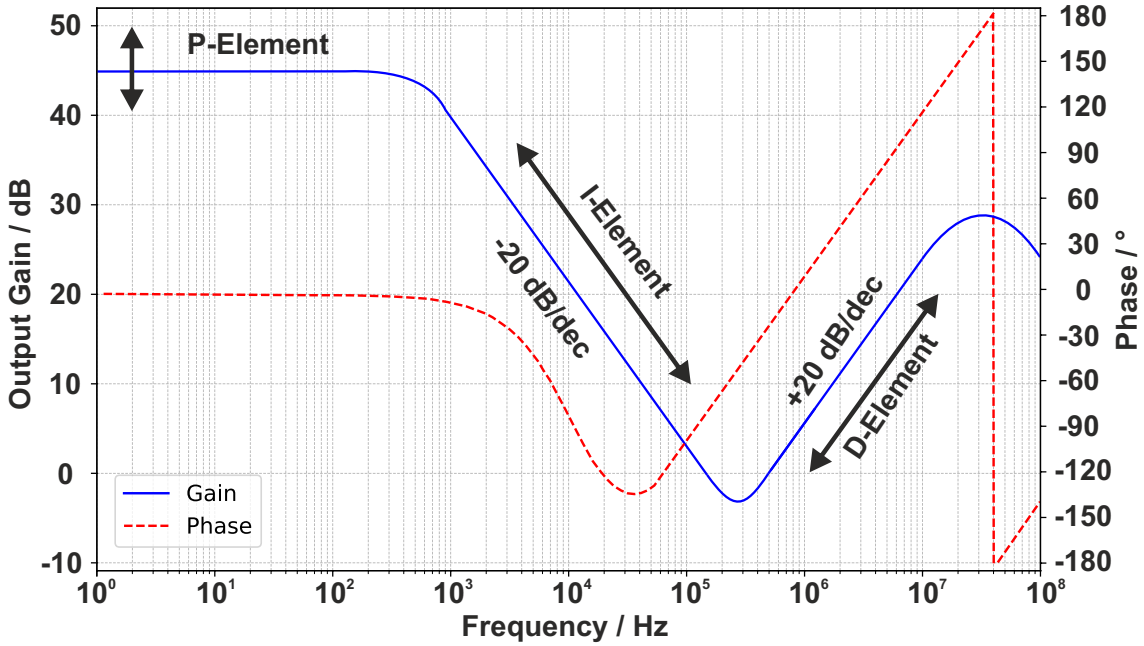

Figure 2.18: Typical transfer function of a PID controller. The P-element maintains constant gain with no phase shift. As the I-element starts to influence the response, the gain decreases by 20 dB/decade, also introducing a phase shift of -90°. For higher frequencies, the D-term allows for a gain increase of 20 dB/decade, while leading to a +90° phase shift, with the system bandwidth limiting the overall gain.

The transfer function of a typical PID controller is shown in Fig. 2.18. In the Bode plot, the P-element primarily determines the output gain of the controller, particularly at low frequencies. As K_p has no frequency dependence, there is no phase shift introduced

by the P-term. At a certain frequency, defined by T_i, the I-element begins to influence the controller's response, resulting in a gain decrease of 20 dB/decade as the frequency increases. In the phase plot, the I-element introduces a constant phase shift of -90° across all frequencies, reflecting the inherent time-delay effect of integration. For higher frequencies, the impact of the I-term diminishes due to its decreasing gain, and the D-element becomes more significant. The D-term allows for a gain enhance of 20 dB/decade and a phase advance of +90°, enabling a faster settling time and a higher proportional gain. However, the output gain of the PID controller at very high frequencies is limited by the bandwidth of the system components, as well as practical factors such as noise and delayed response times. These delays also contribute to phase lag, as the PLL can not respond fast enough to high-frequency disturbances, potentially destabilizing the control loop. When the phase exceeds 180°, the feedback is no longer capable to counteract these distortions, and the control signal interacts with the disturbances, thereby causing oscillations. To mitigate these effects, a low-pass filter can be added to limit the influence of frequencies above the PLL's bandwidth.

Instabilities due to excessive phase lag are not only caused by "wrong" tuning parameters or limitations of the PID controller itself. Instead, propagation times introduced by additional PLL components, such as cables, connectors and other transmission elements, further increase the overall phase delay.

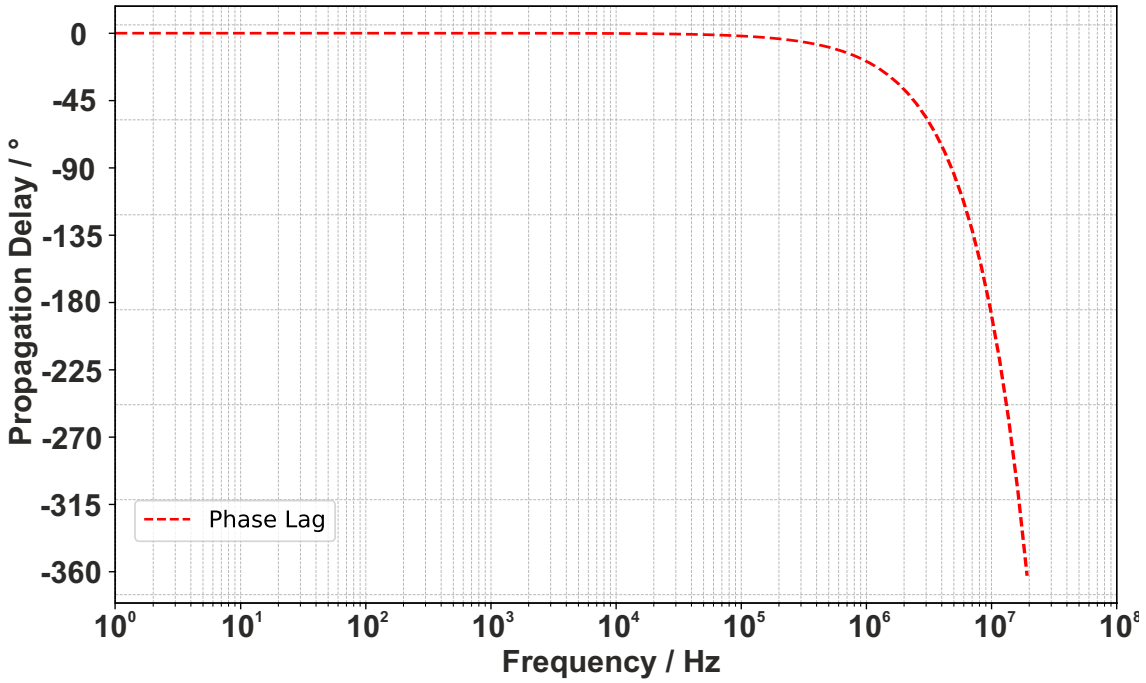

Figure 2.19: Frequency-dependent phase delay of an RF signal propagating through a 10 m coaxial cable.

As an example, Fig. 2.19 shows the phase delay induced by an RF signal propagating through a 10 m coaxial cable ($n \approx 1.5$). To pass along the cable the signal needs a

propagation time of $\tau_{\text{Delay}} \approx 50$ ns. This delay corresponds to a phase lag given by:

$$\Phi_{\text{Delay}} = 2\pi \cdot f \cdot \tau_{\text{Delay}}. \tag{2.35}$$

For the 10 m cable, this results in a phase lag of 180° at a signal frequency of 10 MHz. Equation (2.35) highlights the importance of minimizing signal path lengths, particularly for high-frequency signals. To account for these effects, controllers are often tuned to ensure adequate phase and gain margins, balancing responsiveness and stability. In practical PLLs, gain margins of at least 2 dB to 5 dB and phase margins between 30° to 60° are commonly used to achieve a stable and well-damped system response [126]. A phase margin closer to 30° tends to allow for faster response times but may result in overshoot or oscillations, while a phase margin near 60° ensures smoother performance with greater robustness but slower dynamics. To achieve maximum performance, the system being phase-locked should always be the slowest reacting element in the feedback loop. More information about PLLs and other locking techniques can be found in [73, 125].

In this work, temperature-stabilized DFB laser diodes integrated in OPLLs for the frequency synchronization are employed to generate beat signals, enabling high-resolution terahertz measurements with a photomixing setup. The resulting measurement system is primarily intended to address spectrum and network analysis, which will be elaborated in the next section.

2.4 Spectrum and Vector Network Analysis

Spectrum and (vector) network analysis originated in the mid-20th century, driven by growing needs in radio and telecommunications. Early spectrum analyzers, introduced in the 1930s, enabled visualization of radio frequencies, while vector network analyzers evolved in the 1960s to measure RF and microwave networks more accurately [127]. As telecommunications advanced, so did the need for precise and detailed tools to measure both the amplitude and phase characteristics of signals, leading to the evolution of VNAs that could fully characterize complex signal interactions in high-frequency devices. By the 1970s, these instruments were widely adopted in both military and civilian sectors, addressing the demand for accurate, high-frequency measurements in radar [128], satellite communications [129], and the emerging wireless industries [130]. In recent decades, spectrum and network analyzers have incorporated digital processing, enhancing their accuracy, speed, and frequency coverage. Today, modern SAs and VNAs are indispensable in fields ranging from 5G [131] and terahertz communications [132] to advanced research in quantum computing [133] and material sciences [134, 135].

2.4.1 Spectrum Analyzers

Traditionally, oscilloscopes measure how an electrical signal changes over time, offering valuable insight into time-dependent characteristics. However, this perspective alone doesn't provide a complete understanding of a device's or system's performance. To achieve a more comprehensive analysis, examining the signal in the frequency domain is essential, where amplitude is plotted as a function of frequency. Spectrum analyzers serve this purpose, offering a frequency-domain view, much like oscilloscopes do in the time domain.

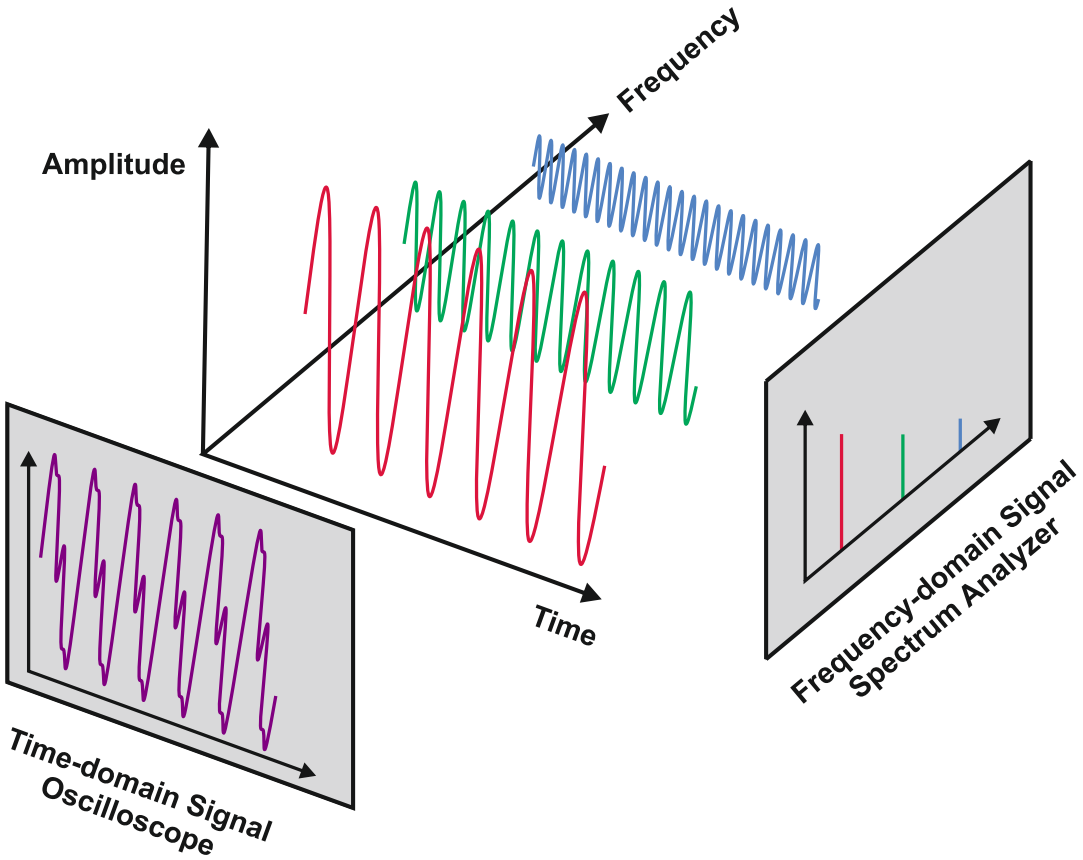

Figure 2.20: Illustration of signal analysis in time domain vs. frequency domain: The time domain displays the combined waveform, while the frequency domain separates the signal into its individual frequency components.

Fig. 2.20 illustrates the relationship between time and frequency domain. In the time domain, the signal is shown as a continuous waveform, where all frequency components are combined (purple). This view provides insight into the signal's time-based dynamic but does not highlight the individual frequency contributions. In contrast, the frequency-domain view breaks down the signal into its constituent frequencies (red, green, and blue), revealing important details about its spectral characteristics, such as harmonic components, noise, or other frequency-specific responses that may not be visible in the time-domain representation.

Operation Principle

Generally, there are two primary methods for obtaining the frequency spectrum of a signal: Fast Fourier transform (FFT) and swept-tuned analysis. In an FFT analyzer, the time-domain signal is digitized and converted into the frequency domain using the FFT algorithm, allowing the analyzer to simultaneously measure the entire frequency range. This method is equivalent to analyzing the signal by applying multiple filters in parallel.With real-time analysis, both the magnitude and phase of periodic and transient signals can be determined. Under certain conditions, such as narrower spans or a high frequency resolution, FFT can be faster than swept analysis, though swept analysis generally performs better for wider spans. Thus, the most commonly used SA architecture is a swept-tuned receiver. This technique allows for continuous measurement of frequency components by sweeping through the frequency range and recording the amplitude at each point. The basic concept involves separating the individual frequencies by filtering the input signal. Since applying a large number of filters can be inefficient, particularly for complex signals with broad frequency ranges, a more efficient approach is to shift the signal to a common frequency using a mixer and a local oscillator. This process, similar to the detection method in heterodyne receivers, enables the incoming signal to be downconverted to a fixed intermediate frequency. If the LO frequency is tunable — a technically feasible requirement — the entire input frequency range can be covered using a single filter at the IF that has a constant center frequency.

The architecture of a heterodyne swept-tuned SA is shown in Fig. 2.21. In this system, a sweep generator produces a sawtooth voltage to control the local oscillator frequency. The LO is typically a YIG (Yttrium Iron Garnet) tuned oscillator or a voltage controlled oscillator (VCO), which is responsible for tuning the analyzer across the desired frequency range. The output is then directed to a mixer, for the heterodyne downconversion of the input signal. Prior to mixing, the incoming RF signal is attenuated to ensure it remains within the mixer's optimal operating range. If the signal is too strong, the mixer may experience gain compression, where the output signal becomes disproportionately weaker relative to the input. Additionally, high-level or broadband signals can lead to distortion due to the nonlinear behavior of the mixer when it exceeds its dynamic range. After the signal is converted to the intermediate frequency, it is amplified to a suitable level before passing through the IF filter. This band-pass filter acts as the "window" for detecting the signal, allowing frequencies within its bandwidth to pass while attenuating others. The bandwidth of the IF filter, known as the resolution bandwidth (RBW), determines the SA's ability to resolve closely spaced signals. To analyze signals across a wide dynamic range simultaneously, the IF signal is processed by a logarithmic amplifier, which compresses its amplitude. Following this, an envelope detector extracts the amplitude of the signal by tracing the outer boundary (envelope) of the modulated waveform. This is achieved by rectifying and smoothing the signal, which allows only slower amplitude variations to pass while discarding high-frequency carrier components. The resulting low-frequency representation reflects the signal's overall amplitude without retaining phase information. Consequently, phase data is lost during this process,

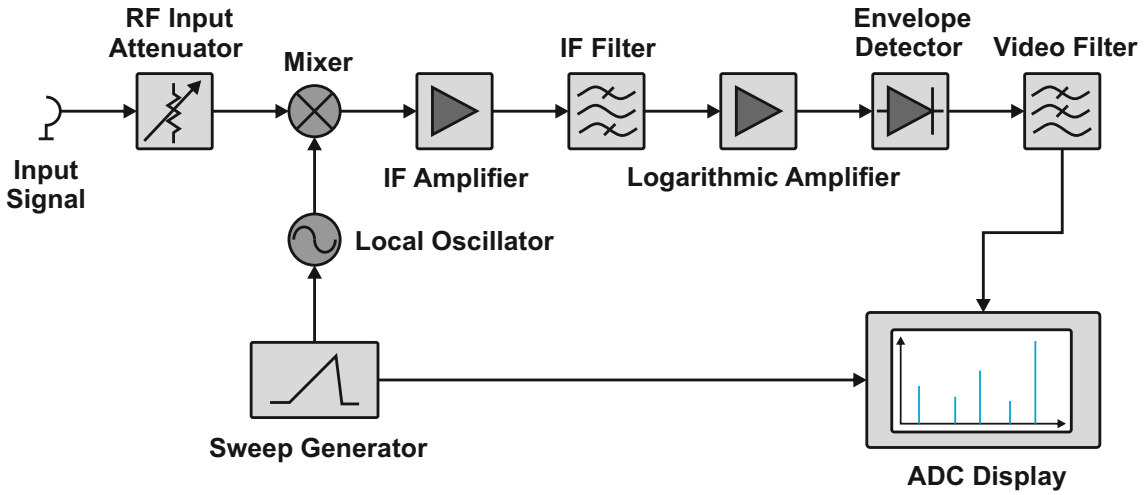

Figure 2.21: Block diagram of a heterodyne swept-tuned spectrum analyzer: The system uses a sweep generator to control the local oscillator, tuning it across the desired frequency range. The incoming RF signal is mixed with the LO to downconvert it to an intermediate frequency, which is then amplified and filtered through an IF band-pass filter. The resolution bandwidth (RBW) of the IF filter defines the analyzer's ability to resolve closely spaced signals. A logarithmic amplifier compresses the amplitude of the IF signal, while an envelope detector traces its amplitude profile. The video filter smooths the output to reduce noise, and the video bandwidth (VBW) setting helps distinguish signals near the noise floor. The resulting data is processed for accurate frequency calibration. Last, the frequency spectrum is displayed.

leaving only the magnitude for display. This is a fundamental distinction from FFT analyzers, which retain both amplitude and phase details. The resulting signal, referred to as the video signal, is sent to a tunable low-pass filter also called video filter. This filter averages or smooths the trace displayed on the spectrum analyzer, helping to reduce noise interference. By adjusting the video bandwidth (VBW) setting, peak-to-peak noise variations can be minimized, making it easier to distinguish signals close to the noise floor. Additionally, the sampling of the video signal by the analog-to-digital converter (ADC) is also synchronized with the sweep generator to ensure accurate frequency calibration. This synchronization allows the spectrum analyzer to map the LO frequency directly to the input signal, with the x-axis of the display representing the actual signal frequency.

Analyzer Metrics

To gain a deeper insight into the capabilities and limitations of a SA, it's important to examine the key parameters that define its performance and functionality. These include:

- **Frequency range**: Defines the span of frequencies the analyzer can measure.

- **Resolution**: Determines the analyzer's ability to distinguish closely spaced frequencies.
- **Sensitivity**: Refers to the minimum detectable signal strength.
- **Dynamic range**: Represents the range between the smallest and largest signal levels the analyzer can measure.
- **Accuracy**: Indicates how closely the measurements match the actual values of the signal being analyzed.
- **Sweep time**: The time it takes for the analyzer to complete a full frequency sweep.

Frequency range is the first fundamental parameter to be discussed for the characterization, as it defines the operational span of the SA. Typically, the low-frequency limit is determined by its internal electronics and the design of its front-end circuitry. For the high-frequency limit, the frequency-dependent characteristics of the internal components play a crucial role. As the frequency increases, the design and manufacture of electronic subsystems such as mixers, oscillators, and amplifiers become exponentially challenging. The performance of these devices diminishes at higher frequencies, limiting their effectiveness in accurately processing high-frequency signals. Additionally, the LO frequency becomes critical in this context, as it sets the operating frequency of the analyzer by mixing with the input signal. As the required LO frequency increases, it introduces additional complexities, including higher power demands and greater susceptibility to noise and nonlinearities in the system. To extend the operational frequency range, particularly in the millimeter-wave and terahertz regions, spectrum analyzers often rely on additional frequency extenders, such as harmonic mixers or frequency multipliers. These extenders enable the analyzer to handle higher-frequency signals that exceed the capabilities of the internal components.

Resolution is an important specification when analyzing signals that are closely spaced in frequency, as it determines the ability of the SA to differentiate between them. The resolution is typically specified as the resolution bandwidth, which refers to the width of the frequency band where the analyzer's response falls to either a 3-dB or 6-dB point down from the peak response. A smaller RBW enables the analyzer to distinguish finer details between signals, but it comes at the cost of longer sweep times and increased noise levels. To achieve optimal resolution, the RBW must be carefully chosen to balance the need for precision with practical considerations such as noise floor and processing speed. Therefore, the optimal RBW can be determined using the following relationship

$$RBW = \sqrt{\frac{\text{Frequency span}}{\text{Sweep time}}}. \tag{2.36}$$

Sensitivity is another key parameter in the performance of a SA, particularly when it comes to detecting and measuring low-level signals. Sensitivity indicates how well the analyzer can detect small signals against the background of thermal noise, which is inherently present in all electronic systems. In an ideal scenario, a receiver would

add no noise beyond the thermal noise. However, in practice, every receiver introduces some amount of internally generated noise. This is typically quantified by the displayed average noise level (DANL), which is expressed in dBm and refers to the noise floor of the instrument when using the smallest possible RBW. The DANL represents the best-case sensitivity of the spectrum analyzer — below this level, signals can not be reliably detected. DANL values are typically in the range of -90 dBm to -145 dBm, with higher-performance instruments achieving lower noise floors and thus posses a higher detectability. Even though trace averaging and video bandwidth settings do not change the actual sensitivity, they can be used to enhance the visibility of weak signals in noisy conditions. Trace averaging reduces random noise by combining multiple sweeps, resulting in a cleaner and more stable trace. A narrower VBW lowers the apparent noise floor by averaging out short-term noise fluctuations, which can make weaker signals more distinguishable.

Dynamic range provides information about the SA's capability to simultaneously process signals with very different levels. It is generally defined as the range between the highest and lowest signal levels that can be accurately measured without distortion or loss of information. In practical terms, the dynamic range is limited by three factors: the broadband noise floor (sensitivity) of the system, the distortion performance of the input mixer (compression), and the phase noise of the LO. Thereby, the lower limit is determined by the DANL, while the upper limit is constrained by the maximum input power that the analyzer can handle without distortion or damage. In modern high-performance spectrum analyzers, the maximum dynamic range can exceed 100 dB, though practical limits are often dictated by the specific application, the quality of the internal components, and the trade-offs between speed and resolution.

Accuracy of a SA refers to how closely the instrument's measurements match the actual values of the signal being analyzed. It includes both frequency accuracy, which depends on the stability of the LO and frequency reference, and amplitude or power accuracy, which relies on proper calibration and signal processing. Frequency accuracy is often specified in terms of ± ppm (parts per million) or absolute error in Hz depending on the frequency range of the instrument. For instance, a typical SA may have a frequency accuracy of ±1 ppm, which equates to an error of ±1 kHz for a 1 GHz signal, and this accuracy can vary with frequency. Environmental factors, such as temperature drifts, and the aging of internal components, such as crystals, can also affect frequency accuracy. Amplitude accuracy errors are often expressed as an absolute value (e.g., ±0.5 dB) or a percentage of the measured value. These errors result from various sources, including internal noise, signal attenuation settings, and the handling of nonlinearities during signal processing. To mitigate these errors, SAs are factory-calibrated by recording the individual error components and storing them in the device. Despite this, regular calibration (typically at the manufacturer's facility) is essential to maintain accuracy, as the signal source used for self-adjustment can experience aging over time, leading to potential shifts in performance.

Sweep time denotes the duration it takes to complete a full frequency sweep across

the defined frequency range. It is directly related to the number of frequency samples (bins) that the analyzer needs to take. As equation (2.36) indicates, sweep time increases inversely with the square of the RBW, so with a decrease by the factor n the required minimum sweep time becomes n^2 longer. If the VBW is smaller than the RBW, the minimum sweep time is also affected by the transient time of the video filter. The video filter, typically a first-order low-pass filter or an analog RC circuit, establishes a linear relationship between VBW and sweep time. Therefore, reducing the VBW by a factor of n results in a sweep time increase by the same factor n. However, even for large resolution and video bandwidths, sweep time can not be reduced indefinitely due to the minimum time required for the LO settings and data processing. For wide frequency spans, the tuning speed of the local oscillator and the sampling rate of the ADC limit the minimum sweep time.

In addition to the primary specifications discussed, SAs can be characterized by several other parameters depending on the specific application. These include distortion performance (e.g., harmonic distortion, intermodulation distortion), spurious-free dynamic range (SFDR), phase noise, and residual responses. For a more comprehensive understanding of SA metrics and their roles in measurement performance, please refer to [136, 137], or other technical literature in RF engineering.

2.4.2 Vector Network Analyzers

Having discussed the basic principles and key metrics of spectrum analyzers, we now shift focus to network analyzers (NAs), which offer a broader range of capabilities. While SAs are primarily used to examine the frequency and signal power of active devices[9], NAs extend this functionality by providing comprehensive measurements of both active and passive components. Unlike SAs, network analyzers measure both phase and magnitude[10], making them essential for complete network analysis. This capability allows NAs to accurately characterize the transmission and reflection properties of networks, facilitating the analysis of electrical systems and devices. A network analyzer generates a sinusoidal signal that is applied to the device under test (DUT) to evaluate its response. The analyzer compares the returning signal's amplitude and phase with the outgoing signal, providing detailed insights into the electrical characteristics of the DUT. Network analyzers are classified into two main types:

- **Scalar Network Analyzer**: Measures only the magnitude between the incident and reflected waves from the DUT.

[9] SAs can also be used to measure passive devices when equipped with a tracking generator, which delivers a swept frequency signal to the passive component, enabling the measurement of its response in terms of amplitude and frequency. However, this method typically does not provide phase information.

[10] Magnitude in VNAs typically represents amplitude or power ratios on a logarithmic scale (dB), whereas spectrum analyzers display amplitude as raw signal levels, like voltage, or convert it to power (dBm).

- **Vector Network Analyzer**: Measures both the magnitude and phase of the incident and reflected waves, providing a more comprehensive analysis of the DUT's characteristics.

Typical applications of a VNA include the characterization of one-port, two-port, and multi-port networks. A one-port network is depicted in Fig. 2.22 (a), where V^+ and V^- represent the amplitudes of the incident and reflected voltage waves traveling to and from the DUT, respectively. The relationship between these waves is described by the reflection coefficient

$$\Gamma = \frac{V^-}{V^+}. \tag{2.37}$$

Γ quantifies how much of the incident signal is reflected back due to impedance mismatch between the network's impedance Z and the reference impedance of the system. A perfect match results in no reflection ($\Gamma = 0$), whereas total reflection occurs in the case of a strong impedance mismatch ($\Gamma = \pm 1$).

To also determine the transmission properties of a DUT, a two-port network, as illustrated in Fig. 2.22 (b), allows for the measurement of both forward and reverse signal propagation, along with the corresponding reflection coefficients. In general, these quantities are represented by so-called scattering parameters (S-parameters)

$$S_{mn} = \frac{V_m^-}{V_n^+}\Big|_{V_{m\neq n}^+=0}, \tag{2.38}$$

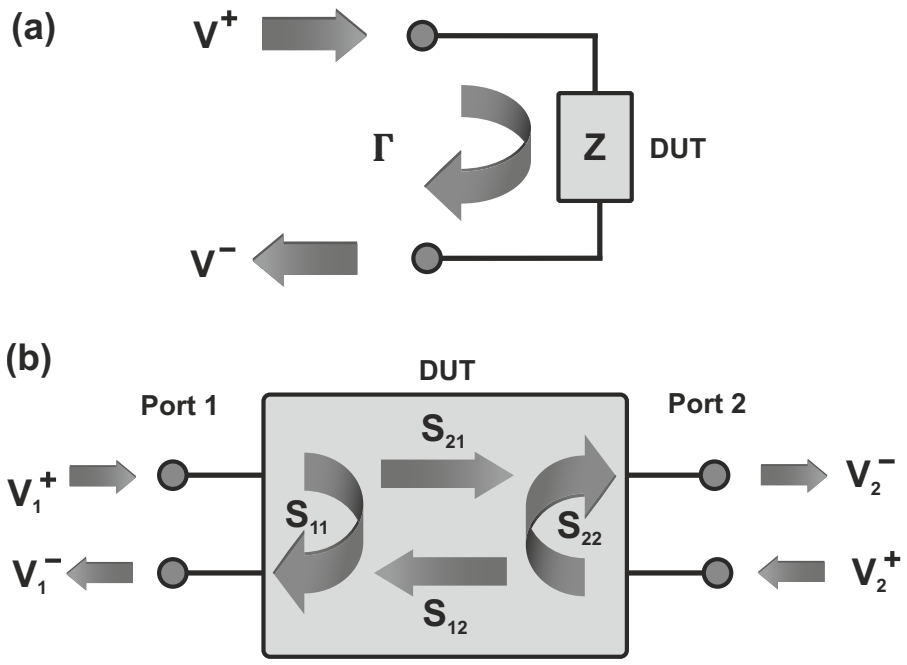

Figure 2.22: Schematic diagram of a one-port (a) and two-port network (b): The one-port network measures the reflection coefficient Γ from incident and reflected voltage waves. The two-port network uses S-parameters (S_{11}, S_{21}, S_{12}, S_{22}) to characterize reflection and transmission between two ports.

where V_m^- is the emerging voltage at port m, and V_n^+ is the incident voltage at port n. The condition $V_{m\neq n}^+ = 0$ isolates the signal at the specific port, enabling the measurement of the S-parameter S_{mn}, which describes the response of the network between ports m and n.

For a two-port measurement, the four S-parameters S_{11}, S_{21}, S_{12}, and S_{22} are required to fully describe the electrical properties of the DUT. The parameters S_{11} and S_{22} represent the input and output reflection coefficients at port 1 and port 2, while S_{21} and S_{12} denote the forward and reverse transmission coefficients. In this case, the S-parameters can be expressed in matrix form as:

$$\begin{pmatrix} V_1^- \\ V_2^- \end{pmatrix} = \begin{pmatrix} S_{11} & S_{12} \\ S_{21} & S_{22} \end{pmatrix} \begin{pmatrix} V_1^+ \\ V_2^+ \end{pmatrix}. \tag{2.39}$$

S-parameters are commonly used to characterize various properties of RF and microwave systems, including gain, return loss, voltage standing wave ratio (VSWR), impedance mismatch, and amplifier stability. By analyzing the S-parameters, engineers can assess the efficiency of signal transmission, identify potential sources of signal degradation, and optimize system performance. For example, gain provides insight into how much a device amplifies a signal, while return loss helps determine the effectiveness of impedance matching. The VSWR indicates the level of power reflected due to impedance mismatches, and amplifier stability ensures reliable operation without unwanted oscillations or feedback. Therefore, measuring S-parameters with a VNA allows for the design, testing, and optimization of high-frequency components, including amplifiers, filters, antennas, and transmission lines.

Operation Principle

Fig. 2.23 provides a simplified block diagram representation of the major components of a two-port VNA. Although some modern VNAs are multi-port instruments designed to analyze more complex networks, their fundamental principles of operation remain the same. At the core of the system is a RF source that operates in a continuous-wave mode, providing a stable and coherent test signal. The RF switch routes this signal to one of the test ports, ensuring that only one port receives a stimulus signal at a time. This is consistent with the previously mentioned definition of S-parameters where each parameter is determined under the condition that only one incident signal is active simultaneously. Along the path between the RF source and the test port, directional couplers separate the signals based on their direction of travel. By tapping off a portion of the outgoing (V^+) and returning (V^-) test signals, they allow the VNA to monitor the signals without significantly affecting the main signal path. These samples are proportional to V^+ and V^-, enabling the calculation of the S-parameters of the DUT.

Since these internal signals have the same high-frequency as the RF stimulus, they can not be processed directly. To address this, they are downconverted to a lower

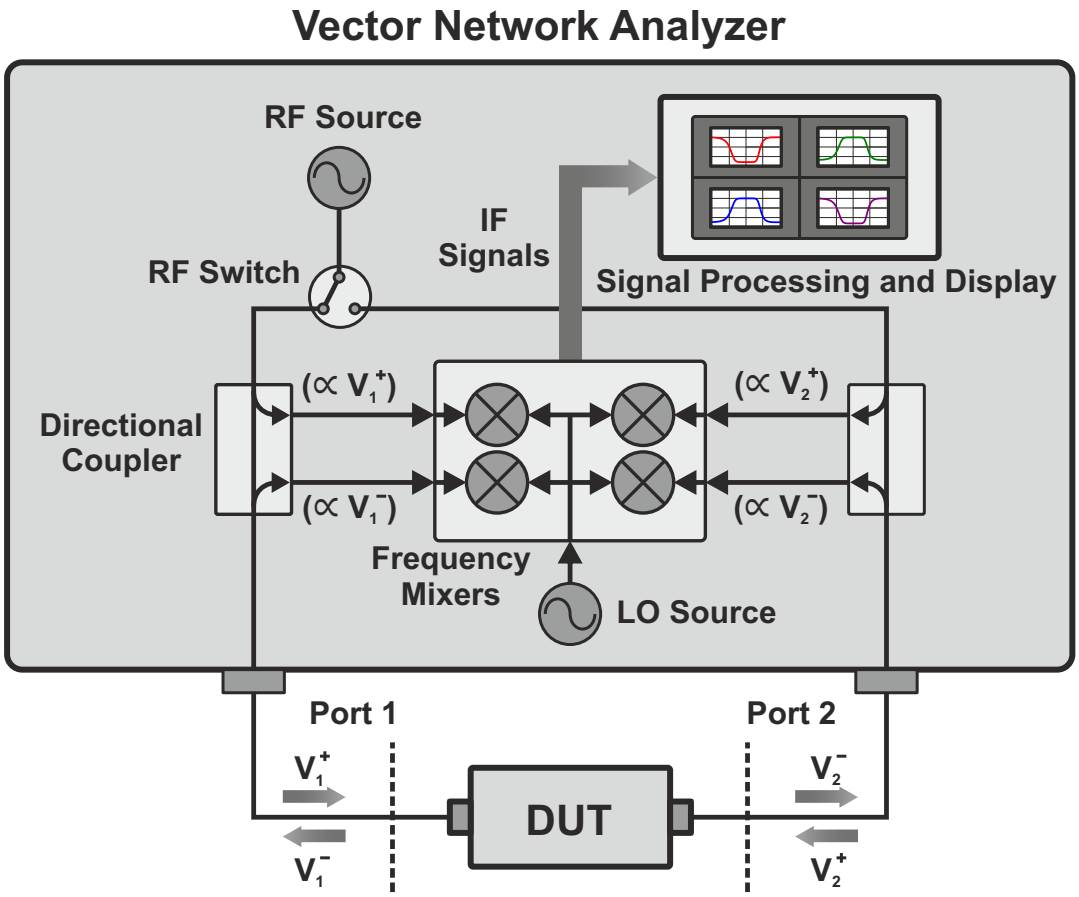

Figure 2.23: Block diagram of a typical two-port vector network analyzer: The continuous-wave test signal, provided by the RF source, is directed to one of the test ports by the RF switch, ensuring that only one port receives the stimulus at a time. Directional couplers separate the incident and reflected signals from the test ports, which are proportional to the voltages V^+ and V^-. These high-frequency signals are downconverted to intermediate frequencies using frequency mixers and an LO source. The IF signals, which retain both amplitude and phase relationships, are digitized for further processing. On the screen, the calculated S-parameters are displayed to characterize the reflection and transmission properties of the DUT.

frequency, following the same heterodyne principle used in spectrum analyzers. This is achieved with frequency mixers and a LO source, resulting in IF signals that are typically found in the MHz range. Importantly, these IF signals maintain both the amplitude proportionality and the phase relationships of the original high-frequency signals. The VNA then digitizes the IF signals, calculates the S-parameters, and displays them.

Reaching Terahertz Frequencies

While older network analyzers consisted of multiple separate components, such as RF generators, directional coupler assemblies, IF/digitizer units, and display processors, all

connected by a complex system of cables, modern VNAs have integrated these functions into a single, compact instrument. Therefore, test solutions that measure below 70 GHz [138] are typically plug-and-play systems, allowing users to easily perform measurements without the need for complex setups or additional hardware. However, to extend VNA capabilities to higher frequencies, a so-called distributed architecture is typically employed. This involves using frequency extenders that upconvert stimulus signals and downconvert response signals, enabling also the analysis of DUTs operating in the terahertz range.

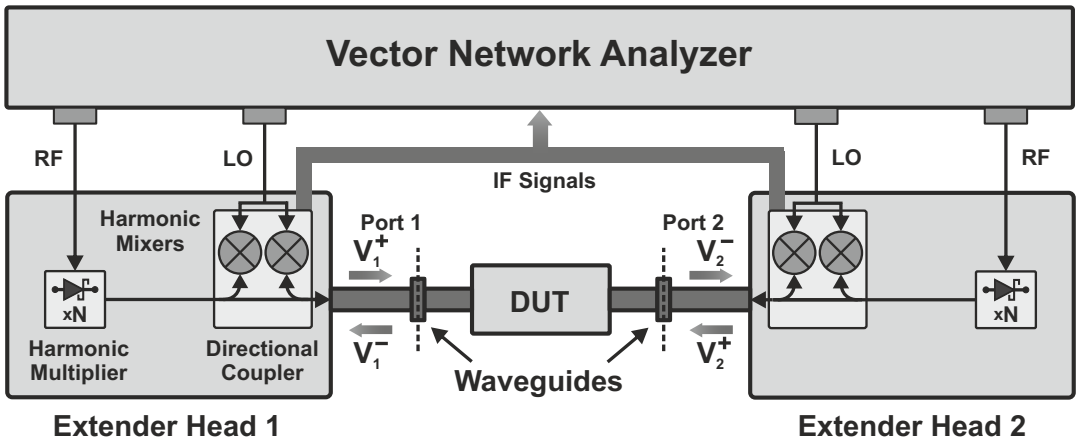

Figure 2.24: Block diagram of a VNA with extender modules for terahertz operation: RF and LO signals from the VNA are sent to the extender heads, where a harmonic frequency multiplier generates the terahertz stimulus. The signal is transmitted through specialized waveguides, with directional couplers separating the signals, and harmonic mixers downconverting it to an intermediate frequency for further processing in the VNA back end.

A typical hardware configuration for a VNA with extender modules[11] is shown in Fig. 2.24. The RF and LO signals coming from the VNA, typically in the range of several tens of gigahertz, are directed to the extender heads via coaxial cables. In the extender, the actual stimulus test signal is generated by a harmonic frequency multiplier chain, which relies on driving a nonlinear semiconductor device, commonly a Schottky diode (see Section 2.1.4). Once the frequency has been upconverted, the terahertz signal is transmitted through specialized waveguides or antennas designed to operate efficiently at these high frequencies. These components ensure minimal signal loss and effective coupling into the DUT. The extenders also include directional couplers for signal separation, as well as mixers for downconverting to IF signals, keeping the terahertz signals limited to the extender heads and the DUT. However, instead of directly mixing the coupled signals with the LO signal, a harmonic of the LO signal is used. One of these

[11] External units providing DC power to the extender heads are not depicted here. Additionally, some systems require external modules to enable signal transmission between the analyzer and the extender heads.

harmonics will generate an IF signal in a convenient frequency range, which can be processed in the same manner as in a conventional vector network analyzer.

In most setups, the user does not need to worry about selecting the correct frequencies for the RF and LO signals, as this is automatically handled by the VNA. Many modern vector network analyzers have this information either preloaded or supplied through an instrument state file from the frequency extender manufacturer.

Measurement Errors and Error Box Model

As previously mentioned, S-parameter measurements with VNAs are crucial for the characterization of HF systems and subsystems, yet they are susceptible to errors caused by imperfections in the VNA, the test setup, and factors such as noise and drift. These errors are commonly categorized into three main types [139]:

- **Systematic errors**: These errors are mainly caused by imperfections in the VNA and test setup. They are repeatable and time-invariant, making them predictable. Most systematic errors can be identified during the calibration process and removed afterwards.
- **Random errors**: Random errors are inherently unpredictable and can not be eliminated through the calibration process. However, they can be minimized to enhance measurement accuracy.
- **Drift errors**: These errors arise from changes in the VNA's performance after calibration. They can be removed by re-calibrating the instrument.

Different **systematic errors** emerge for both reflection and transmission measurements, causing unavoidable magnitude and phase inaccuracies. These errors stem from factors such as signal losses, internal impedance mismatches, and limited directivity in the measurement system. In reflection measurements, errors such as directivity and source match occur. Directivity errors result from leakage in the directional coupler, allowing a portion of the incident signal to interfere with the reflected signal being measured. Source match errors stem from multiple internal reflections between the analyzer and the DUT. These reflections combine with the incident signal and are detected at the receiver port, but not in the reference path. For transmission measurements, isolation errors occur due to signal leakage, also known as crosstalk, where unwanted signals from one port interfere with the measurements at the other. Load match errors are caused by signals reflected off the port during transmission measurements, which can distort the transmitted signal. Additionally, tracking errors can occur for both reflection and transmission measurements due to the non-identical frequency responses of the receivers, leading to discrepancies in measurements across different frequencies. Since all of these errors are repeatable and time-invariant, they can be effectively accounted for through calibration, which will be discussed later in this section.

The main sources of **random errors** are instrument noise and repeatability issues. Low-level noise, or background noise, originates from the broadband noise floor of the

receiver itself, while high-level noise, or jitter, is due to the phase noise of the LO source. Switch repeatability errors arise from the mechanical contacts of RF switches, which can introduce inconsistencies in the signal path each time the switch is activated. Connector repeatability errors result from the wear and tear of connectors, leading to variations in signal transmission over time. To reduce their impact, averaging successive measurements, increasing the source power, and narrowing the IF bandwidth (IFBW) can be effective strategies.

Drift errors are primarily caused by physical movement and thermal expansion of the interconnecting cables within the test setup, which can lead to changes in impedance, signal attenuation, and phase shifts. Furthermore, the stability of the frequency converter plays a significant role, as any instability in the conversion process can also contribute to errors as time progresses. Recalibrating the instrument and maintaining stable ambient conditions are reliable methods to compensate for drift errors.

After understanding the different errors that influence measurement accuracy and reliability, it becomes important to consider how calibration techniques can mitigate these effects, especially for systematic errors. Fortunately, all systematic errors can be merged into a relatively simple model known as the error box model [140]. The error box model (see Fig. 2.25) is a simplified, linear representation of systematic measurement errors in VNA systems. It accounts for various error sources such as directivity, reflection tracking, and source/load match using frequency-dependent parameters. The model is applied through error terms that describe the relationship between incident and reflected signals at each port. To mitigate these errors, VNA calibration is performed using well-defined standards, which are categorized into one-port and two-port types. Calibration standards such as Short, Offset Short, Load, and Thru are used to isolate and correct these errors. Two primary calibration methods, SOLT (Short-Open-Load-Thru) and TRL (Thru-Reflect-Line), are employed to perform the necessary corrections. However, some residual errors may persist due to imperfections in the calibration process and environmental influences. A more detailed explanation of the error box model and calibration standards can be found in Appendix A.

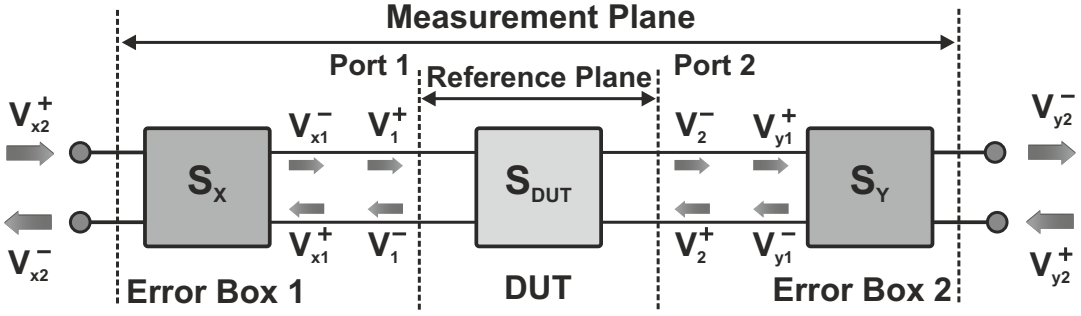

Figure 2.25: Schematic representation of a two-port error box model: The model uses two S-parameter matrices, S_x and S_y, to describe the relationship between incident and reflected signals at both ports. Error terms account for systematic errors, including directivity, reflection and transmission tracking, as well as source and load match.

2.4.3 Spectrum Analyzer vs. Vector Network Analyzer

This section will conclude with an overview of the key characteristics of spectrum analyzers and vector network analyzers. Despite apparent parallels between SAs and VNAs, there are a number of significant differences to keep in mind. When it comes to choosing an analyzer, it is essential to consider what suits best for the intended use case. For instance, if you want to measure the power levels of CW signals to determine strength and spectral purity across a wide frequency range, a spectrum analyzer would be the better choice. Conversely, if you need to analyze the reflection and transmission properties of an electrical DUT or troubleshoot other network problems such as impedance matching, signal loss, or phase shifts, a (vector) network analyzer is the appropriate tool.

The major differences rely on their system architecture and operation principle. A SA is a receive only instrument, similar to an oscilloscope. It just passively measures and displays information (amplitude over frequency) about whatever signals are present at the input. In contrast, a VNA is a stimulus-response instrument. It is not really designed to receive anything other than the test signal that it generates, which is a simple swept RF wave. Therefore, the receivers are only sensitive to signals at the generated stimulus frequency and only within the IF bandwidth of measurement. Importantly, it measures both amplitude and phase relationship between the original stimulus signal and the stimulus signal after it has passed through some DUT, enabling a full characterization.

While SAs equipped with a tracking generator and a directional coupler have the ability to measure transmission and reflection properties of passive devices, they still lack phase information as well as accuracy due to less precise calibration capabilities. On the other hand, in certain instances, a VNA can emulate some of the functionality of a SA. However, there are also inherent limitations, as SA receivers typically exhibit superior harmonic and spurious performance compared to VNA receivers. This will primarily reduce the reliability of the analysis, as SA receivers usually include attenuators, preamplifiers, and tunable filters to handle both large and small signals and improve impedance matching. These factors are less important in a VNA, given that the amplitude and frequency of the stimulus signal can be controlled, facilitating a much simpler and cost-effective receiver design.

As stated in the preceding discussion, each device has a designated scope of application and operational strengths, making them well-suited for distinct tasks. A comprehensive summary of the most prominent features of modern SAs and (V)NAs can be found in Table 2.1.

Table 2.1: Comparison between Spectrum Analyzers and Network Analyzers

Feature	Spectrum Analyzer	Network Analyzer
Measurement focus	Analyze signal spectra: power vs. frequency	S-parameter measurements: magnitude and phase vs. frequency
Frequency range[a]	Broad range; up to 110 GHz for a single instrument	Typically narrower; up to 70 GHz for a single instrument
Resolution	Defined by RBW; wider RBW (up to 1 GHz) for fast or narrow RBW (down to 1 Hz) for detailed measurements	Defined by IFBW (typically 1 Hz to 10 MHz); wider IFBW for more speed or narrower IFBW for more precision
Dynamic range / sensitivity	Higher; DANL of > 160 dB possible (depends on RBW)	Lower; up to 150 dB (strongly effected by IFBW and calibration)
Accuracy	Frequency accuracy < 1 Hz; limited in absolute power values	Frequency accuracy < 1 Hz; superior magnitude and phase accuracy due to advanced calibration
Calibration	Limited capabilities	Advanced capabilities
Error correction	Limited (no phase correction)	Advanced correction for magnitude, phase, and impedance mismatches
Limitations	More susceptible to noise interference	Usable bandwidth limited by calibration accuracy (especially at high frequencies)
Channels	Single channel (receiver only)	Multiple ports (2, 4, or more)
Typical use cases	Analyzing wide-band signals, monitoring interference, identifying spurious signals	Characterization of electronic devices, troubleshooting in networks

[a] With external extender heads both systems can cover ranges up to 1.5 THz [36].

3 Laser Frequency Synchronization

The measurement concepts developed in this thesis are predominantly based on the generation and detection of CW terahertz radiation in a photomixing setup. As discussed in the last chapter, the properties of the emitted terahertz signal are mainly determined by the optical waves creating the beat note. To perform high-resolution spectrum and vector network analysis comparable to state-of-the-art electronic systems, frequency stability at the Hz level is essential. However, the typical frequency resolution of free-running photomixing systems is in the megahertz range, limiting the competitiveness of optical concepts. Therefore, an active laser frequency synchronization is required to phase-lock the beat signal to a highly stable reference source, reducing noise and drift.

In this chapter, the developed laser frequency synchronization concept is introduced. First, the available DFB lasers are analyzed, focusing on key properties essential for stabilization with the OPLL, including tuning range and spectral linewidth stability. Next, the concept of phase-locking in the RF range is discussed, with particular emphasis on beat signal dynamics and noise characteristics. This principle is then adapted to the terahertz domain, where different approaches for heterodyne downconversion are compared. In the last section, methods for extending the frequency range and bandwidth beyond the available reference sources are examined, providing access to highly stable beat frequencies of more than 1 THz.

3.1 Laser Characterization

For the generation of the optical beat signals, the system employs three linearly polarized DFB diode lasers (Model DL 100 DFB, Toptica Photonics AG) with integrated 60 dB optical isolators, preventing feedback into the laser diodes. All lasers operate near 855 nm, with wavelength ranges of 2 nm to 3 nm. The wavelength can be adjusted either through temperature tuning (61 pm/K or 25 GHz/K) using a thermoelectric cooler and a thermistor for precise temperature stabilization, or by modulating the current input (2.4 pm/mA or 1 GHz/mA), offering a fast response for fine-tuning of the spectral output. Fig. 3.1 shows the corresponding thermal frequency tuning range of the three laser diodes for a constant operation current of 190 mA. The two phase-locked lasers #1043 (blue) and #1167 (red), referred to as “Secondary 1” and “Secondary 2” in the following, have mode-hop-free tuning ranges of 843 GHz and 1081 GHz, respectively. However, due to the partial overlap of their frequency spectra, the resulting maximum beat signal frequency is limited to 1794 GHz. The free-running laser #1169 (purple

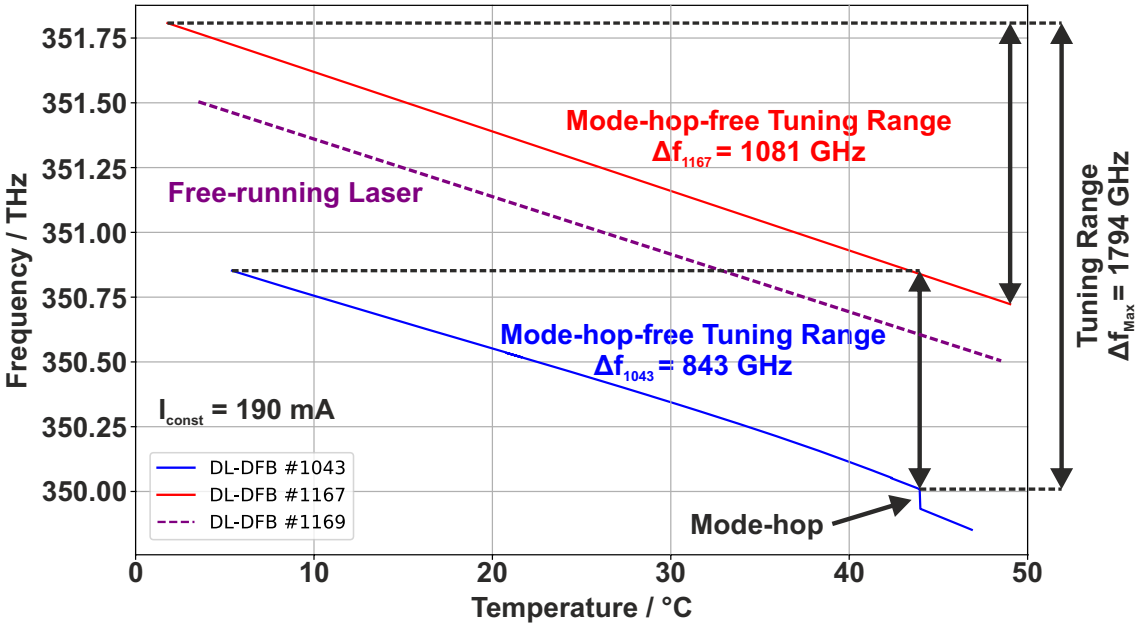

Figure 3.1: Thermal tuning range of the three DFB diode lasers at 190 mA input current: The phase-locked lasers (#1043 and #1167) have mode-hop-free tuning ranges of 843 GHz and 1081 GHz, with a maximum beat signal frequency of 1794 GHz. The free-running laser (#1169) covers 1001 GHz, overlapping with both phase-locked lasers.

dashed), hereafter referred to as "Primary", has a frequency range of 1001 GHz, which intersects with the tuning ranges of both phase-locked lasers. The maximum output power of the lasers is roughly 100 mW after the optical isolator.

A direct and precise measurement of the laser linewidth is challenging due to the optical carrier frequency being around 350 THz. To nevertheless determine whether the spectral linewidth of the secondary lasers is narrow enough for phase-locking by the OPLLs, a delayed self-heterodyne (DSH) linewidth measurement is carried out, converting the measurement into the RF range. DSH interferometry, introduced by Okoshi *et al.* in 1980 [141], is a widely used detection technique that enables high-precision measurements of the linewidth by exploiting the beat note generated between two delayed copies of the same laser beam. The time delay between the two optical fields converts the phase fluctuations of the laser into intensity fluctuations, which are much easier to detect [142].

Fig. 3.2 sketches the optical setup used for the DSH linewidth measurements of lasers Secondary 1 and 2. The output of the DFB laser diode is split by a fiber coupler in two parts of similar power. One portion passes through a 1.5 km long optical fiber, providing a time delay $\tau_{\mathrm{Delay}} \approx 7.25$ µs to the signal, while the other is sent through an acousto-optic modulator (AOM). The AOM, driven at a constant carrier frequency $f_{\mathrm{AOM}} = 200$ MHz, shifts all the optical frequency components by f_{AOM} as a result of the Doppler effect[1]. Subsequently, both beams are superimposed on a beam splitter (BS), and the

[1]The Doppler effect refers to the change in frequency (or wavelength) of a wave in relation to an

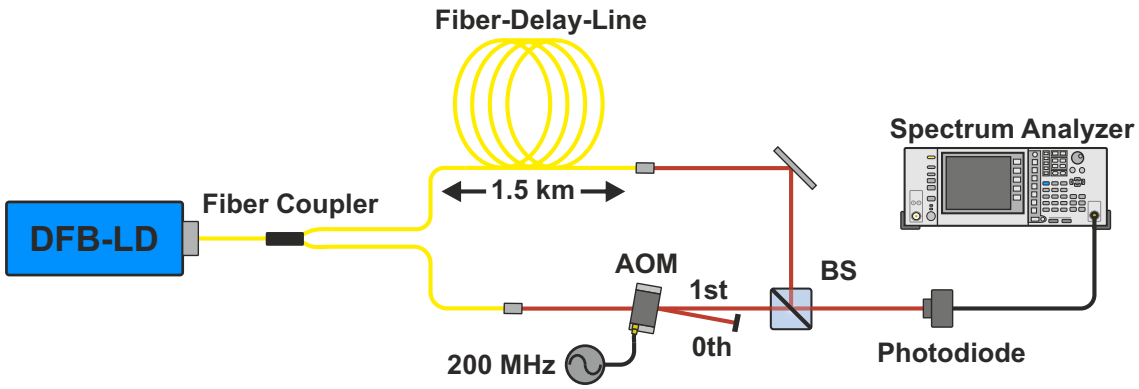

Figure 3.2: Setup for the delayed self-heterodyne (DSH) linewidth measurement of the laser diodes: The laser output is split into two paths: one is delayed by a 1.5 km fiber, while the other is frequency-shifted by an acousto-optic modulator (AOM) at 200 MHz. After both signals interfere at a beam splitter (BS), the resulting beat note is detected by a photodiode and analyzed with a spectrum analyzer.

generated beat note, centered at f_{AOM}, is recorded with a fast photodiode (350 MHz bandwidth). The fluctuations of the photodiode current, which correspond to the DSH spectrum, are then measured using a standard RF spectrum analyzer. Therefore, the frequency shift introduced by the AOM is important, as common SAs have their lower frequency limit above DC, additionally preventing interference with the DC component of the photodiode[2].

For sufficiently long time delays, the phase dynamics of the interfering fields become essentially uncorrelated, and the resulting spectrum is a simple self-convolution of the laser's output spectrum, allowing for the determination of the linewidth. The criterion commonly used to specify the needed time delay is that the optical path delay must be longer than the coherence length of the analyzed laser source. However, as the coherence length is inversely proportional to the linewidth itself, the required delay length depends on the spectral properties of the laser under investigation. Therefore, the time delay τ_{Delay} must satisfy the condition

$$\tau_{\mathrm{Delay}} \gg \frac{1}{\Delta\nu}, \tag{3.1}$$

where $\Delta\nu$ is the linewidth of the laser. The corresponding fiber length L is related to the time delay by

$$L = \tau_{\mathrm{Delay}} \cdot v_g = \frac{1}{\Delta\nu} \cdot \frac{c}{n}, \tag{3.2}$$

where v_g is the group velocity, n is the refractive index of the fiber, and c is the speed of light. Since the characterized lasers are expected to have linewidths below 1 MHz,

observer moving relative to the source of the wave. In this case, the AOM shifts the optical frequency due to the interaction between the ultrasound wave and the light wave.

[2]Photodiodes generate a photocurrent (and consequently a photovoltage) when illuminated due to the built-in potential of the pn-structure. This DC component is inevitable and must be separated from the modulated signal.

the fiber length of 1.5 km ($n \approx 1.5$), corresponding to a linewidth of roughly 138 kHz, is chosen. Extending the fiber length to achieve a longer delay time and therefore better fulfill equation (3.1) introduces drawbacks such as higher propagation losses and greater sensitivity to environmental disturbances.

To deduce the linewidth from the measured DSH spectrum, the different noise components must be considered. A detailed theoretical description of the relationship between the detected photocurrent and the spectral width can be found in [143]. However, for a qualitative analysis, an exact determination of the linewidth is not always required, particularly when the primary goal is to evaluate whether the lasers are suitable for phase-locking in the frequency synchronization scheme.

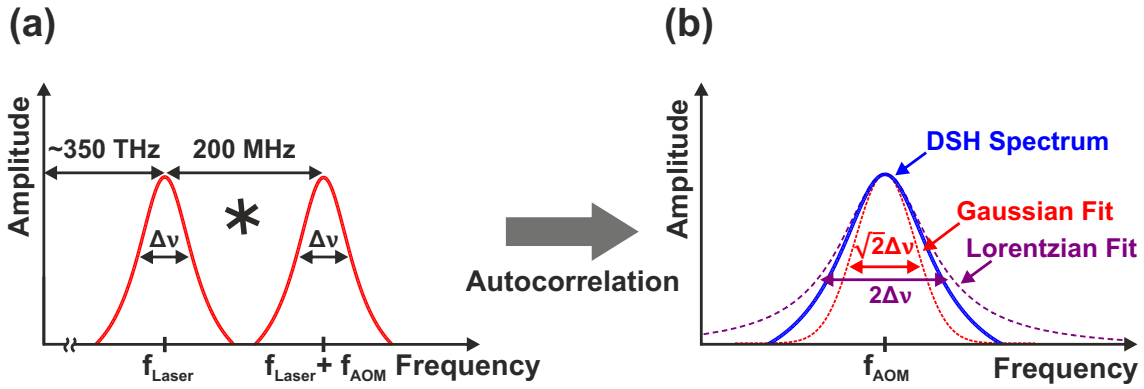

Figure 3.3: (a) Optical spectra of the two branches in the DSH setup. (b) Resulting DSH spectrum of the delayed self-heterodyne linewidth measurement along with corresponding fit curves for pure 1/f noise (Gaussian) and pure white noise (Lorentzian).

Fig. 3.3 illustrates how the laser linewidth $\Delta\nu$ can be calculated from the measured DSH spectrum. In (a), the laser spectra propagating through the two branches of the DSH setup are depicted. One spectrum is delayed due to the optical path difference, while the other is frequency-shifted by the AOM, centering the laser spectra at f_{Laser} and $f_{\text{Laser}} + f_{\text{AOM}}$, respectively. At the photodiode, the interference of the two optical fields is detected, effectively multiplying their time-domain signals. In the frequency domain, this corresponds to the convolution of their spectra, and since both spectra originate from the same laser, the measured signal reflects the laser's autocorrelation properties. Part (b) shows the resulting DSH spectrum (blue), centered at f_{AOM}, together with the Gaussian (red) and Lorentzian (purple) fit curves. The Gaussian fit curve represents pure 1/f noise[3], while pure white noise leads to a Lorentzian shape of the DSH spectrum. If the delay time significantly exceeds the coherence length, the linewidth can be deduced from the FWHM of the DSH spectrum. Here, the relationship between the FWHM and the laser linewidth is characterized by a factor of 2 for white noise and $\sqrt{2}$ for 1/f noise.

[3] 1/f noise, also known as flicker noise, is characterized by a power spectral density inversely proportional to frequency. It can originate from various sources, such as fluctuations in temperature or current, or from spatial hole burning in DFB lasers, contributing to low-frequency noise in their emission.

However, in the measurement various noise sources will contribute to the DSH spectrum, resulting in a combination of these noise types. To account for this, a Voigt[4] profile can be used to fit the measured DSH spectrum [144].

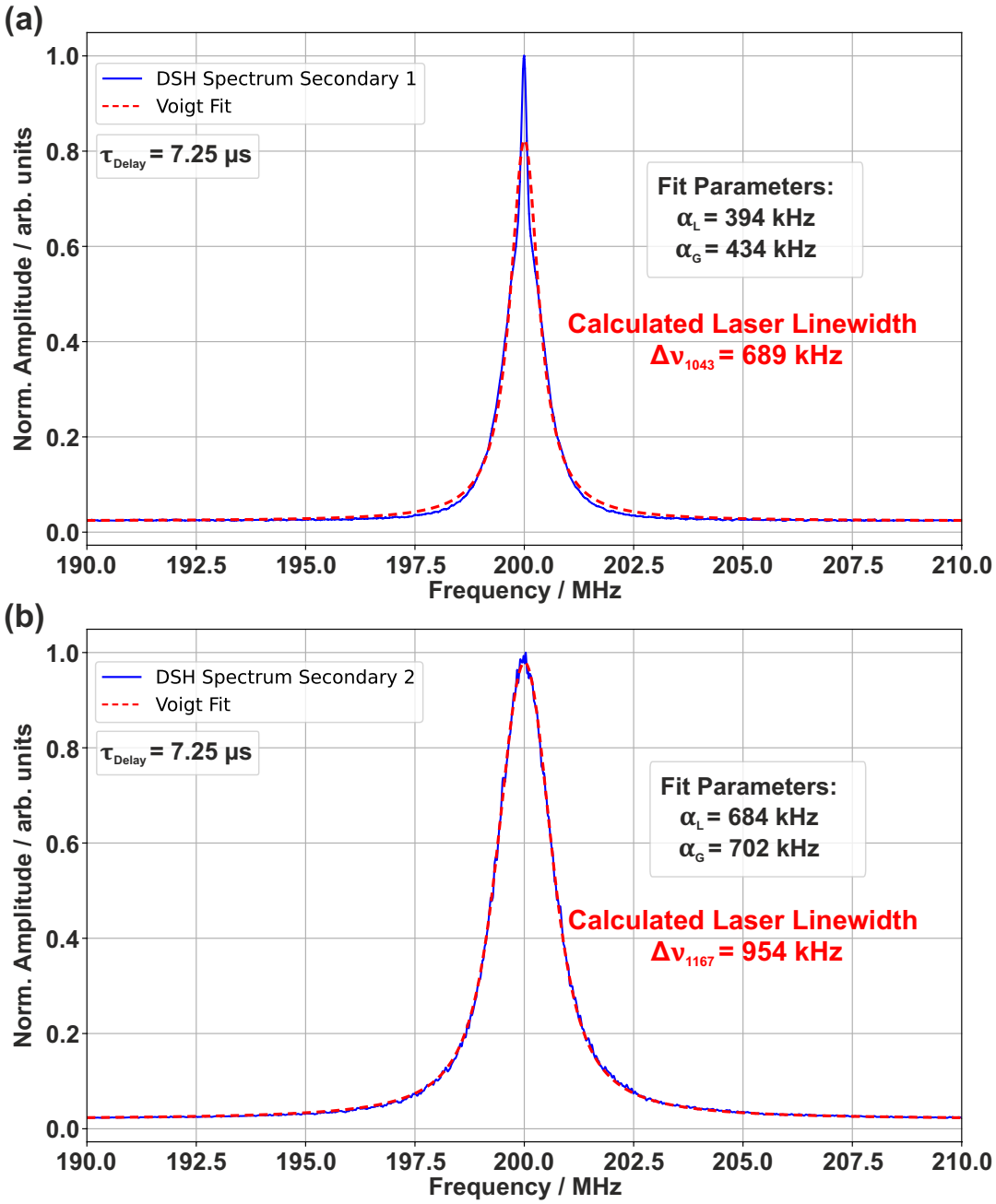

Figure 3.4: Measured DSH spectra with corresponding Voigt fit of (a) Secondary 1 and (b) Secondary 2 for a delay of 7.25 µs and an AOM frequency shift of 200 MHz. From the Voigt fit, linewidths of 689 kHz for Secondary 1 and 954 kHz for Secondary 2 are obtained.

[4] A Voigt fit is a mathematical function that represents the convolution of a Lorentzian and a Gaussian distribution.

Fig. 3.4 depicts the measured DSH spectra of the two Secondary lasers for a delay time of 7.25 µs and an AOM frequency of 200 MHz. By fitting a Voigt profile to the spectra, the Lorentzian and Gaussian components were extracted, allowing the laser linewidths to be calculated by using the relationship from [144]:

$$\Delta\nu = \frac{1}{2}\sqrt{(1.0692 \cdot \alpha_L)^2 + (0.86639 \cdot \alpha_G)^2 + 4 \cdot \alpha_L}, \tag{3.3}$$

where α_{L} and α_{G} are the Lorentzian and Gaussian FWHM values obtained from the fit. From (3.3), the laser linewidths are determined to be 689 kHz for Secondary 1 and 954 kHz for Secondary 2, corresponding to a time scale of 7.25 µs. Yet, in the DSH spectrum shown in (a), the Voigt fit exhibits noticeable deviations from the measured spectrum, particularly at the peak. This can be attributed to the narrowing of the spectrum that occurs when the delay time approaches the coherence time of the laser ($\tau_{\mathrm{c}} = \frac{1}{\Delta\nu}$). As the delay time gets closer to the coherence time, interference effects between the time-delayed and non-delayed components of the laser field become more pronounced, causing a more confined spectrum [145]. Therefore, the fitted Voigt profile fails to accurately match the measured spectrum, leading to inaccuracies in the calculated linewidth for Secondary 1. This observation aligns with the common guideline that the delay length should be at least six times the coherence length of the laser being characterized [146], a condition met only for Secondary 2 in our DSH setup. To account for this, either the fiber length has to be extended to ensure a delay length significantly exceeding the coherence length of the lasers, or alternative approaches such as short delay self-heterodyne interferometry [147] can be employed.

Experimentally it was elaborated that for a successful frequency stabilization in the OPLLs, laser linewidths below 1 MHz are crucial. Since the two Secondary lasers meet this requirement, a more precise determination of their exact linewidths is not conducted in this thesis. Instead, the next step is to phase-lock the DFB laser pairs in the RF range using the developed laser frequency synchronization setup, which will be discussed in the following section.

3.2 Phase-Locking in the RF Range

Although the individual DFB lasers exhibit a narrow linewidth of less than 1 MHz, the beat signal generated between them shows significantly greater fluctuations. This is due to the independent frequency noise contributions of each laser, which combine and amplify the overall instability of the beat note. Nevertheless, using two independent, single-wavelength tunable laser diodes remains the best solution for creating a CW frequency-tunable source that reaches the terahertz frequency range. To overcome the issue of the poor frequency stability, the generated beat note has to be compared and synchronized with a highly stable reference signal. A common approach for this is to lock the two wavelengths to each other by means of an optical phase-locked loop.

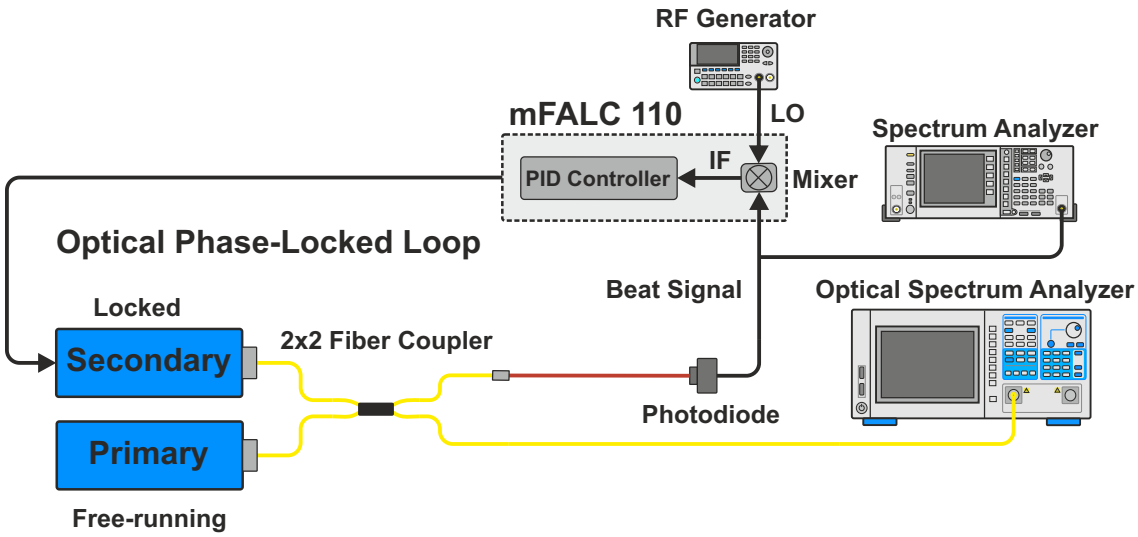

Figure 3.5: Configuration of the optical phase-locked loop for stabilizing the laser beat signal in the RF range: From the combined laser output, one path is detected by a fast photodiode, while the other is sent to an optical spectrum analyzer. The detected beat is mixed with a stable 10 MHz LO signal, producing an intermediate frequency (IF) that serves as an error signal for the PID controller. Adjustments to the Secondary laser current compensate for frequency fluctuations, ensuring phase-locking at the RF offset.

For an effective phase-locking of the laser pairs, it is essential to thoroughly evaluate the synchronization setup and optimize the PID controller settings for stable operation. The available PID controller features multiple independent control elements for selecting different cutoff frequencies, allowing the PLL range to be customized for the individual laser pairs. For this purpose, the stabilization of the laser difference frequency is initially achieved in the RF range using the heterodyne optical phase-locked loop illustrated in Fig. 3.5.

In the OPLL setup, a polarization-maintaining 2×2 fiber coupler is used to combine the light of Secondary and Primary laser. One of the fiber outputs is directed to an amplified 150 MHz photodiode (PDA10A2, Thorlabs GmbH) for the laser synchronization, while the other one is guided to the input of an optical spectrum analyzer (OSA). The recorded beat signal from the photodiode is sent to the laser control unit ("modified Fast Analog Linewidth Control", mFALC 110, Toptica Photonics AG), where it is mixed with a stable LO signal at 10 MHz from the RF generator. The resulting intermediate frequency serves as an error signal for the very fast PID controller. If there is any difference between the beat and the LO signal, the controller alters the input current and thus the frequency of the Secondary laser. For this purpose, the phase-locked laser is equipped with a modulation input that features a high-speed field-effect transistor circuit, enabling direct and reliable control of the laser current. This compensates for both the fast and slow frequency fluctuations of the laser, ensuring that it follows the free-running laser diode at a frequency offset corresponding to the RF signal.

Before enabling the control electronics, the laser difference signal is initially pre-adjusted via temperature tuning to roughly match the RF frequency. To achieve this, the OSA (AQ6370D, Yokogawa Electric Corporation) is used to monitor the laser spectrum, offering a frequency resolution of a few gigahertz. For further fine-tuning and to record the beat signal spectrum, a portion of the photodiode signal is directed to the electronic SA (MS2830A, Anritsu Corporation). After selecting suitable starting settings for the P-, I-, and D-terms of the mFALC controller, one of the lasers is manually scanned by tuning the current. When the frequency difference falls within the capture range of the controller, the output signal modulates the Secondary laser rapidly with the error signal, and the OPLL locks within several microseconds. This is indicated by a narrow peak in the beat signal spectrum, precisely at the RF frequency, as illustrated later in Fig. 3.7. Subsequently, the output gain is increased until the beat note carrier reaches maximum power. If the beat signal shifts to a different frequency during this process, the gain is reduced, and a new set of PID parameters must be tested until the settings that provide the best lock dynamics are found.

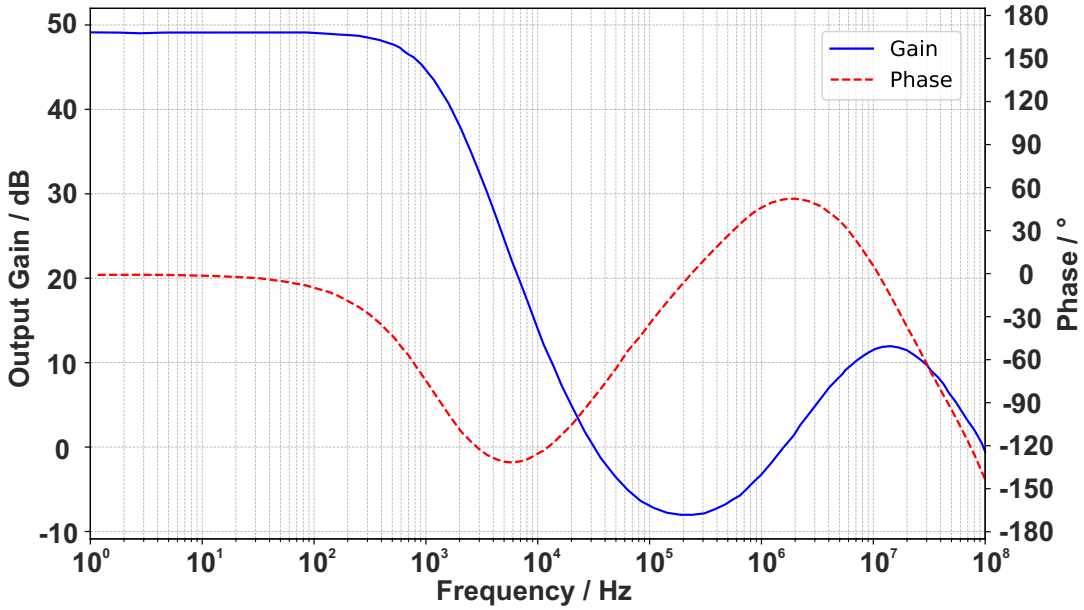

Figure 3.6: Transfer function of the mFALC 110 for the PID settings used in the laser synchronization scheme: To compensate for low-frequency phase noise (up to a few kilohertz), the gain is maximized in this range, while sensitivity to fluctuations between 1 kHz and 100 kHz is reduced. A second gain maximum at 10 MHz offsets megahertz fluctuations, while also generating a phase lead between 250 kHz and 10 MHz to counteract phase lag from signal propagation.

Fig. 3.6 depicts the transfer function of the PID controller settings used for phase-locking the laser pairs in the setup. As most of the phase noise is caused by mechanical oscillations and thermal drifts in the lower frequency range up to a few kilohertz, the gain is maximized in this frequency interval. The integral component causes the controller to become less responsive to fluctuations between 1 kHz and 100 kHz, which also results

in an increased phase delay. Due to the fast D-element, a second gain maximum around 10 MHz is induced, enabling compensation for fluctuations in the beat signal within the megahertz range. Additionally, the derivative component generates a phase lead between 250 kHz and 10 MHz that accounts for phase lag caused by the signal propagation time in the OPLL.

As discussed in section 2.3, all loop components further increase the overall phase delay. To prevent positive feedback in the OPLL, it is crucial to have a fast response from the PID controller, as well as short propagation times. Although very short fiber and cable lengths can be used for locking in the RF range, longer signal paths are necessary due to system limitations when transitioning into the terahertz range. Therefore, the propagation time of the OPLL used for locking to the terahertz reference is taken into account at this stage. With a total fiber length of 2.5 meters ($v_{\mathrm{Fiber}} \approx 0.66\ c$), the optical path introduces a time delay of approximately 12.6 ns. The RF cables in the electronic part of the system can be kept relatively short, around 0.4 meters ($v_{\mathrm{RF}} \approx 0.66\ c$), leading to a delay of 2 ns. Combined with the 15 ns delay from the PID controller and the 25 ns response time of the transimpedance amplifier[5], the total time delay is approximately 55 ns. Using equation (2.35), the frequency-dependent phase delay can be calculated. For instance, a disturbance with a frequency of 9 MHz results in a phase lag, introduced by the propagation time in the OPLL, of roughly 178°. Looking at the phase of the transfer function for the PID controller, this phase delay can still be compensated, though with a small margin. However, additional control electronics, such as the laser frequency modulation, also add some time delay to the system, further decreasing the maximum bandwidth of the control loop. This underscores why a narrow laser linewidth is essential for achieving stable frequency synchronization of the beat signal.

Fig. 3.7 (a) compares the measured spectra of the laser beat note with and without stabilization to a LO frequency of 10 MHz. If the phase-lock is switched off (red), the beat signal starts to drift by several megahertz over a time scale of a few milliseconds. For longer time scales, the frequency shift can even reach some tens of megahertz, driven by slow temperature fluctuations in the free-running lasers. In contrast, when the phase-lock is activated (blue), a narrow peak at the LO frequency of 10 MHz appears, indicating that the controlled laser is following the free-running Primary laser with the expected offset. The small side peaks at 10 MHz ± 3 MHz are caused by so-called servo bumps. They occur near the frequency where the response is 180° out of phase, causing noise at this frequency to be amplified rather than reduced [148]. Therefore, they restrict the loop bandwidth of the OPLL to about 6 MHz, which in this case is attributed to the modulation characteristics of the lasers. However, with the selected PID settings, the servo bumps are effectively flattened and suppressed by 43 dB, minimizing their impact on the synchronized signal.

As the linewidth in (a) is limited by the RBW of 3 kHz, a high-resolution spectrum (BW = 1 kHz, RBW = 10 Hz) of the phase-locked beat signal centered at $f_{\mathrm{LO}} = 10$ MHz

[5]The transimpedance amplifier is essential in the terahertz regime as it converts the photocurrent generated by the photomixer into a voltage signal while simultaneously providing amplification.

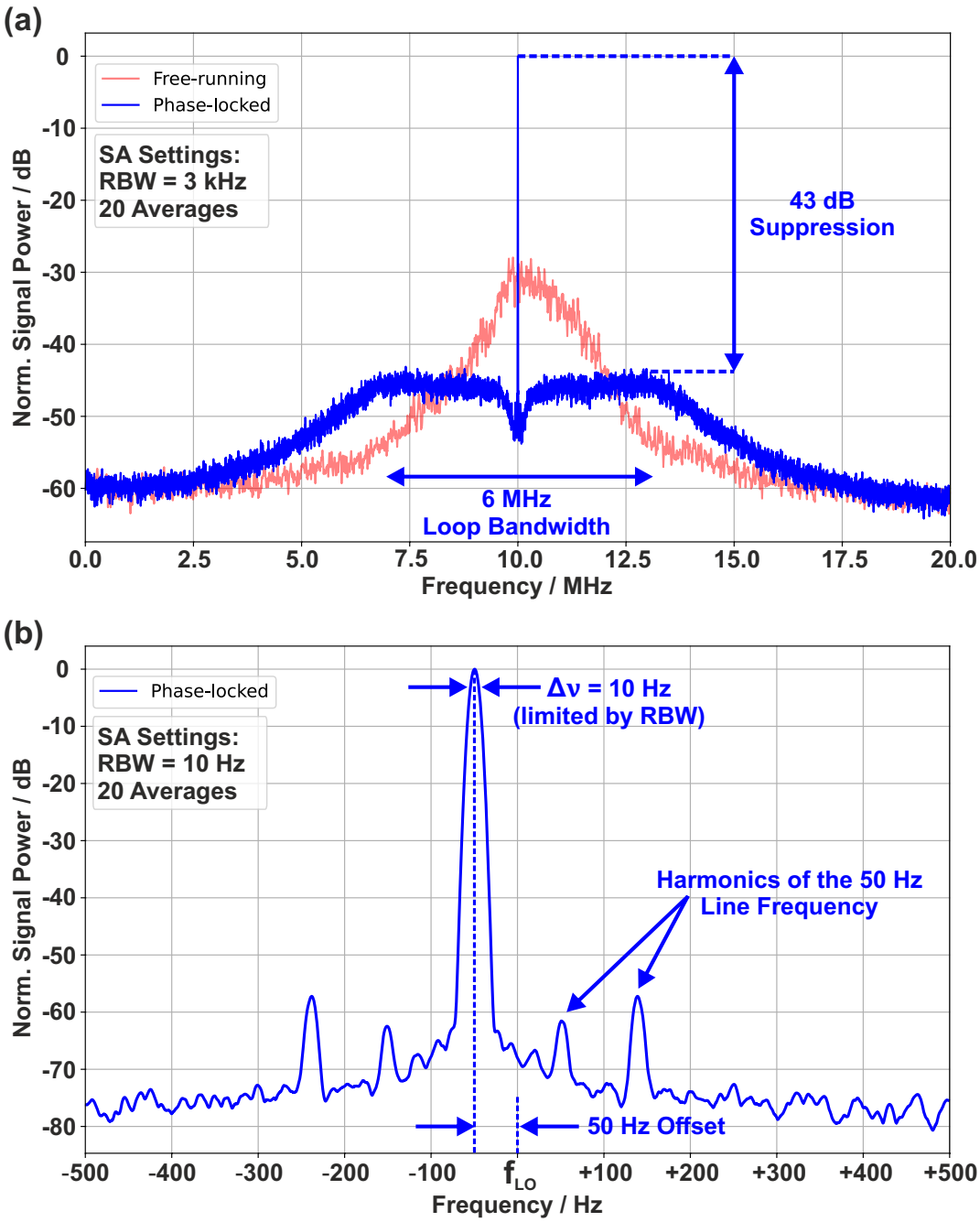

Figure 3.7: (a) Comparison of the laser beat signal with (blue) and without (red) stabilization to a LO frequency of 10 MHz (RBW = 3 kHz, 20 averages). The phase-locked signal shows a narrow peak at 10 MHz, while the free-running beat note drifts by several megahertz. The servo bumps are effectively suppressed by 43 dB. (b) High-resolution spectrum of the phase-locked beat signal centered at $f_{\mathrm{LO}} = 10\ \mathrm{MHz} \pm 500\ \mathrm{Hz}$ (RBW = 10 Hz, 20 averages), showing a linewidth limited by the 10 Hz RBW of the electronic spectrum analyzer, with side peaks likely caused by harmonics of the 50 Hz line frequency.

is presented in part (b) of Fig. 3.7. In this spectrum, the linewidth $\Delta\nu$ is once again determined by the 10 Hz RBW of the electronic SA. The main lobe is shifted slightly by 50 Hz from the designated LO frequency. This deviation can be attributed to the RF generator used, which has a maximum output frequency of 10 MHz but falls just short of achieving it. Nevertheless, the exceptionally narrow linewidth confirms that the beat signal is successfully phase-locked to the local oscillator. Furthermore, periodic side peaks, likely harmonics of the 50 Hz line frequency, are observed alongside a difference in the background level between the normalized spectra in (a) and (b). This difference can be attributed to the substantially smaller RBW used in the high-resolution recording.

Additionally, to complement the beat note spectra, a phase noise measurement of the phase-locked beat signal is performed using the phase noise function of the electronic spectrum analyzer.

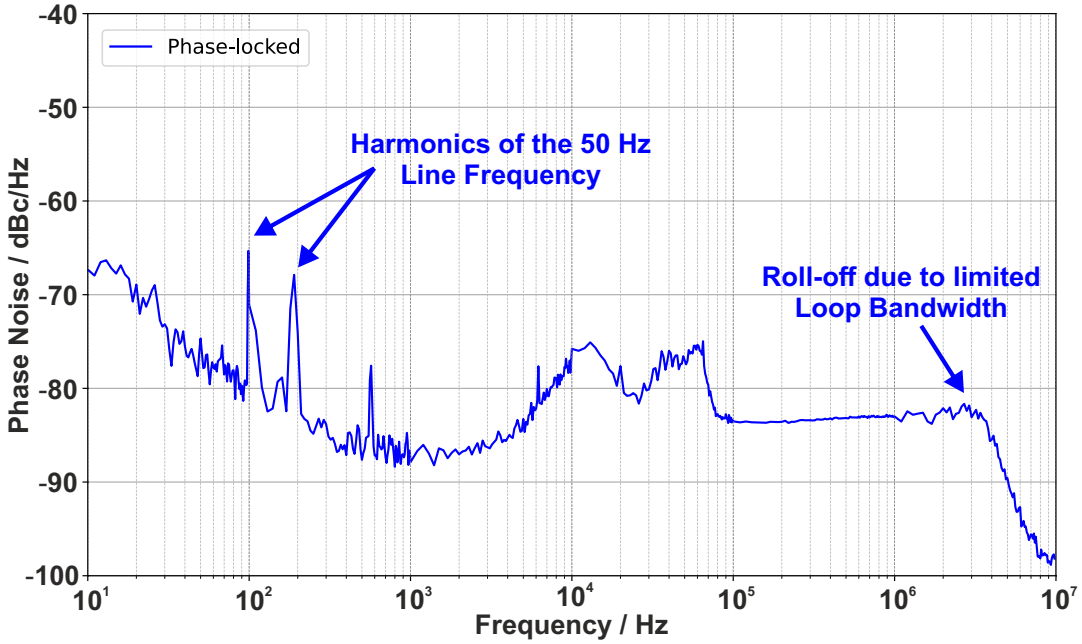

Figure 3.8: Phase noise spectrum of the phase-locked laser beat signal from 10 Hz to 10 MHz relative to the carrier. The spectrum shows reduced noise near the carrier, with harmonics of the 50 Hz line frequency. Broader peaks between 10 kHz and 70 kHz are likely due to mechanical and electronic resonances. From 100 kHz to 3 MHz the phase noise is flat, with a roll-off beyond 3 MHz due to the falling noise level of the beat signal. The measurement was taken using the phase noise function of the electronic spectrum analyzer.

The measured phase noise spectrum of the locked beat signal, spanning a frequency range from 10 Hz to 10 MHz relative to the carrier, is shown in Fig. 3.8. In alignment with the power spectra shown in Fig. 3.7, the noise level decreases close to the carrier frequency, with only a few visible spikes attributed to harmonics of the 50 Hz line frequency. Starting at 1 kHz, an increasing noise level is observed, which can be explained by

the transfer function characteristics of the PID controller within this frequency range (see Fig. 3.6). Between 10 kHz and 70 kHz, two broader noise peaks are visible in the spectrum, likely caused by mechanical vibrations or resonances in the electronic circuitry coupling into the system. From 100 kHz up to the band edge of the control loop at 3 MHz, the phase noise remains essentially flat, indicating stable synchronization and effective suppression of higher-frequency noise components by the loop. Above the band edge, the graph shows a roll-off, due to the falling noise level of the beat signal.

Having successfully locked the laser pair in the RF range, the synchronization concept is now intended to be adapted for the terahertz domain. To achieve this, the beat signal must be stabilized to a highly stable reference source emitting in the terahertz range. In this thesis, electronic frequency multiplier chains, as introduced in Section 2.1.4, are employed together with various CW terahertz sensing techniques in a heterodyne detection scheme, which will be the topic of the next section.

3.3 Adaptation to the Terahertz Range

The key idea for extending the presented synchronization concept to the terahertz regime involves heterodyne downconversion of the laser beat note. A reference source emitting at terahertz frequencies is used to shift the signal into the mFALC controller's input range of 10 MHz to 200 MHz (see Fig. 3.9). This so-called "optoelectronic hybrid concept" combines extremely stable high-frequency electronic components with nonlinear optical or electronic elements to stabilize the laser difference frequency.

The fundamental locking procedure is equivalent to the synchronization in the RF domain. Initially, the laser beat note is temperature-tuned with the control loop open to approximately match the output frequency of the reference source, as monitored using the OSA. Consequently, the downconverted signal from the terahertz reference detection represents the frequency difference between the laser beat and the terahertz reference. Once the laser control is activated, this frequency offset is synchronized with the LO signal from the RF generator. Here, the Secondary laser follows the free-running Primary with a frequency difference of

$$f_{\text{Beat}} = f_{\text{THz Reference}} \pm f_{\text{LO}}. \tag{3.4}$$

As the frequency characteristics of the phase-locked laser signal directly depend on the reference source, any noise or drift in the reference will be reflected in the beat note. To achieve terahertz range laser beat signals with Hz-level resolution, the setup incorporates various highly stable CW electronic frequency multiplier chains, covering frequency ranges from 70 GHz to 500 GHz.

For the downconversion of terahertz frequencies to the megahertz range, three different methods are evaluated in this thesis. The first approach, which is currently the most widely used, relies on the heterodyne detection with photomixers. Secondly, an electro-optic detection setup with a ZnTe crystal is considered, offering an alternative optical

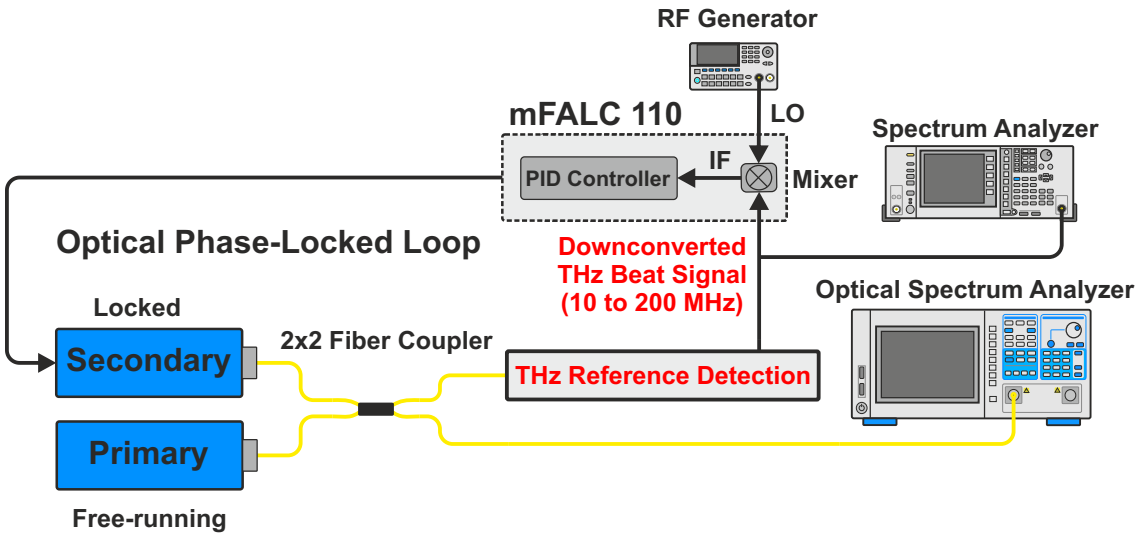

Figure 3.9: Adaptation of the RF locking principle for terahertz frequencies: Initially, the laser beat note is temperature-tuned to match the reference frequency, monitored by the OSA. The downconverted signal from the terahertz reference detection is directed to the mFALC 110 controller for the synchronization with the LO signal. Once the control loop locks, the Secondary laser follows the Primary with a frequency difference, given by $f_{\text{Beat}} = f_{\text{THz Reference}} \pm f_{\text{LO}}$.

solution to shift the terahertz frequencies down to the megahertz range. Last, a Schottky diode mixer is employed, providing an electronic concept for the terahertz reference detection.

3.3.1 Photomixing Detection

In Fig. 3.10 a schematic representation of the terahertz reference detection setup with a GaAs photomixer (PCA-FD-0780-130-RX-1 photomixer with log-spiral antenna, Toptica Photonics AG) and an electronic CW frequency multiplier chain is depicted. An analog signal generator (E8257D, Agilent Technologies Corporation) with an frequency span of 250 kHz to 20 GHz synthesizes a microwave signal, serving as the fundamental frequency of the FMC. Employing various active and passive multipliers, such as doublers or triplers, the FMC converts the input frequency into the terahertz range. The resulting radiation is emitted into free-space and subsequently focused onto the hyperhemispherical silicon lens (f $\approx$ 30 mm) of the photomixer using two OAP mirrors. Together with the fiber-coupled laser beat signal, the terahertz wave irradiates the antenna structures of the photomixer. As detailed in Section 2.1.2, the incident terahertz radiation induces a bias voltage across the photoconductive gap, while the laser beat modulates the conductivity in the semiconductor. This interaction generates a photocurrent oscillating at the frequency difference between the laser beat signal and the terahertz reference, which is then routed to a transimpedance amplifiers (TIA) (DHPCA-100, FEMTO Messtechnik GmbH) with a selected bandwidth of 14 MHz and a gain of 10^5 V/A. Thereafter,

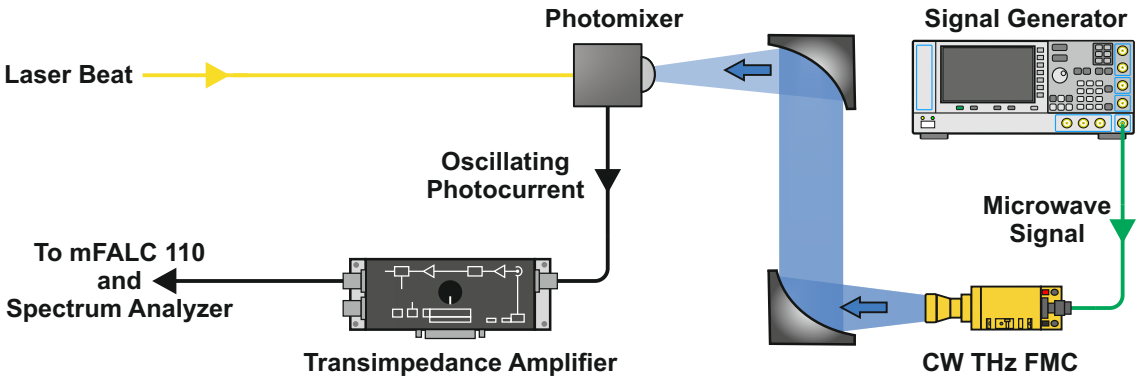

Figure 3.10: Photomixing detection of the terahertz reference signal: A GaAs photomixer with a log-spiral antenna detects terahertz radiation from a CW frequency multiplier chain. The radiation is focused onto the photomixer's silicon lens, where it interacts with the laser beat signal to generate a photocurrent. This signal is then amplified and used for laser synchronization.

the output from the TIA acts as the input signal for synchronizing the lasers, using the mFALC controller and the LO frequency provided by the RF generator.

Fig. 3.11 (a) displays the measured frequency spectra of the laser beat signal, shown in blue with and in red without phase-locking, to an electronic FMC (AFM12 110-170 +10, Radiometer Physics GmbH) operating at 110 GHz with an output power of 10 mW. In the phase-locked state (blue), the central peak at the LO frequency of 10 MHz exhibits a linewidth of approximately 3 kHz, matching the set RBW of the electronic spectrum analyzer. While the suppression of the servo bumps is slightly lower compared to stabilization in the RF range, it remains above 35 dB. Furthermore, the measured loop bandwidth decreases to 3 MHz. Both effects can be attributed to the introduction of the photomixer, the terahertz source, and the transimpedance amplifier used for heterodyne downconversion. These components introduce additional phase delay and contribute supplementary noise to the control loop, which constrains the achievable loop bandwidth and reduces the dynamic range of the error signal. As a result, the control loop becomes less responsive to fast fluctuations and less effective in suppressing high-frequency noise.

In the high-resolution spectrum (Fig. 3.11 (b)), the linewidth is observed to be limited by the 10 Hz RBW of the SA, indicating a laser beat signal with a frequency of 110 GHz and Hz-level resolution. The periodic spurious peaks, which could be caused by environmental noise, also reappear in the high-resolution spectrum but are suppressed by more than 50 dB. Here, the main lobe is shifted by approximately 110 Hz from the intended LO frequency, which can be explained by the use of a different RF generator than the one employed for the RF lock.

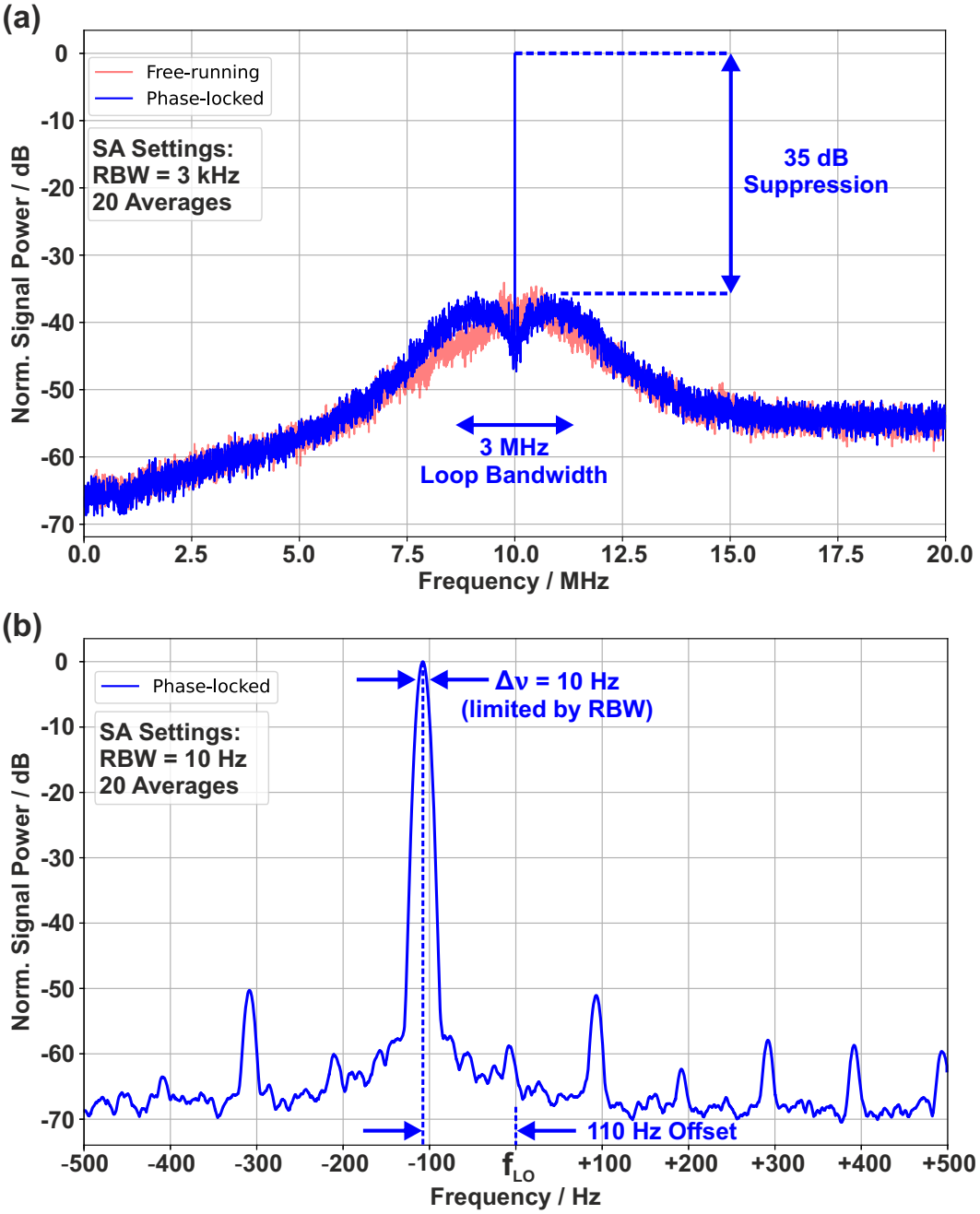

Figure 3.11: (a) Comparison of the laser beat signal with (blue) and without (red) stabilization to a 110 GHz electronic FMC with a photomixer (LO frequency = 10 MHz, RBW = 3 kHz, 20 averages). In the locked state, the central peak exhibits a linewidth of approximately 3 kHz, with servo bump suppression above 35 dB and a loop bandwidth of 3 MHz. (b) High-resolution spectrum of the phase-locked beat signal centered at $f_{\mathrm{LO}} = 10\ \mathrm{MHz} \pm 500\ \mathrm{Hz}$ (RBW = 10 Hz, 20 averages). The linewidth is around 10 Hz, limited by the resolution bandwidth of the spectrum analyzer. Periodic spurious peaks, likely from environmental noise, are suppressed by 50 dB.

3.3.2 Electro-optic Detection

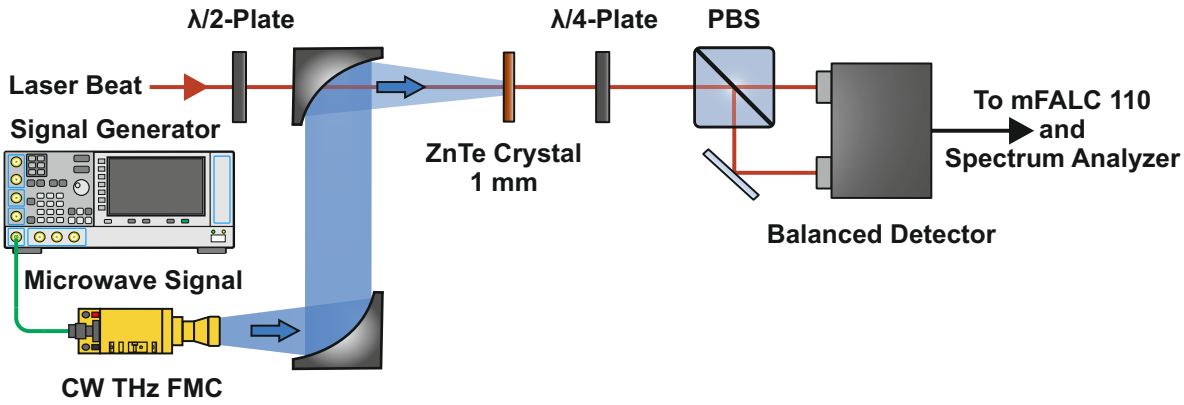

Figure 3.12: EO detection of the terahertz reference signal: A ZnTe crystal enables electro-optic detection of terahertz radiation from a CW frequency multiplier chain. The terahertz wave and laser beat are focused onto the crystal with optimized polarization. The modulated signal is processed using a $\lambda/4$-plate, a polarization beam splitter (PBS), and a balanced photodetector, generating a downconverted signal for laser phase-locking.

Fig. 3.12 illustrates the EO free-space setup for the second optical heterodyne detection method of CW terahertz radiation from the electronic FMC source. Similar to the photomixer setup, the emitted terahertz wave is focused onto the EO crystal using two OAP mirrors, while the linearly polarized laser beat, propagating in free space, is directed to the crystal through a hole in one of the mirrors. Before reaching the EO crystal, the polarization of the laser beat is adjusted by a $\lambda/2$-plate to ensure parallel alignment with the terahertz field. For the EO detection, a 1 mm thick[6] ZnTe crystal is chosen due to its high electro-optic coefficient, particularly for frequencies below 3 THz. As discussed in Section 2.1.3, the field-induced birefringence is maximized when both the terahertz wave and the optical beat are oriented perpendicular to the [001] axis in a $\langle 110 \rangle$-oriented crystal. For this purpose, the crystal is mounted in a rotatable holder, allowing it to be aligned to the optimal orientation. After passing through the EO crystal, the modulated optical beat is directed towards the $\lambda/4$-plate, which alters its polarization state. The polarization beams splitter then separates the modulated laser signal into two orthogonal polarization components, guiding each to one of the photodiodes in the amplified balanced photodetector (PDB450A - AC, Thorlabs GmbH), which operates with a selected bandwidth of 45 MHz and a gain of 10^4 V/A. The resulting modulation represents the frequency difference between laser beat and reference source, providing a downconverted output suitable for phase-locking the lasers with the OPLL.

The obtained spectra of the free-running (red) and phase-locked (blue) beat notes at 233 GHz are shown in Fig. 3.13 (a). An amplifying electronic FMC (AMC 1213B-A, ACST GmbH) with an output power around 60 mW serves as reference source for

[6] A thicker crystal could increase the interaction length, but it would also introduce greater absorption and loss, which would reduce the overall efficiency of the electro-optic modulation.

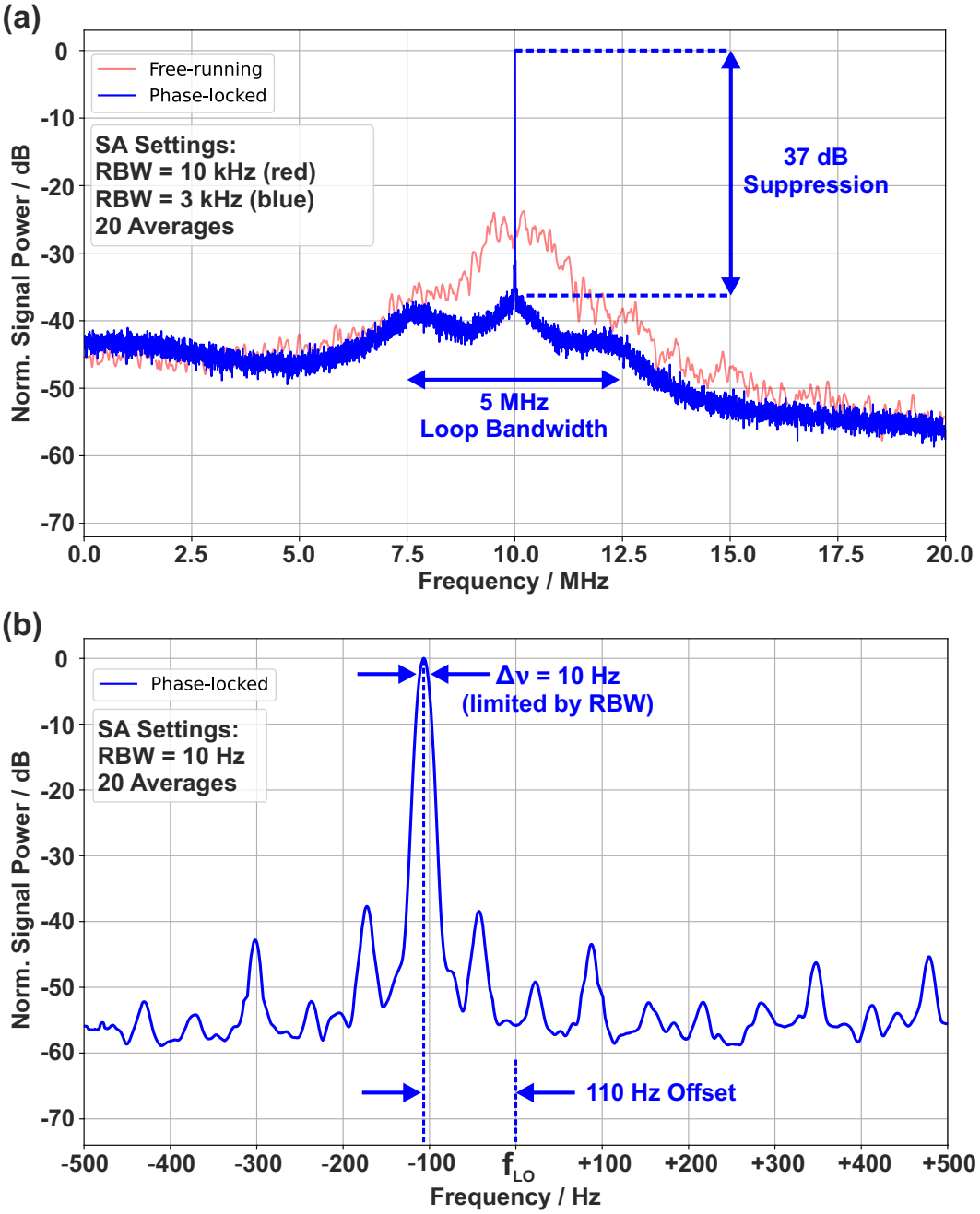

Figure 3.13: (a) Comparison of the laser beat signal with (blue) and without (red) stabilization to a 233 GHz electronic FMC with EO setup (LO frequency = 10 MHz, $\mathrm{RBW}_{\text{free-running}}$ = 10 kHz, $\mathrm{RBW}_{\text{phase-locked}}$ = 3 kHz, 20 averages). The phase-locked signal shows 37 dB noise suppression and a 2 MHz wider loop bandwidth compared to the photomixer setup. (b) High-resolution spectrum of the phase-locked beat signal centered at $f_{\mathrm{LO}} = 10\ \mathrm{MHz} \pm 500\ \mathrm{Hz}$ (RBW = 10 Hz, 20 averages). The linewidth is again limited by the resolution of the SA. Environmental noise increases the noise floor near the carrier, reducing signal dynamics to about 38 dB.

the downconversion. Although the free-running signal is measured with a wider RBW and a lower gain, its peak is about 10 dB higher compared to the photomixer detection. However, the signal strength is also six times higher, which at least partially accounts for the observed difference. In the locked spectrum, the noise contributions are suppressed by 37 dB, which is 2 dB more than with the photomixer. Due to the faster response time ($t_r \approx \frac{0.35}{\text{Bandwidth}} = 7.8$ ns) of the balanced detector, compared to the TIA in the PMD setup, the loop bandwidth is approximately 2 MHz wider for the EO setup, allowing the OPLL to better adjust to fast fluctuations in the beat signal.

The linewidth in the high-resolution spectrum (Fig. 3.13 (b)) is also constrained by the 10 Hz resolution bandwidth of the SA. As before, the peak is shifted by about 110 Hz from the indicated LO frequency. The parasitic frequency components from environmental noise are closer to the carrier and are less suppressed compared to the phase lock with the photomixer, raising the noise floor around the beat tone. This could reduce the signal dynamics, especially in high-resolution spectrum analysis, making it more challenging to accurately resolve weak signals near the carrier.

3.3.3 Schottky Diode Detection

Unlike the previously discussed techniques, in Fig. 3.14, the photomixer functions as an emitter of terahertz radiation, while the Schottky diode mixer serves as the receiver in the electronic downconversion process. For this purpose, a DC bias voltage is applied across the photoconductive gap of the photomixer, as the laser beat modulates its conductivity. The change in the conductivity creates a time-varying current in the photomixer, which results in the emission of terahertz photons due to the nonlinear interaction of the photocarriers with the applied electric field. The transmitted terahertz wave is directed

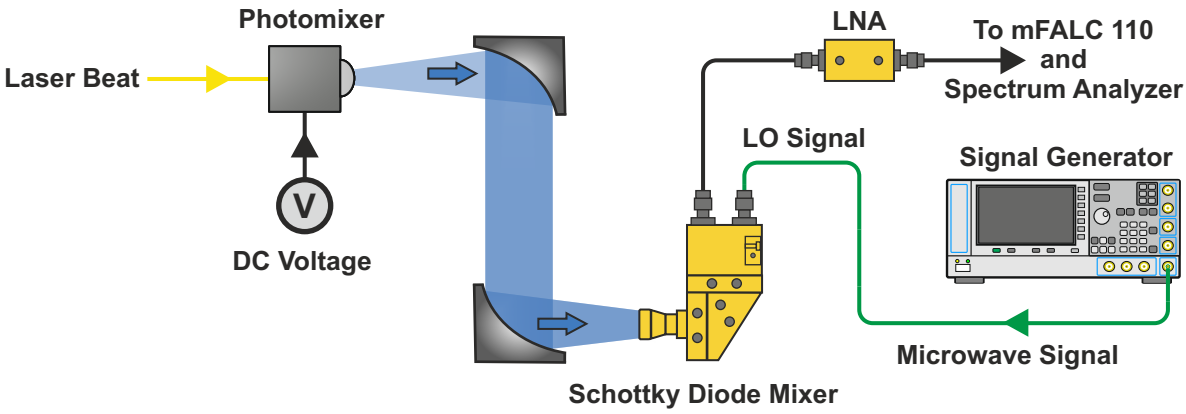

Figure 3.14: Schottky mixer detection of the terahertz reference signal: The photomixer acts as a terahertz emitter, while the Schottky diode mixer operates as the receiver. The generated terahertz radiation is mixed with the sixth harmonic of the 18.33 GHz LO in the Schottky diode mixer. Afterward, the resulting IF signal is amplified by a 33 dB low-noise amplifier (LNA) and routed to the mFALC 110 controller for phase-locking.

towards a harmonic Schottky diode mixer (HMR6 75-110, Radiometer Physics GmbH) employing two OAP mirrors and WR-10 horn antenna for focusing. In the mixer, the terahertz signal is multiplied with the sixth harmonic of the LO signal coming from the signal generator at 18.33 GHz. To ensure proper operation, an impedance matching and filter network is integrated in the input and output ports to optimize power transfer, suppress unwanted frequency components, and isolate the IF signal at the output for further processing. Utilizing the sixth harmonic of the LO for mixing introduces specific challenges, including decreased conversion efficiency and increased noise due to higher-order mixing processes. To address this, the IF output is boosted by a low-noise amplifier (LNA) with a gain of 33 dB. Subsequently, the amplified IF signal is sent to the mFALC 110 controller and spectrum analyzer for phase-locking and monitoring, respectively.

The measured frequency spectra for the laser stabilization with the Schottky mixer setup are illustrated in Fig. 3.15. In panel (a), the beat signals with (blue) and without (red) phase-locking to a 110 GHz electronic FMC source (same as in 3.3.1) are depicted. As with the previous locking schemes, the laser pair is successfully synchronized to the terahertz reference, as evidenced by the narrow line at the LO frequency. The servo bumps introduced by the control loop are effectively suppressed by 36 dB, while maintaining a loop bandwidth of 4 MHz. These results are largely consistent with those obtained from the other two heterodyne detection techniques.

The measured frequency spectra for the laser stabilization with the Schottky mixer setup are illustrated in Fig. 3.15. In panel (a), the beat signals with (blue) and without (red) phase-locking to a 110 GHz electronic FMC source (same as in 3.3.1) are depicted. As

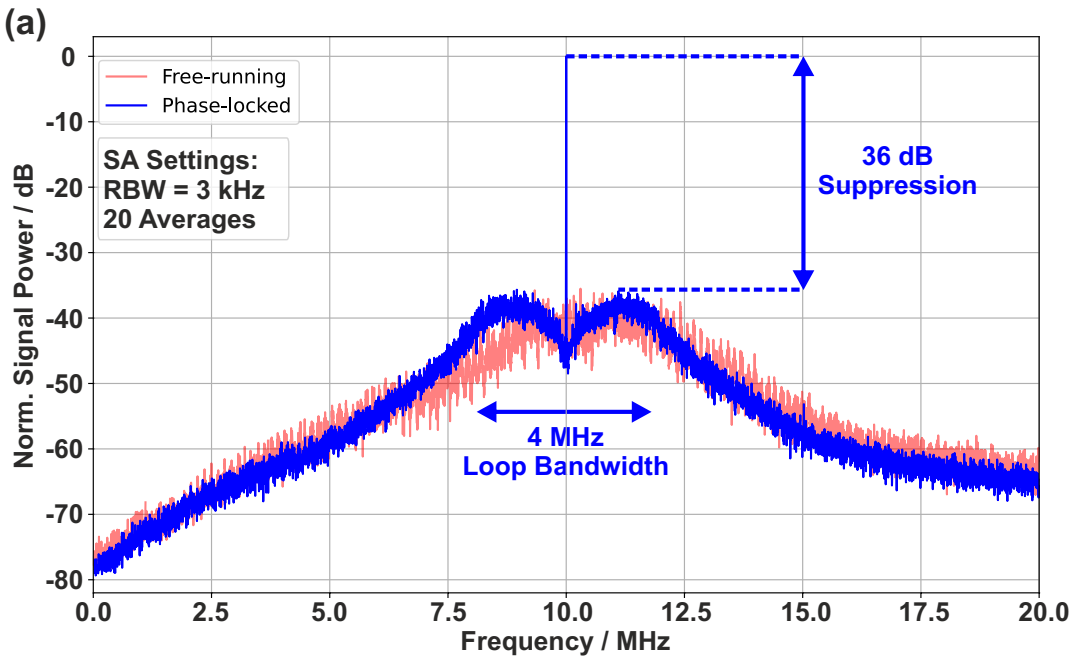

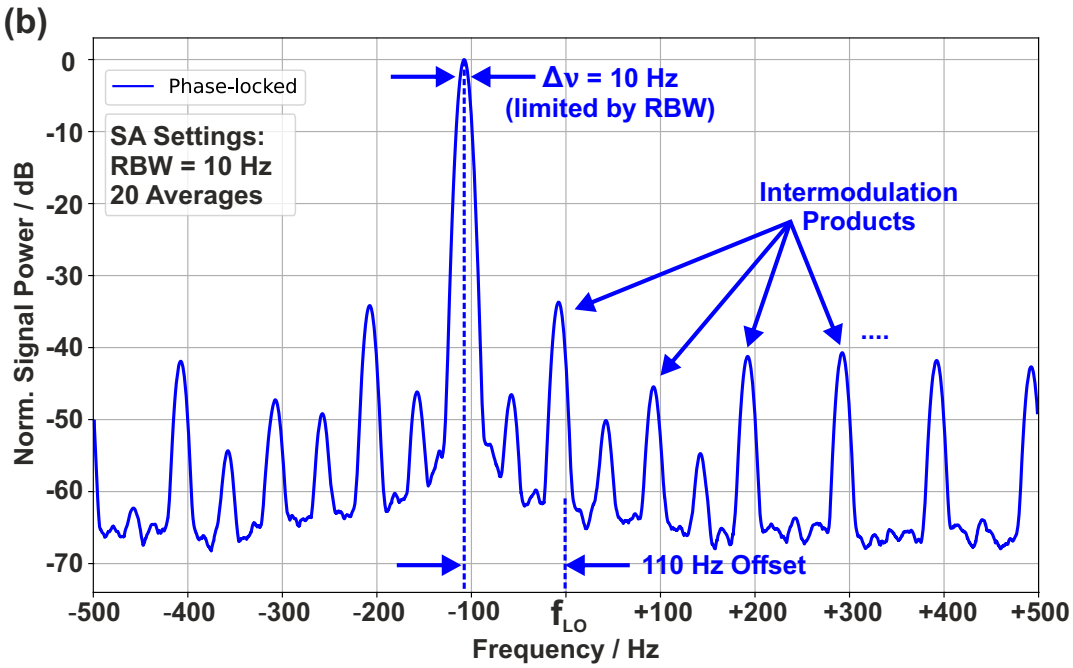

Figure 3.15: (a) Comparison of the laser beat signal with (blue) and without (red) stabilization to a 110 GHz electronic FMC with the Schottky diode mixer setup (LO frequency = 10 MHz, RBW = 3 kHz, 20 averages). The phase-locked signal shows a significantly narrower line at the LO frequency with suppressed servo bumps by 36 dB and a loop bandwidth of 4 MHz. (b) High-resolution spectrum of the phase-locked beat signal centered at $f_{\mathrm{LO}} = 10\ \mathrm{MHz} \pm 500\ \mathrm{Hz}$ (RBW = 10 Hz, 20 averages). The linewidth is again limited by the SA's resolution bandwidth, with side peaks from intermodulation products suppressed by 35 dB.

with the previous locking schemes, the laser pair is successfully synchronized to the terahertz reference, as evidenced by the narrow line at the LO frequency. The servo bumps introduced by the control loop are effectively suppressed by 36 dB, while maintaining a loop bandwidth of 4 MHz. These results are largely consistent with those obtained from the other two heterodyne detection techniques.

Additionally, the linewidth in the high-resolution spectrum is again limited by the 10 RBW of the SA. In contrast to the previous high-resolution plots, more and stronger side peaks are visible. These additional peaks are assumed to be intermodulation products, likely arising from the harmonic mixing process. Despite being suppressed by over 35 dB, these intermodulation products may still affect the reliability and accuracy of fine-resolution measurements with the phase-locked beat signal.

In conclusion, all the investigated heterodyne conversion techniques demonstrate successful synchronization of the laser beat note with a highly stable reference in the terahertz domain. However, given the similar performance of these methods, photomixing detection stands out due to several advantages that make it the preferred solution for the upcoming experimental setups. One key benefit is high dynamic range of the photomixers, particularly for lower terahertz frequencies [149]. Since the available reference

sources in our setup are limited to 70 GHz to 500 GHz, the natural low-pass characteristic of photomixers is not an issue in this context. In contrast, Schottky receivers encounter significant challenges within this range. As their fundamental LO frequency is limited, higher-order harmonics are required to detect frequencies near 500 GHz. This dependence on higher harmonics leads to a growing degradation in conversion efficiency, making Schottky receivers a less suitable option. The main advantage over EO detection is the relatively simple and compact system geometry offered by photomixers. Unlike EO setups, which require free-space alignment and careful consideration of beam overlap and polarization matching, photomixing systems benefit from fiber-coupled configurations. This feature not only simplifies the alignment but also enables an easier integration into future measurement systems. Moreover, the high-resolution spectrum of PMD demonstrated superior suppression of noise and spurious signals, which is crucial for achieving accurate and reliable measurements with resolution at the hertz level.

In the following, the proposed PMD setup will be expanded by adding a third DFB laser and a second OPLL, thereby significantly extending the frequency range of the current synchronization concept up to 1 THz.

3.4 Frequency Extension

Although phase-locked in the terahertz domain, the difference frequency remains restricted to the two laser wavelengths, separated by the maximum frequency of the electronic reference. Moreover, the effective tuning range of the beat signal is determined by the operational bandwidth of the respective FMCs. To overcome this limitations, an additional Secondary laser, along with a second mFALC 110 controller, TIA, and photomixer is integrated into the PMD setup to achieve a broader frequency coverage.

A sketch of the three-laser synchronization setup with two OPLLs is depicted in Fig. 3.16. Initially, the radiation of all three lasers is fiber-coupled and divided using 50:50 power splitters, represented in red, yellow, and blue. The Primary laser is then combined with a portion of each Secondary laser in a 2×2 fiber coupler for synchronization (green and orange), while the remaining portions of Secondary 1 and Secondary 2 are superimposed to generate the frequency-extended beat signal for the measurement (purple). The unconnected fiber outputs can again be used to monitor the lasers with the OSA.

In the free-space section, the radiation of a CW electronic terahertz FMC is directed by two off-axis parabolic mirrors towards one of the photomixers (PM #1). After passing the first OAP mirror, the terahertz wave hits a 525 µm thick silicon wafer, which serves roughly as a 50:50 beam splitter in the terahertz region [150]. The reflected beam is then guided via another mirror to the second photomixer (PM #2). Subsequently, the oscillating photocurrents from both photomixers are fed to two TIAs, where they are converted into voltage outputs for the laser synchronization with the PID controllers and for tracking with the electronic SA. Similar to the two-laser setup, the RF generator provides a LO signal, which is sent to both mFALC controllers.

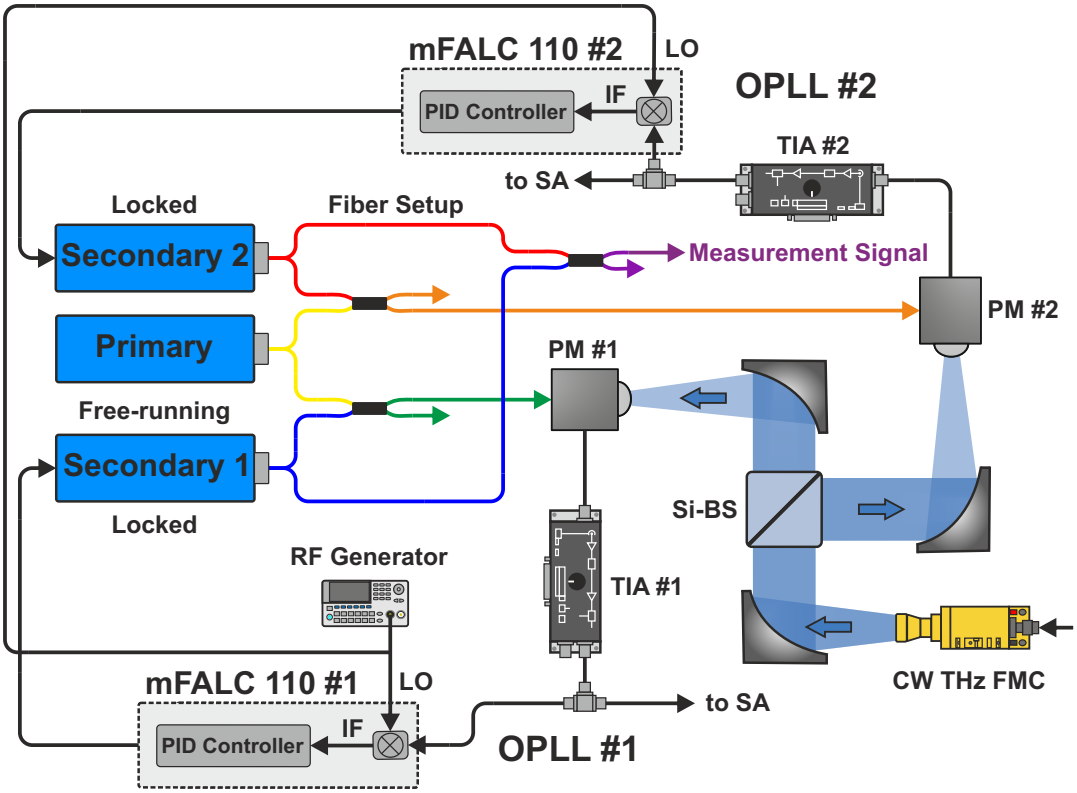

Figure 3.16: Three-laser synchronization setup for phase-locking in the terahertz domain: The radiation of three lasers is fiber-coupled and divided using 50:50 power splitters (color-coded red, yellow, and blue). The Primary laser is combined with portions of the Secondary lasers for synchronization (green and orange), while the remaining fractions generate the frequency-extended beat signal (purple). A CW electronic FMC, directed by off-axis parabolic mirrors, passes through a silicon wafer to photomixer PM #1, while another part is reflected towards PM #2. The oscillating photocurrents are converted to voltage signals for synchronization with PID controllers. Both Secondary lasers are phase-locked to the Primary, generating a beat signal with twice the frequency of the FMC output. BNC and SMA cables are shown in black.

Following the same synchronization concept as described in 3.3, both Secondary lasers are phase-locked to the Primary, with a frequency offset corresponding to the output of the common reference source and the LO signal. With respect to maximize the frequency difference, one of the Secondary lasers is shifted up in frequency relative to the Primary, while the other is shifted down. As a result, the effective measurement beat (purple) now features twice the frequency of the initial FMC output.

Fig. 3.17 shows the measured frequency spectrum of the phase-locked laser beat signals with a reference frequency of 500 GHz and 10 MHz LO signal. An active FMC (Transmitter TX RX-500[7], Radiometer Physics GmbH) with a frequency range of 325 GHz to

[7]The transmitter consists of an active frequency multiplier (AFM12 110-170 +10) extended with a passive frequency tripler (FM3 325-500).

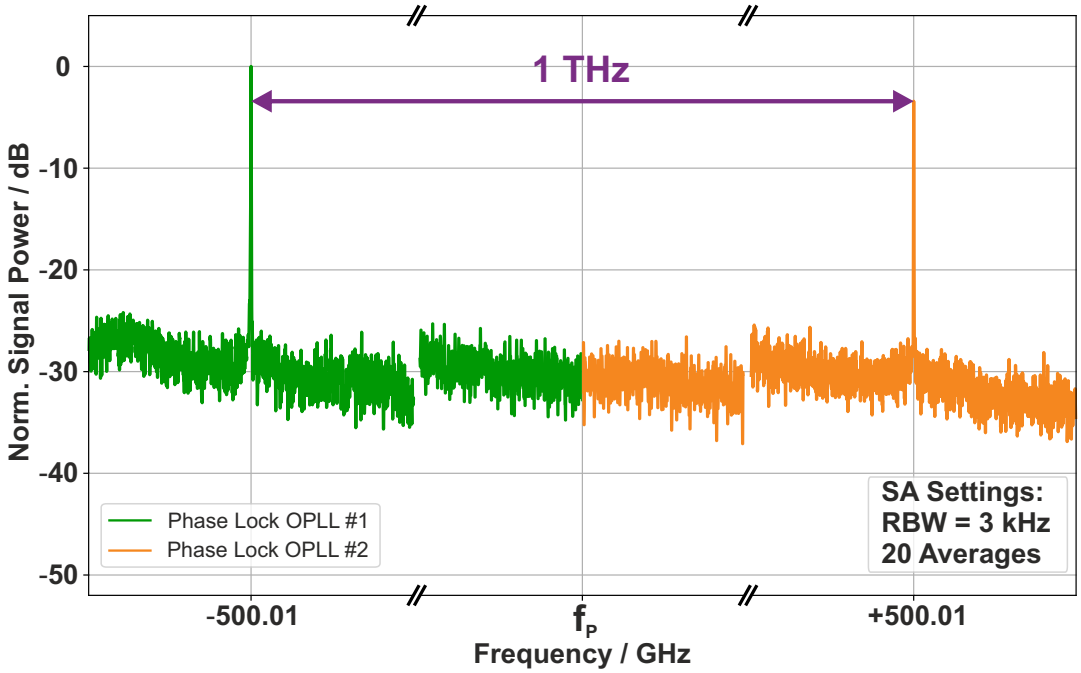

Figure 3.17: Frequency spectrum of the phase-locked laser beat signals at ±500.01 GHz from the Primary laser frequency $f_P = 350.6212$ THz (LO frequency = 10 MHz, frequency span = 4 MHz around central frequency, RBW = 3 kHz, 20 averages). The 1000.02 GHz peak spacing confirms a phase-stabilized signal from the Secondary lasers, achieving a 1 THz beat frequency with hertz-level resolution.

500 GHz and an output power of approximately 150 µW provides the highly stable reference signal. The spectrum reveals two narrow peaks, constrained by the 3 kHz RBW, appearing at -500.01 GHz and +500.01 GHz relative to the Primary laser frequency. It is noticeable that the locked beat signal of OPLL #2 exhibits a slightly lower dynamic than the lock with OPLL #1. A possible reason for this discrepancy could be that a larger fraction of the terahertz wave is transmitted through the silicon wafer rather than reflected. The negative slope in the individual spectra can be attributed to the increased gain setting of the TIAs (10^6 V/A), which also leads to a reduction in the -3 dB bandwidth (3.5 MHz). Despite this limitation, the adjusted settings still offer a higher overall gain at 10 MHz compared to the previous configuration. The amplification is required as the FMC power at 500 GHz is almost 20 dB lower than at 110 GHz. Even with the higher gain, the dynamic of the beat signals remains 10 dB lower compared to locking at lower frequencies[8], though it still exceeds the noise level by more than 25 dB. The frequency difference between the peaks is 1000.02 GHz, indicating a usable phase-stabilized measurement signal generated by the superposition of the two Secondary lasers, with an effective beat frequency exceeding 1 THz and a resolution in the hertz range.

[8]This result also highlights the fundamental power limitation of electronic multiplier chains: To generate higher frequencies, increasingly higher harmonics are needed, which progressively weaken. Although FMCs with higher output frequencies are available, achieving a stable phase lock becomes more challenging. As a result, cascading additional lasers presents a far more promising solution.

Even with the three-laser setup, the achievable bandwidth of the system remains at least partially constrained by the FMC source. For example, locking with the 500 GHz multiplier chain with a bandwidth of 175 GHz enables coverage of the frequency ranges from 325 GHz to 500 GHz and from 650 GHz to 1000 GHz, using the beat signal between one Secondary and the Primary laser or the beat note between Secondary 1 and Secondary 2, respectively. However, to address the residual frequency gaps, the concept from Fig. 3.16 is adapted to employ two different reference sources.

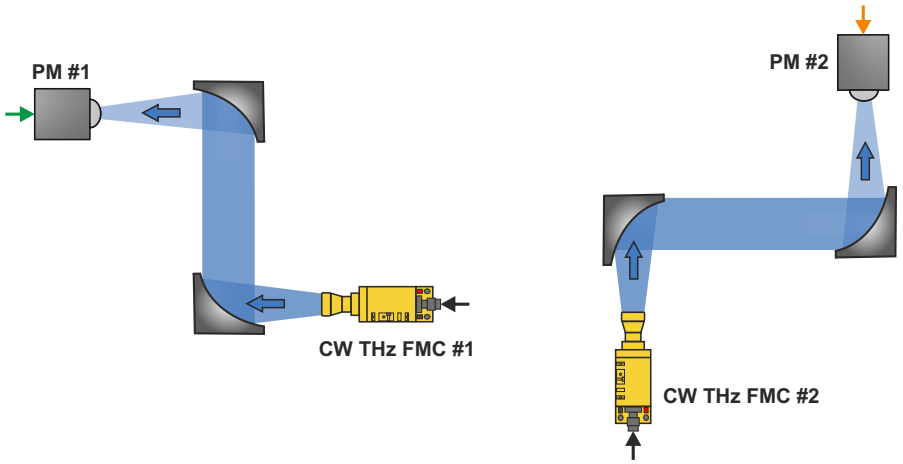

Figure 3.18: Adaptation of the three-laser synchronization setup for phase-locking with two reference sources in the terahertz domain: A fourth OAP mirror directs terahertz radiation to PM #2, while a second synthesizer drives FMC #2. The Secondary laser shift controls whether the beat signals add or subtract.

The modified free-space section is illustrated in Fig. 3.18. In substitution for the silicon beamsplitter, a forth OAP mirror is included in the setup to direct the terahertz radiation from the second CW emitter to PM #2. To provide the fundamental microwave input signal for FMC #2, a second frequency synthesizer (APSYN420, AnaPico AG), capable of generating signals between 0.01 GHz to 20 GHz, is added to the system. The microwave synthesizers are synchronized by connecting the 10 MHz reference output to the respective input of the second device, ensuring phase coherence between them. Shifting the Secondary lasers to the same side of the Primary results in the beat signals of OPLL #1 and #2 being subtracted, whereas moving it to opposite sides leads to their addition.

As an example, the frequency spectrum of phase-locked beat signals with two different reference sources is depicted in Fig. 3.19. In OPLL #1, an active FMC (AFM12 110-170 +10, Radiometer Physics GmbH) with a frequency range of 110 GHz to 170 GHz and an output power of 10 mW is employed, while OPLL #2 utilizes the 500 GHz transmitter. The spectrum reveals two narrow peaks at +150.01 GHz and +432.01 GHz from the Primary frequency f_{P}, with respective dynamics of about 35 dB and 27 dB. Additionally, the superimposed Secondary lasers enable the generation of a beat signal at 282 GHz, allowing three distinct terahertz signals to be extracted from this concept.

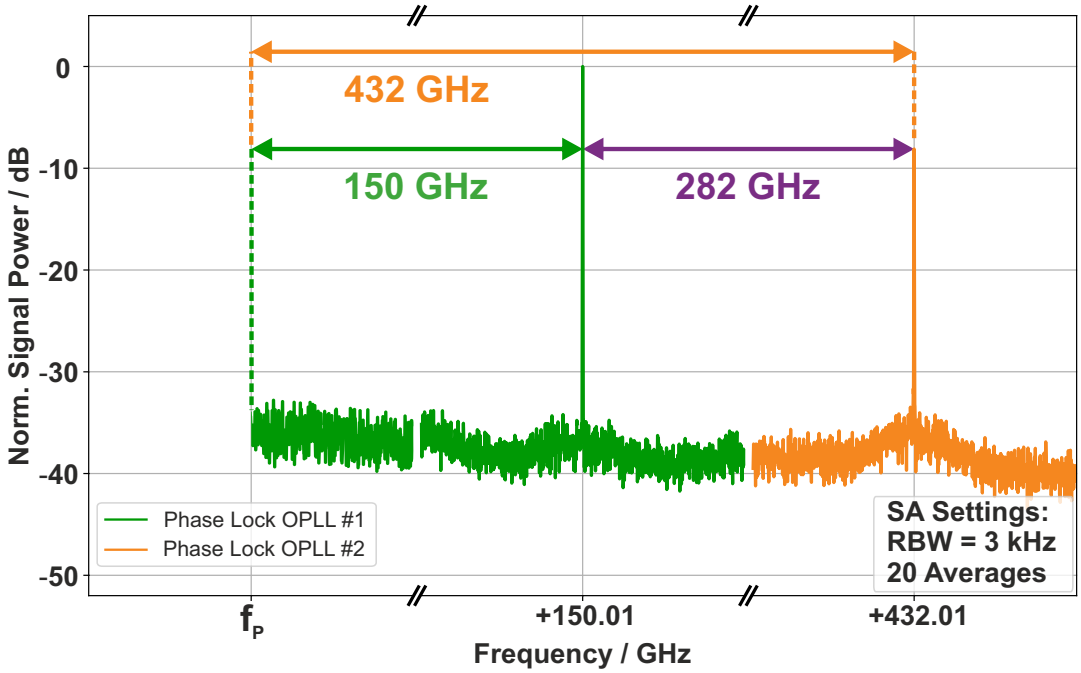

Figure 3.19: Frequency spectrum of the phase-locked laser beat signals at +150.01 GHz and +432.01 GHz from the Primary laser frequency f_P = 350.6212 THz (LO frequency = 10 MHz, frequency span = 4 MHz around central frequency, RBW = 3 kHz, 20 averages). Shifting both Secondary lasers to the same side of the Primary generates a beat signal around 282 GHz.

With these two reference sources, the previously missing frequency bands from 110 GHz to 325 GHz and 500 GHz to 650 GHz can be covered, extending the addressable system bandwidth to nearly 900 GHz. Accessing frequencies below 110 GHz requires an exchange of the reference source, for example, using a W-band emitter spanning 75 GHz to 110 GHz. For even lower frequency ranges, the employed photomixers start to become less effective due to reduced impedance matching and antenna coupling efficiency. Therefore, purely electronic solutions offer more promising approaches for measurements spanning the microwave to lower millimeter-wave range.

An alternative idea to overcome the missing frequency ranges while still relying on only one reference source, is to introduce additional output couplers at intermediate stages of the FMC. For example, coupling out a portion of the signal power before the final tripler in the 500 GHz multiplier chain allows for the generation of frequencies ranging from 110 GHz to 170 GHz. However, since both frequencies can no longer be set independently, it is possible that some gaps cannot be covered using this technique. Considering the current upper frequency limit of 1 THz, it remains constrained by the maximum frequency of the reference source. Nevertheless, the developed synchronization concept is scalable by cascading additional Secondary lasers with their respective OPLLs, enabling the extension of the frequency range far into the terahertz domain. Even though this introduces some complexity, the system would still offer significant cost advantages

compared to electronic frequency extender sources, which are inherently bandwidth-limited. Another approach that can be considered is so-called "four-wave mixing". FWM is a nonlinear optical process that occurs in a medium with a sufficiently strong third-order nonlinearity, such as a semiconductor optical amplifier (SOA). Injecting the phase-locked beat signal from a laser pair into an SOA generates two additional sidebands, effectively tripling the initial beat frequency.

A first poof-of-concept of FWM and its planned adaptation for future frequency extension approaches will be provided in Chapter 6. In the following two chapters, the presented laser frequency synchronization scheme will be integrated into high-resolution photonic spectrum analyzer and photonic vector network analyzer extender setups, both of which were developed as part of this thesis, to investigate and also characterize various devices in frequency ranges up to 1 THz and 520 GHz, respectively.

4 High-resolution Photonic Spectrum Analyzer

As already outlined in the introduction, photonic spectrum analysis is becoming increasingly important for advancing high-frequency technologies across various fields. Driven by the growing demand for higher data rates and the development of emerging systems operating at sub-millimeter and terahertz frequencies, high-resolution spectrum analysis in this domain has become a central topic in both research and industry [6]. To meet this need, this thesis presents a high-resolution photonic spectrum analyzer for the characterization of continuous-wave terahertz signals. Building on the laser frequency synchronization concept introduced in the previous chapter, the system is extended with a free-space configuration to enable ultra-high-resolution spectroscopy of HF components in the terahertz range.

Throughout this chapter, the fundamental operating principles and achieved specifications, as well as the identified limitations of the newly developed PSA platform, are discussed. After explaining the SA section of the system, the calibration procedure of the PSA is elaborated. Subsequently, the measurement results of spurious harmonics for different electronic FMCs are shown, followed by a critical evaluation of the overall system performance. The presented results were published in [151].

4.1 Experimental Setup

4.1.1 System Architecture

The schematic concept of the high-resolution photonic spectrum analyzer is depicted in Fig. 4.1. Initially, the phase-locked beat signal from the two Secondary lasers, generated by the laser frequency synchronization system (Fig. 3.16), is guided via fiber into a tapered amplifier (TA). The TA (BoosTA pro 850, Toptica Photonics AG) increases the power of the beat signal before it enters the photomixer, while preserving the residual optical properties. This is done to maximize the laser power reaching the photomixer, enhancing detection sensitivity, since the generated photocurrent is directly proportional to the optical power. Additionally, the integrated optical isolator suppresses reflections at the photomixer, preventing feedback into the lasers and ensuring stable and reliable

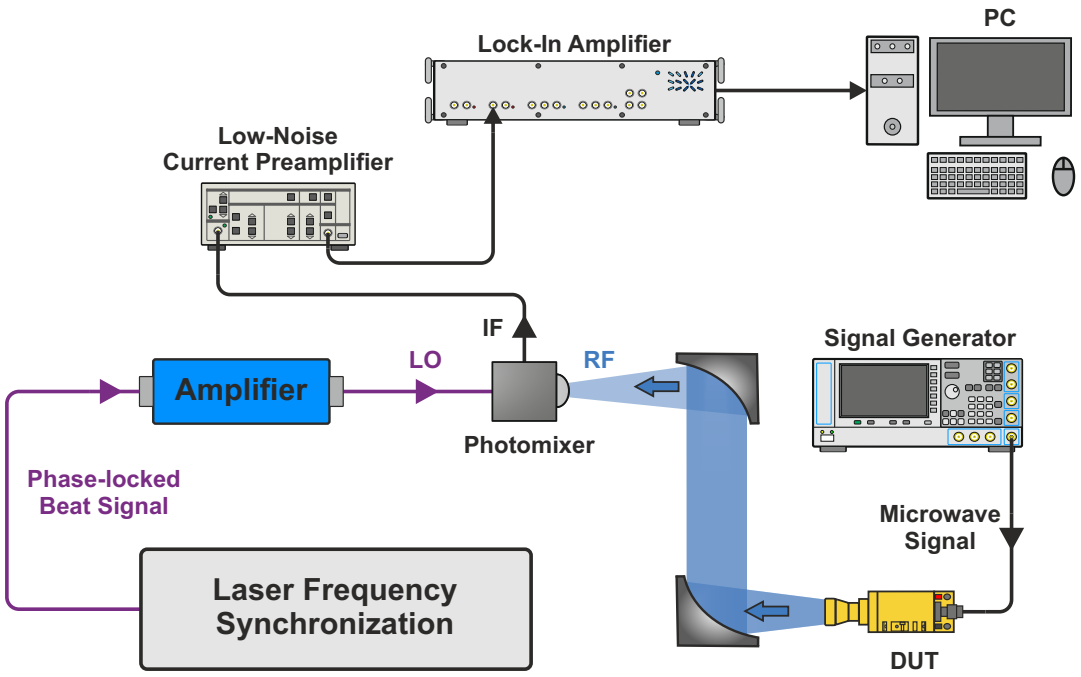

Figure 4.1: Schematic illustration of the high-resolution photonic spectrum analyzer setup: The amplified phase-locked beat signal of the two Secondary lasers is employed in the photomixer to downconvert the signal from the device under test (DUT) into the intermediate frequency (IF). This IF current is boosted in a preamplifier and analyzed using the FFT function of the lock-in amplifier.

operation[1]. To direct the radiation from the DUT to the terahertz input port of the photomixer, a free-space beam path is included. It consists of two off-axis parabolic mirrors with an effective focal length of 101.8 mm in a standard 4f configuration, along with the hyperhemispherical silicon lens (f ≈ 30 mm) attached to the PM. Together with the modulated conductivity, the incident terahertz wave induces a photocurrent that oscillates at the frequency difference between the laser beat and the DUT output. Subsequently, the modulated signal is sent to a low-noise current preamplifier (Model SR570, Stanford Research Systems) with a gain of 10^6 V/A and a bandwidth of 200 kHz, which is connected to a lock-in amplifier (LIA) (HF2LI, Zurich Instruments) and a PC for the data acquisition.

4.1.2 Operation Principle

The PSA measurement follows the same coherent detection scheme employed for frequency synchronization. The photomixer downconverts the DUT radiation from the terahertz to the radio frequency range, enabling further spectrum analysis using well-

[1]It was observed that reflections at the GaAs photomixers can reduce the phase stability of the locks, particularly when the frequency is swept over wide ranges. To mitigate this issue, optical isolation is also added to the laser synchronization setup.

established measurement techniques. Similar to a conventional microwave mixer, the input signal, referred to as "RF"[2], is combined with the LO signal — in this case, the laser beat — resulting in an intermediate frequency that corresponds to the difference between the RF and LO signals. For the measurement, the LO frequency is varied across the desired bandwidth by tuning one or both secondary lasers to cover the entire measurement window. In the low-noise preamplifier, the IF signal is amplified and filtered to a narrow bandwidth of 100 kHz before entering the lock-in amplifier. The LIA serves as an analog-to-digital converter, digitizing the voltage signal of the preamplifier using a sampling rate of 103 kSa/s. After capturing the time-domain signal, it is converted into the frequency domain using the FFT function of the lock-in amplifier. Finally, the resulting signal spectrum is displayed on the PC.

This two-step strategy effectively combines key principles of both swept-tuned and FFT-based spectrum analysis. Like a swept-tuned analyzer, the LO frequency is incrementally adjusted to scan across the full measurement bandwidth. However, instead of measuring signal power at a single frequency point, the PSA simultaneously captures a broader spectrum in each LO step, similar to an FFT-based analyzer. This is achieved by utilizing the lock-in amplifier, which records the IF signal within its 51 kHz bandwidth and subsequently applies an FFT to extract the frequency components. Still, to maintain a resolution at the Hz level, the FFT analysis is performed with a frequency point spacing of 50 Hz. To ensure accurate frequency coverage and minimize potential aliasing effects, the LO step size is set to 20 kHz. Selecting much smaller increments would significantly increase the measurement time, as it takes approximately 200 ms to adjust for the next LO step, while the FFT analysis (averaged 10 times) only requires around 100 ms for the whole 51 kHz spectrum. Higher LO frequency steps are constrained by the bandwidth and filter settings of the preamplifier.

By leveraging this hybrid approach, the PSA achieves high spectral resolution while maintaining a balanced scanning speed, optimizing both accuracy and measurement time. The relatively slow LO tuning speed is due to the various subsystems involved in the frequency synchronization setup. For instance, as the resolution of our digital-to-analog converter (DAC) alone is insufficient for the required fine voltage steps, a pulse width modulation (PWM) module is employed to provide finer voltage adjustments. This process, on its own, results in a 130 ms delay in the laser synchronization. However, since the developed PSA is still in the experimental stage, the primary focus is not necessarily on minimizing the measurement time. In addition to frequency range, resolution, and sweep time, other key parameters determine the performance of spectrum analyzers. Consequently, a comprehensive system characterization is conducted, which is the topic of the following subsection.

[2]The use of the term "RF" for the input signal can be confusing, as it typically refers to microwave frequencies, but it is retained here due to established nomenclature in mixer theory.

4.1.3 System Characterization

To further analyze the PSA capabilities, the accuracy, sensitivity, and responsivity of the developed system platform are evaluated through the following calibration procedure, using an active FMC emitting in the D-band as DUT. Initially, the FMC is set to a nominal frequency of 140 GHz, and the output power is varied from 10 mW down to 1 pW by reducing the input signal from the microwave synthesizer. To determine the output power of the DUT, a pyroelectric detector (THz 10, SLT Sensor und Lasertechnik GmbH) is positioned at the photomixer location. The broadband pyroelectric detector underwent calibration at 1.4 THz at the Physikalisch-Technische Bundesanstalt in Berlin and has an operational range from 8 µW to 10 mW. Due to the disparity between the measurement and the calibration frequency a systematic error of 30% is considered. For lower power levels, the pyroelectric detector is replaced with a Golay cell (Model OAP Golay Cell, CDP System Corporation), which can detect signals as low as 1 nW. To ensure comparability between the measured values of the Golay cell and the calibrated pyroelectric detector, both detectors are cross-referenced within their overlapping measurement range for multiple output powers. Values below the noise floor of the Golay cell are estimated by extrapolating the input-output power relationship of the FMC, assuming linear behavior. The linearity is confirmed down to 1 nW by simultaneously monitoring the input power with a microwave power sensor (LB5926A, Ladybug Technologies LLC) and measuring the DUT signal with the Golay detector.

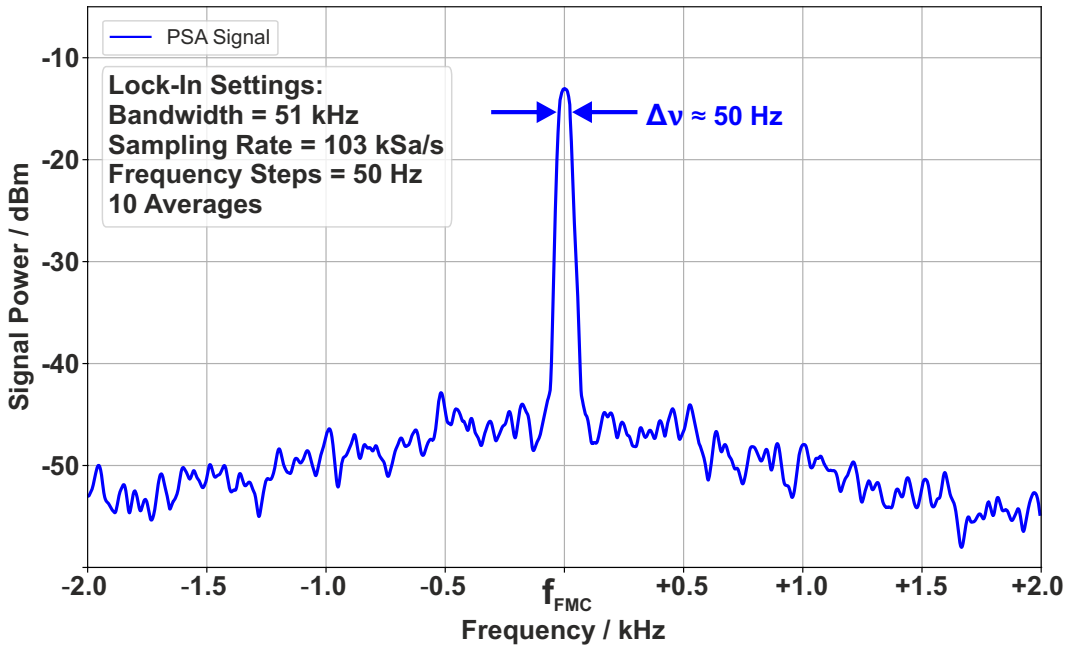

Figure 4.2: Measured FMC spectrum at $f_{\mathrm{FMC}} = 140$ GHz $\pm$ 2 kHz with an output power of 50 µW. The 3-dB bandwidth of approximately 50 Hz is limited by the selected frequency step size.

Fig. 4.2 displays the calibrated power spectrum within a ±2 kHz range around 140 GHz for an output power of 50 µW (-13 dBm). For the calibration, the integrated spectral power of the PSA is matched with the recorded signal of the pyroelectric detector. The spectrum is acquired using a gain factor of 10^6 V/A, a bandwidth of 51 kHz, and an acquisition time of 100 ms (averaged over 10 measurements) with frequency steps of 50 Hz. The peak at f_{FMC} exhibits a 3-dB bandwidth of approximately 50 Hz, corresponding to the combined linewidth of the FMC and the LO signal, with the resolution limited by the 50 Hz FFT step size. Given that the expected linewidth of the FMC is within 1 Hz [152] and the determined laser beat linewidth is below 10 Hz, the minimum achievable RBW of the system is estimated to be around 10 Hz with a smaller FFT step size.

To calibrate the spectral sensitivity of the PSA at 140 GHz, the measured peak values for different output powers are correlated with the power readings from either the pyroelectric detector or the Golay cell.

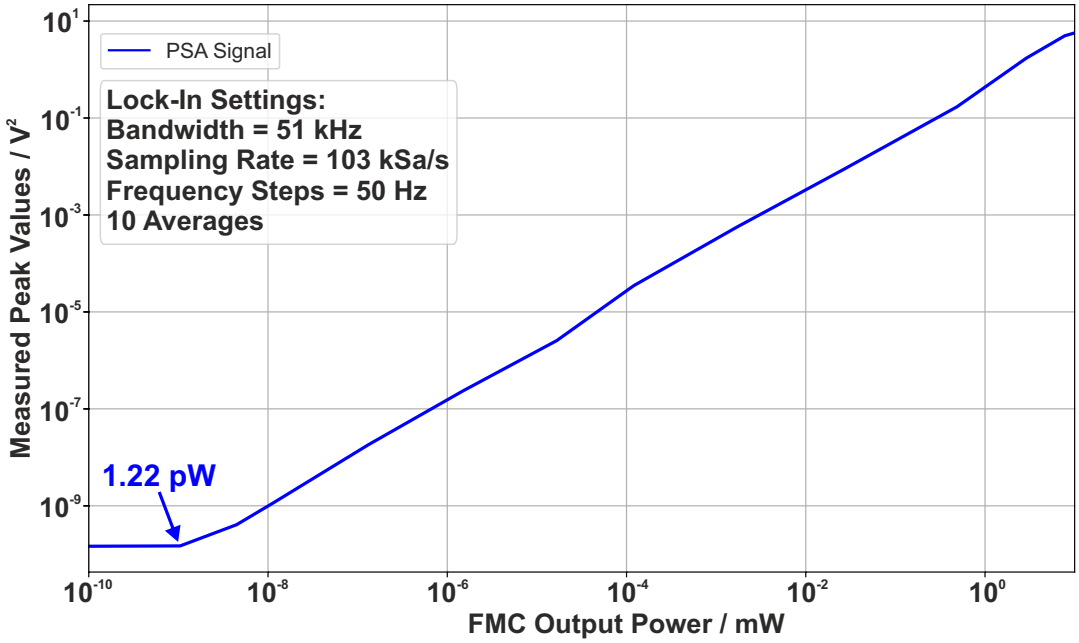

Figure 4.3: Measured peak values of the FMC spectra at 140 GHz as a function of output power. The displayed average noise level (DANL) is calculated to be -106.3 dBm/Hz based on the obtained noise power level of 1.22 pW and the step size of 50 Hz.

The measured peak voltage values in Fig. 4.3 show excellent linearity of the developed PSA platform for different power levels, extending down to an FMC output power of 4.47 pW. As the signal power continues to decrease, the signal flattens out, eventually reaching the noise power level of 1.22 pW. From this, the displayed average noise level of the system can be determined, serving as a benchmark for the measurement sensitivity of the PSA. The DANL is calculated by dividing the noise power level by the measurement bandwidth, which in this case corresponds to the frequency bin size of 50 Hz. Consequently, this results in a DANL of -106.3 dBm/Hz at a frequency of 140 GHz.

For the characterization of the frequency response of the photonic SA, additional FMCs across frequency ranges from 75 GHz to 110 GHz (W-band), 110 GHz to 170 GHz (D-band), 220 GHz to 325 GHz (J-band), and 325 GHz to 500 GHz (Y-band) are employed as reference DUTs, allowing for an analysis of the system's responsivity over a wide frequency span. As with the previous measurements, the output power of the different DUTs has to be calibrated. This is achieved by using the pyroelectric detector to measure the required input power that corresponds to a signal strength of 50 µW. Since these measurements require precise adjustments, only 12 frequencies (indicated by black markers in Fig. 4.4), ranging from 75 GHz to 500 GHz, with an approximate spacing of 50 GHz are considered. After calibrating the power of the different DUTs, the peak spectral values of the PSA are measured and correlated with the respective frequency points.

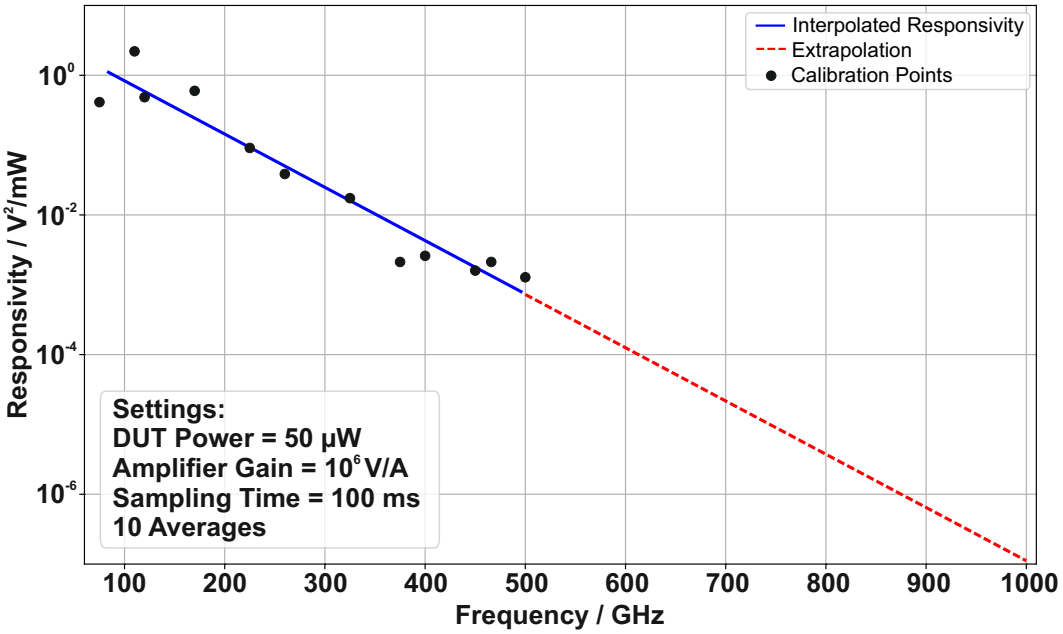

Figure 4.4: Spectral responsivity of the PSA across a frequency range of 75 GHz to 1000 GHz. The blue line represents the interpolated responsivity obtained with the reference DUTs (black markers indicating calibration points), while the dashed red line denotes the extrapolated values.

In Fig. 4.4, the spectral responsivity of the PSA is illustrated for frequencies ranging from 75 GHz to 1000 GHz. The responsivity reaches a peak around 100 GHz and then gradually decreases with increasing frequency. This decline is primarily attributed to roll-offs in the dynamic range of the photomixer at higher frequencies. Since no FMCs above 500 GHz are available, the responsivity values for higher frequencies are estimated by extrapolating the measured data. Frequencies below 75 GHz must be considered separately due to the extremely steep roll-off of the silicon antenna beneath 50 GHz. Therefore, the PSA calibration bandwidth is specified for frequencies ranging from 75 GHz to 1 THz.

The photomixer in the setup features a log spiral antenna designed for circularly polarized light. Log spiral antennas are generally frequency-independent, maintaining consistent radiation patterns, impedance, and polarization across a wide bandwidth. However, at higher frequencies, the axial ratio of elliptical polarization increases, eventually transitioning to linear polarization. This occurs when the tapered section of the antenna becomes comparable to the effective wavelength, causing the antenna to behave more like a dipole [153]. As the FMCs in the setup utilize rectangular waveguides with Pickett–Potter horn antennas for free-space transmission, the generated radiation is linearly polarized, with a typical cross-polarization level above -20 dB [154]. Hence, the effect of the incident radiation's polarization direction is also investigated. For this purpose, the photomixer is rotated by approximately 90°, and the peak voltages are measured at different frequencies. The measured voltages, however, vary by less than 10% across the frequencies tested. Since the polarization-related deviations are small compared to other sources of measurement uncertainty, such as calibration errors from the pyroelectric detector as well as free-space adjustments, and because all DUTs are measured with the same polarization orientation, the influence of polarization is not further considered in the calibration process. Nevertheless, it is important to note that this effect may become more significant at higher frequencies as the dipole effect intensifies.

After completing the calibration and determining the key SA parameters, initial measurements are conducted to examine the capabilities of the developed system platform for high-resolution spectrum analysis. In the following section, the investigation of spurious harmonics in FMCs is presented as an application-oriented example.

4.2 Detection and Analysis of Spurious Harmonics

As highlighted in the introduction to this thesis, future communication technologies will heavily depend on hardware capable of emitting and receiving signals in the terahertz spectral range. Consequently, signal generation plays a crucial role, as it is susceptible to various unwanted spectral components, including phase noise, intermodulation products, and spurious harmonics [155]. Harmonics are integer multiples of a fundamental frequency that arise due to nonlinearities within a device. They can originate during microwave signal generation but are more commonly introduced by amplifier stages or frequency multipliers within the signal chain. For example, an FMC operating at a nominal frequency of f_0 will likely induce harmonics at $2f_0$, $3f_0$, $4f_0$, and higher integer multiples. Looking towards ultra-broadband modulated signals with tens of gigahertz of bandwidth or the combination of multiple narrow-band channels for advanced 6G transmission networks, the need for efficient and reliable carrier generation grows even more critical. To deal with those spurious spectral components, effective filtering and suppression techniques must be implemented. The most common approach to mitigating harmonics is the use of high-quality band-pass or notch filters that selectively attenuate or block unwanted frequency parts. These filters must be carefully designed to ensure they precisely target the spurious frequencies while preserving the integrity of the de-

sired signal. Thus, appropriate measurement tools, such as VNAs, which operate in the respective frequency domains, are required to accurately analyze the frequency response of the devices. Details of a (photonic) VNA operating in the terahertz range and the characterization of different HF devices will be provided in Chapter 5. However, before delving into the development and testing, it is essential to first identify the spurious signals that need to be addressed through filtering.

Spurious Harmonics of Frequency Multiplier Chains

As an application example, the spurious harmonics of two different FMCs are investigated using the developed PSA platform. The measured voltage values are converted to power based on the determined receiver responsivity (see Fig. 4.4). This conversion also contributes to the rising slope of the noise floor in the spectra.

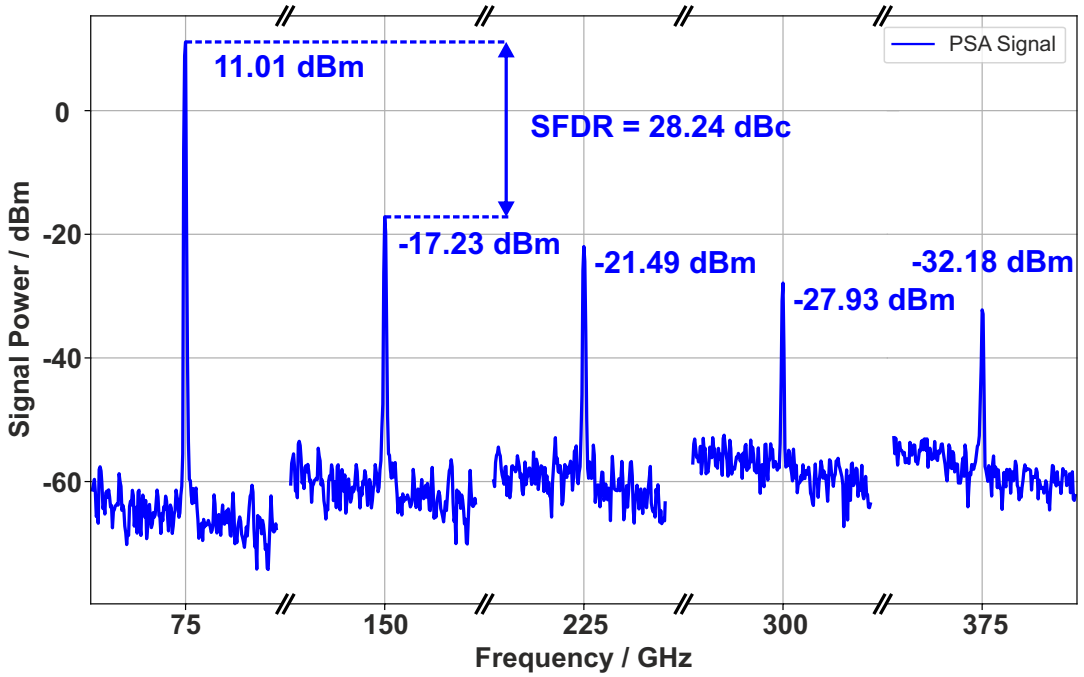

Figure 4.5: Frequency spectrum of the fundamental frequency and the first to fourth harmonics of a W-band FMC emitter at $f_0 = 75$ GHz. The signal powers continue to decrease for higher harmonic numbers, resulting in a spurious-free dynamic range (SFDR) of almost 30 dBc. Settings: Gain factor 10^6 V/A, sampling rate 103 kSa/s, acquisition time 100 ms per single 51 kHz spectrum (10 averages), frequency steps 50 Hz.

Fig. 4.5 depicts the obtained frequency spectrum of the spurious harmonics from a W-band FMC source, emitting at a fundamental frequency of 75 GHz. Each individual spectrum shows a section of ±10 kHz around the respective harmonic. In the spectrum, the five narrow peaks at 75 GHz, 150 GHz, 225 GHz, 300 GHz, and 375 GHz correspond to the fundamental frequency and its first to fourth harmonics. The spike at 75 GHz exhibits a maximum signal power of 11.01 dBm with a dynamic range of more than 70 dB.

For the second peak in the spectrum, associated with the first harmonic, the signal power drops to -17.23 dBm. As the harmonic order increases, the power continues to decline, yielding peak values of -21.49 dBm (second harmonic), -27.93 dBm (third harmonic), and -32.28 dBm (fourth harmonic). This reduction in signal strength is expected, as their amplitude typically diminishes with higher harmonic numbers, resulting in a SFDR[3] of 28.24 dBc.

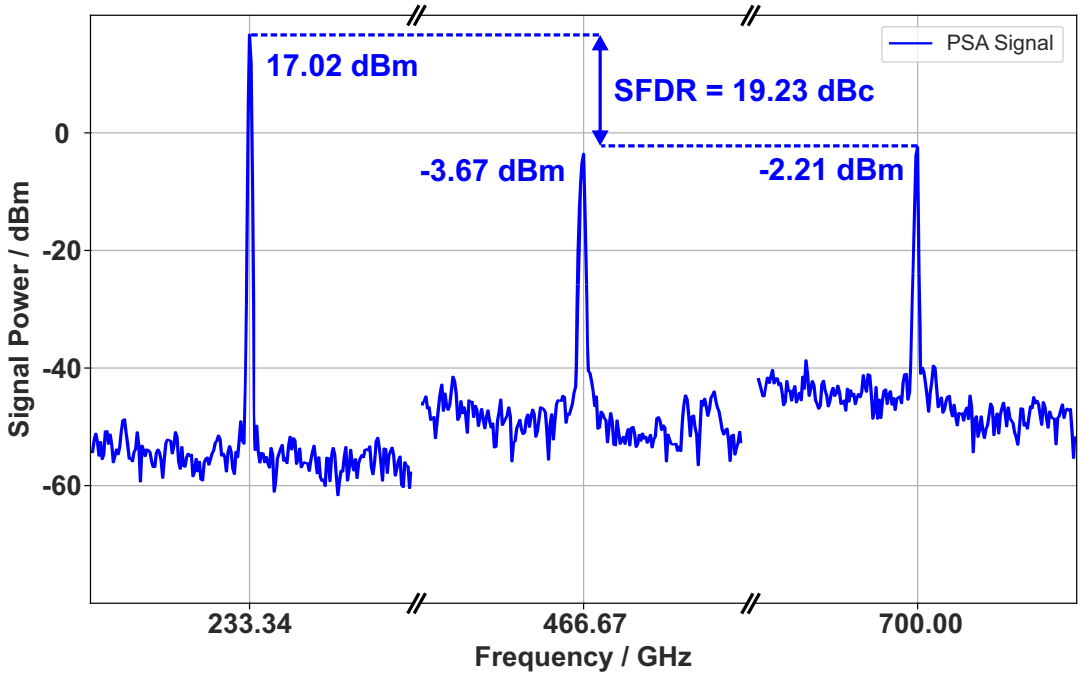

Figure 4.6: Frequency spectrum of the fundamental frequency and the first and second harmonics of a 225 GHz to 265 GHz high-power FMC emitter at $f_0 = 233.33$ GHz. Settings: Gain factor 10^6 V/A, sampling rate 103 kSa/s, acquisition time 100 ms per single 51 kHz spectrum (10 averages), frequency steps 50 Hz.

The second DUT evaluated in this application example is a high-power active multiplier chain, operating within the 225 GHz to 265 GHz frequency range. Fig. 4.6 shows the measured frequency spectrum, including the fundamental frequency at 233.33 GHz and the first and second harmonics at 466.67 GHz and 700.00 GHz, respectively. The carrier frequency reaches a peak power of 17.02 dBm with a signal to noise distance exceeding 60 dB, while the first and second harmonic are measured at -3.67 dBm and -2.21 dBm. The observation that the second harmonic is higher than the first harmonic may be attributed to the extrapolated responsivity calibration for frequencies above 500 GHz or to characteristics of the multiplier chain itself. Therefore, further analysis would be needed to determine the exact cause of this discrepancy. However, regardless of this uncertainty, the SFDR is around 20 dBc, which is significantly lower than that of the W-

[3]It should be noted that in this application example only spurious harmonics of the nominal output frequency are evaluated, while other unwanted signals, such as intermodulation products or multiples of the individual multiplier stages, may also impact the SFDR.

band emitter. A possible reason for this is that the high-power source operates closer to the limit of the multiplier stages, which results in higher output power but also increased nonlinearities in the system [156].

To validate that the measured peaks match their respective harmonic numbers, the frequency of the LO signal is slightly shifted, causing a proportional shift in the frequency spectrum. For instance, a 5 kHz change compared to the fundamental frequency results in a 10 kHz offset for the first harmonic, 15 kHz for the second harmonic, and so forth. Additionally, the direction of the shift helps to determinate whether the signal appears in the upper or lower sideband of the LO frequency, which is crucial for correctly identifying spectral components in heterodyne receivers. This principle is similar to the "Signal ID Function" in electronic spectrum analyzers, where a small frequency shift is applied to observe how the measured signal moves in the spectrum. If the signal moves in the same direction as the shift, it is in the upper sideband; if it moves in the opposite direction, it is in the lower sideband.

4.3 System Limitations and Possible Improvements

Since the presented photonic SA is still in a highly experimental phase, the system currently exhibits some limitations in terms of sensitivity, calibration for precise power measurements, acquisition speed, and resolution when compared to state-of-the-art frequency-extended electronic spectrum analyzers (ESAs). Therefore, the concept leaves some room for future improvements, which will be elaborated during the following discussion.

With respect to sensitivity, the measured DANL of -106.3 dBm/Hz at 140 GHz for the photonic architecture is noticeably lower compared to the typical range of -130 dBm/Hz to -150 dBm/Hz found in commercial high-end electronic systems with frequency extension [157]. However, it is important to note that the developed PSA concept operates in a free-space environment, unlike the waveguide-coupled structure of ESAs with extender modules. Therefore, a comparison with other free-space configurations is more reasonable. In this context, the value remains in good agreement with the reported DANL of -113.8 dBm/Hz at 100 GHz for another PSA setup presented in [158]. As the obtainable DANL is primarily limited by the performance of the photomixer, it can be significantly improved by employing advanced PCA designs. A key requirement for efficient photomixers is a high optical photon-to-charge carrier conversion efficiency, which relies on enhanced absorption in the photoconductive material. Various strategies can be found in the literature, including the deposition of metallic nanostructures directly on the active region [159], as well as the integration of metallic or dielectric metasurfaces within a thin dielectric film [160]. These approaches optimize light-matter interaction by either concentrating the electromagnetic field at nanoscale hotspots or manipulating wavefront propagation to improve absorption and carrier dynamics. For instance, sputtering Au nanoislands onto the dipole gap region of an LT-GaAs pho-

toconductive detector enhanced its sensitivity by 29% [161]. Another idea to increase the sensitivity is an integrated aperture on the far side of the photoconductive region, isolating the terahertz field in a specific area before it enters the detector [162]. With ongoing advancements in PCA technologies, the sensitivity gap between optoelectronic and purely electronic systems is expected to diminish, making photonic concepts even more competitive.

Another essential aspect of SAs is the accuracy of power measurements. Modern ESAs provide power calibration with an precision better than ±1 dB [163]. For the PSA developed in this thesis, determining the precision of power measurements is quite challenging due to the numerous assumptions and estimations involved in the calibration process. Further, the system is calibrated at only 12 frequency points between 75 GHz and 500 GHz, with higher frequencies relying solely on extrapolation. To overcome these uncertainties, a higher number of calibration points with smaller frequency intervals can be applied, though this would significantly increase the calibration time. However, even with this approach, the concept would still suffer from limited accuracy due to beam path alignment and reflections in the free-space section. For example, reflections at the silicon lens of the PCA lead to an optical power loss of approximately 30% [164]. To eliminate the free-space related issues, waveguide-coupled photoconductive antennas [165] or integrated on-chip solutions [166] could significantly enhance the reliability of the measurements.

In terms of acquisition speed, there is the most notable discrepancy compared to commercial electronic solutions. For the current settings with 20 kHz LO steps and an acquisition time of roughly 300 ms per interval, it would take more than 3800 hours to complete a full sweep from 75 GHz to 1 THz, which is highly impractical. Even though electronic swept-tuned analyzers can scan the LO faster, they still face the same challenge when it comes to covering large frequency ranges. Since sweep time increases with the square of the RBW, modern ESAs provide a maximum RBW in the gigahertz range, allowing for faster measurements of wide frequency bands. However, as previously mentioned, the bottleneck for the highest achievable RBW lies in the bandwidth of the preamplifier and the data acquisition speed, which are currently limited to 1 MHz and 210 MSa/s, respectively. Consequently, replacing the amplifier with a device offering a wider bandwidth could tremendously decrease the measurement time.

Of course, selecting a much larger bandwidth comes at the expense of reduced resolution. Maintaining extremely high resolution while scanning a broad frequency range results in unreasonably long measurement times. Therefore, implementing two distinct modes of operation would be a more suitable approach. The first is a fast mode, capable of covering large frequency intervals with a step size of several megahertz, eliminating the need for phase-locking of the laser and additionally speeding up the measuring process. The second is the already established high-resolution mode, designed for measurements of smaller frequency spans with an RBW on the order of hertz, comparable to the narrowest resolution achievable with commercial high-end ESAs. Realizing an RBW in the gigahertz range would be challenging, as increasing the bandwidth typically leads to

a decrease in gain, which in turn reduces sensitivity. However, even a modest raise in the RBW to 10 MHz would still result in a significant reduction in measurement time, bringing the total time for a complete sweep from 75 GHz to 1 THz down to around 2.5 hours.

A non-technical but still crucial factor, especially from a commercial perspective, is the system's cost. While state-of-the-art electronic systems rely on multiple frequency extender modules, the developed photonic concept is a fully integrated system platform that spans frequencies from the millimeter-wave to the terahertz domain. For instance, addressing the same frequency range with a commercial SA would require at least seven frequency extender modules [157], which significantly increases both the overall system expenses and complexity. Furthermore, the newly developed approach has the potential to be scaled for even larger bandwidths by cascading additional lasers. This, combined with its relatively simple design and high-resolution capability, offers a promising approach for extending the PSA concept to enable comprehensive network analysis of various HF components, spanning from the low gigahertz range deep into the terahertz spectrum within a single system platform. This idea will be expanded upon and further explored in the upcoming chapters.

5 Photonic Vector Network Analyzer

Generally, spectrum analyzers, such as the PSA presented in the last chapter, are limited to measuring the amplitude or, respectively, the power spectrum of active devices. To analyze both active and passive components, the hybrid concept must be advanced, facilitating complete network analysis that also accounts for phase information. Today, modern commercial VNAs operating in the terahertz domain rely entirely on external frequency extender modules, which are inherently constrained in both maximum frequency and achievable bandwidth. To address these drawbacks, a photonic vector network analyzer extender is developed and integrated into a conventional electronic VNA system (VectorStar MS4644B, Anritsu Corporation). Like the PSA scheme, the PVNA approach involves two individual stages: one for synchronizing the laser beat signals with two optical phase-locked loops, and another for performing free-space S-parameter measurements, both utilizing the VNA as the backend architecture.

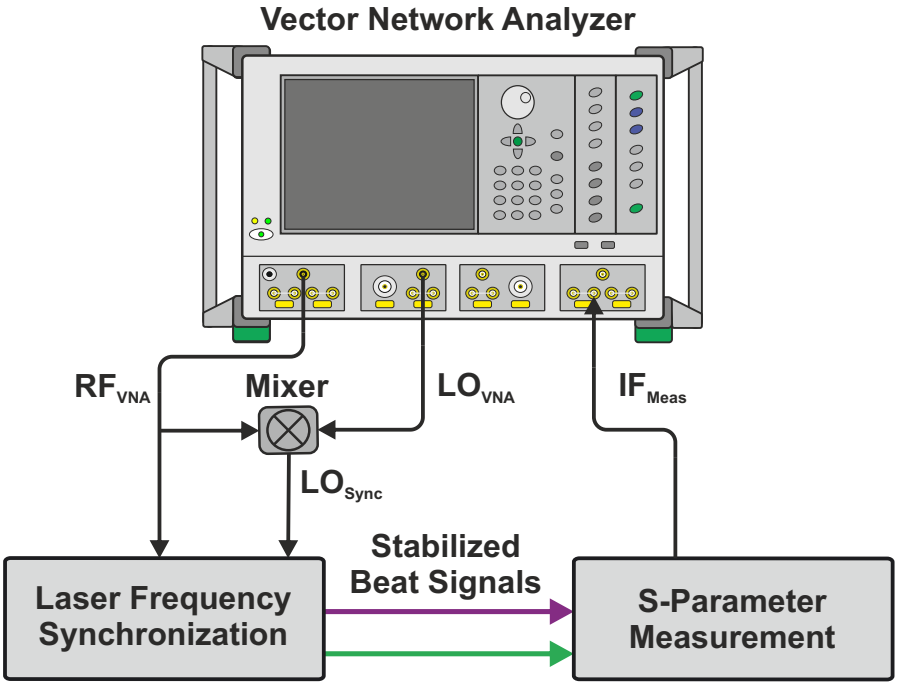

Figure 5.1: Schematic of the PVNA extender concept with its two stages: The laser pairs are synchronized with the LO_{Sync} signal derived from mixing the RF_{VNA} and LO_{VNA} outputs from the VNA. The two stabilized beat signals are directed to the S-parameter measurement setup, from which the IF_{Meas} modulation is routed to the test input port of the VNA.

A schematic representation of the PVNA extender concept is illustrated in Fig. 5.1. Similar to commercial electronic extension modules, stimulus signals from a VNA are employed for the upconversion and downconversion of the test signal. However, instead of being part of purely electronic generation and detection (see 2.4.2), the stimulus signals are applied to phase-lock the beat notes of the three lasers. To this end, both laser pairs are synchronized with the LO_{Sync} signal derived from mixing the RF_{VNA} and LO_{VNA} outputs from the VNA backend. Using a shared clock for both signal generation and demodulation ensures phase stability between the reference and test signals, effectively minimizing phase drifts that could degrade measurement accuracy. Once synchronized, the beat signals are directed to two photomixers within the S-parameter measurement section. One photomixer serves as a terahertz emitter, releasing radiation onto the DUT, while the second operates as a receiver, simultaneously downconverting the incoming terahertz wave. The heterodyne detection scheme generates an intermediate frequency IF_{Meas}, which is routed to the test input port of the VNA for S-parameter analysis.

Within this chapter, the experimental setup and operating principles of the two subsystems, along with the applied calibration procedure, are elaborated upon. Furthermore, S-parameter measurements of various terahertz filters and waveguide components using the developed PVNA extender are presented and compared with simulations as well as results from commercial electronic extension modules. To end the chapter, a performance analysis of the current PVNA status is given, followed by a concluding discussion of potential approaches for further advancements. This chapter is based on work that was published in [167].

5.1 Experimental Setup and Operation Principle

5.1.1 Laser Frequency Synchronization

Since the underlying VNA architecture is designed to exclusively receive the intended test signal frequency, it applies narrow filtering to the IF_{Meas} signal, making the preservation of high IF frequency stability crucial to the concept. Consequently, the frequency difference between the two stabilized beat signals must be highly precise and match the expected value. To achieve this, the laser frequency synchronization setup from Chapter 3 has to be adapted.

Fig. 5.2 provides a schematic overview of the modified laser synchronization setup. Except for the terahertz path, the optical part of the system is fully fiber-coupled, allowing for easy adjustment and alignment while ensuring flexibility and compact design. In OPLL#1, the beat signal between Secondary 1 and Primary, denoted as "S1+P" (green), is phase-locked to a terahertz reference, following a similar approach to the original configuration. For this purpose, various electronic terahertz sources operating between 70 GHz and 500 GHz are driven by the stimulus signal RF_{VNA} from the VNA. The emitted terahertz radiation is captured and downconverted by the photomixer to

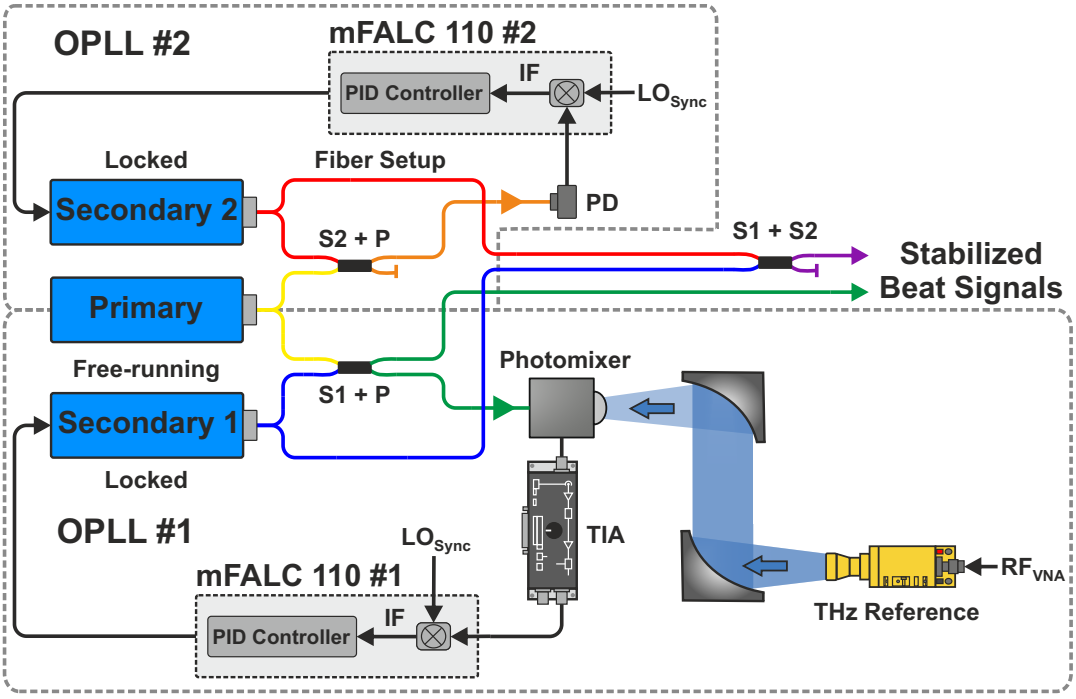

Figure 5.2: Schematic of the modified laser synchronization setup for the PVNA extender concept: The beat signals from two laser pairs are phase-locked to a terahertz reference (frequencies between 70 GHz and 500 GHz) and a megahertz reference (12.35 MHz) within two optical phase-locked loops, using a photomixer and a photodiode (PD), respectively. Beat signal frequencies: S1+P = (70 GHz to 500 GHz) + 12.35 MHz; S2+P = 12.35 MHz; S1+S2 = (70 GHz to 500 GHz) + 12.35 MHz + 12.35 MHz. The stabilized beat signals S1+P and S1+S2 are sent to the measurement section for S-parameter analysis. Fiber connections are color-coded, while BNC and SMA cables are shown in black.

serve as error signal in OPLL#1. Since the second laser synchronization between Secondary 2 and Primary, labeled "S2+P" (orange), only needs to maintain stability in the megahertz range, an amplified photodiode is sufficient for detecting the corresponding beat. The recorded difference frequency is sent to the mFALC controller in OPLL#2. In both controllers, the error signal is mixed with the $\mathrm{LO_{Sync}}$ reference at 12.35 MHz, derived from the RF and LO outputs of the VNA. Additionally, the outputs of Secondary 1 and Secondary 2 are superimposed, generating the beat note "S1+S2" (purple). Thus, the resulting beat frequencies are:

- **S1+P** = (70 GHz to 500 GHz) + 12.35 MHz
- **S2+P** = 12.35 MHz
- **S1+S2** = (70 GHz to 500 GHz) + $2 \cdot$ 12.35 MHz

By directing the stabilized beat signals S1+P and S1+S2 to the emitter and receiver in the measurement section, an intermediate frequency $\mathrm{IF_{Meas}}$ of exactly 12.35 MHz is detected, matching the expected input frequency for accurate signal processing.

5.1.2 S-Parameter Measurement Setup

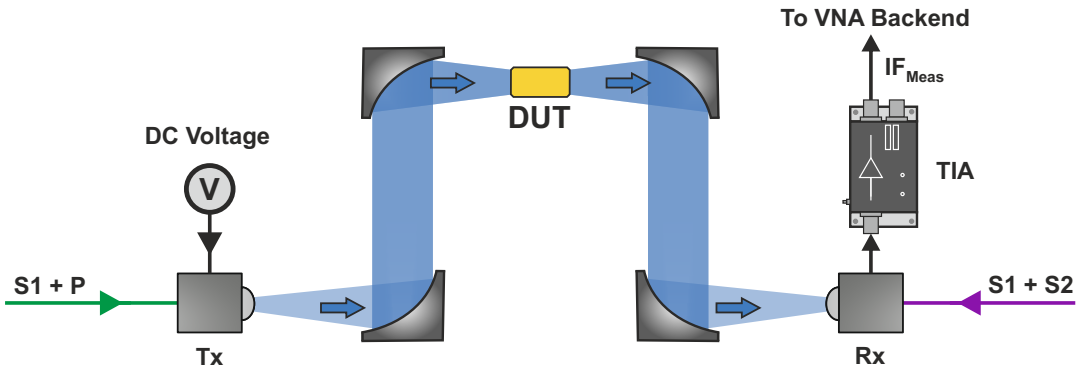

Figure 5.3: Sketch of the S-parameter measurement setup in S21 configuration: The stabilized beat signals S1+P and S1+S2 illuminate the transmitter (Tx) and receiver (Rx) photomixers. By applying a DC voltage to Tx, a terahertz wave is generated and directed towards the DUT. After propagating through the DUT, the Rx photomixer downconverts the received terahertz signal to an intermediate frequency, $\mathrm{IF}_{\mathrm{Meas}}$, which is then sent to the VNA for S-parameter analysis.

In Fig. 5.3 a sketch of the S-parameter measurement setup in the S21 configuration is depicted. The stabilized laser beat signals S1+P and S1+S2, coming from the synchronization section (see 5.1.1), are directed to the transmitting (Tx) and receiving (Rx) GaAs photomixers, respectively, inducing a periodic variation in carrier density that modulates the conductivity of the photoconductor at the corresponding beat frequency. Applying a DC voltage at Tx generates a time-dependent photocurrent, which, in combination with the antenna, leads to the emission of continuous-wave terahertz radiation at the frequency of S1+P. This terahertz wave propagates towards the device under test in a free-space setup, where it is focused onto the DUT using two off-axis parabolic mirrors. After interacting with the DUT, the terahertz beam is received by the Rx photomixer via two additional OAP mirrors. Following the coherent detection scheme outlined in Chapters 3 and 4, the captured terahertz signal is downconverted by the second synchronized laser beat oscillating at S1+S2, which results in a modulated photocurrent at the intermediate frequency

$$\mathrm{IF}_{\mathrm{Meas}} = |(\mathrm{S1} + \mathrm{P}) - (\mathrm{S1} + \mathrm{S2})| = 12.35\ \mathrm{MHz}. \tag{5.1}$$

This AC current is then directed to a transimpedance amplifier (HCA-10M-100K-C, FEMTO Messtechnik GmbH) with a bandwidth of 10 MHz and a gain of 10^5 V/A. After conversion, the voltage output of the TIA is routed to the input port of the VNA backend, where it provides the test signal for the S-parameter analysis. As the maximum IF bandwidth of the VNA is 1 kHz, beat signals with a wider linewidth will have frequency components outside the VNA's capture range, leading to loss of information. Thus, maintaining frequency stability at the hertz level is crucial for reliable and precise S-parameter measurements.

5.2 System Calibration

As extensively discussed in Section 2.4.2, every measurement with vector network analyzers is inevitably affected by errors. Consequently, it is commonly stated that an uncalibrated VNA is rarely useful for most measurement applications, whereas a properly calibrated one, employing suitable standards and calibration procedures, can achieve high accuracy and consistency [168]. Fortunately, at least time-independent systematic errors can be identified and then removed through calibration. For this purpose, commercial VNAs equipped with extender heads are typically supplied with individual calibration kits, containing a selection of calibration standards. Such kits often include standards for short, offset short, load, and thru, which are essential for reliable calibration across a wide range of frequencies. Precise alignment of the waveguide coupled structure simplifies calibration and ensures high quality, repeatable results even at terahertz frequencies. In contrast, the free-space coupling in the introduced PVNA extender concept adds more degrees of freedom in alignment, making it more challenging to achieve the same level of consistency and precision as with electronic extenders. Furthermore, finding calibration standards that are universally applicable across a wide frequency range becomes difficult, as they must also account for the specific coupling method used to connect the free-space beam to the DUT. Despite these challenges, proper system calibration remains crucial, which is why the following calibration process has been applied.

Considering that the current free-space measurement configuration grants direct access only to the transmission S21 parameter, the use of full 2-port S-parameter calibration standards is inherently limited. Accordingly, measurements with the PVNA extender are corrected using a frequency response calibration. In this procedure, which is equivalent to a normalization process, the obtained data is divided by a "Thru" measurement taken without the DUT in the setup. When characterizing 1-inch-long waveguide structures, such as band-pass filters, instead of planar DUTs, the coupling horn antennas are attached to a corresponding transmission waveguide of the same length to account for both the coupling from free space to the DUT and the additional propagation length (see Fig. 5.4). This calibration method effectively compensates for frequency-dependent system responses, such as amplitude variations and phase distortions introduced by the measurement setup, while also correcting transmission tracking errors across the respective frequency range [169].

Moreover, a discrete Fourier transform (DFT)-based digital filtering technique is applied to reduce unwanted reflections caused by various components in the setup. This approach acts similarly to a time-gating window in the time domain. A low-pass filter with a cutoff frequency of 1 GHz is selected to retain the desired low-frequency components while suppressing higher frequencies associated with noise and spurious reflections. As a result, high-frequency oscillations in the spectrum are minimized, improving clarity and enhancing measurement accuracy. However, this method primarily mitigates systematic errors related to multiple reflections and standing waves, such as Fabry-Pérot interferences and high-frequency oscillations. Yet, it does not correct for other issues such

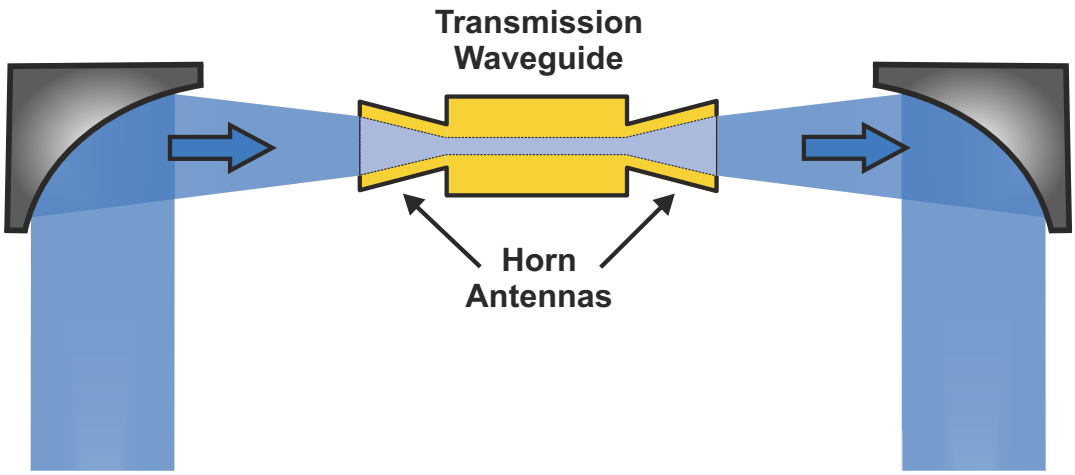

Figure 5.4: Sketch of the calibration setup for measuring waveguide structures: The Thru calibration accounts for free-space coupling, impedance mismatches of the horn antennas, and the additional propagation length within the DUT.

as directivity and reflection tracking errors, as the filtering process does not explicitly address them. Additionally, source and load matching errors remain, since impedance mismatches at the interfaces are not directly corrected but are partially compensated through the averaging effect of the calibration procedure.

To fully account for the residual systematic errors, a more comprehensive calibration like SOLT or TRL is needed. These methods require additional measurements, including S11 and S22 to address reflection errors, and S12 to correct transmission and directivity-related inaccuracies. Besides the missing S-parameters, the applicability of common calibration techniques is limited due to the free-space nature of the setup, making alternative approaches like the Thru-Thru-Network (TTN) self-calibration for broadband free-space measurements [170] more suitable for the PVNA extender concept. To accomplish this, the setup can be extended by integrating additional photomixers, along with wire grid polarizers (WGP), which function as directional couplers to effectively separate transmitted signals from reflected ones (see Section 5.4 for further details).

While systematic errors can at least partially be corrected, random and drift errors continue to affect the measurement. These error, which are often caused by environmental factors such as temperature fluctuations, mechanical vibrations, or noise in the system, cannot be fully eliminated through calibration. Even measurements using modern commercial electronic extender modules, which are directly connected by cables, can still be compromised by environmental influences. Consequently, it is anticipated that these errors will have an even greater impact on the experimental solution presented in this thesis, as the additional laser synchronization and free-space coupling make the system more susceptible to these random fluctuations. To mitigate their effects, the optical table is isolated from mechanical vibrations, and the fiber setup is shielded from ambient temperature changes.

However, small deviations, especially in the phase response, are found in the PVNA measurements despite these stabilization measures. A possible cause of this issue is phase noise in the beat notes originating from the fiber components in the setup. Since the laser beams from Secondary 1 and Secondary 2 propagate through separate fibers before being combined, even slight temperature changes or mechanical vibrations can alter the optical path length. These variations introduce phase shifts that remain uncompensated, as the affected fiber sections are located outside the feedback control of the OPLLs. To validate this assumption, a rough estimation is carried out to evaluate the extent of phase fluctuations caused by the fiber setup. Considering only thermal expansion and the thermo-optic effect in optical fibers, the expected phase shift due to small temperature variations can be approximated by

$$\Delta\phi = \frac{2\pi}{\lambda}\Delta L_{\mathrm{opt}}, \tag{5.2}$$

where λ is the optical wavelength, and ΔL_{opt} is the change in optical path length, given by [171]

$$\Delta L_{\mathrm{opt}} = L_{\mathrm{geo}}\left(n\alpha + \frac{\mathrm{d}n}{\mathrm{d}T}\right)\Delta T. \tag{5.3}$$

In equation (5.3), L_{geo} is the geometrical fiber length, n its refractive index, α the thermal expansion coefficient, $\frac{\mathrm{d}n}{\mathrm{d}T}$ the thermo-optic coefficient, and ΔT the temperature change. Substituting typical values for a standard silica fiber ($\alpha \approx 5.0 \cdot 10^{-7}\,\mathrm{K}^{-1}$ [172], $\frac{\mathrm{d}n}{\mathrm{d}T} \approx 1.2 \cdot 10^{-5}\,\mathrm{K}^{-1}$ [173], and $n \approx 1.45$ [174]), the optical path variation for the system's fiber length $L_{\mathrm{geo}} \approx 2.4\,\mathrm{m}$ can be estimated as

$$\Delta L_{\mathrm{opt}} = 3.054 \cdot 10^{-5}\,\mathrm{m/K} = 30.54\,\mu\mathrm{m/K}. \tag{5.4}$$

Inserting this optical path variation into equation (5.2) for a wavelength of $\lambda = 855$ nm, the corresponding phase shift per unit temperature change is determined as

$$\Delta\phi = \frac{2\pi}{8.55 \cdot 10^{-7}} \cdot 3.072 \cdot 10^{-5} \approx 224.4\,\mathrm{rad/K}. \tag{5.5}$$

This rough estimation of the phase shift supports the assumption that thermally caused variations in the optical fibers likely contribute to the observed phase noise. Even minor fluctuations in the range of µK can lead to significant phase shifts of several degrees, which cannot be compensated by the OPLL due to the affected fiber sections lying outside its feedback loop. Hence, to mitigate these and other instabilities, it is essential to implement stabilization methods that address environmental factors affecting the system's performance. Some potential approaches to address these issues will be discussed in Section 5.4.

In the following, the S-parameter measurements obtained using the developed PVNA extender are presented, highlighting the performance and accuracy of the system at its current experimental stage.

5.3 S-parameter Measurements

Building on the previous chapter's discussion of high-resolution photonic spectrum analyzers and their role in addressing spurious spectral components, this section delves into the characterization of crucial passive elements, particularly band-pass filters and transmission lines. Especially terahertz (band-pass) filters will play a key role in future 6G technologies, ensuring signal integrity by allowing desired frequencies to pass while effectively suppressing interference and out-of-band noise.

To evaluate spectral properties of various HF devices in the terahertz domain, S-parameter measurements are conducted with the PVNA extender concept. For this purpose, different DUTs are positioned in the free-space measurement configuration. As initial application example, the transmission parameters of free-standing metal-mesh band-pass filters (Fig. 5.5 (a)) are measured across a frequency range from 75 GHz to 520 GHz with a selected step size of 5 MHz. In the second test, the cutoff frequency of a WR-5.1 transmission line (Fig. 5.5 (b)) is analyzed within the range of 110 GHz to 140 GHz, using frequency steps of 10 MHz. The last sample characterized with the PVNA extender is a 160 GHz waveguide iris band-pass filter (Fig. 5.5 (c)). The measurement range for this filter spans from 140 GHz to 170 GHz, with a frequency step size of 10 MHz. To verify the accuracy of the developed system, the obtained results are compared with electromagnetic simulations or measurement data from commercial electronic frequency extenders.

In its current configuration, the setup provides access only to the S21 parameter of the DUTs. Since the primary interest lies in the transmission properties, this limitation does not affect the analysis. However, it is possible to expand the setup to include S11, S12, and S22 for a more comprehensive network analysis (see Section 5.4).

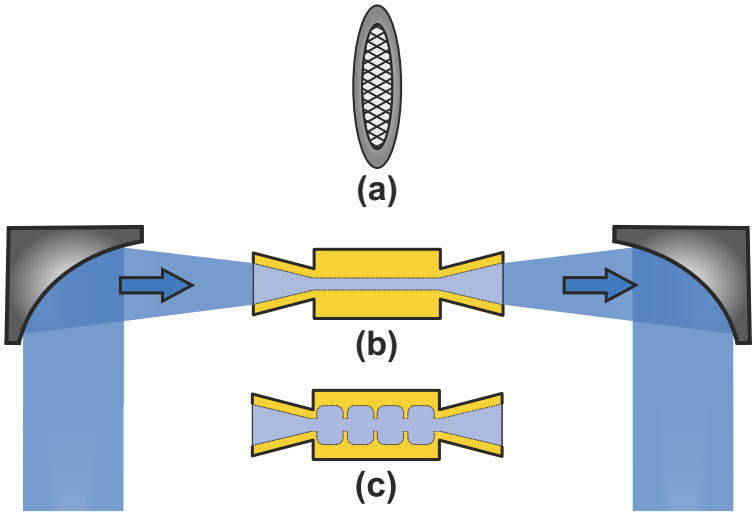

Figure 5.5: Schematic of the S21 parameter measurement configuration for: (a) free-standing metal-mesh band-pass filters, (b) waveguide-coupled transmission line, and (c) waveguide iris band-pass filter.

5.3.1 S21 Measurements of Metal-mesh Band-pass Filters

For the first experiment with the PVNA extender, free-standing metal-mesh frequency filters are designed using frequency selective surfaces (FSS) with cross-shaped unit cells, functioning as transmissive band-pass filters. The working principle of the filters is based on the collective excitation of unit cell structures, where each cross-shaped unit cell acts as a resonant element that interacts with incoming electromagnetic radiation. When the incident wave reaches the filter, it induces an oscillatory response in the electric charges within the arms of each cross-shaped unit cell. This oscillation, which can be thought of as similar to dipole oscillations, is the result of the coupling between the incident electric field and the conductive material of the unit cell. As these oscillations are excited, they lead to the radiation of electromagnetic waves, which share the same frequency as the incoming wave. However, the idea of an oscillating dipole is a simplification, as the real behavior involves plasmonic effects in the metal (e.g., Wood's anomaly[1]) and coupling between adjacent unit cells, which also affect the resonant frequency and transmission characteristics.

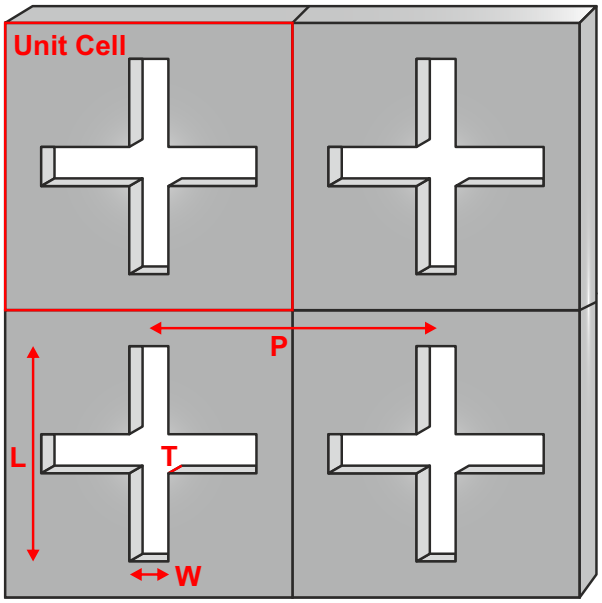

Figure 5.6: Sketch of four frequency selective surfaces (FSS) unit cells with cross-shaped apertures of the metal-mesh band-pass filter with geometric parameters L (length), W (width), P (period of the unit cells), and T (thickness).

Fig. 5.6 illustrates the cross-shaped unit cell design of the resonant metal-mesh filters. While the geometry of the unit cell defines the filter characteristic (reflective or transmissive, low-pass, high-pass, or band-pass), the periodicity influences the coupling between

[1] Wood's anomaly refers to a phenomenon where the propagation of electromagnetic waves through a periodic structure leads to dips due to the excitation of surface plasmon polaritons at certain resonant frequencies. This occurs when the wavelength of the incident wave matches a multiple of the periodicity of the structure.

adjacent unit cells, modifying the overall resonant behavior and frequency response. The spectral properties can be scaled by tuning the mesh period (P), cross-arm length (L), and width (W). Together with the material thickness (T), these parameter define the transmission performance. The resonant wavelength of the cross-shaped filter can be approximated using the empirical formula from [175]

$$\lambda_{\text{res}} = 1.8L - 1.35W + 0.2P. \tag{5.6}$$

Extending the length of the cross-arms shifts the resonance toward longer wavelengths, lowering the central frequency of the band-pass response. Enlarging the width broadens the bandwidth and slightly raises the resonant frequency. Increasing the center-to-center spacing of the crosses reduces the bandwidth by weakening the coupling between adjacent unit cells, which in turn lowers the resonant frequency. Further, a thicker metal foil will also lead to a reduction in the resonant frequency, while the symmetrical shape of the aperture makes the filter polarization independent [176].

To cover the frequency range from 75 GHz to 520 GHz, six band-pass filters are designed, each tailored to target specific segments within this broad spectrum. The fabrication process utilizes laser ablation, where a high-energy laser beam selectively removes metal through vaporization, engraving the cross-shaped unit cells into the aluminum foil. Direct removal of the metal ensures efficient and accurate fabrication without the need for photoresist coating, development, or chemical etching processes. Post-manufacturing, the geometric parameters of the crosses are measured under a light microscope (see Fig. 5.7) to determine the actual dimensions for the electromagnetic simulations. The design frequencies, along with the determined cross-sectional parameters and evaluated resonant frequencies, can be found in Table 5.1.

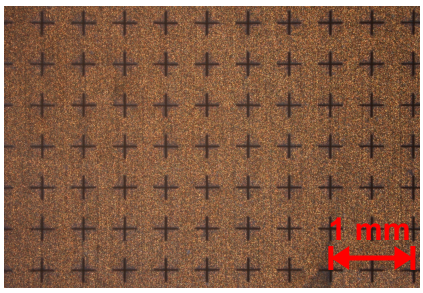

Figure 5.7: Light microscope image of the 480 GHz filter.

Table 5.1: Geometric parameters of the cross-shaped unit cells for different design and resonant frequencies.

Design Freq. / GHz	L / µm	W / µm	P / µm	Resonant Freq. / GHz
100	1472	79	2504	98.5
150	989	68	1647	148.4
200	764	57	1283	192.8
300	505	40	823	294.2
400	379	38	636	395.4
480	316	31	503	477.6

Table 5.1 demonstrates good agreement between designed and obtained resonant frequencies for all six cross-shaped filters, highlighting the precision of the laser ablation manufacturing process. As indicated in Section 5.2, a reference measurement without any filter in the setup is conducted to calibrate for system-specific parameters, such as frequency-dependent variations in the output power of the emitter and the receiver's responsivity. Each spectrum is measured by scanning at least ±25 GHz around the designed resonant frequency of each filter, using a step size of 5 MHz.

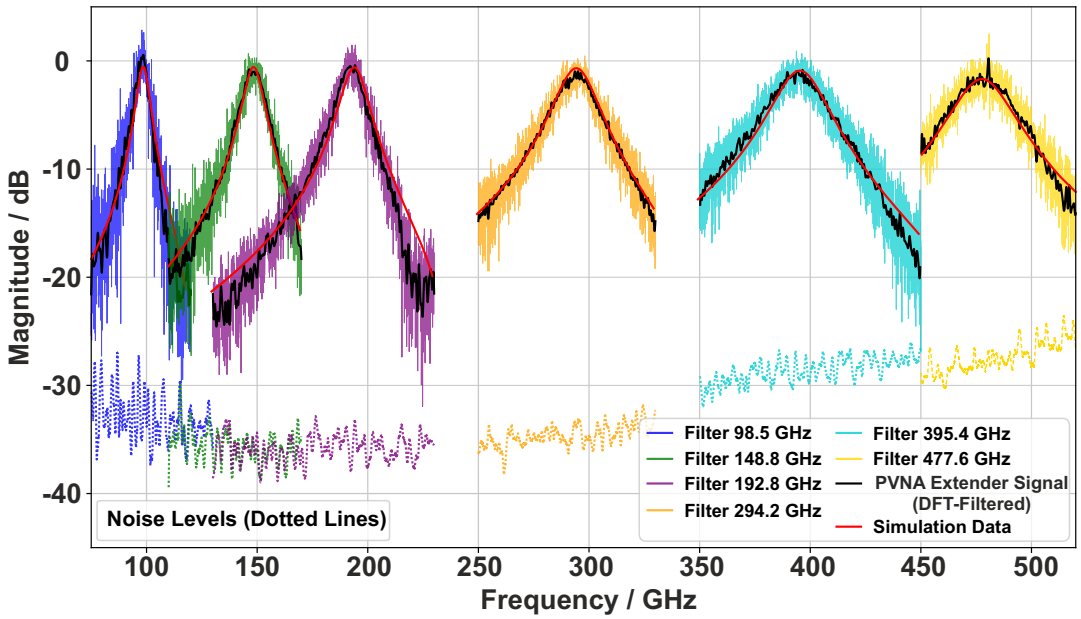

Figure 5.8: S21 measurements of cross-shaped metal-mesh band-pass filters within a frequency range of 75 GHz to 520 GHz. The spectra show strong agreement between measurement and simulation data for all analyzed filters, exhibiting minimal losses at resonance. The dotted lines beneath the spectra indicate the noise level for each frequency span.

The S21 transmission measurement results of the cross-shaped metal-mesh band-pass filters are presented in Fig. 5.8. After calibration with the Thru reference, the PVNA extender spectra (colored) are digitally filtered (black curves) to account for potential measurement errors, such as standing waves in the free-space path. The noise levels for each investigated frequency range are represented by the dotted lines beneath the measurement curves, reflecting the system's dynamic range within the corresponding frequency band. All filters exhibit the expected band-pass characteristics with minimal transmission loss at their intended resonances. For higher frequencies the bandwidth of the filters gets wider, while the maximum transmission slightly decreases. Although the stop-band rejection is not fully captured within the measurement range of each filter, the data trends suggest attenuation exceeding 20 dB for all foil filters, which is in good agreement with values reported in the literature [176, 177]. Furthermore, comparing the

obtained spectra with the simulation data[2] (red) demonstrates strong alignment between the measured and calculated results. However, small deviations from the simulated data are noticeable, especially at lower signal levels further from the resonant frequency. In this region, standing waves in the system may have a greater impact on the measured signals, potentially reducing the accuracy of the measurements.

Another noticeable aspect is the distortion in the raw signals, even after DFT filtering, and well above the respective noise levels. One possible explanation for this is fluctuations in the photocurrent of the source photomixer, which are observed during the measurements when using the optical amplifier. These fluctuations correlate strongly with the measured output power of the emitter. However, the exact cause of this signal noise remains unclear and may be linked to variations in the polarization of the beat signal introduced by the optical amplifier (see Section 6.4).

5.3.2 S21 Measurements of a WR-5.1 Transmission Line

A core function of network analyzers is to determine the electrical characteristics of HF components by directing precise stimulus signals to the DUT. Coaxial cables are commonly applied for the signal transmission, but their performance is limited by factors such as skin effect, dielectric losses, and structural design, which impact their effectiveness at very high frequencies. Standard coaxial cables typically operate reliably up to frequencies between 18 GHz and 67 GHz. Beyond this range, signal attenuation increases, and the cables may no longer maintain the integrity required for accurate measurements. For applications exceeding these frequencies, modern vector network analyzers employ waveguides or quasi-optical setups for the signal transmission, offering significantly lower attenuation and effectively guiding high-power HF signals over longer distances. To achieve good performance, transmission waveguides must be machined with high precision, as even minor deviations in geometry can cause impedance mismatches, increased insertion losses, and undesired mode conversions. Therefore, a well-characterized WR-5.1 transmission line (see Fig. 5.9) from a calibrated waveguide kit is employed as DUT to evaluate the reliability of the S21 measurements with the PVNA extender.

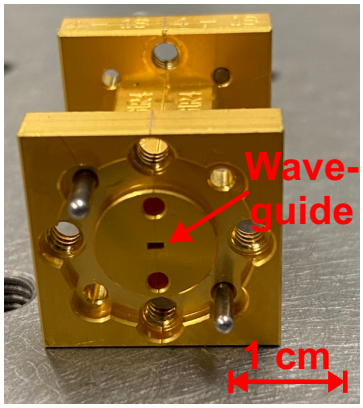

Figure 5.9: WR-5.1 transmission line.

The WR-5.1 waveguide is specifically designed for operation within the G-band frequency range, spanning from 140 GHz to 220 GHz. Generally, the transmission characteristics of the waveguide, including the cutoff frequency and the modes it supports, are primarily determined by its physical dimensions. Fig. 5.10 shows a rectangular metallic waveguide of width a and height b. Most waveguides that are used today have a

[2]Simulations were performed with CST Studio Suite [178].

width-to-height aspect ratio of 2:1. For a rectangular waveguide, the cutoff frequency for a general TE_{mn} mode is given by

$$f_{\text{cutoff}_{mn}} = \frac{c}{2}\sqrt{\left(\frac{m}{a}\right)^2 + \left(\frac{n}{b}\right)^2}, \tag{5.7}$$

where m and n are integers representing the mode numbers of the electric field along the waveguide's dimensions a and b. In general, waveguides are designed for single-mode propagation, limiting the maximum frequency to twice the cutoff frequency. For the dominant TE_{10} mode, equation (5.7) simplifies to

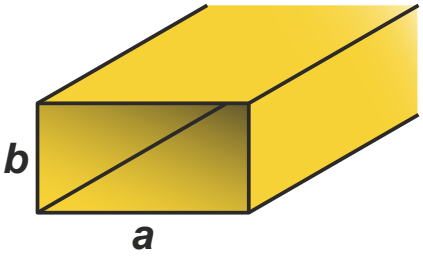

Figure 5.10: Schematic of a rectangular metallic waveguide of width a and height b.

$$f_{\text{cutoff}_{10}} = \frac{c}{2a}. \tag{5.8}$$

Therefore, the cutoff frequency of the WR-5.1 transmission line, with a width of $a = 1.295$ mm, is calculated to be 115.71 GHz. Ideally, this allows for a single-mode propagation range from approximately 115 GHz to 230 GHz. However, as the frequency approaches the cutoff, dispersion[3] and losses increase significantly, while for frequencies close to $2f_{\text{cutoff}}$, the risk of higher-order modes being excited becomes more pronounced. To avoid these problems, the operational bandwidth of a waveguide is usually reduced to [168]

$$f_{\text{min}} = 1.25\ f_{\text{cutoff}} = 144.64\ \text{GHz} \tag{5.9}$$

$$f_{\text{max}} = 1.90\ f_{\text{cutoff}} = 219.85\ \text{GHz} \tag{5.10}$$

For calibration, a WR-6 transmission line, coupled with WR-6 horn antennas, is used as the Thru reference, covering the frequency range from 110 GHz to 140 GHz. The WR-6 transmission line has a cutoff frequency of 90.79 GHz, which ensures it operates within the desired frequency range. Although there is a impedance mismatch between WR-6 and WR-5.1, the WR-6 antennas are also employed in the measurement setup as no WR-5.1 horn antennas are available.

Fig. 5.11 presents the S21 measurements of a WR-5.1 transmission line, recorded over a frequency range of 110 GHz to 140 GHz with a step size of 10 MHz. Similar to the measurements of the metal-mesh filters, the raw signal is DFT-filtered (black) to eliminate unwanted reflections in the setup. As expected, the magnitude spectrum reveals a distinct transition at the calculated cutoff frequency of 115.71 GHz. For a comparative measurement, the same WR-5.1 waveguide is tested using fully waveguide-coupled commercial electronic frequency extender modules (MA25300A Broadband mmWave Module, Anritsu Corporation) across the same frequency range (red). Overall, there is

[3]Dispersion in a waveguide occurs when the guide wavelength (wavelength of the signal within the waveguide) becomes longer than the free-space wavelength, with the difference increasing as the frequency decreases. As the frequency approaches the cutoff frequency, the guide wavelength becomes infinite, and no signal can propagate below this frequency.

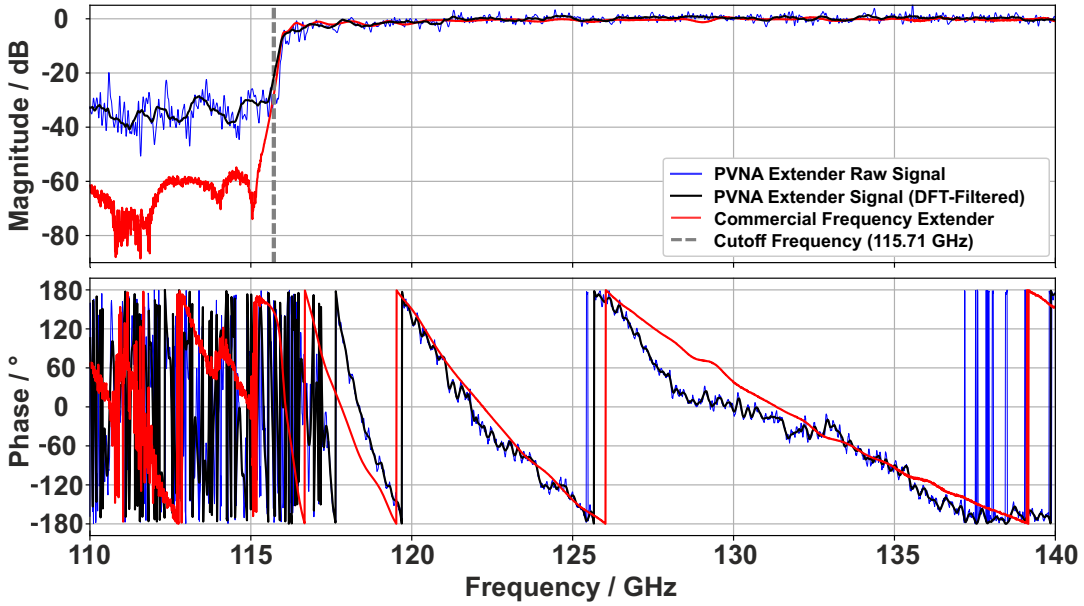

Figure 5.11: S21 measurement of a WR-5.1 transmission line from 110 GHz up to 140 GHz. The magnitude spectrum shows a sharp step at the calculated cutoff frequency of 115.71 GHz. In the phase signal, the expected longer phase delay near the cutoff frequency is observed, reflecting the influence of dispersion in the waveguide. Apart from the dynamic behavior, both the magnitude and phase spectra exhibit a strong correlation with the data obtained from commercial electronic frequency extenders.

strong agreement between the PVNA extender measurements and the S21 parameters obtained from the commercial system. However, the only notable discrepancy is the relatively low SNR of approximately 40 dB, which can be attributed to factors such as the limited terahertz output power and the free-space nature of the PVNA extender concept. A more in-depth discussion of this issue will be given in section 5.4.

The lower part of Fig. 5.11 displays the phase of the S21 signals measured with the developed PVNA extender and the commercial electronic system. Inside a rectangular waveguide, the phase delay $\Delta\Phi$ induced by the transmission line is determined by the propagation constant β. The propagation constant describes how the phase of the electromagnetic wave progresses along the waveguide and is given by

$$\beta = \sqrt{k^2 - \left(\frac{m\pi}{a}\right)^2 - \left(\frac{n\pi}{b}\right)^2}, \tag{5.11}$$

where $k = \frac{2\pi f}{c}$ is the wavenumber in the medium. The phase delay $\Delta\phi$ through a waveguide with a length L is expressed as

$$\Delta\phi = \beta \cdot L. \tag{5.12}$$

At frequencies approaching the cutoff frequency, the propagation constant converges to zero. This results in a significantly increased phase delay, as the wave travels more

slowly through its phase progression. The effect is a direct consequence of the increased dispersion and the waveguide's inability to efficiently support the propagating mode near the cutoff. When β reaches zero, the wave transitions into an evanescent mode, where instead of propagating, the wave decays exponentially along the waveguide.

The phase spectrum clearly shows the anticipated longer phase delay at frequencies near the cutoff, showing good alignment with the extender data. However, some deviations are observed, especially just above the cutoff frequency, where the signal is highly sensitive to reflections and mode conversion. One possible explanation is that WR-6 antennas are utilized in the current experimental setup to couple the free-space signal into the WR-5.1 waveguide. The impedance mismatch between the WR-6 and WR-5.1 waveguides likely causes considerable reflections at the interface, resulting in signal distortion. This mismatch introduces standing waves and phase shifts that do not appear in the calibration measurements, where a WR-6 waveguide served as the Thru reference. Moreover, the phase signal remains noticeably noisy compared to the extender response, even after filtering. This is likely due to phase fluctuations introduced by the fiber components of the setup, as previously discussed in Section 5.2.

5.3.3 S21 Measurement of a Waveguide Iris Band-pass Filter

The last sample characterized with the PVNA extender concept is a waveguide iris band-pass filter (see Fig. 5.12) with a designated center frequency of 158.5 GHz. Designed for operation within the WR-5.1 waveguide range, the filter exhibits a passband spanning from 152 GHz to 165 GHz.

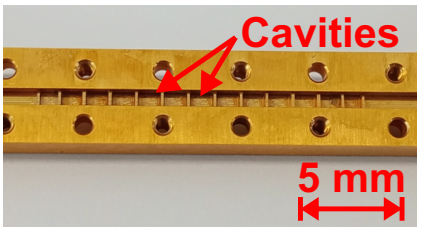

Figure 5.12: Side view of a waveguide iris band-pass filter with a center frequency of 158.5 GHz (only one symmetrical half shown).

Fig. 5.13 illustrates a schematic top view of a rectangular waveguide iris band-pass filter. It consists of multiple coupled cavities formed by inserting a series of iris elements inside the waveguide. The number of cavities directly affects the filter order, which in turn determines the steepness of the transition between the passband and stopbands. A higher-order filter, achieved by increasing the number of cavities, results in a sharper roll-off and better out-of-band rejection. However, this comes at the expense of increased complexity and potential challenges with fabrication tolerances. In this design, each cavity acts as a resonant structure, while the coupling between them is defined by the size and positioning of the iris apertures [179]. These irises create a reactive coupling, which controls the energy transfer between adjacent cavities. By adjusting the iris dimensions and their placement along the waveguide, the center frequency, bandwidth, and overall selectivity can be finely tuned.

The upper cutoff frequency of the filter can be approximately estimated by calculating the resonant frequency of the largest cavity, typically located in the middle of the filter.

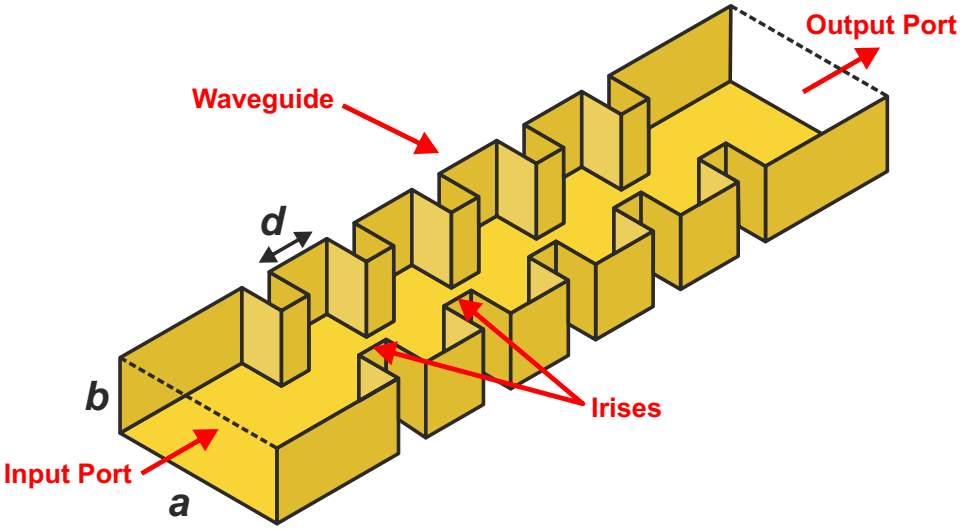

Figure 5.13: Schematic (top view) of a rectangular waveguide iris band-pass filter with waveguide dimensions a and b and a cavity length d. The top surface is removed to show the internal structure.

A simplified estimation for the resonant frequency of a cavity is given by

$$f_{mnl} = \frac{\mathrm{c}}{2\pi}\sqrt{\left(\frac{m\pi}{a}\right)^2 + \left(\frac{n\pi}{b}\right)^2 + \left(\frac{l\pi}{d}\right)^2}, \tag{5.13}$$

where a and b are the waveguide aperture dimensions, and d is the cavity length. The variables m, n, and l represent the mode numbers in the x-,y-, and z-directions of the waveguide, respectively. For the dominant TE_{101} mode with WR-5.1 dimensions $a = 1.295$ mm and cavity length $d \approx 1.275$ mm, the resonant frequency f_{101} is about 165.10 GHz. Because the cavities are not completely closed but formed with the open irises, the center frequency of the filter will be lower than the resonant frequency of the largest cavity. While the center frequency is determined by the physical dimensions of the resonators, the fractional bandwidth (FBW) — the ratio of the filter's bandwidth to the center frequency — is controlled by the coupling strength between resonators and their Q-factors.

The passband, typically defined between the -3 dB points where signal power drops to half, represents the frequency range the filter allows to pass with minimal attenuation. The FBW quantifies how wide or narrow this passband is relative to the center frequency f_0 and is specified as

$$\mathrm{FBW} = \frac{\Delta f}{f_0} = \frac{f_2 - f_1}{f_0}, \tag{5.14}$$

where f_1 and f_2 denote the lower and upper -3 dB cutoff frequencies of the passband, respectively. The quality factor Q provides an alternative characterization of the filter's selectivity and is related to the FBW by

$$Q = \frac{f_0}{\Delta f} = \frac{1}{\mathrm{FBW}}. \tag{5.15}$$

A higher Q value indicates a narrower passband and higher selectivity, while a lower Q corresponds to a broader bandwidth with reduced frequency discrimination.

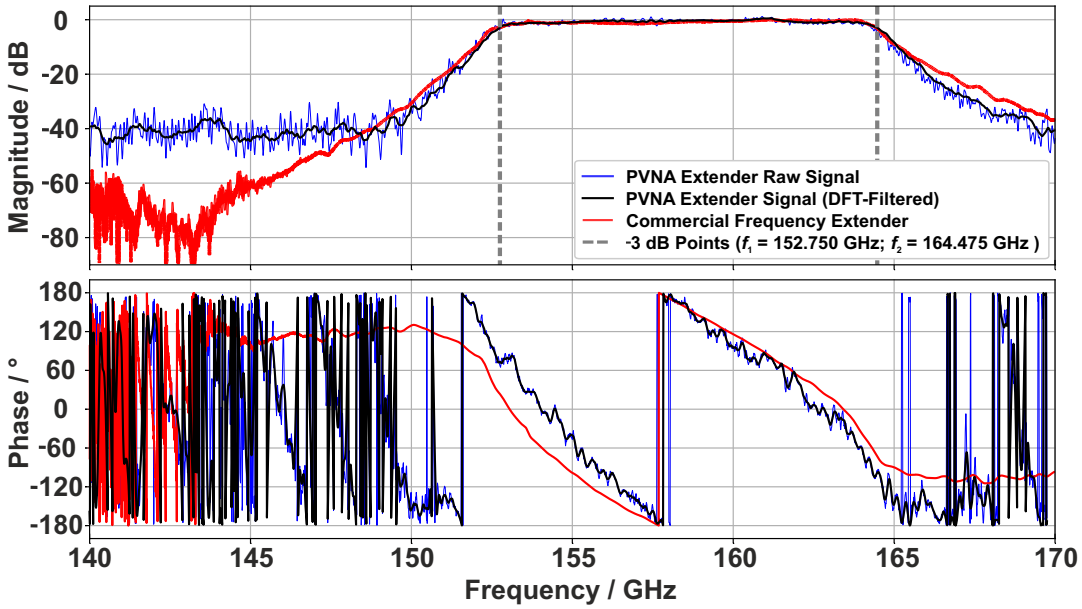

Figure 5.14: S21 measurement of a waveguide iris band-pass filter from 140 GHz up to 170 GHz. The band-pass shows a center frequency of 158.615 GHz with a passband width of 11.725 GHz. In both spectra, the measured PVNA extender data corresponds reasonably well with the commercial extender data.

In Fig. 5.14, the S21 measurement of a waveguide iris band-pass filter is displayed, covering frequencies from 140 GHz to 170 GHz in 10 MHz increments. For calibration, the WR-5.1 transmission line with WR-6 horn antennas is used, and the same post-processing technique as before is applied to the raw signal. The upper graph shows the recorded magnitude data, with a center frequency of 158.615 GHz and a passband width of 11.725 GHz. This corresponds to a FBW of 7.39% and a Q-factor of approximately 13.5. Within the passband, the response remains essentially flat, exhibiting almost no ripples, which indicates well-matched impedance and minimal reflection effects. Additionally, the insertion loss remains low, measuring less than 1 dB, suggesting efficient power transmission through the filter with minimal attenuation. Across the magnitude spectrum, the data closely match the comparison measurements obtained using the waveguide-coupled commercial extender module (WR5.1-VNAX, Virginia Diodes Inc.). Nevertheless, some deviations are noted near the edges of the band-pass filter range. The sharper roll-off observed in the PVNA extender data during the transitions from the passband to the stopbands could be due to impedance mismatch and diffraction effects inherent in the free-space environment. Further, the relatively low SNR of just 40 dB, compared to the dynamic range of more than 60 dB achieved by the electronic

extenders, is also evident in this measurement. In the phase spectrum (lower graph), the measured phase delay corresponds well with the electronic extender response, although some deviations are noticeable, especially near the edges of the band-pass. Furthermore, the PVNA extender signal is again found to be markedly noisier than the reference signal, even after filtering.

5.4 Performance Analysis and Future Advancements

Despite minor deviations from the commercial electronic extender, the S-parameter measurements confirm that the developed PVNA extender reliably characterizes key parameters of HF components operating in the terahertz range. However, at this stage, the presented PVNA concept still has limitations in sensitivity, measurement accuracy, and acquisition speed when compared to state-of-the-art, fully electronic frequency-extension VNA architectures.

In particular, the relatively low SNR of only 40 dB at present is a crucial factor for future system enhancements. Nowadays, electronic extender modules can achieve dynamic ranges of up to 120 dB for frequencies up to 220 GHz, though this rapidly decreases to around 60 dB at 1.5 THz [36]. In the developed PVNA extender system, the dynamic range is mainly limited by the terahertz output power of the 850 nm GaAs photomixers used for both generating and detecting the terahertz signals. During a power measurement of the source photomixer, a relatively low output power of approximately 16 nW at 100 GHz and 38 nW at 500 GHz is observed. Today, state-of-the-art CW photomixers, especially PIN diode emitters operating at the 1550 nm telecom wavelength, can achieve output power levels of several hundred µW at frequencies up to 300 GHz, and still deliver tens of µW at 1 THz [180]. Switching to this technology is expected to increase the system's measurement dynamic range to around 87 dB, comparable to that of commercial electronic extender modules in this frequency range.

Regarding accuracy, some instabilities, primarily in the phase measurements, are noticed and attributed to minor temperature drifts and vibrations in the fibers outside the OPLLs. To significantly reduce these fluctuations, either active or passive phase stabilization methods can be employed. Active stabilization techniques, such as piezoelectric fiber stretchers, adjust the fiber length in real-time to counteract environmental changes. Another approach is electronic feedback stabilization, where real-time phase data is used to correct deviations. Passive techniques minimize external influences through thermal and mechanical shielding. Additionally, reducing the fiber length outside the OPLLs is crucial, as longer fibers are more prone to environmental fluctuations. These measures help isolate the system, maintaining phase stability and improving measurement reliability.

Another crucial aspect for practical applications is measurement speed. In general, the acquisition time is determined by the scanned bandwidth and the chosen frequency step resolution. At present, the acquisition speed is approximately 200 ms per data

point, primarily constrained by various subsystems within the setup. For instance, a full sweep across a 30 GHz bandwidth with a 10 MHz step size takes approximately 10 minutes, which is considerably slower than conventional extender modules. As previously discussed, the PWM module enables the fine voltage adjustments required for precise temperature control, compensating for the DAC's limited resolution and introducing a 130 ms delay in laser synchronization. Additional sources of delay include spectrum acquisition and analysis within the OPLLs, which are crucial for precise phase-locking but contribute to the overall system latency. Faster measurement times could, therefore, be attained by using more advanced hardware components and parallelizing various program steps.

As shown in Chapters 3 and 4, the phase-locked laser beat signals exhibit linewidths in the range of a few hertz. Consequently, the developed PVNA extender is expected to achieve a similar resolution, approaching that of purely electronic systems. However, since a resolution in the megahertz range is more than sufficient to investigate the key features of the metal-mesh filters and waveguide components, a resolution on the hertz level is not chosen, as it would significantly increase the acquisition time without providing additional information.

At the current state, the system is capable to perform free-space S21 parameter measurements over a frequency range from 70 GHz to 520 GHz. However, future plans aim to extend the design to a fully functional two-port PVNA extender, enabling the measurement of S11, S12, and S22. To achieve this, additional photomixers and optical components for transmission and reflection signal separation need to be incorporated into the current PVNA extender setup.

Fig. 5.15 outlines a possible implementation of the two-port PVNA extender concept. In order to measure all S-parameters simultaneously, the beat signals S1+P and S1+S2 must be split to drive the two additional photomixers Tx2 and Rx2. Moreover, two wire grid polarizers (WGPs) are integrated on either side of the DUT to function as frequency-independent directional couplers. To isolate the transmitted from the received signals, the WGPs manipulate the polarization state of the terahertz radiation by reflecting or transmitting different components of the incident wave based on its polarization. For this purpose, WGP1 and WGP4 are oriented at 45° (projected on the optical axis) and aligned under 45° to the optical axis to turn the emitted circular polarized radiation from Tx1 and Tx2 to a diagonal state. WGP2 and WGP3, oriented vertically, transmit the vertical component of the diagonally polarized radiation while reflecting the horizontal part. To prevent any radiation reflected at WGP2 and WGP3 from reaching the receivers, both WGPs are slightly tilted relative to the optical axis. After interacting with the sample, one portion of the signals gets reflected (S11 and S22), while another part propagates through the DUT and is transmitted (S21 and S12). If the sample does not alter the polarization state, the signals pass through WGP2 and WGP3 without any change in polarization. WGP1 and WGP4 then reflect 50% of the signals at a 90° angle towards receivers Rx1 and Rx2 for detection. Due to the orientation of the wire grid polarizers, four changes in polarization occur as the terahertz radiation propagates

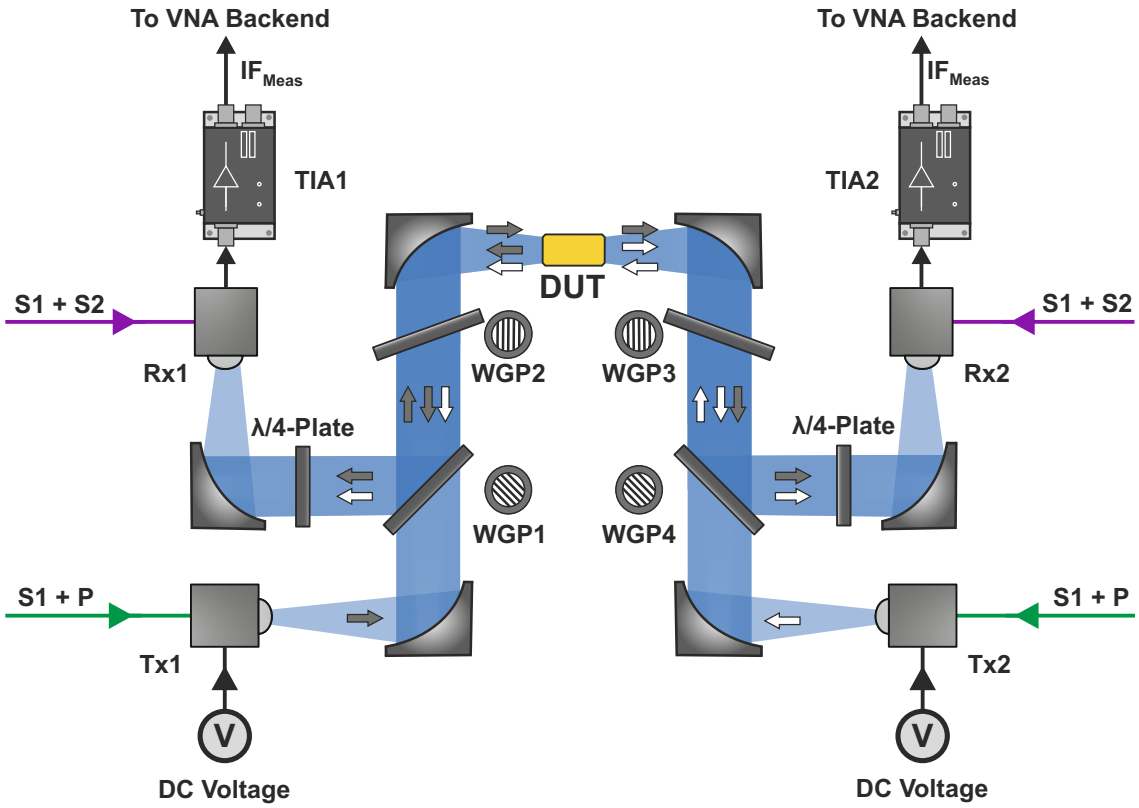

Figure 5.15: Sketch of the two-port PVNA extender configuration: The stabilized beat signals S1+P and S1+S2 illuminate the transmitters (Tx1 and Tx2) and receivers (Rx1 and Rx2), respectively. By applying a DC voltage to the transmitters, terahertz radiation is generated and directed towards the DUT. Along the optical path, four wire grid polarizers (WGP) are employed to separate the transmitted and reflected signals. After detection at the receivers, the downconverted terahertz signals are routed to the VNA for S-parameter analysis. The gray arrows represent the path of the terahertz wave emitted by Tx1, while the signal from Tx2 is indicated by the white arrows.

through the system, each corresponding to a loss of 3 dB. These changes accumulate to an overall loss of around 12 dB for each S-parameter. To prevent an additional 3 dB loss, a quarter-wave plate is positioned before the receivers to transform the linearly polarized light back into circular polarization.

As Rx1 and Rx2 receive signals from both Tx1 and Tx2 — one reflected from the DUT and the other transmitted through the DUT — it is crucial to ensure that only one emitter is active at a time. This can be achieved by using a time-division approach where each emitter is switched on sequentially, allowing the PVNA system to distinguish between the different signal paths. This method is commonly used in commercial VNAs with frequency extenders, where the same principle is applied to verify that the transmitted and reflected signals are clearly separated (see Section 2.4.2). In the final step, two TIAs connected to the receivers convert the detected photocurrent into a voltage signal before it is read out by the VNA backend.

Besides the capability to provide a full network analysis of all S-parameters, measurement range is a key parameter to improve in future system designs. Currently, the highest frequency measured with the PVNA extender concept is 520 GHz, providing a total bandwidth of 450 GHz for the extension. With only three DFB lasers available, the second laser pair is required to generate the expected IF frequency for the VNA backend. As a result, the frequency extension described in Section 3.4 is not feasible with the current setup. However, by cascading additional laser pairs, the maximum frequency and bandwidth can, in principle, be easily extended to 1 THz or even beyond.

In conclusion, the developed PVNA extender system offers a promising alternative to conventional electronic frequency extenders, particularly for bridging the transition into the terahertz domain. By utilizing photonic mixing techniques, the system achieves high spectral purity and narrow linewidths, matching the performance of state-of-the-art electronic solutions. While electronic approaches may remain superior in dynamic range at lower frequencies, a key advantage of the PVNA extender is its ability to seamlessly span the entire frequency spectrum from the low gigahertz range to several terahertz. Covering a frequency range up to 1.5 THz with conventional electronic extenders typically requires at least eight to nine different Tx and Rx modules [36], each costing between approximately 70,000 and 400,000 USD per pair depending on the band. Altogether, this means a total investment of roughly 1.5 to 1.8 million USD for a fully equipped system spanning 75 GHz to 1.5 THz, excluding additional costs for local oscillators, waveguide adapters, and calibration kits. In contrast, the PVNA extender's photonic approach enables continuous frequency coverage with a single system platform, drastically reducing hardware complexity and cost. A complete PVNA extender setup covering this range can be realized for roughly 100,000 to 200,000 USD, providing a cost-effective solution with competitive measurement performance and spectral quality. Moreover, the scalability of the PVNA extender concept allows for straightforward frequency expansion by incorporating additional laser sources, enabling operation well beyond 1.5 THz — the current upper limit for electronic extension modules. Altogether, the presented PVNA extender design holds significant potential to become a valuable and cost-effective solution for full two-port vector network analysis, extending deep into the terahertz frequency range with a single system platform.

As an additional option to further extend the bandwidth of the existing system without the need for additional laser pairs, the next chapter explores the concept of four-wave mixing in an optical amplifier. This approach presents an innovative method for broadening the frequency range while maintaining a simplified system architecture. The following discourse will delve into how FWM can be incorporated into the current setup, along with initial steps toward its implementation.

6 Four-Wave Mixing

Four-wave mixing is a nonlinear optical process that occurs when three electromagnetic fields interact in a dielectric material, generating a fourth field through the mixing of the input waves (Fig. 6.1 (a)). Physically, this mechanism can be understood by considering the individual interactions of the fields within a dielectric medium. The first input wave induces an oscillating polarization in the dielectric, which re-radiates with a phase shift determined by dipole damping — this corresponds to Rayleigh scattering in linear optics. A second field similarly drives the polarization, and the interference between the two waves generates harmonics at both the sum and difference frequencies. Introducing a third field further excites the polarization, producing additional beat frequencies involving both the input fields and the newly generated sum and difference components. This beating with the sum and difference frequencies gives rise to the fourth field in FWM. As each beat frequency can serve as a new source field, a complex network of interactions and generated waves emerges from this fundamental nonlinear process.

Over the course of this chapter, the fundamental principles of four-wave mixing will first be outlined, followed by a examination of the special case of degenerate FWM, which serves as the underlying mechanism in the concept presented here. Next, the operating principle of a tapered amplifier will be briefly explained with a focus on its role in facilitating the FWM process, before introducing the experimental setup. The chapter concludes with first experimental results, accompanied by a discussion of encountered challenges and intended future actions. It is important to note that the explanations provided in this chapter offer only a general overview of the essential physical mechanisms. For a more comprehensive understanding of the detailed theoretical foundations and advanced models, the reader is referred to [181].

6.1 Fundamental Process

Mathematically, the nonlinear response of an optical material is modeled by expanding the induced polarization as a power series in the electric field strength

$$P(t) = \epsilon_0(\chi^{(1)}E(t) + \chi^{(2)}E^2(t) + \chi^{(3)}E^3(t) + ...). \tag{6.1}$$

In this context, ϵ_0 represents the vacuum permittivity, while the expansion coefficients $\chi^{(i)}$ are referred to as susceptibilities, which include the material's relative permittivity ϵ_r. This approach assumes that higher-order susceptibilities become progressively smaller, allowing the power series expansion to converge to a finite polarization.

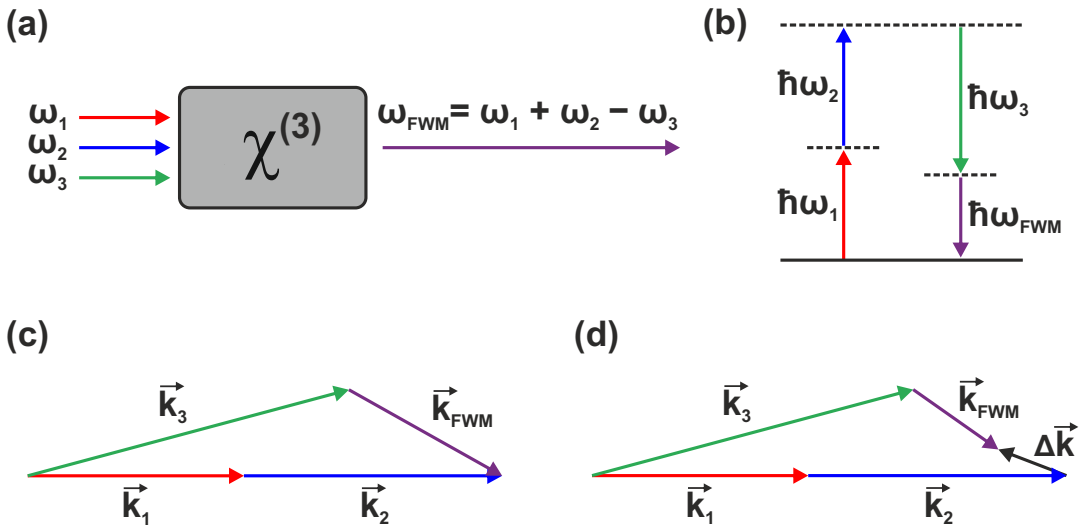

Figure 6.1: Illustration of the four-wave mixing process: (a) Incident and generated frequency components (b) Energy level diagram (c) Perfectly phase matched case (d) Wave vector mismatch of $\Delta\vec{k}$.

At low energy levels, typical of everyday conditions, the relationship between the electromagnetic polarization and the magnitude of the electromagnetic field is linear. In this regime, the material's response is proportional to the electric field, and only the first term in equation (6.1) contributes. As the intensity increases, the contributions from $\chi^{(2)}$ and $\chi^{(3)}$ become more significant, giving rise to various nonlinear optical effects, including second- and third-harmonic generation, sum- and difference-frequency generation, as well as four-wave mixing. However, the focus of the following discussion will be on the third-order nonlinear susceptibility, $\chi^{(3)}$, as it is directly responsible for the occurrence of FWM.

$$P^{(3)}(t) = \epsilon_0 \chi^{(3)} E^3(t) \tag{6.2}$$

To describe the FWM process, we consider three input electric fields at frequencies ω_1, ω_2, and ω_3:

$$E(t) = E_1 e^{-i\omega_1 t} + E_2 e^{-i\omega_2 t} + E_3 e^{-i\omega_3 t} + c.c. \tag{6.3}$$

Substituting this in equation (6.2) and expanding the cubic expression yields multiple combinations of frequency mixing products[1]. Among the many generated terms, those responsible for FWM processes take the form

$$P^{(3)}_{\mathrm{FWM}}(t) \propto \epsilon_0 \chi^{(3)} E_i E_j E_k^* e^{-i(\omega_i + \omega_j - \omega_k)t}. \tag{6.4}$$

Here, the indices i, j, k run over the different input fields. Each of these terms represents a frequency component at

$$\omega_{\mathrm{FWM}} = \omega_i + \omega_j - \omega_k. \tag{6.5}$$

[1]In total, the expansion contains 216 terms, but "only" 44 distinct frequency components arise when positive and negative frequencies are considered separately.

This frequency relation directly reflects energy conservation in the nonlinear interaction, where the sum of input photon energies equals the energy of the generated photon (see also Fig. 6.1 (b)). In other words, two photons at frequencies ω_i and ω_j are effectively annihilated, while one photon at ω_k is stimulated, resulting in the generation of a new photon at ω_{FWM}.

For efficient coupling between the four waves, however, not only energy but also momentum must be conserved [182]. This condition, commonly referred to as "phase matching", requires that the wave vectors of the interacting waves satisfy

$$\vec{k}_{\mathrm{FWM}} = \vec{k}_i + \vec{k}_j - \vec{k}_k, \tag{6.6}$$

where $\vec{k}_i$, $\vec{k}_j$, and $\vec{k}_k$ are the wave vectors of the input fields, and $\vec{k}_{\mathrm{FWM}}$ is the wave vector of the generated FWM signal (Fig. 6.1 (c)). Only when this condition is met does the nonlinear polarization efficiently drive the FWM signal along the propagation direction. If phase matching is not perfectly satisfied ($\Delta\vec{k} = \vec{k}_i + \vec{k}_j - \vec{k}_k - \vec{k}_{\mathrm{FWM}} \neq 0$), misalignment of the wave vectors (Fig. 6.1 (d)) leads to destructive interference and reduced energy transfer. Consequently, four-wave mixing is effectively suppressed in media with strong phase mismatch. Another equivalent way of understanding conditions (6.5) and (6.6) is by recognizing that, since the energy transfer is a coherent process, all four waves must maintain a constant phase relationship to prevent the cancellation of the FWM frequency component.

6.1.1 Degenerate Four-wave Mixing

With the fundamental theory of four-wave mixing established, this section centers on the special case of degenerate four-wave mixing (DFWM), the core mechanism driving the subsequent experimental investigation. In DFWM, two of the four participating waves are identical, leading to the generation of new frequency components, commonly referred to as idler waves.

Assuming two copropagating input waves with frequencies ω_1 and ω_2 ($\omega_2 > \omega_1$), the nonlinear interaction between these waves results in the generation of the two idler frequencies

$$\omega_{\mathrm{idler1}} = \omega_1 + \omega_1 - \omega_2 = 2\omega_1 - \omega_2 \tag{6.7}$$

and

$$\omega_{\mathrm{idler2}} = \omega_2 + \omega_2 - \omega_1 = 2\omega_2 - \omega_1. \tag{6.8}$$

The generated idler frequencies, ω_{idler1} and ω_{idler2}, are symmetric with respect to the pump frequencies ω_1 and ω_2 (see Fig. 6.2). This symmetry results in the two idler peaks being spaced by $3\Delta\omega$ from each other, where $\Delta\omega = \omega_2 - \omega_1$.

However, as discussed in the previous section, the efficiency of the four-wave mixing process, and hence the strength of the generated idler waves, depends significantly on phase matching. To maximize output power, the individual phase mismatches

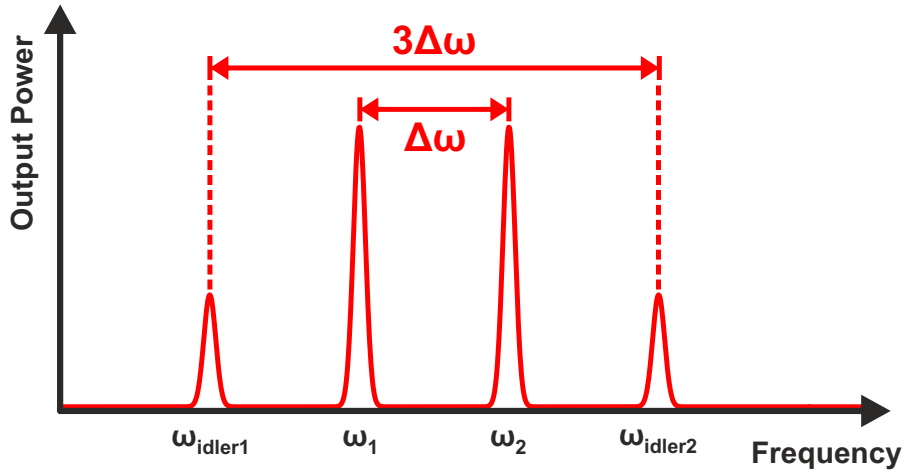

Figure 6.2: Degenerate four-wave mixing spectrum: The two pump frequencies ω_1 and ω_2, with a frequency difference of $\Delta\omega = \omega_2 - \omega_1$, interact to generate two idler frequencies, $\omega_{\text{idler1}} = 2\omega_1 - \omega_2$ and $\omega_{\text{idler2}} = 2\omega_2 - \omega_1$. The idler frequencies are symmetrically spaced around the pump frequencies, with a spectral separation of $3\Delta\omega$ between the idler peaks.

for each generated idler should be minimized. In particular, the DFWM processes $\Delta\vec{k}_1 = 2\vec{k}_1 - \vec{k}_2 - \vec{k}_{\text{idler1}}$ and $\Delta\vec{k}_2 = 2\vec{k}_2 - \vec{k}_1 - \vec{k}_{\text{idler2}}$ should both satisfy phase matching as closely as possible. As the phase matching condition is primarily influenced by chromatic dispersion, which describes the dependence of the refractive index on frequency, the efficiency of FWM can be greatly affected by the material's dispersion profile. In DFWM, the idler and pump frequencies are spectrally close, allowing the interacting waves to more easily satisfy the phase-matching condition due to their small frequency difference. Nevertheless, in addition to chromatic dispersion, nonlinear phase shifts induced by the high optical intensities involved in FWM can also significantly influence phase matching. Specifically, the Kerr effect[2], which arises from the intensity-dependent refractive index, introduces additional phase shifts that must be considered in phase-matching calculations. Consequently, the phase-matching condition is not only determined by the frequencies of the interacting waves but also by the intensities of the optical fields.

To satisfy the phase-matching condition, various methods can be applied depending on the specific application. These include tailoring the dispersion properties of the medium, adjusting the propagation angles of the interacting beams, or tuning the temperature to modify the refractive index. Moreover, the nonlinear phase shifts induced by high optical intensities can be exploited to compensate for residual phase mismatch and improve the efficiency of the process. Alternatively, quasi-phase matching can be achieved by periodically modulating the nonlinear coefficient of the medium to compensate for phase mismatch, as realized, for example, in periodically poled crystals.

[2]The Kerr effect refers to the intensity-dependent change in the refractive index of a material, where the refractive index increases with the applied optical intensity ($n(I) = n_0 + n_2 I$), leading to nonlinear optical effects such as self-phase modulation and cross-phase modulation.

6.2 Tapered Amplifiers

Since high optical intensities are essential for efficient FWM, optical amplifiers provide a promising approach for generating the necessary power to produce strong mixing frequencies. Semiconductor optical amplifiers are particularly well-suited for this task, as they combine high gain with strong intrinsic nonlinearities in a compact, electrically pumped design. Tapered amplifiers, as a specialized form of SOAs, further enhance this potential by enabling higher output powers (gain of up to 20 dB) while preserving high beam quality (M^2 factor below 2), even at peak power levels [183].

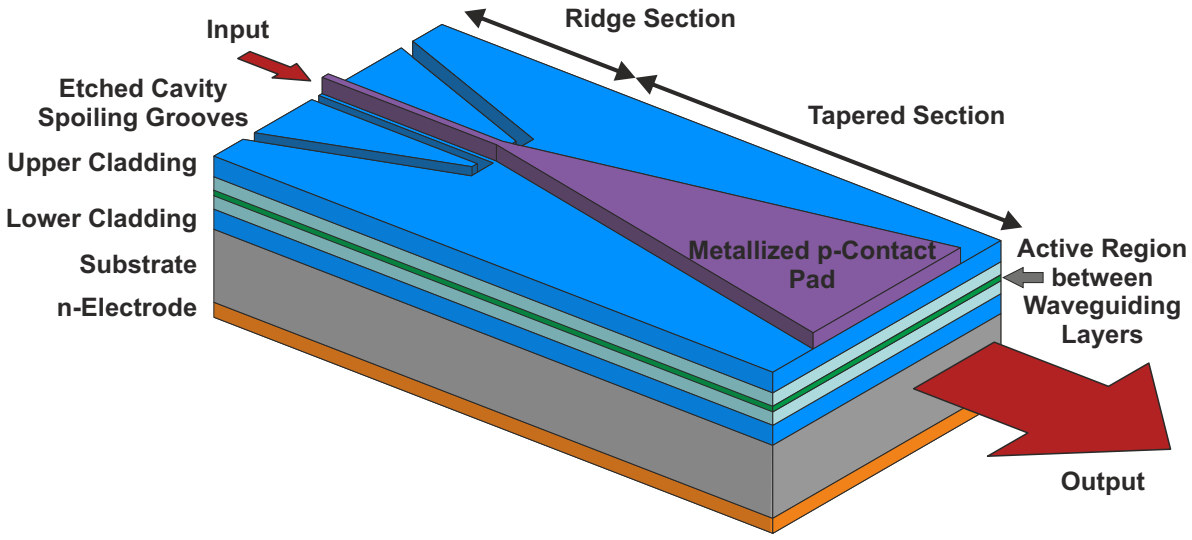

Figure 6.3: Cross-sectional view of a tapered amplifier (TA) diode. Layer sequence from bottom to top: n-electrode (orange), substrate (gray), cladding (blue), waveguiding layers (turquoise), active region (green), and metallized p-contact pad (violet). The TA features a narrow ridge section for seed light coupling, followed by a tapered section that increases the mode area for power amplification. Cavity spoiling grooves are etched next to the ridge to prevent parasitic reflections and unintended lasing. Both facets are AR-coated to minimize feedback and ensure stable single-pass amplification.

Fig. 6.3 shows the cross-sectional view of a TA diode. The TA features a narrow ridge waveguide section at the input, designed for single-mode propagation to efficiently couple the seed light from the laser source and minimize beam divergence. Subsequently, the light enters the tapered section, where the waveguide gradually widens (up to several hundreds of micrometers) towards the rear facet, while the height remains equal to that of the ridge section. This gradual tapering of the waveguide increases the mode area, facilitating the amplification of the laser light without degrading the beam quality. Further, the significantly larger output facet allows for much higher laser powers, eliminating the risk of catastrophic optical damage (COD). The whole taper region is covered by a metallized p-electrode that supplies an electric current, typically a few amperes, which excites the active region (made of GaAs or InP). Similar to a diode laser, stimulated emission within the active layer amplifies the injected seed light as it

propagates through the structure. In most cases, the input waveguide is also pumped to minimize losses at the beginning. Additionally, cavity spoiling grooves are etched next to the ridge waveguide section to suppress parasitic reflections. These grooves also help prevent the formation of a stable optical cavity, ensuring that the TA operates as an amplifier rather than as a laser. Both facets have an anti-reflection (AR) coating to minimize reflection losses and maintain stable single-pass amplification.

TAs are commonly employed in master oscillator power amplifier (MOPA) systems, with DFB laser diodes or ECDLs serving as wavelength-adjustable seed lasers. Even with AR coating, fully eliminating reflections at the input remains challenging, making it necessary to place a Faraday isolator between the seed laser and the amplifier. Moreover, collimation and focusing optics are required both before and after the isolator. To further reduce the risk of feedback in high-gain amplifiers, a second Faraday isolator may be needed at the output. Due to their wide spectral gain profile, TAs can operate over a broad range of wavelengths, making them suitable for wavelength-tunable applications. In addition to amplification, TAs are commonly employed in frequency conversion setups to generate new wavelengths, where they enhance the power of tunable seed lasers, facilitating efficient harmonic generation and other nonlinear optical processes.

6.2.1 DFWM in Tapered Amplifiers

One such effect is DFWM, which is of particular relevance to this thesis. As discussed in the prior section DFWM occurs when two input photons at frequencies ω_1 and ω_2 ($\omega_2 > \omega_1$) interact within a nonlinear medium, resulting in the generation of the two conjugate frequencies[3] $\omega_{\text{conj1}} = 2\omega_1 - \omega_2$ and $\omega_{\text{conj2}} = 2\omega_2 - \omega_1$.

In the context of a TA, the process begins when the pump photons are injected into the active region of the amplifier. Due to the nonlinear properties of the material, the beating between these photons modulates the carrier density and carrier distribution in the active medium, thereby creating dynamic refractive index and gain gratings. These gratings, in turn, interact with the injected waves, generating new frequency components, the DFWM signals, which can be observed in the output spectrum. The dynamics of these nonlinear effects are influenced by both interband and intraband processes within the semiconductor material. Interband effects are primarily associated with transitions between the conduction and valence band of the semiconductor, whereas intraband effects are related to carrier-carrier and carrier-phonon scattering, which alter the carrier distribution within a single band. In the following, a rather qualitative description of the FWM effects in a semiconductor amplifier is given. For a more comprehensive theo-

[3] In the context of DFWM in SOAs, the term "conjugate" is often used to describe the generated frequency components rather than "idler". This is because, in SOAs, the nonlinear mixing process creates dynamic carrier gratings, which act as a phase-conjugating mirror. The generated waves undergo reflection at this grating, leading to a reversal of their phase relative to the pump waves. This distinguishes them from parametric amplification in fibers or crystals, where idler waves are typically generated without phase inversion.

retical explanation of these processes, please refer to the detailed models and equations found in [184, 185].

In DFWM, interband effects cause changes in carrier density due to carrier depletion, resulting from the stimulated emission of photons. This phenomenon, known as carrier density pulsation (CDP), involves fluctuations in the carrier population that alter the refractive index of the material. The characteristic timescale of CDP is typically on the order of several hundred picoseconds, which corresponds to the effective carrier lifetime in the active region of the amplifier. On the other hand, intraband mechanisms within the conduction band also play a crucial role in FWM. Two dominant processes contribute here: First, spectral-hole burning (SHB) occurs when stimulated emission depletes carriers at specific energy levels, "burning a hole" in the carrier distribution at the frequency of the emitted light. This local deviation from the Fermi distribution reduces gain at that frequency until carrier-carrier scattering restores equilibrium. Commonly, SHB is on a timescale of several tens to a few hundred femtoseconds, determined by the carrier-carrier scattering time. Second, carrier heating (CH) involves the excitation of carriers to higher energy states due to stimulated emission or free-carrier absorption. CH acts on a similar timescale of several hundred femtoseconds, as carriers rapidly scatter with phonons and cool back down to the lattice temperature.

The distinct response times of these mechanisms determine their relative contributions to FWM across different frequency detunings. CDP, with its slower timescale of several hundred picoseconds, mainly influences FWM at low detunings up to a few tens of gigahertz. In contrast, the much faster intraband effects, such as SHB and CH, occur on femtosecond timescales and enable efficient FWM generation even at terahertz detunings. Consequently, it has been shown that FWM processes in amplifiers are predominantly governed by CDP, SHB, and CH as long as the frequency difference $\Delta f = \frac{\Delta\omega}{2\pi}$ remains in the lower terahertz range [186].

An important advantage of using a TA instead of passive devices such as highly nonlinear (HNL) optical fibers or nonlinear crystals is its high FWM conversion efficiency, which allows for shorter interaction lengths of the injected waves. As a result, phase matching is less critical in amplifiers, since the short interaction length (around 1 mm) limits the

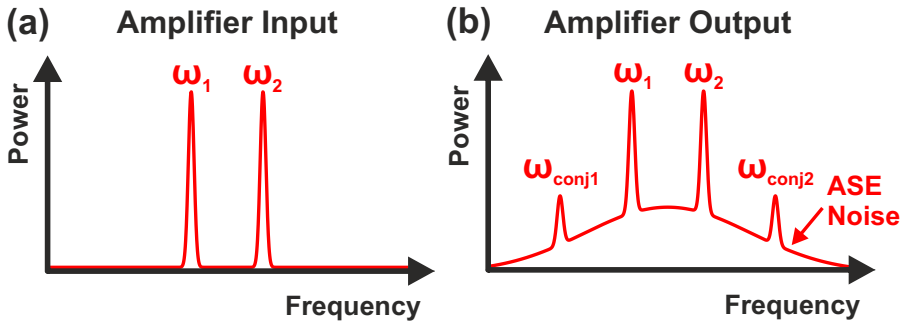

Figure 6.4: Input (a) and output (b) spectra of a tapered amplifier showing DFWM and the impact of amplified spontaneous emission (ASE) noise.

impact of phase mismatch. Moreover, only low optical input powers, typically a few tens of milliwatts, are required for the pump waves in TAs. However, one drawback of employing an active component rather than a passive one is the amplified spontaneous emission (ASE) noise introduced by the amplifier (see Fig. 6.4). This broadband noise can overlap with the generated DFWM signals, reducing the SNR or even completely masking them. This effect is particularly critical at low pump powers, where the DFWM conversion efficiency is reduced. Optimized operating conditions, such as controlling the injection current and using spectral filtering, can help mitigate these effects but cannot fully eliminate the trade-off between signal strength and noise.

6.3 Experimental Setup

The key aspect of DFWM that makes the effect particularly relevant in the context of this thesis is its ability to enable a bandwidth extension of the available beat signals through frequency tripling, while maintaining a strong correlation with the optical parameters of the pump waves, including linewidth and polarization properties. In addition to generating the DFWM frequencies, suppressing the two pump frequencies presents another significant challenge in extending the frequency range. Since the conjugate signals are much weaker than the injected pump frequencies, it is essential to remove the pump signals before the beat note can be used for terahertz generation or detection in a photomixer. Furthermore, any residual pump light can introduce unwanted noise and interference, compromising the accuracy of the measurements.

One potential solution to address this issue is the use of optical notch filters. These filters are designed to block the unwanted pump frequencies while allowing the conjugate frequencies to pass through. For instance, cascading two narrow fiber Bragg gratings (FBGs) is an effective method to filter out the unwanted pump signals [187]. However, due to the limited tunability of FBGs an alternative approach is adopted in the proposed concept. Here, two transmission gratings are employed to spatially separate the individual frequencies. After the generated DFWM frequencies are successfully isolated, the unwanted pump signals can be removed by simply blocking them. This technique offers superior frequency tunability compared to FBGs, as the blocking can be easily adjusted according to the diffraction angle of the transmitted beams, allowing for a wider range of frequencies to be filtered.

The configuration of the experimental setup used for DFWM measurements is illustrated in Fig. 6.5. Two phase-locked DFB lasers are superimposed in a polarization-maintaining 2×2 fiber coupler. One output is directed to an OPLL for the frequency synchronization, while the other is injected into a tapered amplifier (BoosTA pro 850, Toptica Photonics AG). The first TA amplifies the pump frequencies ω_1 and ω_2, providing the high input power necessary for efficient DFWM conversion and reducing ASE noise [188]. While the first TA operates with moderate gain, the second TA (miniTA EYP-TPA-0850, eagleyard Photonics GmbH) utilized for the DFWM generation is driven near the maximum current

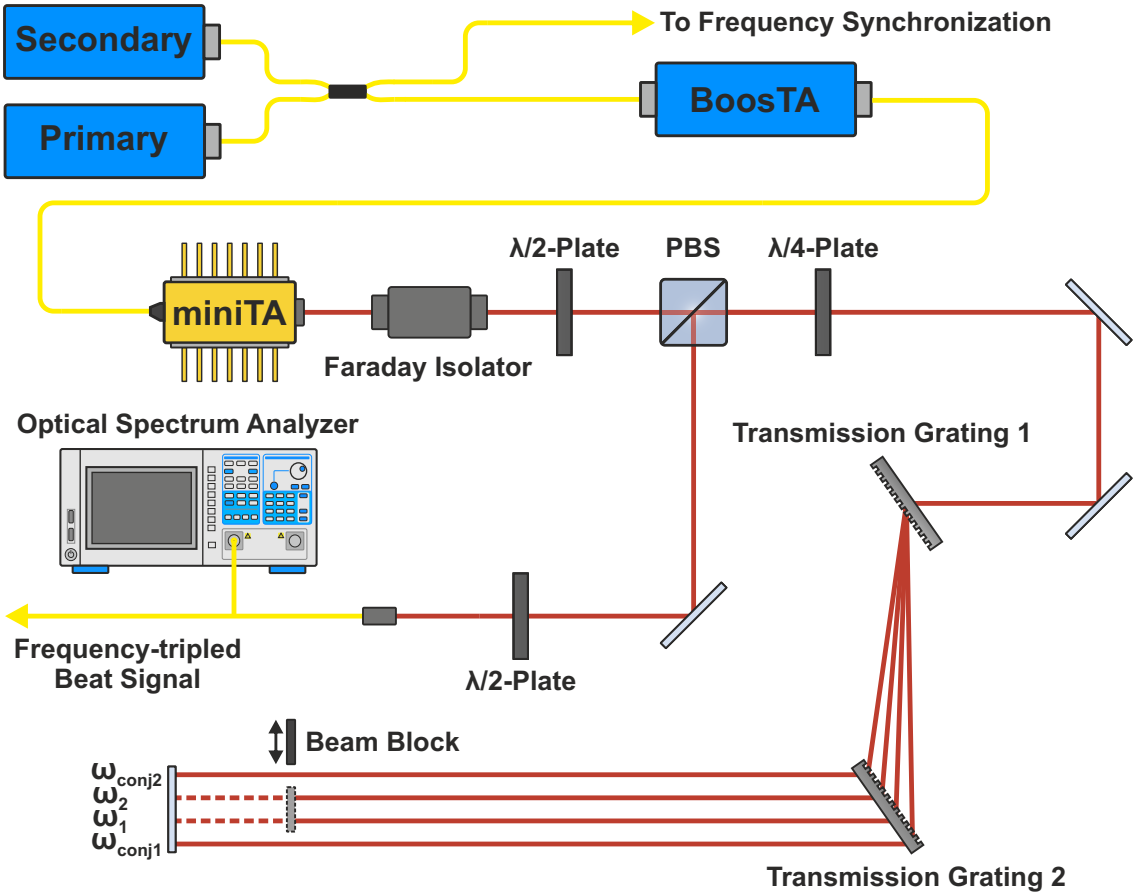

Figure 6.5: Sketch of the DFWM generation and filtering setup: The beat note of two phase-locked DFB lasers is amplified in the first tapered amplifier (BoosTA) before entering the second tapered amplifier (miniTA) for DFWM generation. A free-space optical filter setup, consisting of two transmission gratings, spatially separates the generated frequencies. The pump frequencies ω_1 and ω_2 are then filtered out with a beam block, while the remaining conjugate frequencies ω_{conj1} and ω_{conj2} are reflected off a plane mirror. After reflection, the conjugate frequencies are collimated and co-propagate along the original optical axis. Finally, the remaining signals are coupled into a polarization-maintaining fiber and sent to an OSA for measurement. As a result, the output beat signal now has three times the frequency of the original input beat. Fibers are shown in yellow, while freely propagating radiation is represented in red.

of 3.5 A, pushing it to its gain saturation limit to further enhance nonlinear conversion efficiency [188]. The miniTA features a fiber-coupled input and emits into free space with a maximum output power of 2.2 W. A Faraday isolator is placed after the second TA to suppress optical feedback into the amplifier. Subsequently, the light propagates through a half-wave plate, followed by a PBS and a quarter-wave plate. The half-wave plate rotates the polarization of the linearly polarized light, ensuring its full transmission through the PBS. Following this, the quarter-wave plate converts the linearly polarized light into circularly polarized light. Later in the setup, when the beam is reflected and

passes through the quarter-wave plate again, it is converted back to the linearly polarized state, but in the opposite direction.

To spatially separate the generated DFWM frequencies, the beam is directed via two mirrors onto the first transmission grating (PING-Sample-012, Ibsen Photonics A/S), which has a grating resolution of 1764.7 lines/mm and a diffraction efficiency of over 85% in the first order. The diffraction angle θ_{diff} for the first order of diffraction is given by the grating equation

$$\theta_{\text{diff}} = \arcsin\left(\frac{\lambda}{d} - \sin\theta_{\text{inc}}\right), \tag{6.9}$$

where λ is the wavelength of the incident light, d is the grating spacing, and θ_{inc} is the angle of incidence. After passing through the first grating, the spatially separated beams are directed onto a second transmission grating, oriented such that its structured surface faces the diffracted beams. This inverted alignment causes the diffraction to occur in the opposite direction, effectively reversing the angular separation introduced by the first grating. As a result, the beams propagate in parallel while preserving their spatial distance.

With the frequencies now spatially separated, a beam block can be employed to selectively filter out the two pump frequencies. The remaining conjugate frequencies propagate towards a plane mirror, where they are reflected. Upon reflection, the conjugate frequencies travel the optical path in reverse. Due to the symmetric configuration, the angular separation introduced earlier is compensated, and the conjugate beams emerge collimated and co-propagating along the original optical axis. After the polarization is converted back to linear by the quarter-wave plate, the PBS reflects the beam into the output path. The polarization is rotated by a second half-wave plate to ensure efficient coupling into a polarization-maintaining fiber for the measurement with the optical spectrum analyzer. Consequently, the output beat signal now exhibits a frequency three times that of the original input beat.

6.4 DFWM Measurements and Discussion

In the experiment, the two pump lasers are set to frequencies of $f_1 = 350.58562$ THz and $f_2 = 350.91895$ THz, resulting in a beat frequency of $\Delta f = f_2 - f_1 = 333.33$ GHz. After the pump power has been amplified to 80 mW, the signals enter the miniTA to generate the DFWM frequencies. Following the free-space filtering setup, the frequency spectrum of the output light is analyzed using an OSA with a resolution of 4 GHz.

To quantify the effectiveness of the DFWM process in the TA, the signal power of the generated conjugate frequencies is compared to the total input power. Hence, the conversion efficiency is given by

$$\eta_{\text{DFWM}} = \frac{P_{\text{conj, out}}}{P_{pump,\ in}}. \tag{6.10}$$

However, due to optical losses in the filtering setup and the fiber coupling, the measured output signals are subject to attenuation. To account for these losses and better isolate the performance of the DFWM process itself, a normalized conversion efficiency is used instead. According to [188], this normalized efficiency can be defined as

$$\eta_{\text{DFWM, norm.1,2}} = \frac{P_{\text{conj1,2, out}}}{(P_{\text{pump1,2, out}})^2 \; P_{\text{pump2,1, out}}}, \tag{6.11}$$

where the indices 1,2 represent the corresponding pump and conjugate powers in the output signal.

Another crucial parameter for practical applications of DFWM signal is the noise performance of the amplifier. For this purpose, the signal-to-background ratio (SBR) is introduced as

$$\text{SBR} = \frac{P_{\text{conj}}}{P_{\text{noise}}}, \tag{6.12}$$

where P_{noise} denotes the noise power level measured at the conjugate frequency within a certain optical bandwidth [189].

Fig. 6.6 shows the measured DFWM spectra, illustrating the signal before (a) and after (b) filtering of the pump frequencies. The two generated conjugate frequencies are separated by $3\Delta f = 1$ THz, with respective output powers of $P_{\text{conj1}} = -24.97$ dBm and $P_{\text{conj2}} = -26.52$ dBm, which are approximately 30 dB lower than the corresponding pump frequencies. Hence, the results for the normalized conversion efficiencies are calculated as $\eta_{\text{DFWM, norm.1}} \approx -38.66$ dB/mW^2 and $\eta_{\text{DFWM, norm.2}} \approx -36.21$ dB/mW^2. These values are consistent with the normalized DFWM efficiency reported in [189] for similar input pump powers.

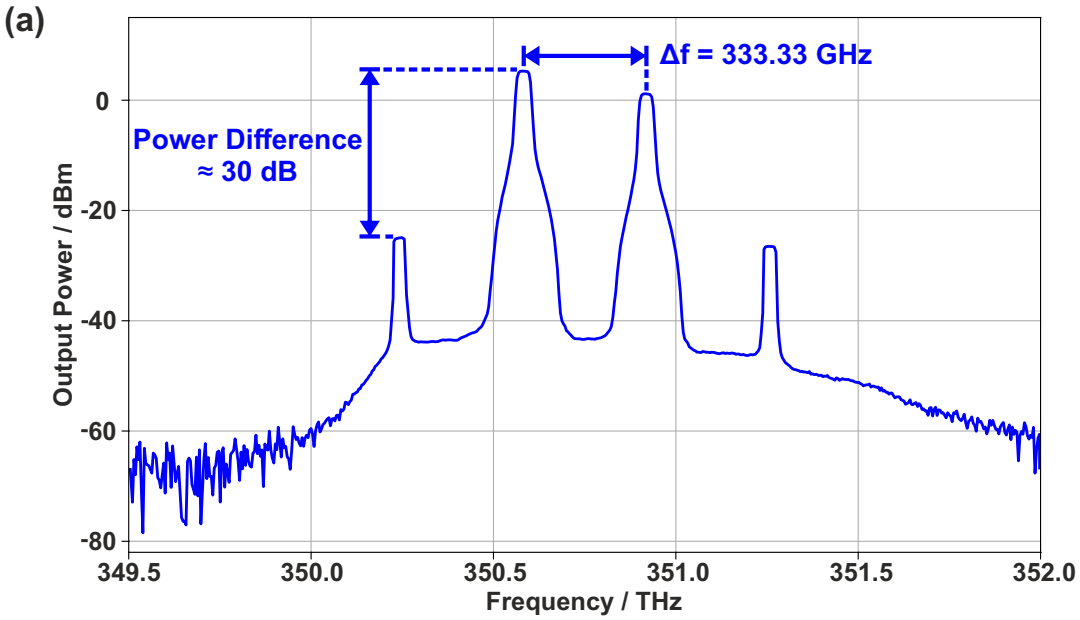

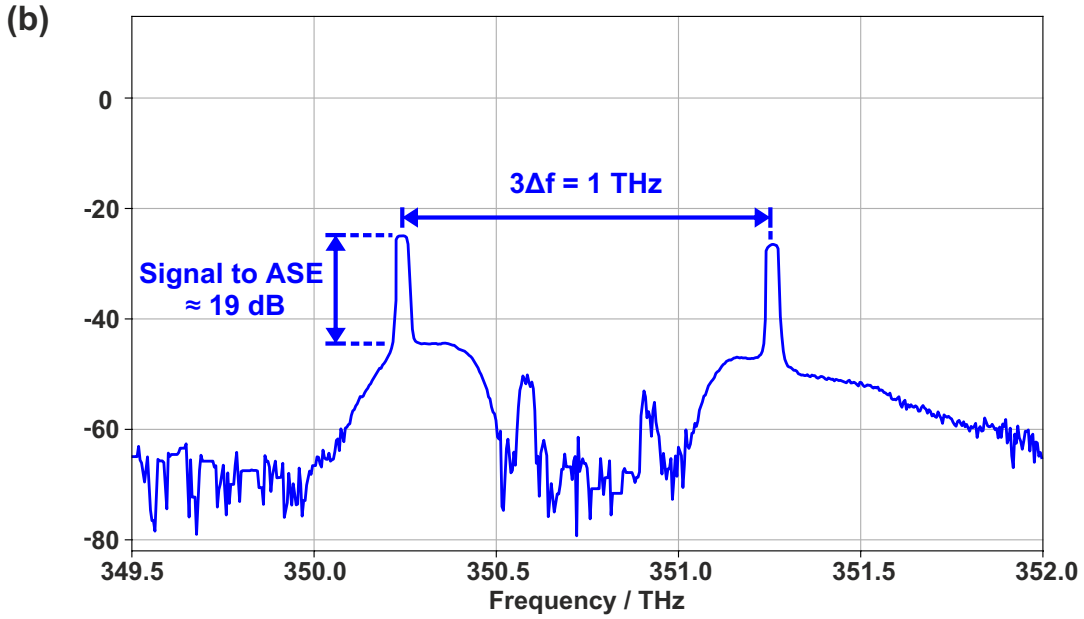

Figure 6.6: (a) Spectrum of the DFWM signal without filtering the pump frequencies ($\Delta f = 333.33$ GHz). (b) Filtered DFWM spectrum with conjugate frequencies separated by 1 THz. (Resolution 4 GHz, 100 averages).

Comparing the spectra before and after filtering, it can be seen that the power level of the pumps is suppressed by more than 50 dB, which is 25 dB lower than the power of the two conjugate waves. Therefore, the residual pumps will not considerably contribute to terahertz generation and detection in the photomixer. The SBR, primarily dominated by the ASE noise of the TA, is found to be 19.28 dB, which is in good agreement with SBR values of around 20 dB for detunings between 1 THz and 2 THz presented in [190]. However, the relatively lower dynamic range between the conjugate signals and background noise is expected to reduce the SNR of the beat note, thereby negatively impacting the terahertz measurements.

To significantly improve conversion efficiency and reduce the impact of ASE noise degradation in DFWM, it has been shown that using longer SOAs can effectively address these issues. For instance, in [191] it is demonstrated that the conversion efficiency can be increased by 40 dB and the SBR by 23 dB when using a 1-mm-long SOA instead of a 0.25 mm amplifier. This enhancement can be understood by considering the dependence of DFWM and ASE noise on the amplifier length L. In the unsaturated regime, the optical gain follows an exponential dependence on length, meaning that for a small-signal gain coefficient g, the total gain can be approximated as $G \approx e^{gL}$. Since the conjugate waves in DFWM are generated by a nonlinear interaction involving three waves, their power is proportional to the cube of the total gain, $P_{\text{conj}} \propto G^3 \approx e^{3gL}$. In saturation, the gain no longer increases exponentially with the length but instead reaches a steady-state value due to gain depletion ($G = 1$). Here, both pump waves propagate with nearly constant intensity along the amplifier. However, since DFWM is a coherent process, the generated conjugate fields accumulate in amplitude along the entire length of the amplifier, leading to a quadratic scaling of the conjugate power with the length,

$P_{\text{conj}} \propto L^2$. In contrast, amplified spontaneous emission is an incoherent process, where individual noise contributions combine in intensity rather than in amplitude. Therefore, the intensity of ASE noise grows linearly with the amplifier length, $P_{\text{ASE}} \propto L$, as the noise is generated at a constant rate along the amplifier. For the SBR, this results in a quadratic increase with length in the unsaturated regime, whereas in saturation, it grows linearly. Consequently, both conversion efficiency as well as SBR benefit from longer amplifier lengths.

Beyond signal power and dynamic range, the impact of nonlinear mixing and amplification on the spectral characteristics of the terahertz signal must also be considered when using DFWM for frequency extension in the developed systems. Unfortunately, the generated conjugate frequencies do not provide enough power to effectively drive the available photomixers for terahertz generation and detection. To overcome this limitation, an additional amplifier capable of boosting the conjugate signal power would be necessary. However, a suitable amplifier capable of handling low input powers is currently not available. Therefore, the following aspects must be investigated in upcoming experiments.

Ideally, an optical amplifier preserves the spectral characteristics of the seed lasers, especially when operated in the linear gain regime with sufficient input power. However, if the amplifier is driven close to saturation or seeded with low power, ASE noise and nonlinear effects, like self-phase modulation (SPM) or cross-phase modulation (XPM) can induce spectral broadening. Moreover, the nonlinear effects inherent to the DFWM process itself, such as SHB and CH, further contribute to linewidth enhancement [192], potentially degrading the linewidth of the terahertz output. This degradation can therefore reduce the frequency resolution and increase phase noise, negatively impacting both the PSA and PVNA measurements presented in the previous chapters. Nevertheless, in [193], it is demonstrated that a 41.7 GHz millimeter-wave signal generated via DFWM in an SOA can achieve a 3 dB linewidth below 20 Hz and phase noise better than -75 dBc/Hz at a 1.6 kHz offset.

Another significant challenge is that FWM in SOAs exhibits strong polarization sensitivity, primarily due to the polarization dependence of underlying processes such as CDP, SHB, and CH, where their conversion efficiency varies based on the alignment of the optical fields with each other and with the waveguide modes of the amplifier [194]. As the two pump waves in the proposed DFWM setup are co-polarized, meaning they are both linearly polarized in the same direction, it can be expected that the polarization of the conjugate waves will largely follow the polarization direction of the pump waves. However, minor changes in the output polarization may still occur due to thermal effects or structural imperfections within the amplifier, leading to fluctuations or slight rotations in the polarization state of the beat note, thereby modulating the output power of the terahertz radiation. These effects may also account for the observed fluctuations in the photocurrent recognized in the S-parameter measurements with the PVNA (see Section 5.3), given that the employed photomixers, with their interdigitated electrode structure, are inherently sensitive to polarization-induced variations.

Despite existing limitations in output power, signal dynamics, and potential spectral integrity issues, DFWM in optical amplifiers presents a promising alternative for frequency extension deep into the terahertz regime. Its ability to generate phase-locked high-frequency signals without the need for additional laser pairs or supplementary electronic multiplier chains makes it particularly attractive for next-generation terahertz applications. Consequently, the findings from this work on DFWM will be integrated into a future measurement concept aimed at ultra-broadband, high-resolution spectrum analysis up to 2 THz. The new system will be developed for applications such as EMC testing and evaluating advanced wireless communication environments in the context of the emerging 6G standard.

7 Summary and Outlook

Within this thesis, two innovative methodologies for spectrum and network analysis in the terahertz domain were developed. Both platforms, leveraging a combination of electronic and photonic components, offer exceptional frequency resolution at the hertz level, while simultaneously achieving a broad bandwidth of up to 1 THz. This hybrid approach allows the use of conventional DFB laser diodes with a wide tuning range, paired with CW photomixers for terahertz generation and detection, providing a highly advanced and cost-effective alternative to current state-of-the-art solutions.
The backbone of both systems is the laser frequency synchronization concept, which facilitates the precise stabilization of the beat signal(s), ensuring stable phase coherence for efficient terahertz generation. The synchronization minimizes frequency drift and phase noise, which are critical for achieving high spectral resolution and system stability. To realize this level of precision, the laser pair was phase-locked to a highly stable electronic reference source within an optical feedback loop. After establishing the developed synchronization concept in the RF range, the scheme was adapted for the terahertz domain. For this purpose, several techniques were evaluated for downconverting terahertz frequencies to the RF regime, including photomixing detection, electro-optic detection, and electronic detection using a Schottky diode mixer. All methods successfully phase-locked the laser pair in the terahertz range, with photomixing proving most advantageous due to its high dynamic range, ease of integration, and superior noise suppression. However, since the achievable frequency and bandwidth of the terahertz signal were constrained by the maximum output frequency and range of the reference, an additional laser diode was introduced into a second feedback loop (see Fig. 7.1). With this cascadation a maximum frequency of 1 THz could be achieved, along with a doubling

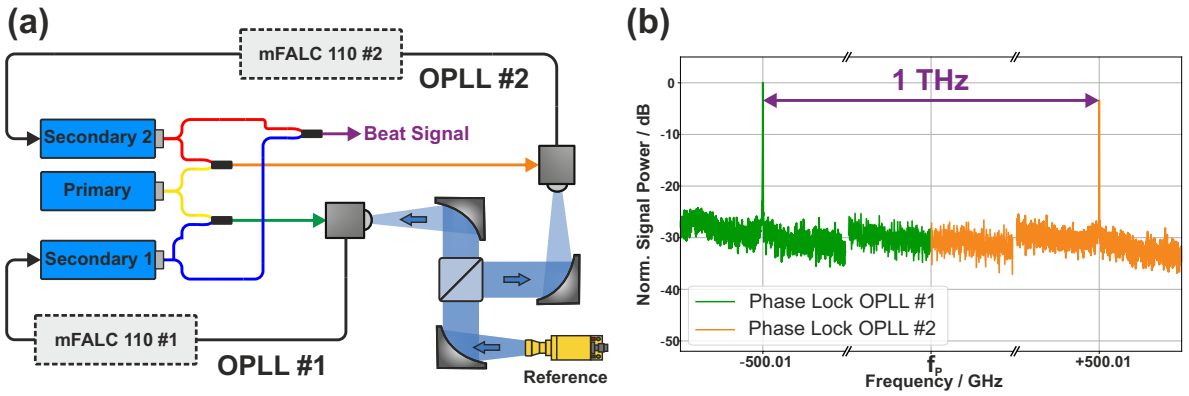

Figure 7.1: (a) Three-laser synchronization setup for phase-locking in the terahertz domain. (b) Resulting frequency spectrum of the phase-locked beat signal at 1 THz.

of the available bandwidth for each employed electronic reference source. Furthermore, existing gaps between the frequency bands of the different electronic sources could be eliminated by expanding the three-laser synchronization scheme to include a second reference. By adding and subtracting the respective beat signals from each other, the total bandwidth was extended to more than 900 GHz, providing continuous phase-stabilized frequency coverage from 70 GHz to 1 THz.
Building upon the established synchronization scheme, a photonic spectrum analyzer capable of performing high-resolution measurements in the terahertz frequency range was realized (see Fig. 7.2). Accordingly, the three-laser synchronization setup was extended by incorporating a free-space optical path, featuring an additional photomixer for detecting the measurement signal. Following the coherent detection principle employed in the synchronization setup, the PSA consistently characterized the spectral properties and output power of various active terahertz sources up to 1 THz. By calibrating the system with commercially calibrated power detectors, absolute power values could be measured, paving the way for precise EMC testing, particularly in the context of emerging 6G technologies. To demonstrate the capability and reliability of the developed PSA platform, a series of spurious harmonic signals emitted by two electronic frequency multiplier chains were measured. The data obtained indicated that the system was able to analyze single spurious harmonics up to 700 GHz with a resolution of a few hertz [151]. Although the current experimental implementation of the PSA concept still exhibits limitations in power measurement accuracy and acquisition speed, it has already proved strong potential as a promising alternative to leading-edge electronic frequency extension modules for SAs, particularly at frequencies of 1 THz and beyond.

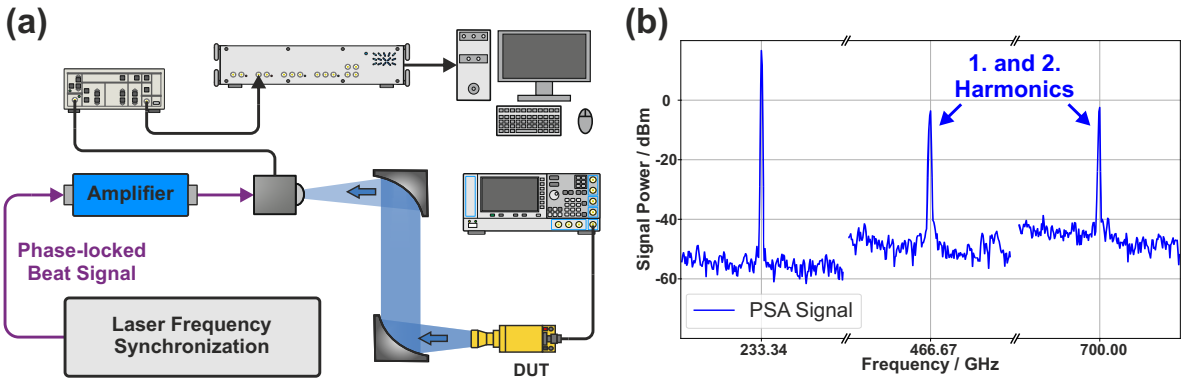

Figure 7.2: (a) High-resolution photonic spectrum analyzer setup. (b) Frequency spectrum showing the fundamental frequency at 233.33 GHz, along with the first and second harmonics at 466.67 GHz and 700.00 GHz, respectively.

Since the measurement functions of a spectrum analyzer are inherently restricted to analyzing the power spectrum of active devices, the hybrid idea to address the terahertz gap by merging electronic and photonic components was further developed to enable comprehensive network analysis. Similar to today's commercial approach of expanding the frequency range of electronic VNAs using extension modules, the innovative PVNA concept was designed as an extension rather than a standalone VNA, allowing

for scalable and flexible integration into existing test hardware. For this intent, stimulus signals from an electronic VNA were employed to phase-lock the beat notes between the three lasers (Fig. 7.3 (a)). As the VNA architecture was configured to exclusively receive its own test signal within a very narrow frequency range, one laser pair had to be employed to lock the difference frequency precisely at the expected value, which in turn, reduced the available bandwidth to only around 500 GHz. For the S-parameter measurements, the two phase-locked beat signals were routed to two additional photomixers within a heterodyne detection scheme. After downconversion to the desired intermediate frequency, the measurement signal is directed back to the VNA for analysis. Despite the challenges posed by the PVNA extender in its current experimental stage, a calibration was carried out to minimize time-invariant systematic errors, as reliable measurements cannot be obtained with an uncalibrated VNA. To validate the overall system performance, S21 transmission parameters of various free-standing (Fig. 7.3 (b)) and waveguide-based (Fig. 7.3 (c)) band-pass filters operating in the terahertz range were measured and compared with either simulation data or results obtained from commercial electronic extension modules. The outcome of these investigations confirmed the accuracy and reliability of the developed PVNA extender approach, demonstrating strong agreement with both simulated responses and measurement data from conventional extension modules [167]. However, the limited SNR and residual phase stability issues, when benchmarked against high-end electronic frequency extenders, currently remain key challenges to the competitiveness of the photonic concept. Nevertheless, its intrinsic capability to provide continuous frequency coverage from the microwave domain well into the terahertz regime — combined with a cost-efficient architecture that can be easily extended to higher frequencies via cascaded laser sources — highlights its potential as a versatile and scalable next-generation system platform for broadband vector network analysis.

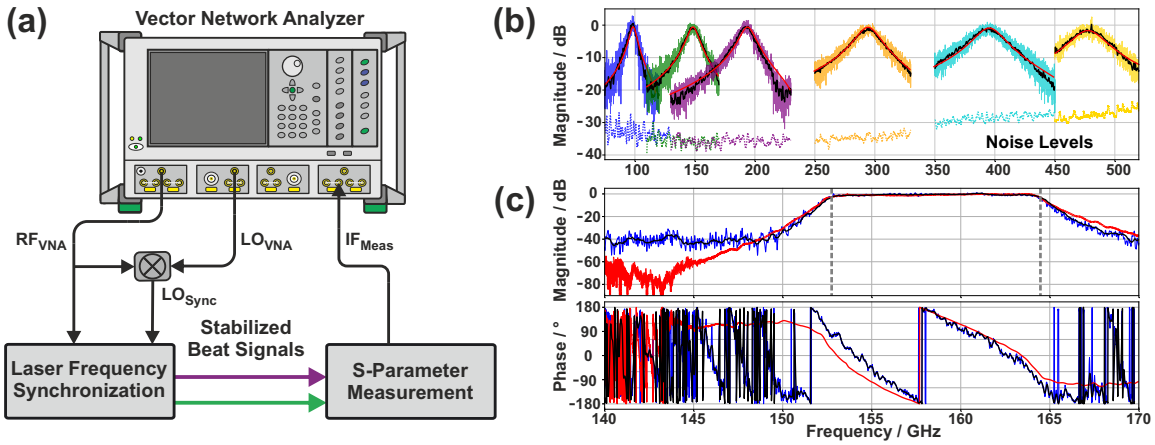

Figure 7.3: (a) PVNA extender concept with its two subsystems. (b) S21 measurement of free-standing cross-shaped metal-mesh band-pass filters. (c) S21 measurement of a waveguide iris band-pass filter.

Beyond cascading additional laser sources, one promising approach to further extend the accessible frequency range — exceeding even the individual tuning ranges of the lasers — involves generating new spectral components through nonlinear optical processes such as four-wave mixing. A preliminary demonstration of how (degenerate) FWM can be incorporated into the laser frequency synchronization to triple the available phase-locked beat signal has already been shown within the framework of this thesis. Here, the nonlinearity of a semiconductor optical amplifier was exploited to induce DFWM, resulting in the generation of two conjugate frequencies separated by three times the frequency of the initial beat signal. Since the output power of these conjugate frequencies was considerably lower than that of the original beat signal, the two pump waves needed to be removed to make the generated frequencies suitable for practical applications. To achieve this, a free-space filtering setup, consisting of two transmission gratings, was implemented after the SOA (see Fig. 7.4 (a)). The spatial separation of the beams based on their optical frequencies allowed for the suppression of the unwanted pump components, while the conjugate frequencies were selectively coupled back into an optical fiber. Successfully, this technique enabled the generation of a 1 THz beat signal using only a single laser pair and a reference source emitting at 333.33 GHz, as verified by the OSA measurements in Fig. 7.4 (b). However, due to insufficient DFWM power and the lack of a suitable amplifier, their effect on the spectral properties of the terahertz radiation could not be investigated any further. To overcome this limitation, a fiber amplifier, for example, an erbium doped fluoride fiber optical amplifier (EDFFA) for wavelengths around 850 nm [195], could be implemented, providing the necessary gain to boost the DFWM frequencies, thus facilitating more efficient terahertz generation and detection. Therefore, the concept of DFWM is belived to hold significant promise for further extending the accessible frequency range in future measurement systems.

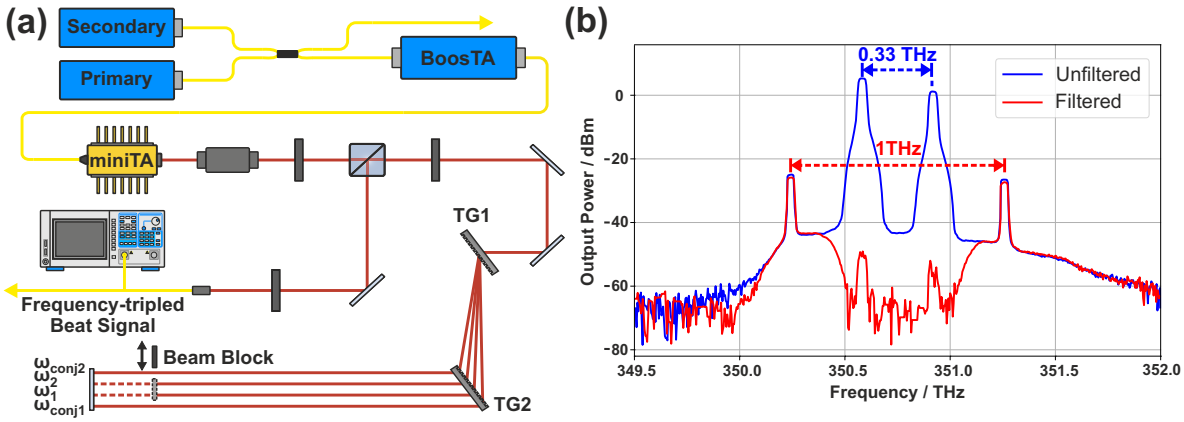

Figure 7.4: (a) DFWM generation and filtering setup. (b) Spectra of the DFWM signals with (red) and without (blue) filtering the pump frequencies.

7.1 Future Perspectives

Looking ahead, the field of high-resolution spectrum and network analysis in the terahertz domain is expected to attract increasing interest, driven by the growing demand for higher data rates and faster transmission speeds in upcoming 6G communication networks. As these systems move toward utilizing higher frequency bands, precise characterization and understanding of HF components emitting in the terahertz range — from several hundred gigahertz up to 1 THz and beyond — will be essential to secure efficient signal generation, transmission, and detection. Continued advancements in measurement techniques and instrumentation will thus play a crucial role in enabling reliable design and seamless integration of new technologies, ranging from individual modules to complex subsystems and full-scale measurement platforms — facilitating next-generation applications in high-speed communication, real-time imaging, and smart sensing.

A key challenge in this context is translating experimental concepts from the laboratory into fully integrated, compact systems ready for commercial use. Therefore, an important step toward bridging the gap between research and real-world application is the miniaturization of the system architecture into a plug-and-play format. This ensures compatibility with commercial measurement equipment, allowing users to simply connect their external devices and launch the control software. Consequently, within this thesis, the two subsystems from the PVNA extender concept were integrated separately into compact modules, supporting straightforward connection of external hardware such as lasers and PID controllers.

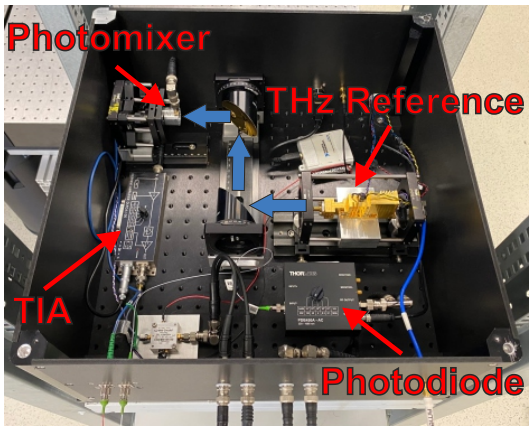

Figure 7.5: Laser frequency synchronization module in a standard 19-inch rack. Blue arrows show the THz path.

In the module for the laser frequency synchronization (see Fig. 7.5), all components — except for the three DFB lasers with their fiber setup and the associated mFALC controllers — were assembled into a single housing suitable for installation in a standard 19-inch rack.

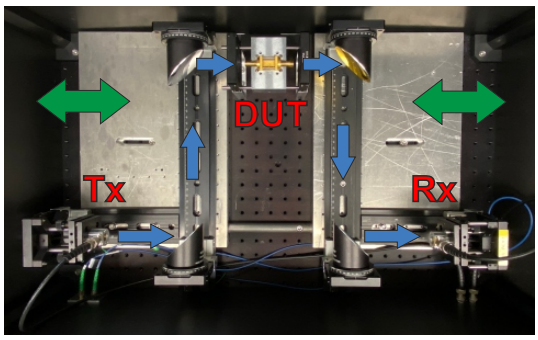

Figure 7.6: S-parameter measurement module in waveguide configuration . Blue arrows show the THz path.

Additionally, the S-parameter measurement setup was enclosed in a second module to enhance portability and improve robustness against environmental influences such as temperature fluctuations (Fig. 7.6). Furthermore, all components were mounted on adjustable rails to simplify alignment and enable easier transition from the waveguide configuration to terahertz measurements of thin-film samples at the beam focus by making the metallic ground plates horizontally movable (indicated by the green arrows in Fig. 7.6).

Of course, the presented prototype is only the first step toward a fully integrated solution suitable for use in commercial or industrial contexts. Particularly, the rather bulky DFB lasers, together with their supporting infrastructure — including temperature and current control units, fiber optics, and PID controllers — currently limit the compactness and scalability of the concept. Future developments should therefore focus on the implementation of photonic integrated circuits (PICs), meaning the integration of a large number of optical devices on a common substrate [196]. Apart from making the setup more compact, the use of PICs for optical components also offers significant performance benefits. As all optical couplings between the elements of the system occur directly on the chip, the optical losses will become smaller, while packaging complexity will be significantly reduced. Moreover, monolithic integration also minimizes sensitivity to environmental fluctuations. For instance, when all laser sources are on the same chip, they experience identical temperature shifts, less affecting the frequency difference between the optical outputs. Additionally, phase stability is improved as the phase fluctuations inherent to free-space or fiber-optic interfaces in non-integrated systems are largely eliminated, potentially leading to a more stable frequency synchronization between the lasers.
However, despite the numerous advantages, there is one significant drawback that cannot be overlooked: the limited commercial availability of suitable devices, as PICs lag several generations behind integrated circuits (ICs) in the field of modern electronics [197]. Nevertheless, in addition to a large number of scientific reports demonstrating the integration of multiple DFB or distributed Bragg reflector (DBR) laser sources for the heterodyne generation of widely tunable terahertz beat notes on a single chip [198–202], the literature also includes examples of fully integrated optical phase-locked loops. For instance, Arafin *et al.* [203] demonstrated an integrated heterodyne OPLL that phase-locks a 1550 nm DBR laser to an optical frequency comb, achieving a total beat frequency span of 3 THz with a tuning resolution better than 100 Hz. The entire device, including the DBR laser, SOAs, coupling optics, electronics, and temperature control, fits into a volume of less than 0.2 cm^3. An example more closely related to the locking scheme presented in this thesis can be found in [204]. In their publication, the authors propose a difference-frequency locking scheme for two external lasers using a heterogeneously integrated OPLL consisting of a photonic and an electronic integrated circuit (EIC). On the PIC, the laser beat signal is detected by a fast photodiode and transferred via wire bonding to the feedback loop on the EIC. This approach enables continuous frequency locking over a range of 10 GHz to 40 GHz, with the total chip area being smaller than 2 mm^2.
Still, many of these demonstrations remain confined to laboratory environments and are not yet suitable for commercial applications. One of the main challenges in the field of photonics is the high cost of developing and fabricating chips, as setting up and operating cleanroom facilities is extremely expensive [205]. A promising solution is to provide designers with access to shared fabrication platforms, where chip space is divided among multiple users to reduce costs. An example is the JePPIX platform [206], which emerged from EU-funded initiatives (e.g., ePIXnet [207]) and offers multi-project wafer runs and standardized design tools to support cost-effective prototyping and accelerate

the development of PICs. Another currently running initiative as part of Horizon Europe is the QPIC1550 project (2023 to 2027, €6 million) [208]. It aims to merge the fields of quantum mechanics and photonics technology by developing a universal quantum photonic integrated circuit platform at 1550 nm, integrating InP sources, quantum dots, and InGaAs detectors onto SiN PICs for the first time. These ambitious initiatives, involving leading academic institutions and industry partners across Europe, underscore the increasing recognition of PICs as a crucial technology for future applications, paving the way for the broader availability of commercially accessible devices.

As shown in the previous examples, many of these new PIC concepts, along with non-integrated ones, operate near the low-loss or low-dispersion fiber optic windows at 1550 nm and 1310 nm, respectively. Especially, transitioning to the telecom wavelength of 1550 nm offers several key advantages, including the wide accessibility of compact, tunable, and low-cost semiconductor laser components, as well as the low transmission loss of optical fibers at this wavelength. Furthermore, photomixers designed for 1550 nm operation exhibit significantly higher efficiency, delivering terahertz output powers more than an order of magnitude greater than the 850 nm photomixers used in this work [180]. Utilizing these photomixers as both transmitters and receivers in a coherent detection scheme has achieved a dynamic range exceeding 80 dB at 1 THz, with a total frequency bandwidth of 4.5 THz [149]. For these reasons, adopting the 1550 nm range should be considered for the future, as it would significantly enhance the performance of the photonic systems developed in this thesis, further increasing their competitiveness with current state-of-the-art solutions.

In conclusion, whether photonic or electronic concepts will lead the next generation of cutting-edge measurement tools in addressing the upcoming challenges in high-frequency spectrum and network analysis remains to be seen. Recent advancements in both areas over the past decades suggest that scientific and industrial progress will continue to accelerate, driven by the increasing demand for innovation, efficiency, and performance of future key emerging technologies like 6G communication, artificial intelligence, and quantum computing. However, as each method possesses its own complementary advantages —from the precision and stability of electronic sources to the broad bandwidth of photonic systems — the hybrid approach explored in this thesis emerges as a promising starting point for future research, uniting the hallmark strengths of both technologies.

Appendix

Appendix to Chapter 2.4.2

This appendix provides a detailed overview of the error correction framework used in vector network analyzer (VNA) calibration, focusing on the error box model and the calibration standards and methods that enable accurate compensation of systematic measurement errors.
To effectively reduce measurement uncertainty and improve reliability, it is essential to understand the various error sources that influence VNA measurements. Among these, systematic errors are especially critical, as they are repeatable and therefore correctable through proper calibration. These errors can be collectively described by a relatively simple yet powerful representation known as the error box model [140]. This model treats the VNA system as a linear, time-invariant system with frequency-dependent parameters, providing a structured way to characterize and correct systematic influences.

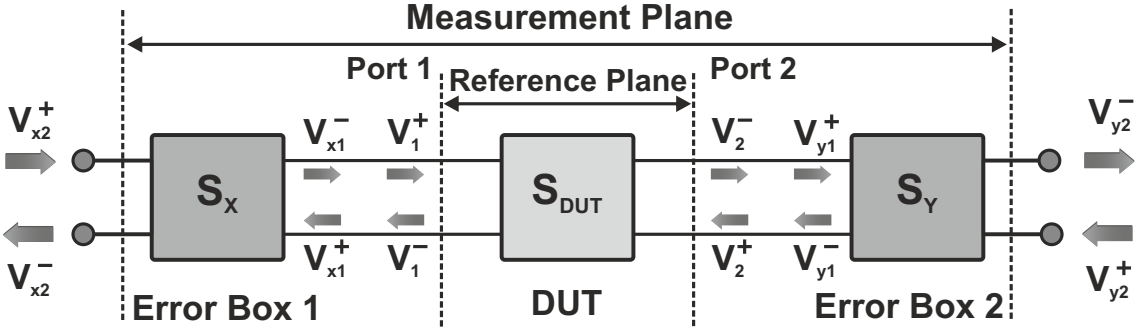

Figure 7: Schematic representation of a two-port error box model: The model uses two S-parameter matrices, S_x and S_y, to describe the relationship between incident and reflected signals at both ports. Error terms (e_{mn}) account for systematic errors, including directivity, reflection and transmission tracking, as well as source and load match.

The error box model for a two-port VNA with four receivers is illustrated in Fig. 7. It consists of two error boxes, represented by the S-parameter matrices S_x and S_y between the reference plane and the measurement plane of the VNA. The S-parameter equations for S_x and S_y can be described as

$$\begin{pmatrix} V_{x1}^- \\ V_{x2}^- \end{pmatrix} = S_x \begin{pmatrix} V_{x1}^+ \\ V_{x2}^+ \end{pmatrix} = \begin{pmatrix} e_{11} & e_{10} \\ e_{01} & e_{00} \end{pmatrix} \begin{pmatrix} V_{x1}^+ \\ V_{x2}^+ \end{pmatrix}, \tag{.1}$$

and

$$\begin{pmatrix} V_{y1}^- \\ V_{y2}^- \end{pmatrix} = S_y \begin{pmatrix} V_{x1}^+ \\ V_{x2}^+ \end{pmatrix} = \begin{pmatrix} e_{22} & e_{23} \\ e_{32} & e_{33} \end{pmatrix} \begin{pmatrix} V_{y1}^+ \\ V_{y2}^+ \end{pmatrix}, \tag{.2}$$

where $V_{x,y}^-$ refers to the emerging voltage signals, and $V_{x,y}^+$ to the incoming voltage signals corresponding to the error matrices S_x and S_y, respectively. The eight error terms are denoted by e_{mn}, where m denotes the incident port and n the outgoing port. The error model applies to both forward and reverse measurements, as indicated by e and e', respectively. Thus, the systematic errors are represented by the following error terms:

- $\boldsymbol{e_{00}, e'_{33}}$: Directivity error
- $\boldsymbol{e_{10}e_{01}, e'_{23}e'_{32}}$: Reflection tracking error
- $\boldsymbol{e_{11}, e'_{22}}$: Source match error
- $\boldsymbol{e_{10}e_{32}, e'_{01}e'_{23}}$: Transmission tracking error
- $\boldsymbol{e_{22}, e'_{11}}$: Load match error

Together with the two isolation error terms ($\boldsymbol{e_{30}, e'_{03}}$)[1], these 10 terms form the so-called 12-term error model, which is the widely favored standard model for the description of systematic measurement errors due to its direct correlation with real and comprehensible error sources [209].

Calibration Standards and Methods

To determine the different error terms, a VNA must undergo a calibration process using well-defined calibration standards. Since the calibration process directly impacts the integrity of VNA measurements, selecting appropriate calibration standards is essential. These standards are typically categorized into one-port and two-port types, designed to systematically measure and isolate the contributions of each error term. They are available in various configurations to suit coaxial, waveguide, and on-wafer measurement environments. In terahertz measurements, waveguide standards are most commonly used due to their ability to support propagation of the high-frequency signals. This discussion will, therefore, focus on on waveguide-based one-port and two-port calibration standards.
One-port standards are used to calibrate a single measurement port by defining its reference impedance and correcting systematic errors such as directivity, source match, and reflection tracking. The common one-port standards include:

- **Short**: This standard provides a perfect electrical short circuit at the calibration plane, offering a known reflection coefficient ($\Gamma = -1$) that helps isolate directivity and source match errors. In case of waveguide systems, the Short standard can be a conductive plate mounted on the waveguide flange of the test port.

[1]Isolation error terms accounts for any signal which bypasses the DUT entirely. In most cases, the isolation error is smaller than the VNA receiver noise, even at the lowest IF bandwidths, and can typically be disregarded.

- **Offset Short (Waveguide Open equivalent[2])**: The Offset Short is often designed to produce a reflection coefficient of $\Gamma = +1$, simulating the Open termination. This substitution allows for accurate calibration while maintaining the necessary reflection characteristics, which is crucial for characterizing reflection tracking errors in combination with the Short standard.

- **Load**: A matched load absorbs incident waves with minimal reflection, helping to isolate and refine measurements of directivity and source match errors. In waveguide Match standards, a ferrite material cone or pyramid-shaped structure is attached to the closed end of a waveguide. This structure serves as an absorber of electromagnetic energy, ensuring minimal reflection

- **Reflect**: The Reflect standard is any calibration standard with a reflection coefficient greater than zero ($|\Gamma| > 0$). Unlike the Short or Offset Short standards, the Reflect standard does not require a precise value for the reflection coefficient. It is commonly used in calibration methods that rely on relative phase and magnitude measurements.

Two-port standards define the reference impedance across both ports and correct systematic errors such as source match, load match, and transmission tracking. Two-port calibration standards typically are:

- **Thru**: A direct connection between the two ports of the VNA with minimal loss and reflection is known as Thru standard. It serves as a reference for the insertion loss and phase delay between the ports. In waveguide systems, this is typically achieved by directly aligning the flanges of two waveguides, ensuring a seamless path for signal transmission. The Thru standard is critical for characterizing transmission tracking and port match errors.

- **Line**: The Line standard introduces a precise electrical delay between the two ports, resulting in a phase shift of approximately 90 ° relative to the Thru at the center frequency. In waveguide calibration, a waveguide section of a specific length, often a quarter wavelength longer, is used to create this delay. The Line standard complements the Thru by helping to resolve phase ambiguities and refine error correction, especially in broadband applications.

After measuring the calibration standards and mathematically determining the error terms, the systematic errors can be mostly removed from the measurement by applying calibration methods. The two primary calibration methods used to achieve this are **SOLT** (Short, Offset Short, Load, Thru) and **TRL** (Thru, Reflect, Line) [209].
The **SOLT** calibration method involves performing a one-port calibration (Short, Open/Offset Short, Load) at each test port, followed by additional measurements of a Thru connection between the two test ports. It is a widely used technique, particularly

[2]In waveguide systems, the Open standard does not exist because of the radiation effects at the open end of the waveguide. Thus, a true Open-circuit is substituted by an Offset Short-circuit.

where the calibration standards are accessible and can be manufactured with high precision, such as in coaxial and waveguide systems. The accuracy of this method depends significantly on how well the reference standards are defined and can be measured.
TRL is a more flexible calibration technique that is often employed in scenarios where the SOLT standards are difficult to implement, especially in high-frequency measurements. Unlike the SOLT method, the TRL calibration requiring less knowledge about the electrical properties of the standards. The TRL method is particularly advantageous in terahertz waveguide systems, where traditional standards may be hard to fabricate due to factors like radiation effects and waveguide geometry. Additionally, TRL is less effected by the physical limitations in high-frequency environments, as it does not rely on idealized standards. However, since the standards require a distinct phase relationship, the usable calibration frequency span is limited. This limitation can be mitigated by introducing additional Line standards with phase shifts designed for corresponding frequency bands.
Beyond TRL and SOLT, several other VNA calibration approaches are available, each tailored for specific scenarios and system requirements. The most common methods, including SOLT, SOLR, TRL, and LRM, are summarized in Table 1, providing a comparative overview of their description, advantages, and disadvantages.
Although the discussed calibration techniques can successfully remove systematic errors, some residual errors will always remain. These residual errors typically result from inaccuracies in the calibration process as well as random factors (e.g., noise) and environmental influences such as temperature fluctuations. Nevertheless, thorough calibration can minimize the impact of these residual errors, ensuring reliable and repeatable VNA measurements.
For a more detailed mathematical consideration of the various calibration standards and methods, please refer to [210].

Table 1: Comparison of the most common VNA calibration methods

Calibration Method	Description	Advantages	Disadvantages
SOLT (Short-Open-Load-Thru)	Most common used two-port calibration method; needs all (Short, Open/ Offset Short, Load, and Thru) standards to define the reference plane and correct systematic errors	Highly accurate; wide applicability in coaxial and waveguide systems	Requires very well-defined standards; difficult to implement at very high frequencies
SOLR (Short-Open-Load-Reflect)	Variation of SOLT; replaces the Thru standard with a Reflect standard	Ideal for on-wafer or systems where a Thru connection is impractical	Lower accuracy than SOLT; dependent on quality of the Reflect standard
TRL (Thru-Reflect-Line)	Most accurate two-port calibration technique; uses transmission lines and Reflection standards, avoiding reliance on ideal Open/ Short definitions	Well-suited for high-frequency (terahertz) applications; less affected by limitations of physical standards	Setup can be complex; needs very good transmission lines; limited bandwidth
LRM (Line-Reflect-Match)	Simplified TRL using one reflection and two (Matched) Line standards	Fewer standards required; easier to implement	Lower accuracy; limited ability to correct all systematic errors

Bibliography

[1] I. F. Akyildiz, J. M. Jornet, and C. Han: "Terahertz band: Next frontier for wireless communications", *Phys. Commun.* **12**, 16–32 (2014), doi: 10.1016/j.phycom.2014.01.006.

[2] M. Alsabah, M. A. Naser, B. M. Mahmmod, S. H. Abdulhussain, M. R. Eissa, A. Al-Baidhani, N. K. Noordin, S. M. Sait, K. A. Al-Utaibi, and F. Hashim: "6G wireless communications networks: A comprehensive survey", *IEEE Access* **9**, 148191–148243 (2021), doi: 10.1109/access.2021.3124812.

[3] D. Serghiou, M. Khalily, T. W. C. Brown, and R. Tafazolli: "Terahertz channel propagation phenomena, measurement techniques and modeling for 6G wireless communication applications: A survey, open challenges and future research directions", *IEEE Commun. Surv. Tutor.* **24**(4), 1957–1996 (2022), doi: 10.1109/COMST.2022.3205505.

[4] W. Jiang, Q. Zhou, J. He, M. A. Habibi, S. Melnyk, M. El-Absi, B. Han, M. Di Renzo, H. D. Schotten, F.-L. Luo, T. S. El-Bawab, M. Juntti, M. Debbah, and V. C. M. Leung: "Terahertz communications and sensing for 6G and beyond: A comprehensive review", *IEEE Commun. Surv. Tutor.* **26**(4), 2326–2381 (2024), doi: 10.1109/comst.2024.3385908.

[5] C. Isaia and M. P. Michaelides: "A review of wireless positioning techniques and technologies: From smart sensors to 6G", *Signals* **4**(1), 90–136 (2023), doi: 10.3390/signals4010006.

[6] C. de Lima, D. Belot, R. Berkvens, A. Bourdoux, D. Dardari, M. Guillaud, M. Isomursu, E.-S. Lohan, Y. Miao, A. N. Barreto, M. R. K. Aziz, J. Saloranta, T. Sanguanpuak, H. Sarieddeen, G. Seco-Granados, J. Suutala, T. Svensson, M. Valkama, B. van Liempd, and H. Wymeersch: "Convergent communication, sensing and localization in 6G systems: An overview of technologies, opportunities and challenges", *IEEE Access* **9**, 26902–26925 (2021), doi: 10.1109/access.2021.3053486.

[7] B. Ji, Y. Wang, K. Song, C. Li, H. Wen, V. G. Menon, and S. Mumtaz: "A survey of computational intelligence for 6G: Key technologies, applications and trends", *IEEE Trans. Ind. Inf.* **17**(10), 7145–7154 (2021), doi: 10.1109/tii.2021.3052531.

[8] F. Guo, F. R. Yu, H. Zhang, X. Li, H. Ji, and V. C. M. Leung: "Enabling massive IoT toward 6G: A comprehensive survey", *IEEE Internet of Things J.* **8**(15), 11891–11915 (2021), doi: 10.1109/jiot.2021.3063686.

[9] R. Chataut, M. Nankya, and R. Akl: "6G networks and the AI revolution—exploring technologies, applications, and emerging challenges", *Sensors* **24**(6), 1888 (2024), doi: 10.3390/s24061888.

[10] A. Alhammadi, I. Shayea, A. A. El-Saleh, M. H. Azmi, Z. H. Ismail, L. Kouhalvandi, and S. A. Saad: "Artificial intelligence in 6G wireless networks: Opportunities, applications, and challenges", *Int. J. Intell. Syst.* **2024**(1), 1–27 (2024), doi: 10.1155/2024/8845070.

[11] M. R. Mahmood, M. A. Matin, P. Sarigiannidis, and S. K. Goudos: "A comprehensive review on artificial intelligence/machine learning algorithms for empowering the future IoT toward 6G era", *IEEE Access* **10**, 87535–87562 (2022), doi: 10.1109/access.2022.3199689.

[12] University of Oulu: "White paper on RF enabling 6G: Opportunities and challenges from technology to spectrum", 2021, available at: `https://oulurepo.oulu.fi/handle/10024/36613`.

[13] I. F. Akyildiz, D. M. Gutierrez-Estevez, R. Balakrishnan, and E. Chavarria-Reyes: "LTE-Advanced and the evolution to beyond 4G (B4G) systems", *Phys. Commun.* **10**, 31–60 (2014), doi: 10.1016/j.phycom.2013.11.009.

[14] D. Soldani: "6G fundamentals: Vision and enabling technologies", *J. Telecommun. Digit. Econ.* **9**(3) (2021), doi: 10.18080/jtde.v9n3.418.

[15] HEXA-X-II: "European level 6G flagship project", available at: `https://hexa-x-ii.eu/`.

[16] 6G-ANNA: "Ganzheitliche Ansätze für Mobilfunknetze der 6. Generation", available at: `https://6g-anna.de/#projekt`.

[17] B. Yang, X. Wang, Y. Zhang, and R. S. Donnan: "Experimental characterization of hexaferrite ceramics from 100 GHz to 1 THz using vector network analysis and terahertz-time domain spectroscopy", *J. Appl. Phys.* **109**(3), 033509 (2011), doi: 10.1063/1.3544477.

[18] J. Hammler, A. J. Gallant, and C. Balocco: "Free-space permittivity measurement at terahertz frequencies with a vector network analyzer", *IEEE Trans. Terahertz Sci. Technol.* **6**(6), 817–823 (2016), doi: 10.1109/TTHZ.2016.2609204.

[19] L.-F. Shi, A. Zahid, A. Ren, M. Z. Ali, H. Yue, M. A. Imran, Y. Shi, and Q. H. Abbasi: "The perspectives and trends of THz technology in material research for future communication—a comprehensive review", *Phys. Scr.* **98**(6), 065006 (2023), doi: 10.1088/1402-4896/accd9d.

[20] S. Zhong: "Progress in terahertz nondestructive testing: A review", *Front. Mech. Eng.* **14**(3), 273–281 (2019), doi: 10.1007/s11465-018-0495-9.

[21] F. Ellrich, M. Bauer, N. Schreiner, A. Keil, T. Pfeiffer, J. Klier, S. Weber, J. Jonuscheit, F. Friederich, and D. Molter: "Terahertz quality inspection for automotive and aviation industries", *J. Infrared Millim. Terahertz Waves* **41**(4), 470–489 (2020), doi: 10.1007/s10762-019-00639-4.

[22] M. Bauer, R. Hussung, C. Matheis, A. Mashkin, S. Krane, F. Pohlmann, and F. Friederich: "Terahertz non-destructive testing of power generator bars with a dielectric waveguide antenna", *Int. J. Microw. Wirel. Technol.* **15**(6), 1038–1047 (2023), doi: 10.1017/s175907872200126x.

[23] C. Yu, S. Fan, Y. Sun, and E. Pickwell-MacPherson: "The potential of terahertz imaging for cancer diagnosis: A review of investigations to date", *Quant. Imaging Med. Surg.* **2**(1), 33–45 (2012), doi: 10.3978/j.issn.2223-4292.2012.01.04.

[24] G. G. Hernandez-Cardoso, L. F. Amador-Medina, G. Gutierrez-Torres, E. S. Reyes-Reyes, C. A. Benavides Martínez, C. Cardona Espinoza, J. Arce Cruz, I. Salas-Gutierrez, B. O. Murillo-Ortíz, and E. Castro-Camus: "Terahertz imaging demonstrates its diagnostic potential and reveals a relationship between cutaneous dehydration and neuropathy for diabetic foot syndrome patients", *Sci. Rep.* **12**(1), 3110 (2022), doi: 10.1038/s41598-022-06996-w.

[25] J. F. Federici, B. Schulkin, F. Huang, D. Gary, R. Barat, F. Oliveira, and D. Zimdars: "THz imaging and sensing for security applications—explosives, weapons and drugs", *Semicond. Sci. Technol.* **20**(7), S266–S280 (2005), doi: 10.1088/0268-1242/20/7/018.

[26] G. Tzydynzhapov, P. Gusikhin, V. Muravev, A. Dremin, Y. Nefyodov, and I. Kukushkin: "New real-time sub-terahertz security body scanner", *J. Infrared Millim. Terahertz Waves* **41**(6), 632–641 (2020), doi: 10.1007/s10762-020-00683-5.

[27] D. Molter, D. Hübsch, T. Sprenger, K. Hens, K. Nalpantidis, F. Platte, G. Torosyan, R. Beigang, J. Jonuscheit, G. von Freymann, and F. Ellrich: "Mail inspection based on terahertz time-domain spectroscopy", *Appl. Sci.* **11**(3), 950 (2021), doi: 10.3390/app11030950.

[28] M. Maiuri, M. Garavelli, and G. Cerullo: "Ultrafast spectroscopy: State of the art and open challenges", *J. Am. Chem. Soc.* **142**(1), 3–15 (2020), doi: 10.1021/jacs.9b10533.

[29] J. Jang, J. Park, and H. J. Shin: "Terahertz spectral analysis: An in-depth exploration of spectroscopy approaches for ultrafast dynamics", *Curr. Appl. Phys.* **59**, 197–207 (2024), doi: 10.1016/j.cap.2023.11.015.

[30] E. F. Nichols: "A study of the transmission spectra of certain substances in the infra-red", *Phys. Rev. (Ser. I)* **1**(1), 1–18 (1893), doi: 10.1103/physrevseriesi.1.1.

[31] G. P. Williams: "Filling the THz gap—high power sources and applications", *Rep. Prog. Phys.* **69**(2), 301–326 (2006), doi: 10.1088/0034-4885/69/2/R01.

[32] Rohde & Schwarz: "FPC1500 Spektrumanalysator", available at: `https://www.rohde-schwarz.com/de/produkte/messtechnik/benchtop-analysatoren/rs-fpc-spektrumanalysator_63493-542324.html`.

[33] Anritsu Company: "VectorStar Family of RF, microwave, mmW VNAs", available at: `https://www.anritsu.com/en-in/test-measurement/products/ms4640b-series`.

[34] Rohde & Schwarz: "Millimeterwave Converters", available at: `https://www.rohde-schwarz.com/ae/products/test-and-measurement/converters/rs-zcxxx-millimeterwave-converters_63493-133190.html`.

[35] D. Koller, S. Durant, C. Rowland, E. Bryerton, and J. Hesler: "Initial measurements with wm164 (1.1–1.5 THz) VNA extenders", *41st International Conference on Infrared, Millimeter, and Terahertz Waves (IRMMW-THz)*, Baltimore, MD, USA (2016), doi: 10.1109/irmmw-thz.2016.7758434.

[36] Virginia Diodes Inc: "Vector Network Analyzer Extenders", available at: `https://www.vadiodes.com/en/products/vector-network-analyzer-extension-modules`.

[37] Toptica Photonics AG: "TeraScan", available at: `https://www.toptica.com/products/terahertz-systems/frequency-domain/terascan`.

[38] Toptica Photonics AG: "TeraFlash pro", available at: `https://www.toptica.com/products/terahertz-systems/time-domain/teraflash-pro`.

[39] A. R. Criado, C. de Dios, P. Acedo, and H. L. Hartnagel. "New concepts for a Photonic Vector Network Analyzer based on THz heterodyne phase-coherent techniques", *7th European Microwave Integrated Circuit Conference*, Nuremberg, Germany (2012).

[40] J.-M. Rämer and G. von Freymann: "A terahertz time-domain spectroscopy-based network analyzer", *J. Lightwave Technol.* **33**(2), 403–407 (2015), doi: 10.1109/jlt.2015.2388954.

[41] F. R. Faridi and S. Preu: "Pulsed free space two-port photonic vector network analyzer with up to 2 THz bandwidth", *Opt. Express* **29**(8), 12278–12291 (2021), doi: 10.1364/oe.418120.

[42] A. D. J. F. Olvera, A. K. Mukherjee, and S. Preu: "A fully optoelectronic continuous-wave 2-port vector network analyzer operating from 0.1 THz to 1 THz", *IEEE J. Microw.* **1**(4), 1015–1022 (2021), doi: 10.1109/jmw.2021.3107472.

[43] Rohde & Schwarz: "Ultrastabiles, abstimmbares THz-System für 6G auf photonischer Basis", available at: `https://www.rohde-schwarz.com/de/unternehmen/news-und-presse/all-news/rohde-schwarz-praesentiert-auf-der-eumw-2024-ultrastabiles-abstimmbares-thz-system-fuer-6g-auf-photonischer-basis-pressemitteilungen-detailseite_229356-1519478.html`.

[44] S. Yokoyama, R. Nakamura, M. Nose, T. Araki, and T. Yasui: "Terahertz spectrum analyzer based on a terahertz frequency comb", *Opt. Express* **16**(17), 13052–13061 (2008), doi: 10.1364/OE.16.013052.

[45] T. Yasui, R. Nakamura, K. Kawamoto, A. Ihara, Y. Fujimoto, S. Yokoyama, H. Inaba, K. Minoshima, T. Nagatsuma, and T. Araki: "Real-time monitoring of continuous-wave terahertz radiation using a fiber-based, terahertz-comb-referenced spectrum analyzer", *Opt. Express* **17**(19), 17034–17043 (2009), doi: 10.1364/OE.17.017034.

[46] G. Hu, T. Mizuguchi, X. Zhao, T. Minamikawa, T. Mizuno, Y. Yang, C. Li, M. Bai, Z. Zheng, and T. Yasui: "Measurement of absolute frequency of continuous-wave terahertz radiation in real time using a free-running, dual-wavelength mode-locked, erbium-doped fibre laser", *Sci. Rep.* **7**(1), 42082 (2017), doi: 10.1038/srep42082.

[47] A. D. J. Fernandez Olvera, B. L. Krause, and S. Preu: "A true optoelectronic spectrum analyzer for millimeter waves with Hz resolution", *IEEE Access* **9**, 114339–114347 (2021), doi: 10.1109/ACCESS.2021.3105030.

[48] K. Wynne and J. J. Carey: "An integrated description of terahertz generation through optical rectification, charge transfer, and current surge", *Opt. Commun.* **256**(4–6), 400–413 (2005), doi: 10.1016/j.optcom.2005.06.065.

[49] N. E. Yu, C. Jung, C.-S. Kee, Y. L. Lee, B.-A. Yu, D.-K. Ko, J. Lee, W.-J. Lee, J.-E. Kim, and H. Y. Park: "Terahertz generation in quasi-phase-matching structures using femtosecond laser pulses", *J. Korean Phys. Soc.* **51**(2), 493–497 (2007), doi: 10.3938/jkps.51.493.

[50] G. Chattopadhyay, E. Schlecht, J. S. Ward, J. J. Gill, H. H. S. Javadi, F. Maiwald, and I. Mehdi: "An all-solid-state broad-band frequency multiplier chain at 1500 GHz", *IEEE Trans. Microw. Theory Techn.* **52**(5), 1538–1547 (2004), doi: 10.1109/TMTT.2004.827042.

[51] A. Maestrini, J. Ward, J. Gill, H. Javadi, E. Schlecht, G. Chattopadhyay, F. Maiwald, N. R. Erickson, and I. Mehdi: "A 1.7–1.9 THz local oscillator source", *IEEE Microw. Wireless Compon. Lett.* **14**(6), 253–255 (2004), doi: 10.1109/LMWC.2004.828027.

[52] R. Köhler, A. Tredicucci, F. Beltram, H. E. Beere, E. H. Linfield, A. G. Davies, D. A. Ritchie, R. C. Iotti, and F. Rossi: "Terahertz semiconductor-heterostructure laser", *Nature* **417**(6885), 156–159 (2002), doi: 10.1038/417156a.

[53] B. S. Williams: "Terahertz quantum-cascade lasers", *Nature Photonics* **1**(9), 517–525 (2007), doi: 10.1038/nphoton.2007.166.

[54] L. Ajili, G. Scalari, J. Faist, H. Beere, E. Linfield, D. Ritchie, and G. Davies: "High power quantum cascade lasers operating at $\lambda = 87$ and $130\,\mu$m", *Appl. Phys. Lett.* **85**, 3986–3988 (2004), doi: 10.1063/1.1810217.

[55] G. Scalari, C. Walther, M. Fischer, R. Terazzi, H. Beere, D. Ritchie, and J. Faist: "THz and sub–THz quantum cascade lasers", *Laser Photon. Rev.* **3**(1-2), 45–66 (2009), doi: 10.1002/lpor.200810030.

[56] L. Gao, C. Feng, and X. Zhao: "Recent developments in terahertz quantum cascade lasers for practical applications", *Nanotechnology Reviews* **12**, 20230115 (2023), doi: 10.1515/ntrev-2023-0115.

[57] D. Grischkowsky, S. Keiding, M. van Exter, and C. Fattinger: "Far-infrared time-domain spectroscopy with terahertz beams of dielectrics and semiconductors", *J. Opt. Soc. Am. B* **7**(10), 2006-2015 (1990), doi: 10.1364/JOSAB.7.002006.

[58] A. Maestrini, B. Thomas, H. Wang, C. Jung, J. Treuttel, Y. Jin, G. Chattopadhyay, I. Mehdi, and G. Beaudin: "Schottky diode-based terahertz frequency multipliers and mixers", *Comptes Rendus Phys.* **11**(7-8), 480–495 (2010), doi: 10.1016/j.crhy.2010.05.002.

[59] M. Dyakonov and M. Shur: "Detection, mixing, and frequency multiplication of terahertz radiation by two-dimensional electronic fluid", *IEEE Trans. Electron Devices* **43**(3), 380–387 (1996), doi: 10.1109/16.485650.

[60] E. Brundermann, H.-W. Hübers, and M. F. Kimmitt: *Terahertz Techniques*, vol. 151 of *Springer Series in Optical Sciences*, Springer, Heidelberg and New York (2010), ISBN: 978-3-642-02591-4.

[61] N. M. Burford and M. O. El-Shenawee: "Review of terahertz photoconductive antenna technology", *Opt. Eng.* **56**(1), 010901 (2017), doi: 10.1117/1.OE.56.1.010901.

[62] H. A. Hafez, X. Chai, A. Ibrahim, S. Mondal, D. Férachou, X. Ropagnol, and T. Ozaki: "Intense terahertz radiation and their applications", *J. Opt.* **18**(9), 093004 (2016), doi: 10.1088/2040-8978/18/9/093004.

[63] E. Isgandarov, X. Ropagnol, M. Singh, and T. Ozaki: "Intense terahertz generation from photoconductive antennas", *Front. Optoelectron.* **14**(1), 64–93 (2021), doi: 10.1007/s12200-020-1081-4.

[64] H. Hertz: 'Über einen Einfluss des ultravioletten Lichtes auf die electrische Entladung", *Ann. Phys. Chem.* **267**(8), 983–1000 (1887), doi: 10.1002/andp.18872670827.

[65] A. Einstein: "Über einen die Erzeugung und Verwandlung des Lichtes betreffenden heuristischen Gesichtspunkt", *Ann. Phys.* **517**(S1), 164–181 (2005), doi: 10.1002/andp.2005517S111.

[66] D. H. Auston, K. P. Cheung, and P. R. Smith: "Picosecond photoconducting Hertzian dipoles", *Appl. Phys. Lett.* **45**(3), 284–286 (1984), doi: 10.1063/1.95174.

[67] E. R. Brown, K. A. McIntosh, F. W. Smith, M. J. Manfra, and C. L. Dennis: "Measurements of optical-heterodyne conversion in low-temperature-grown GaAs", *Appl. Phys. Lett.* **62**(11), 1206–1208 (1993), doi: 10.1063/1.108735.

[68] E. R. Brown, F. W. Smith, and K. A. McIntosh: "Coherent millimeter-wave generation by heterodyne conversion in low-temperature-grown GaAs photoconductors", *J. Appl. Phys.* **73**(3), 1480–1484 (1993), doi: 10.1063/1.353222.

[69] H. F. Mataré: "Field dependence of photoresponse and heterodyning of optical signals", *Int. J. Electron.* **19**(5), 405–437 (1965), doi: 10.1080/00207216508937829.

[70] H.-J. Song, N. Shimizu, T. Furuta, K. Suizu, H. Ito, and T. Nagatsuma: "Broadband-frequency-tunable sub-terahertz wave generation using an optical comb, AWGs, optical switches, and a uni-traveling carrier photodiode for spectroscopic applications", *J. Lightwave Technol.* **26**(15), 2521–2530 (2008), doi: 10.1109/JLT.2008.927170.

[71] E. Rouvalis, C. C. Renaud, D. G. Moodie, M. J. Robertson, and A. J. Seeds: "Traveling-wave uni-traveling carrier photodiodes for continuous wave THz generation", *Opt. Express* **18**(11), 11105–11110 (2010), doi: 10.1364/OE.18.011105.

[72] S. Preu, F. H. Renner, S. Malzer, G. H. Döhler, L. J. Wang, M. Hanson, A. C. Gossard, T. L. J. Wilkinson, and E. R. Brown: "Efficient terahertz emission from ballistic transport enhanced n-i-p-n-i-p superlattice photomixers", *Appl. Phys. Lett.* **90**(21), 211121 (2007), doi: 10.1063/1.2743400.

[73] G. Carpintero, E. Garcia-Munoz, H. Hartnagel, S. Preu, and A. Räisänen: *Semiconductor Terahertz Technology: Devices and Systems at Room Temperature Operation*, John Wiley & Sons Inc, Hoboken, NJ (2015), ISBN: 978-1-118-92040-4.

[74] B. E. A. Saleh and M. C. Teich: *Fundamentals of Photonics*, 3rd edition, John Wiley & Sons Inc, Hoboken, NJ (2019), ISBN: 978-1-118-77009-2.

[75] R. Singh, C. Rockstuhl, C. Menzel, T. P. Meyrath, M. He, H. Giessen, F. Lederer, and W. Zhang: "Spiral-type terahertz antennas and the manifestation of the Mushiake principle", *Opt. Express* **17**(12), 9971–9980 (2009), doi: 10.1364/oe.17.009971.

[76] S. M. Sze: *Physics of Semiconductor Devices*, 3rd edition, Wiley-Interscience online books, John Wiley & Sons Inc, Hoboken, NJ (2006), ISBN: 978-0-470-06832-8.

[77] M. S. Alam, M. S. Rahman, M. R. Islam, A. G. Bhuiyan, and M. Yamada: "Refractive index, absorption coefficient, and photoelastic constant: Key parameters of InGaAs material relevant to InGaAs-based device performance", *19th International Conference on Indium Phosphide & Related Materials (ICIPRM)*, Sapporo, Japan (2007), doi: 10.1109/iciprm.2007.381193.

[78] R. Safian, G. Ghazi, and N. Mohammadian: "Review of photomixing continuous-wave terahertz systems and current application trends in terahertz domain", *Opt. Eng.* **58**(11), 110901 (2019), doi: 10.1117/1.OE.58.11.110901.

[79] K. A. McIntosh, K. B. Nichols, S. Verghese, and E. R. Brown: "Investigation of ultrashort photocarrier relaxation times in low-temperature-grown GaAs", *Appl. Phys. Lett.* **70**(3), 354–356 (1997), doi: 10.1063/1.118412.

[80] N. Vashistha, M. Kumar, R. K. Singh, D. Panda, L. Tyagi, and S. Chakrabarti: "A comprehensive study of ultrafast carrier dynamics of LT-GaAs: Above and below bandgap regions", *Physica B* **602**, 412441 (2021), doi: 10.1016/j.physb.2020.412441.

[81] I. Cámara Mayorga: *Photomixers as tunable terahertz local oscillators*, Dissertation, Bonn (2008), available at `https://core.ac.uk/download/pdf/304637504.pdf`.

[82] S. Verghese, K. A. McIntosh, and E. R. Brown: "Highly tunable fiber-coupled photomixers with coherent terahertz output power", *IEEE Trans. Microw. Theory Techn.* **45**(8), 1301–1309 (1997), doi: 10.1109/22.618428.

[83] C. A. Balanis: *Antenna Theory: Analysis and Design*, 3rd edition, John Wiley & Sons, New York, NY (2012), ISBN: 978-1-118-58573-3.

[84] S. Verghese, K. A. McIntosh, and E. R. Brown: "Optical and terahertz power limits in the low-temperature-grown GaAs photomixers", *Appl. Phys. Lett.* **71**(19), 2743–2745 (1997), doi: 10.1063/1.120445.

[85] D. Mittleman (ed.): *Sensing with Terahertz Radiation*, vol. 85 of *Springer Series in Optical Sciences*, Springer Berlin Heidelberg, Berlin and Heidelberg (2003), ISBN: 978-3-540-45601-8.

[86] G. Santarelli, A. Clairon, S. N. Lea, and G. M. Tino: "Heterodyne optical phase-locking of extended-cavity semiconductor lasers at 9 GHz", *Opt. Commun.* **104**(4-6), 339–344 (1994), doi: 10.1016/0030-4018(94)90567-3.

[87] Á. R. Criado, C. de Dios, G. H. Döhler, S. Preu, S. Malzer, S. Bauerschmidt, H. Lu, A. C. Gossard, and P. Acedo: "Ultra-narrow linewidth CW sub-THz generation using GS-based OFCG and N-i-PN-i-P superlattice photomixers", *Electron. Lett.* **48**(22), 1425 (2012), doi: 10.1049/el.2012.3158.

[88] K. Balakier, M. J. Fice, F. van Dijk, G. Kervella, G. Carpintero, A. J. Seeds, and C. C. Renaud: "Optical injection locking of monolithically integrated photonic source for generation of high purity signals above 100 GHz", *Opt. Express* **22**(24), 29404–29412 (2014), doi: 10.1364/OE.22.029404.

[89] G. Nazarikov, S. Rommel, W. Yao, and I. Tafur Monroy: "Optical injection locking for generation of tunable low-noise millimeter wave and THz signals", *Appl. Sci.* **11**(21), 10185 (2021), doi: 10.3390/app112110185.

[90] R. J. B. Dietz, B. Globisch, H. Roehle, D. Stanze, T. Göbel, and M. Schell: "Influence and adjustment of carrier lifetimes in InGaAs/InAlAs photoconductive pulsed terahertz detectors: 6 THz bandwidth and 90 dB dynamic range", *Opt. Express* **22**(16), 19411–19422 (2014), doi: 10.1364/OE.22.019411.

[91] Q. Wu and X.-C. Zhang: "Free-space electro-optic sampling of terahertz beams", *Appl. Phys. Lett.* **67**(24), 3523–3525 (1995), doi: 10.1063/1.114909.

[92] A. Nahata, D. H. Auston, T. F. Heinz, and C. Wu: "Coherent detection of freely propagating terahertz radiation by electro-optic sampling", *Appl. Phys. Lett.* **68**(2), 150–152 (1996), doi: 10.1063/1.116130.

[93] P. U. Jepsen, C. Winnewisser, M. Schall, V. Schyja, Keiding, and H. Helm: "Detection of THz pulses by phase retardation in lithium tantalate", *Phys. Rev. E* **53**(4), R3052–R3054 (1996), doi: 10.1103/physreve.53.r3052.

[94] A. Nahata, J. T. Yardley, and T. F. Heinz: "Free-space electro-optic detection of continuous-wave terahertz radiation", *Appl. Phys. Lett.* **75**(17), 2524–2526 (1999), doi: 10.1063/1.125065.

[95] N. C. J. van der Valk, T. Wenckebach, and P. C. M. Planken: "Full mathematical description of electro-optic detection in optically isotropic crystals", *J. Opt. Soc. Am. B* **21**(3), 622 (2004), doi: 10.1364/JOSAB.21.000622.

[96] P. C. M. Planken, H.-K. Nienhuys, H. J. Bakker, and T. Wenckebach: "Measurement and calculation of the orientation dependence of terahertz pulse detection in ZnTe", *J. Opt. Soc. Am. B* **18**(3), 313 (2001), doi: 10.1364/JOSAB.18.000313.

[97] B. Pradarutti, G. Matthäus, S. Riehemann, G. Notni, S. Nolte, and A. Tünnermann: "Highly efficient terahertz electro-optic sampling by material optimization at 1060 nm", *Opt. Commun.* **281**(19), 5031–5035 (2008), doi: 10.1016/j.optcom.2008.06.055.

[98] S. Casalbuoni, H. Schlarb, B. Schmidt, P. Schmüser, B. Steffen, and A. Winter: "Numerical studies on the electro-optic detection of femtosecond electron bunches", *Phys. Rev. ST Accel. Beams* **11**(7), 072802 (2008), doi: 10.1103/physrevstab.11.072802.

[99] M. Nagai, K. Tanaka, H. Ohtake, T. Bessho, T. Sugiura, T. Hirosumi, and M. Yoshida: "Generation and detection of terahertz radiation by electro-optical process in GaAs using 1.56 μm fiber laser pulses", *Appl. Phys. Lett.* **85**(18), 3974–3976 (2004), doi: 10.1063/1.1813645.

[100] C. Vicario, C. Ruchert, and C. P. Hauri: "High field broadband THz generation in organic materials", *J. Mod. Opt.* **62**(18), 1480–1485 (2015), doi: 10.1080/09500340.2013.800242.

[101] D. M. Pozar: *Microwave Engineering*, 4th edition, John Wiley & Sons Inc, Hoboken, NJ (2017), ISBN: 978-8-126-54190-4.

[102] A. Maestrini, J. S. Ward, J. J. Gill, H. S. Javadi, E. Schlecht, C. Tripon-Canseliet, G. Chattopadhyay, and I. Mehdi: "A 540-640-GHz High-Efficiency Four-Anode Frequency Tripler", *IEEE Trans. Microw. Theory Techn.* **53**(9), 2835–2843 (2005), doi: 10.1109/tmtt.2005.854174.

[103] S. Makhlouf, O. Cojocari, M. Hofmann, T. Nagatsuma, S. Preu, N. Weimann, H.-W. Hübers, and A. Stöhr: *Terahertz Sources and Receivers: From the Past to the Future*, IEEE (2023), doi: 10.36227/techrxiv.23227130.

[104] J. C. Pearson, B. J. Drouin, A. Maestrini, I. Mehdi, J. Ward, R. H. Lin, S. Yu, J. J. Gill, B. Thomas, C. Lee, G. Chattopadhyay, E. Schlecht, F. W. Maiwald, P. F. Goldsmith, and P. Siegel: "Demonstration of a Room Temperature 2.48-2.75 THz Coherent Spectroscopy Source", *Rev. Sci. Instrum.* **82**(9), 093105 (2011), doi: 10.1063/1.3617420.

[105] E. Bryerton, S. Retzloff, and J. Hesler: "High-power submillimeter wave solid-state sources", *12th Global Symposium on Millimeter Waves (GSMM)* in Orlando, FL, USA (2019), doi: 10.1109/gsmm.2019.8797648.

[106] I. Mehdi, J. V. Siles, C. Lee, and E. Schlecht: "THz Diode Technology: Status, Prospects, and Applications", *Proc. IEEE* **105**(6), 990–1007 (2017), doi: 10.1109/jproc.2017.2650235.

[107] Y. Zhang, C. Wu, X. Liu, L. Wang, C. Dai, J. Cui, Y. Li, and N. Kinar: "The Development of Frequency Multipliers for Terahertz Remote Sensing System", *Remote Sens.* **14**(10), 2486 (2022), doi: 10.3390/rs14102486.

[108] ACST GmbH: "ACST sources", available at: `https://acst.de/product-category/thz-sources/`.

[109] A. Maestrini, J. S. Ward, C. Tripon-Canseliet, J. J. Gill, C. Lee, H. Javadi, G. Chattopadhyay, and I. Mehdi: "In-phase power-combined frequency triplers at 300 GHz", *IEEE Microw. Wirel. Compon. Lett.* **18**(3), 218–220 (2008), doi: 10.1109/lmwc.2008.916820.

[110] I. Capan: "4H-SiC Schottky barrier diodes as radiation detectors: A review", *Electronics* **11**(4), 532 (2022), doi: 10.3390/electronics11040532.

[111] W. C. B. Peatman and T. W. Crowe: "Design and fabrication of 0.5 micron GaAs Schottky barrier diodes for low-noise terahertz receiver applications", *Int. J. Infrared Millim. Waves* **11**(3), 355–365 (1990), doi: 10.1007/BF01010434.

[112] A. Rogalski: "Progress in performance development of room temperature direct terahertz detectors", *J. Infrared Millim. Terahertz Waves* **43**(9–10), 709–727 (2022), doi: 10.1007/s10762-022-00882-2.

[113] M. T. Faber, J. Chramiec, and M. E. Adamski: *Microwave and Millimeter-Wave Diode Frequency Multipliers*, Artech House Microwave Library, Artech House, Boston, MA (1995), ISBN: 0-89006-611-6.

[114] S. Bennetts, G. D. McDonald, K. S. Hardman, J. E. Debs, C. C. N. Kuhn, J. D. Close, and N. P. Robins: "External cavity diode lasers with 5 kHz linewidth and 200 nm tuning range at 1.55 μm and methods for linewidth measurement", *Opt. Express* **22**(9), 10642–10654 (2014), doi: 10.1364/OE.22.010642.

[115] W. D. Lee, J. C. Campbell, R. J. Brecha, and H. J. Kimble: "Frequency stabilization of an external-cavity diode laser", *Appl. Phys. Lett.* **57**(21), 2181–2183 (1990), doi: 10.1063/1.103928.

[116] J. Hult, I. S. Burns, and C. F. Kaminski: "Wide-bandwidth mode-hop-free tuning of extended-cavity GaN diode lasers", *Appl. Opt.* **44**(18), 3675–3685 (2005), doi: 10.1364/ao.44.003675.

[117] S. D. Saliba, M. Junker, L. D. Turner, and R. E. Scholten: "Mode stability of external cavity diode lasers", *Appl. Opt.* **48**(35), 6692–6700 (2009), doi: 10.1364/AO.48.006692.

[118] G. Morthier and P. Vankwikelberge: *Handbook of Distributed Feedback Laser Diodes*, 2nd edition, Artech House Applied Photonics Series, Artech House, Boston (2013), ISBN: 978-1-60807-701-4.

[119] M. Xiang, Y. Zhang, G. Li, C. Liu, Q. Chen, Q. Lu, L. Huang, M. Lu, J. DoneGan, and W. Guo: "Wide-waveguide high-power low-RIN single-mode distributed feedback laser diodes for optical communication", *Opt. Express* **30**(17), 30187–30197 (2022), doi: 10.1364/oe.464598.

[120] C. Ye: *Tunable external cavity diode lasers*, EBSChost eBook Collection, World Scientific Publishing Co Pte Ltd, Hackensack, NJ (2004), ISBN: 978-981-256-088-9

[121] A. L. Schawlow and C. H. Townes: "Infrared and optical masers", *Phys. Rev.* **112**(6), 1940–1949 (1958), doi: 10.1103/physrev.112.1940.

[122] X. Pan, H. Olesen, and B. Tromborg: "Spectral linewidth of DFB lasers including the effects of spatial holeburning and nonuniform current injection", *IEEE Photon. Technol. Lett.* **2**(5), 312–315 (1990), doi: 10.1109/68.54690.

[123] J. E. Carroll, J. Whiteaway, and D. Plumb: *Distributed Feedback Semiconductor Lasers*, vol. 10 of *IEE Circuits, Devices and Systems Series*, The Institution of Electrical Engineers and SPIE Optical Engineering Press, London (1998), ISBN: 0-85296-917-1.

[124] D. S. Patil (ed.): *Semiconductor Laser Diode: Technology and Applications*, IntechOpen, London (2012), ISBN: 978-953-510549-7.

[125] U. Tietze and C. Schenk: *Halbleiter-Schaltungstechnik: Neuer Teil: nachrichtentechnische Schaltungen*, 12. Auflage, Springer, Berlin and Heidelberg (2002), ISBN: 978-3-540-42849-7.

[126] W. K. Ho, K. W. Lim, and W. Xu: "Optimal gain and phase margin tuning for PID controllers", *Automatica* **34**(8), 1009–1014 (1998), doi: 10.1016/S0005-1098(98)00032-6.

[127] D. Rytting: "ARFTG 50 year network analyzer history", *71st ARFTG Microwave Measurement Conference*, Anaheim, CA, USA, (2008), doi: 10.1109/ARFTG.2008.4633319.

[128] B. B. Balsley: *A Portable, Frequency-Coherent Spectrum Analyzer for Radar Applications*, Environmental Research Laboratories (1971).

[129] R. J. Matheson: "Automated spectrum analysis", *Proceedings of the IEEE* **66**(4), 392–402 (1978), doi: 10.1109/PROC.1978.10931.

[130] John F. Mason: "Aerospace and military: Progress in space structure research, aircraft landing systems, integrated optics, and digital communications", *IEEE Spectrum* **16**(1), 71–75 (1979), doi: 10.1109/MSPEC.1979.6368072.

[131] J. Luo, E. Mendivil, M. Christopher, and T. Chou: "On the measurement of radiated power for 5G mobile device with spectrum analyzer", *14th European Conference on Antennas and Propagation (EuCAP)*, Copenhagen, Denmark (2020), doi: 10.23919/EuCAP48036.2020.9135480.

[132] N. Khalid, N. A. Abbasi, and O. B. Akan: "Statistical characterization and analysis of low-THz communication channel for 5G Internet of Things", *Nano Commun. Netw.* **22**, 100258 (2019), doi: 10.1016/j.nancom.2019.100258.

[133] E. M. Wei, R. A. Chamberlin, N. Kilmer, J. Kast, J. A. Connors, and D. Williams: "On-wafer vector-network-analyzer measurements at MK temperatures", *IEEE J. Microw.* **3**, 587–598 (2023), doi: 10.1109/jmw.2022.3232076.

[134] E. J. Riley, E. H. Lenzing, and R. M. Narayanan: "Characterization of carbon fiber composite materials for RF applications", *Radar Sensor Technology XVIII*, SPIE Proceedings, 907704 (2014), doi: 10.1117/12.2050132.

[135] K. Pubby, K. Vijay Babu, and S. Bindra Narang: "Magnetic, elastic, dielectric, microwave absorption and optical characterization of cobalt-substituted nickel spinel ferrites", *Mater. Sci. Eng. B* **255**, 114513 (2020), doi: 10.1016/j.mseb.2020.114513.

[136] A. D. Helfrick: *Electrical Spectrum and Network Analyzers: A Practical Approach*, Academic Press, San Diego, CA (1991), ISBN: 0-12-338250-5.

[137] S. A. Imam and V. K. Sachan: *Electronic Measurement and Instrumentation*, I.K. International Publishing House Pvt. Ltd, New Delhi (2018), ISBN: 978-93-86768-13-1.

[138] Anritsu Corporation: "Vector Network Analyzers", available at: `https://www.anritsu.com/en-us/test-measurement/products/ms4640b-series`.

[139] Keysight Technologies: "VNA measurement errors", available at: `https://helpfiles.keysight.com/csg/e5080b/S3_Cals/Errors.htm`.

[140] M. Hiebel: *Fundamentals of Vector Network Analysis*, 8th edition, Rohde & Schwarz, München (2019), ISBN: 978-3-939837-06-0.

[141] T. Okoshi, K. Kikuchi, and A. Nakayama: "Novel method for high resolution measurement of laser output spectrum", *Electron. Lett.* **16**, 630–631 (1980), doi: 10.1049/el:19800437.

[142] P. Gallion and G. Debarge: "Quantum phase noise and field correlation in single frequency semiconductor laser systems", *IEEE J. Quantum Electron.* **20**(4), 343–349 (1984), doi: 10.1109/jqe.1984.1072399.

[143] B. Rein: *Drei-Photonen Kohärenzeffekte in Quecksilberdampf*, Dissertation, Technische Universität Darmstadt (2016), available at: `https://tuprints.ulb.tu-darmstadt.de/5862/1/Dissertation_Rein.pdf`.

[144] L. B. Mercer: "1/f frequency noise effects on self-heterodyne linewidth measurements", *J. Lightwave Technol.* **9**(4), 485–493 (1991), doi: 10.1109/50.76663.

[145] Z. Fang, F. Wei, F. Yang, D. Chen, Q. Ye, H. Cai, and R. Qu: "Line shape of a delayed self-heterodyne varied with noise types and delays", *Appl. Opt.* **61**(13), 3761–3770 (2022), doi: 10.1364/AO.455130.

[146] L. Richter, H. Mandelberg, M. Kruger, and P. McGrath: "Linewidth determination from self-heterodyne measurements with subcoherence delay times", *IEEE J. Quantum Electron.* **22**(11), 2070–2074 (1986), doi: 10.1109/jqe.1986.1072909.

[147] Z. Zhao, Z. Bai, D. Jin, Y. Qi, J. Ding, B. Yan, Y. Wang, Z. Lu, and R. P. Mildren: "Narrow laser-linewidth measurement using short delay self-heterodyne interferometry", *Opt. Express* **30**(17), 30600–30610 (2022), doi: 10.1364/OE.455028.

[148] W. Rhee and Z. Yu: *Phase-Locked Loops: System Perspectives and Circuit Design Aspects*, Wiley-IEEE Press, Hoboken, NJ (2023), ISBN: 978-1-119-90906-4.

[149] M. Deumer, S. Breuer, R. Kohlhaas, S. Nellen, L. Liebermeister, S. Lauck, M. Schell, and B. Globisch: "Continuous wave terahertz receivers with 4.5 THz bandwidth and 112 dB dynamic range", *Opt. Express* **29**(25), 41819 (2021), doi: 10.1364/OE.443098.

[150] C. C. Homes, G. L. Carr, R. P. S. M. Lobo, J. D. Laveigne, and D. B. Tanner: "Silicon beam splitter for far-infrared and terahertz spectroscopy", *Appl. Opt.* **46**(32), 7884–7888 (2007), doi: 10.1364/AO.46.007884.

[151] A. Theis, M. Kocybik, G. von Freymann, and F. Friederich: "Free-space terahertz spectrum analysis with an optoelectronic hybrid system", *IEEE Trans. Terahertz Sci. Technol.* **13**(6), 688–697 (2023), doi: 10.1109/TTHZ.2023.3301450.

[152] S. Daryoosh: *Handbook of Terahertz Technology for Imaging, Sensing and Communications*, WP Woodhead Publishing, Oxford, England and Philadelphia, PA (2013), ISBN: 978-0-85709-649-4.

[153] P. Yagoubov, W. J. Vreeling, and P. de Korte: "Characterization of an integrated lens antenna at terahertz frequencies", *Sci. Rep.* **12**, 1476 (2022), doi: 10.1038/s41598-022-05338-0.

[154] P. Kittara, G. Yassin, and S. Withington: "Theoretical analysis of the Pickett Potter horn-reflector antenna for submillimetre-wave applications", *MTT/ED/AP/LEO Societies Joint Chapter United Kingdom and Republic of Ireland Section*, 139–144 (1999), doi: 10.1109/hfpsc.1999.809294.

[155] J. Dittmer, J. Tebart, P. Matalla, S. Wagner, A. Tessmann, A. Bhutani, C. Koos, A. Stöhr, and S. Randel: "Comparison of electronic and optoelectronic signal generation for (sub-)THz communications", *Int. J. Microw. Wireless Technol.*, 1–11 (2024), doi: 10.1017/s1759078724000667.

[156] Y. Shan, Y. Liang, C. Li, W. Sun, and Z. Fang: "Review of recent progress on solid–state millimeter–wave and terahertz signal sources", *Int. J. Circuit Theory Appl.* **52**(1), 439–472 (2024), doi: 10.1002/cta.3726.

[157] Virginia Diodes Inc: "Spectrum Analyzer Extension Modules", available at: `https://www.vadiodes.com/en/products/spectrum-analyzer`.

[158] B. L. Krause, A. D. J. Fernandez Olvera, and S. Preu: "Photonic spectrum analyzer for wireless signals in the THz range", *IEEE Access* **10**, 42061–42068 (2022), doi: 10.1109/access.2022.3168162.

[159] N. T. Yardimci and M. Jarrahi: "Nanostructure-enhanced photoconductive terahertz emission and detection", *Small* **14**(44), e1802437 (2018), doi: 10.1002/smll.201802437.

[160] A. E. Yachmenev, D. V. Lavrukhin, I. A. Glinskiy, N. V. Zenchenko, Y. G. Goncharov, I. E. Spektor, R. A. Khabibullin, T. Otsuji, and D. S. Ponomarev: "Metallic and dielectric metasurfaces in photoconductive terahertz devices: A review", *Opt. Eng.* **59**(6), 061608 (2020), doi: 10.1117/1.OE.59.6.061608.

[161] H. Murakami, T. Takarada, and M. Tonouchi: "Low-temperature GaAs-based plasmonic photoconductive terahertz detector with Au nano-islands", *Photonics Res.* **8**(9), 1448 (2020), doi: 10.1364/prj.395517.

[162] O. Mitrofanov, R. J. Thompson, T. Siday, I. Brener, T. S. Luk, and J. L. Reno: "Nanostructured photoconductive terahertz detector for near-field microscopy", *41st International Conference on Infrared, Millimeter, and Terahertz Waves (IRMMW-THz)*, Hong Kong, China (2016), doi: 10.1109/IRMMW-THz.2016.7758750.

[163] Keysight Technologies: "Spectrum analyzer basics", available at: `https://citeseerx.ist.psu.edu/document?repid=rep1&type=pdf&doi=fbe0bd00db704c2ac8f3f8a74d041d587eeba321`.

[164] D. F. Filipovic, S. S. Gearhart, and G. M. Rebeiz: "Double-slot antennas on extended hemispherical and elliptical silicon dielectric lenses", *IEEE Trans. Microwave Theory Tech.* **41**(10), 1738–1749 (1993), doi: 10.1109/22.247919.

[165] H. Page, S. Malik, M. Evans, I. Gregory, I. Farrer, and D. Ritchie: "Waveguide coupled terahertz photoconductive antennas: Toward integrated photonic terahertz devices", *Appl. Phys. Lett.* **92**(16), 163502 (2008), doi: 10.1063/1.2909539.

[166] S. Iwamatsu, M. Ali, J. L. Fernández Estévez, M. Grzeslo, S. Makhlouf, A. Rivera, G. Carpintero, and A. Stöhr: "Terahertz photodiode integration with multi-octave-bandwidth dielectric rod waveguide probe", *Opt. Lett.* **48**(23), 6275–6278 (2023), doi: 10.1364/OL.504354.

[167] A. Theis, M. Kocybik, M. Bauer, G. von Freymann, and F. Friederich: "Enhancing vector network analysis with a photonic frequency extender setup", *IEEE Trans. Microwave Theory Tech.* **73**(8), 5372–5382 (2025), doi: 10.1109/TMTT.2025.3549530.

[168] M. Naftaly: *Terahertz Metrology*, Artech House, Norwood, MA (2014), ISBN: 978-1-60807-777-9.

[169] Anritsu Company: "Understanding VNA calibration", available at: `https://anlage.umd.edu/Anritsu_understanding-vna-calibration.pdf`.

[170] B. Will and I. Rolfes: "A new approach on broadband calibration methods for free space applications", *IEEE/MTT-S International Microwave Symposium Digest*, Montreal, Canada (2012), doi: 10.1109/MWSYM.2012.6259615.

[171] A. Koike and N. Sugimoto: "Temperature dependences of optical path length in inorganic glasses", available at: `https://www.agc.com/en/innovation/library/pdf/56-01.pdf`.

[172] T. A. Hahn, R. K. Kirby, H. C. Wolfe, M. G. Graham, and H. E. Hagy: "Thermal expansion of fused silica from 80 to 1000 K – standard reference material 739", *AIP Conf. Proc.* **3**(1), 13–24 (1972), doi: 10.1063/1.2948551.

[173] T. Toyoda and M. Yabe: "The temperature dependence of the refractive indices of fused silica and crystal quartz", *J. Phys. D: Appl. Phys.* **16**(5), L97–L100 (1983), doi: 10.1088/0022-3727/16/5/002.

[174] I. H. Malitson: "Interspecimen comparison of the refractive index of fused silica", *J. Opt. Soc. Am.* **55**(10), 1205 (1965), doi: 10.1364/JOSA.55.001205.

[175] Y. Demirhan, H. Alaboz, L. Ozyuzer, M. A. Nebioğlu, T. Takan, H. Altan, and C. Sabah: "Metal mesh filters based on Ti, ITO and Cu thin films for terahertz waves", *Opt. Quantum Electron.* **48**(2), 1–11 (2016), doi: 10.1007/s11082-016-0427-z.

[176] D. W. Porterfield, J. L. Hesler, R. Densing, E. R. Mueller, T. W. Crowe, and R. M. Weikle II: "Resonant metal-mesh bandpass filters for the far infrared", *Appl. Opt.* **33**(25), 6046–6052 (1994), doi: 10.1364/AO.33.006046.

[177] M. A. Tarasov, von d. Gromov, G. D. Bogomolov, E. A. Otto, and L. S. Kuzmin: "Fabrication and characteristics of mesh band-pass filters", *Instrum. Exp. Tech.* **52**(1), 74–78 (2009), doi: 10.1134/S0020441209010114.

[178] Dassault Systèmes: "CST Studio Suite", available at: `https://www.3ds.com/products/simulia/cst-studio-suite`.

[179] R. J. Cameron, C. M. Kudsia, and R. R. Mansour: *Microwave Filters for Communication Systems*, John Wiley & Sons Inc, Hoboken, NJ (2018). ISBN: 978-1-118-27434-7.

[180] S. Nellen, T. Ishibashi, A. Deninger, R. B. Kohlhaas, L. Liebermeister, M. Schell, and B. Globisch: "Experimental comparison of UTC- and PIN-photodiodes for continuous-wave terahertz generation", *J. Infrared Millim. Terahertz Waves* **41**(4), 343–354 (2020), doi: 10.1007/s10762-019-00638-5.

[181] R. W. Boyd: *Nonlinear optics*, 3rd edition, Academic Press, Amsterdam and Boston, MA (2008), ISBN: 978-0-12-369470-6.

[182] N. Bloembergen: "Conservation laws in nonlinear optics", *J. Opt. Soc. Am.* **70**(12), 1429 (1980), doi: 10.1364/JOSA.70.001429.

[183] H. Tang, C. Yang, L. Qin, L. Liang, Y. Lei, P. Jia, Y. Chen, Y. Wang, Y. Song, C. Qiu, C. Zheng, X. Li, D. Li, and L. Wang: "A review of high-power semiconductor optical amplifiers in the 1550 nm band", *Sensors (Basel)* **23**(17) (2023), doi: 10.3390/s23177326.

[184] G. P. Agrawal: "Population pulsations and nondegenerate four-wave mixing in semiconductor lasers and amplifiers", *J. Opt. Soc. Am. B* **5**(1), 147 (1988), doi: 10.1364/JOSAB.5.000147.

[185] A. Uskov, J. Mork, and J. Mark: "Wave mixing in semiconductor laser amplifiers due to carrier heating and spectral-hole burning", *IEEE J. Quantum Electron.* **30**(8), 1769–1781 (1994), doi: 10.1109/3.301641.

[186] K. Kikuchi, M. Amano, C. E. Zah, and T. P. Lee: "Analysis of origin of nonlinear gain in 1.5 μm semiconductor active layers by highly nondegenerate four-wave mixing", *Appl. Phys. Lett.* **64**(5), 548–550 (1994), doi: 10.1063/1.111099.

[187] Q. Wang, H. Rideout, F. Zeng, and J. Yao: "Millimeter-wave frequency tripling based on four-wave mixing in a semiconductor optical amplifier", *IEEE Photonics Technol. Lett.* **18**(23), 2460–2462 (2006), doi: 10.1109/LPT.2006.886826.

[188] I. Koltchanov, S. Kindt, K. Petermann, S. Diez, R. Ludwig, R. Schnabel, and H. G. Weber: "Gain dispersion and saturation effects in four-wave mixing in semiconductor laser amplifiers", *IEEE J. Quantum Electron.* **32**(4), 712–720 (1996), doi: 10.1109/3.488846.

[189] S. Diez, C. Schmidt, R. Ludwig, H. G. Weber, K. Obermann, S. Kindt, I. Koltchanov, and K. Petermann: "Four-wave mixing in semiconductor optical amplifiers for frequency conversion and fast optical switching", *IEEE J. Sel. Top. Quantum Electron.* **3**(5), 1131–1145 (1997), doi: 10.1109/2944.658587.

[190] F. Girardin, J. Eckner, G. Guekos, R. Dall'Ara, A. Mecozzi, A. D'Ottavi, F. Martelli, S. Scotti, and P. Spano: "Low-noise and very high-efficiency four-wave mixing in 1.5-mm-long semiconductor optical amplifiers", *IEEE Photonics Technol. Lett.* **9**(6), 746–748 (1997), doi: 10.1109/68.584977.

[191] F. Martelli, A. Mecozzi, A. D'Ottavi, S. Scotti, P. Spano, R. Dall'Ara, J. Eckner, and G. Guekos: "Noise in wavelength conversion using four-wave mixing in semiconductor optical amplifiers", *Appl. Phys. Lett.* **70**(3), 306–308 (1997), doi: 10.1063/1.118400.

[192] C. Politi, D. Klonidis, and M. J. O'Mahony: "Dynamic behavior of wavelength converters based on FWM in SOAs", *IEEE J. Quantum Electron.* **42**(2), 108–125 (2006), doi: 10.1109/JQE.2005.861822.

[193] T. Wang, M. Chen, H. Chen, and S. Xie: "Millimetre-wave signal generation using FWM effect in SOA", *Electron. Lett.* **43**(1), 36–38 (2007), doi: 10.1049/el:20072637.

[194] R. Paiella, G. Hunziker, U. Koren, and K. J. Vahala: "Polarization-dependent optical nonlinearities of multiquantum-well laser amplifiers", *IEEE J. Sel. Top. Quantum Electron.* **3**(2), 529–540 (1997), doi: 10.1109/2944.605704.

[195] B. Sridhar, H. R. D. Sunak, B. R. Strauss, and S. P. Bastien: "Experimental measurement of gain in erbium-doped fluoride fiber amplifier in the 850-nm signal band", *IEEE Photonics Technol. Lett.* **8**(2), 215–217 (1996), doi: 10.1109/68.484245.

[196] M. Smit, X. Leijtens, E. Bente, J. van der Tol, H. Ambrosius, D. Robbins, M. Wale, N. Grote, and M. Schell: "Generic foundry model for InP-based photonics", *IET Optoelectron.* **5**(5), 187–194 (2011), doi: 10.1049/iet-opt.2010.0068.

[197] Z. Xiao, W. Liu, S. Xu, J. Zhou, Z. Ren, and C. Lee: "Recent progress in silicon-based photonic integrated circuits and emerging applications", *Adv. Opt. Mater.* **11**(20) (2023), doi: 10.1002/adom.202301028.

[198] F. van Dijk, A. Accard, A. Enard, O. Drisse, D. Make, and F. Lelarge: "Monolithic dual wavelength DFB lasers for narrow linewidth heterodyne beat-note generation", *International Topical Meeting on Microwave Photonics jointly held with the Asia-Pacific Microwave Photonics Conference*, Singapore (2011), doi: 10.1109/MWP.2011.6088672.

[199] T. Göbel, D. Stanze, U. Troppenz, J. Kreissl, B. Sartorius, and M. Schell: "Integrated continuous-wave THz control unit with 1 THz tuning range", *37th International Conference on Infrared, Millimeter, and Terahertz Waves (IRMMW-THz)*, Wollongong, Australia (2012), doi: 10.1109/IRMMW-THz.2012.6380405.

[200] J. W. Zimmerman, R. K. Price, U. Reddy, N. L. Dias, and J. J. Coleman: "Narrow linewidth surface-etched DBR lasers: Fundamental design aspects and applications", *IEEE J. Sel. Top. Quantum Electron.* **19**(4), 1503712 (2013), doi: 10.1109/JSTQE.2013.2260731.

[201] M. Sun, S. Tan, F. Guo, S. Liu, Q. Kan, D. Lu, R. Zhang, W. Zhao, S. Liang, W. Wang, R. Broeke, F. M. Soares, and C. Ji: "Integrated four-wavelength DFB diode laser array for continuous-wave THz generation", *IEEE Photonics J.* **8**(4), 1–8 (2016), doi: 10.1109/JPHOT.2016.2580940.

[202] S. Jia, M.-C. Lo, L. Zhang, O. Ozolins, A. Udalcovs, D. Kong, X. Pang, R. Guzman, X. Yu, S. Xiao, S. Popov, J. Chen, G. Carpintero, T. Morioka, H. Hu, and L. K. Oxenløwe: "Integrated dual-laser photonic chip for high-purity carrier generation enabling ultrafast terahertz wireless communications", *Nat. Commun.* **13**(1), 1388 (2022), doi: 10.1038/s41467-022-29049-2.

[203] S. Arafin, A. Simsek, S.-K. Kim, S. Dwivedi, W. Liang, D. Eliyahu, J. Klamkin, A. Matsko, L. Johansson, L. Maleki, M. Rodwell, and L. Coldren: "Towards chip-scale optical frequency synthesis based on optical heterodyne phase-locked loop", *Opt. Express* **25**(2), 681–695 (2017), doi: 10.1364/OE.25.000681.

[204] X. Shen, R. Costanzo, P. Singaraju, T. N. Blalock, A. Beling, and S. M. Bowers: "Compact heterogeneously integrated optical phase-locked loop for 10 GHz to 40 GHz optical frequency difference locking", *J. Lightwave Technol.* **42**(8), 2784–2791 (2024), doi: 10.1109/JLT.2024.3351090.

[205] Y. Wang, Y. Jiao, and K. Williams: "Scaling photonic integrated circuits with InP technology: A perspective", *APL Photonics* **9**(5), 050902 (2024), doi: 10.1063/5.0200861.

[206] JePPIX: "JePPIX – the Joint European Platform for Photonic Integrated Components", available at: `https://www.jeppix.eu/`.

[207] JePPIX ROADMAP 2015: "The road to a multi-billion euro market in integrated photonics", available at: `https://www.jeppix.eu/wp-content/uploads/2020/04/JePPIXRoadmap2015.pdf`.

[208] QPIC1550: "QPIC1550 project", available at: `https://qpic1550-project.eu/`.

[209] A. Rumiantsev and N. Ridler: "VNA calibration", *IEEE Microw. Mag.* **9**(3), 86–99 (2008), doi: 10.1109/MMM.2008.919925.

[210] N. Shoaib: *Vector Network Analyzer (VNA) Measurements and Uncertainty Assessment*, 1st edition, Springer International Publishing, Cham (2017), ISBN: 978-3-319-44772-8.

Publications

Peer-Reviewed Publications

[**P1**] A. Theis, M. Kocybik, G. von Freymann, and F. Friederich: "Free-space Terahertz Spectrum Analysis With an Optoelectronic Hybrid System", *IEEE Trans. Terahertz Sci. Technol.* **13**(6), 688–697 (2023), doi: 10.1109/TTHZ.2023.3301450.

[**P2**] A. Theis, M. Kocybik, M. Bauer, G. von Freymann, and F. Friederich: "Enhancing Vector Network Analysis With a Photonic Frequency Extender Setup", *IEEE Trans. Microw. Theory Techn.* **73**(8), 5372–5382 (2025), doi: 10.1109/TMTT.2025.3549530.

Conference Proceedings

[**C1**] A. Theis, G. von Freymann, and F. Friederich: "Phase-locking of the beat signal of two distributed feedback diode lasers to a frequency tunable local oscillator", *10th THz Young Scientists Meeting / French-German THz Conference*, Frankfurt am Main, Germany (2019).

[**C2**] A. Theis, M. Kocybik, G. von Freymann, and F. Friederich: "Free space Terahertz Spectrum Analysis with a Hybrid System", *10th International Workshop on Terahertz Technology and Applications*, Kaiserslautern, Germany (2022).

[**C3**] A. Theis, M. Kocybik, G. von Freymann, and F. Friederich: "Free-space Terahertz Spectrum Analysis with an Optoelectronic Hybrid System", *48th International Conference on Infrared, Millimeter and Terahertz Waves (IRMMW-THz)*, Montreal, Canada (2023).

[**C4**] A. Theis, M. Kocybik, G. von Freymann, and F. Friederich: "Free-space Terahertz Measurements with a Photonic Spectrum Analyzer", *14th Terahertz Young Scientists Meeting*, Kaiserslautern, Germany (2024).

[**C5**] A. Theis, M. Kocybik, G. von Freymann, and F. Friederich: "Continuous-wave Photonic Terahertz Frequency Synthesis for Spectrum and Vector Network Analysis", *49th International Conference on Infrared, Millimeter and Terahertz Waves (IRMMW-THz)*, Perth, Australia (2024).

Acknowledgments

I must admit that the past years have been quite a journey — filled with excitement, inspiration, fulfillment, and not least, a fair share of stress and challenges. Now, as I sit here at the end of this path, it feels both surreal and rewarding to look back. In these acknowledgements, I want to express my deepest appreciation to all the people who have supported, encouraged, and accompanied me through this intense and transformative period of my life.

First and foremost, I would like to express my sincere gratitude to my advisor, **Prof. Dr. Georg von Freymann**, for his support and valuable input throughout my PhD. I feel very fortunate to have been given the opportunity to work on such a fascinating and challenging topic in such a great environment. His trust in my work and the academic freedom I was granted throughout this journey are things I deeply appreciate.
I would also like to sincerely thank **Prof. Dr. Mathias Weiler** for kindly agreeing to be the second examiner of this thesis. I truly appreciate the time and effort he dedicated to evaluating my work, as well as his interest in the topic.
My deepest and most extraordinary thanks go to **Dr. Fabian Friederich**, who acted as my direct advisor throughout my thesis. His continuous support, encouragement, and deep understanding of the subject were essential throughout every stage of this work. Without his inspiring ideas and technical expertise, this project would not have been possible. I am especially grateful for the tremendous effort he put into acquiring the necessary equipment and creating the right conditions for this research — even when there was hardly any budget to begin with. Furthermore, I truly appreciated the many fruitful discussions both in and outside the lab. Despite his demanding schedule, he was always approachable and had an open ear for my questions, concerns, and ideas.
A very big thank you goes to **Michael Kocybik**, who supported me not only during his master's thesis but even more so in the time that followed. It was always a pleasure working with you — even during the many frustrating weeks (or months) in the lab when nothing seemed to work as expected, or the long days (and nights) before a paper deadline. Your perseverance and positive attitude helped make those challenges more manageable. Over time, you became not only a reliable colleague, but also a good friend. I wish you all the best on your way to your PhD!
I would also like to thank **Dr. Maris Bauer**, **Raphael Hussung**, **Dr. Daniel Molter**, and **Mirco Kutas** for their valuable support throughout my work. Maris helped me tremendously with proofreading several papers and contributed many helpful ideas and suggestions along the way. Raphael's technical expertise in electronics was an immense help on many occasions, and I'm especially grateful for his patience and practical advice when things got complicated. Daniel and Mirco supported me with their

broad and in-depth knowledge of optics, always offering insightful input and solutions to a wide range of optical challenges.
Further, I want to express my appreciation to **Dominik Gundacker**, **Dmytro Kharik**, and **Carsten Matheis** for their essential technical support. They played a key role in designing and manufacturing many components of the demonstrator system. Their practical expertise and reliability greatly contributed to the success of the experimental setup.
For the great working atmosphere that made coming to work each day truly enjoyable, I would like to sincerely thank all my current and former colleagues in the **Department of Material Characterization and Testing** at **Fraunhofer ITWM**. I especially thank **Dr. Tobias Pfeiffer** and **Dr. Karl Henrik May** for organizing memorable barbecue events on the rooftop terrace and LAN parties in the seminar room, which added a special sense of community beyond everyday work.
Last, but by no means least, I owe my greatest thanks to **my family** and **close friends**. Your continuous support, patience, and faith in me have been the foundation that carried me through this entire journey.

Da nicht alle von euch fließend Englisch sprechen — und weil ich auf Deutsch einfach besser ausdrücken kann, was ich wirklich fühle — möchte ich den letzten Teil meiner Danksagung auf Deutsch schreiben.
Mein größter Dank gilt meinen Eltern, **Ingrid** und **Klaus Theis**. Ihr habt mir über all die Jahre den nötigen Freiraum gegeben, eigene Wege zu gehen, Entscheidungen zu treffen und an Herausforderungen zu wachsen. Euer Vertrauen, eure Geduld und eure bedingungslose Unterstützung haben mir stets den Rücken gestärkt – nicht nur während dieser Arbeit, sondern weit darüber hinaus.
Ein ganz besonderer Dank geht auch an meinen Bruder **Maximilian** und seine Frau **Lena**. **Max**, du warst für mich immer eine verlässliche Stütze – ehrlich, direkt und hilfsbereit. Deine klare und pragmatische Art hat mir oft geholfen, den Überblick zu behalten und mich auf die wirklich wichtigen Dinge zu konzentrieren.
Meiner Freundin **Michelle Stegner** möchte ich an dieser Stelle ebenfalls von Herzen danken. Auch wenn du erst gegen Ende dieser Arbeit an meiner Seite warst, hast du mich mit viel Verständnis begleitet und mir in stressigen Phasen geholfen, wieder zur Ruhe zu kommen und den Fokus nicht zu verlieren.
Ein herzliches Dankeschön geht auch an meine vielen engen Freunde, die mich immer wieder daran erinnert haben, dass das Leben nicht nur aus Arbeit besteht. Mit gemeinsamen Unternehmungen, Urlauben und unvergesslichen Momenten habt ihr mir geholfen, den Kopf frei zu bekommen und neue Kraft zu schöpfen.

Den letzten Teil dieser Danksagung möchte ich meinem verstorbenen Vater widmen. Auch wenn du den Abschluss dieser Arbeit nicht mehr miterleben konntest, warst du in Gedanken immer bei mir. Vieles von dem, was mich heute ausmacht, habe ich durch dich gelernt — deine Haltung, deine ruhige und besonnene Art und deine Fähigkeit, auch in schwierigen Situationen stets zu wissen, was zu tun ist. Du fehlst, aber dein Einfluss ist geblieben. Diese Arbeit widme ich dir.

Alexander Theis

Curriculum Vitae

Academic Background

04/2011–03/2017 **Diploma in Physics**, Technical University of Kaiserslautern (TUK)
Thesis: *"Design und Optimierung eines FMCW Terahertz Messsystems für die Schichtdickenmessung"*
Fraunhofer Institute for Industrial Mathematics (ITWM)

01/2018–10/2025 **PhD Researcher**, University of Kaiserslautern–Landau (RPTU)
and Fraunhofer Institute for Industrial Mathematics (ITWM)

Research Experience

04/2015–06/2015 **Industrial Internship**, Prüf- und Forschungsinstitut (PFI), Pirmasens

03/2016–12/2024 **Research Assistant**, Fraunhofer Institute for Industrial Mathematics (ITWM), Kaiserslautern

Fachbereich Physik

Rheinland-Pfälzische Technische
Universität Kaiserslautern Landau

Postfach 3049
67653 Kaiserslautern, Germany

www.physik.rptu.de/

Rheinland-Pfälzische
Technische Universität
Kaiserslautern
Landau